Numerical Investigation of the Steady-State Interaction Between Surface Effect Ship Seals, Air Cushion, Free-Surface Waves, and Vessel Motion

by

Matthew Robert Kramer

A dissertation submitted in partial fulfillment
of the requirements for the degree of
Doctor of Philosophy
(Naval Architecture and Marine Engineering)
in the University of Michigan
2013

Doctoral Committee:

Associate Professor Yin Lu Young, Chair
Professor Steven L. Ceccio
Associate Professor Dale G. Karr
Assistant Professor Kevin J. Maki
Associate Professor Joaquim R. R. A. Martins
Brant R. Savander, Maritime Research Associates, LLC

“Somewhere, something incredible is waiting to be known.”

– *Carl Sagan*

©Matthew Robert Kramer

2013

For Amanda

Acknowledgments

I would first like to thank Professor Young. Without her constant support and guidance, this thesis would never have reached completion. It is rare to find someone so passionate about their work. I would also like to thank the rest of my committee members, whose guidance and impact cannot be overlooked.

Sir Isaac Newton once said "If I have seen further it is by standing on the shoulders of giants." I would like to thank Professor Lawrence Doctors, without whose foundational work this thesis would not be possible, and whose insightful discussions have helped me immeasurably over the past few years. I would also like to thank Mr. Bob Wilson for his endless enthusiasm and support, without which I may never have been able to find an interest in such a topic. I hope that this work has helped to confirm some of the things that you witnessed first-hand during the early days of SES development.

Finally, I would like to thank and acknowledge the assistance of Ms. Kelly Cooper of the US Navy Office of Naval Research for travel funds through grants N00014-10-1-0170 and N00014-11-1-0833, and I would like to acknowledge my primary source of funding, which was provided by the Department of Defense via the National Defense Science and Engineering Graduate fellowship.

TABLE OF CONTENTS

LIST OF FIGURES

LIST OF TABLES

LIST OF APPENDICES

LIST OF ABBREVIATIONS

2-D Two-Dimensional

ACV Air Cushion Vehicle

CFD Computational Fluid Dynamics

DoF Degree of Freedom

EEDI Energy Efficiency Design Index

FEM Finite Element Method

FSI Fluid-Structure Interaction

IMO International Maritime Organization

RANS Reynolds-Averaged Navier-Stokes

SES Surface Effect Ship

SESPO Surface Effect Ship Program Office

SIT Stevens Institute of Technology

SS Sea State

SSBM Stay-Stiffened Bag and Membrane

T-Craft Transformable Craft

VOF Volume of Fluid

VSV Very Slender Vessel

WIG Wing in Ground Effect Vessel

LIST OF SYMBOLS

A wave amplitude

A_C cushion area

B_C cushion beam

B chord length at the base

b pressure element width

C_i influence coefficient of pressure element i

C_{ij} influence coefficient at point j due to element i

C_l 2-D lift coefficient

C_d 2-D drag coefficient

C_m 2-D moment coefficient

C_l' standard deviation of 2-D lift coefficient

C_d' standard deviation of 2-D drag coefficient

$\mathcal{D}$ drag

$\mathcal{D}_{\mathrm{tot}}$ total drag (air and hydrodynamic)

d draft

E Young's modulus

$\bar{E}$ non-dimensional Young's modulus

Fr_b Froude number based on the element width

Fr_C Froude number based on the cushion length

Fr_i Froude number based on twice the immersed length

Fr_h immersion-depth-based Froude number

F_{int} internal tensile force

F_{tip} vertical tip force

f_F frictional form factor

f_W wave resistance form factor

$\mathbf{g}$ gravitational acceleration vector

g gravitational acceleration

h transom submergence depth

h_{step} step height

h_{SA} stern seal height

h_{SF} bow seal height

h_{base} pressure head at the base of the dam

$\bar{h}_{\text{base}}$ non-dimensional pressure head at the base of the dam

I_z mass-moment of inertia

K_δ torsional spring stiffness

k_0 fundamental wave number

$\mathcal{L}$ lift

L_w wetted length

L_a afterbody length

L_i immersed length

$\mathcal{L}_{\text{tot}}$ total lift (air and hydrodynamic)

L_C cushion length

L_{CG} Longitudinal center of gravity

ℓ_s total arc length of seal membrane material

ℓ initial arc length of the membrane

$\bar{\ell}$ non-dimensional initial arc length of the membrane

$\mathcal{M}$ moment

$\mathcal{M}_{\text{tot}}$ total moment (air and hydrodynamic)

$\mathcal{M}_o$ moment about the hinge point

m mass

$\hat{\mathbf{n}}$ normal vector into the fluid

$\hat{\mathbf{t}}$ tangent vector

P_C cushion pressure

P_s seal pressure

$P_{s,f}$ bow seal pressure

P_{atm} atmospheric pressure

P_{base} pressure at the base of the dam

$\mathbf{P}$ power

p total pressure

p^* dynamic pressure

p_∞ far-field pressure

p_o pressure element strength

p_{kutta} assumed (desired) trailing edge pressure

p_{TE} pressure of trailing edge element

R_A correlation resistance

R_a air resistance

R_F frictional resistance

$R_{F,\mathrm{SW}}$ sidewall frictional resistance

R_H transom stern resistance

R_M momentum resistance

R_S seal resistance

R_T total resistance

R_W wave resistance

Re_i Reynolds number based on twice the immersed length

Re_w Reynolds number based on the wetted length

Re_s Reynolds number based on wetted arc length

$\mathcal{R}$ residual

s s-coordinate

s arc length coordinate

S wetted surface area of the sidehulls

t time

$t_{\max}$ maximum simulation time

U forward speed

$\mathbf{u}$ fluid velocity vector

$\mathbf{w}$ vector of nodal displacements

V_s ship speed

$\mathbf{x}$ spatial location vector

$\mathbf{x}_B$ body coordinate

x x-coordinate

x_B x-coordinate of body surface

x_o pressure element location

x_{CG} x-location of center of gravity

x_{CR} x-location of center of rotation

$\mathbf{x}_{CR}$ center of rotation

y y-coordinate

y_B y-coordinate of body surface

y_{CG} y-location of center of gravity

y_{CR} y-location of center of rotation

z z-coordinate

α volume fraction

α_s longitudinal smoothing factor

β angle of attack

β_s transverse smoothing factor

η free surface elevation

Δ vessel displacement

δ seal deformation angle

Δh_{tip} tip deflection

λ far field wavelength

λ_0 nondimensional x-location

μ fluid dynamic viscosity

μ_w water dynamic viscosity

μ_a air dynamic viscosity

ν_w water kinematic viscosity

ν_a air kinematic viscosity

Φ velocity potential in an earth-fixed reference frame

ϕ velocity potential in a body-fixed reference frame

ρ fluid density

ρ_w water density

ρ_a air density

θ trim angle

τ fluid shear stress

ABSTRACT

The calm-water resistance for Surface Effect Ships (SESs) is studied with consideration for bow and stern seal interaction effects. Existing methods for SES resistance prediction have been unable to accurately predict bow/stern seal drag, which have been experimentally observed to be dominant in some cases in the low-speed regime. Prediction of the total resistance in the low-speed regime is of particular importance for SESs intended to operate at relatively low speeds ($\approx 40\,\mathrm{knots}$) to ensure adequate propulsion power is installed to surpass the secondary drag hump.

The primary objective of this work is to study the effects of bow/stern seal interaction on SES total resistance in steady-state operations. A simple, effective, 2-D numerical model is developed based on coupling a linearized potential-flow solver with a single-degree-of-freedom seal model and rigid body vessel motion model. Systematic validation studies are shown for the fluid and solid models. The resistance of a model-scale SES is predicted with both rigid and flexible seals to determine the influence of seal flexibility. The predicted seal resistance and vessel motion, as well as surface wave patterns, are compared with published experimental results.

The numerical model is found to offer accurate predictions for the low-speed resistance of SES seal drag and vessel motion. When combined with other methods for predicting the other components of resistance, the total resistance is predicted reasonably accurately across a large range of Froude numbers. In addition, the physical mechanism that causes the large drag hump at lower speeds is identified as being related to the interaction of the bow seal wave with the stern seal. This interaction is found to be most important at

the subhump and to become relatively minor at higher speeds. Thus, a hybrid method is proposed where the numerical model for seal drag is used at low speeds and a more traditional prediction method that ignores seal effects is used at higher speeds, where seal effects are small. Based on the results of this work, it may be possible to improve SES seal designs and overall vessel performance by introducing the possibility for actively-controlled morphing/contouring seals.

CHAPTER 1

Introduction

1.1 Overview

A Surface Effect Ship (SES) is a type of high-speed marine vessel that is partially supported by an air cushion, with the goal of minimizing ship resistance to allow for higher-speed operations. The SES concept was originally developed by Mr. Allen Ford in 1960 as a solution to the air-leakage problem for hovercraft-type vessels, which allow air to leak from beneath the entire perimeter of the vessel. Instead, an SES has two rigid catamaran sidehulls designed to restrict air leakage from the port and starboard sides, thus limiting air leakage to the bow and stern only. Minimizing the leakage enables the required power of the lift fan system to be reduced.

Several prototype and operational SESs have been developed over the past fifty years. Correspondingly, many design tools have been developed as a means of performance prediction. One of the most important aspects of performance prediction is the ability to accurately estimate the full-scale resistance in order to ensure adequate powering. Prediction of drag for SESs introduces several complexities compared to traditional non-air-supported vessels. These complexities are associated with modeling of the air cushion and lift fan system, as well as the seals (or skirts), which aid in minimizing air leakage at the bow and stern.

Drag predictions for SESs typically ignore the effects of the seals on the vessel per-

formance, or use simplified models that ignore the interaction between the bow and stern seals, and have been shown to be accurate at high speeds ($Fr_C > 0.5$, where Fr_C is the Froude number based on the cushion length) using hydrodynamic models based both on potential-flow theory as well as more recent Computational Fluid Dynamics (CFD) tools. Experimental results have shown, however, that for certain SESs, the bow- and stern-seal-generated wave systems interact at lower speeds, leading to a large change (often an increase) in the total resistance at the secondary drag hump ($Fr_C \approx 0.3 - 0.45$). Although this interaction has been observed experimentally, it has not been captured by existing drag-prediction methods. It is important to capture this interaction in order to ensure that the vessel will have adequate installed power to surpass the secondary drag hump to reach higher speeds, and to determine the root physical cause, with the goal being to offer advice to designers on how to minimize resistance in the low-speed regime.

The primary objective of this thesis is to develop a numerical model for predicting the resistance of SES seals with consideration for the interaction of the seals, air cushion, free-surface waves, and vessel motion. By developing and validating the numerical model, the physics of this interaction are studied in order to provide insight into possible design modifications that may help minimize the amount of required installed power, thus enabling a lighter craft with higher attainable speeds.

By applying the numerical method, several major findings will be presented. First, a simple method for incorporating the bow/stern seal wave interaction has been developed, allowing these effects to be calculated using a relatively simple and efficient Two-Dimensional (2-D) potential-flow-based model fully coupled with a rotational spring-supported seal model. By incorporating seal-generated wave interaction, the magnitude and speed of the secondary drag hump may be accurately predicted. The physical causes of the secondary and primary drag humps are identified, and possible means for avoiding the large increase in drag are explored. Finally, the effects of seal flexibility on the drag at the secondary hump are examined, opening up the possibility for global drag reductions by using

actively- or passively-controlled adaptive/contouring seals.

This chapter provides a brief background of the development history of SESs as well as a description of the physical concept that drove the early development of SESs, and their continued development today. A brief overview of the performance characteristics is then given, as well as a review of past modeling efforts for SES performance prediction to highlight the important physical attributes for which there are knowledge gaps that the work presented in this thesis intends to fill. The objectives of this work are then presented in a more formal manner and the organization is discussed.

1.2 Historical and Physical Context

As our ancestors first took to the sea, a sequence of events was initiated, eventually leading to the globalization of trade and culture. Today, new means for trans-oceanic transportation, commerce, and military support are continually being developed, primarily consisting of maritime vessels and aircraft. Maritime options tend generally to offer the benefits of larger carrying capacities and higher transport efficiency per tonnage-mile, while air-borne craft offer the benefits of higher speeds with the penalty of a lower payload. For global improvements to be made, improvements in both classes of craft must be realized, particularly when increased energy efficiency requirements in the near future are considered (e.g. International Maritime Organization (IMO) Energy Efficiency Design Index (EEDI) (EED, 2012)).

Since the advent of large ships, the standards for ship design have continually evolved, with major innovations leading to significant improvements in vessel performance. Through the incremental improvement of ship subsystems, and recently through the application of systems-engineering concepts to ship design, ships have generally improved to the point where many modern monohull displacement ships have reached a near-optimum with physically-imposed maximum speeds in the 30-40 knot range.[1] In order to push the bound-

[1]This statement assumes a "well-rounded" ship and not specially-built high-speed, light displacement

ary for the maximum speed of surface craft, new and innovative ship design technologies must be developed that can "change the game" by taking advantage of new physical phenomena and by operating in previously unexplored or unimagined regimes.

One major impedance to ships that can operate at very high speeds is the amount of propulsion power required, which is directly related to the total resistance (drag) of the vessel. Many concepts have been proposed to answer the call for drag reduction, including catamarans, trimarans, Very Slender Vessels (VSVs), Wing in Ground Effect Vessels (WIGs), and Air Cushion Vehicles (ACVs), among others. The term Air Cushion Vehicle generally refers to any vessel that is largely supported by an air cushion, which provides lift support by raising the air pressure beneath the vessel. Examples of ACVs include plenum-chamber craft (a.k.a. hovercraft), peripheral-jet craft, and sidehull ACVs, often called Surface Effect Ships (SESs).

The general concept of an ACV is illustrated in Fig. 1.1. These craft aim to achieve significant reductions in frictional drag by fully or partially supporting the weight of the hull using a pressurized volume of air contained beneath the vessel, thereby reducing the wetted area. The pressurized volume of air, referred to as the plenum or "pressure cushion," is typically generated by a lift fan system fed by air from the atmosphere. To minimize the amount of air that escapes from beneath the vessel (leakage), flexible skirts are typically included to conform to the shape of the water surface. Air leakage is thus minimized to reduce the required fan power, making the concept feasible.

The ACV concept essentially aims to take advantage of the scaling behavior of the various power requirements to minimize the required power at higher speeds. In order to provide further explanation for the mechanics that drive the development of ACVs, it is useful to compare the relative magnitudes of the various power requirements, as illustrated in Fig. 1.2. Consider a notional plenum-chamber craft, a.k.a. hovercraft, with a fixed vessel displacement (Δ) supported by a fixed cushion pressure (P_C) applied over a fixed cushion

vessels

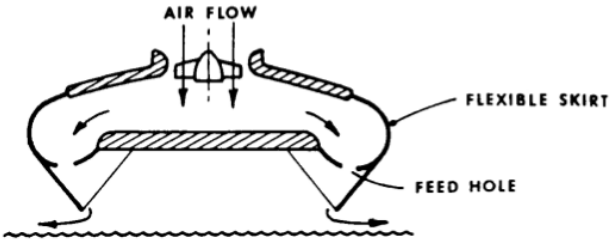

Figure 1.1: An example of a plenum-chamber craft illustrating the Air Cushion Vehicle (ACV) concept. The craft is supported by a high-pressure air cushion (plenum), which is created via a lift fan system. (from Doctors, 1985)

area (A_C), as shown in Fig. 1.3. In this case, the entire hull weight is supported by air pressure and the wetted area is nominally zero. The cushion pressure required to support the total displacement is given by the relation $P_C = \Delta / A_C$. In order to raise the pressure of the air to P_C, power must be provided to the fans. Based on a first-order analysis, where changes in leakage due to changes in trim and free-surface profile are ignored, the power required by the fan system is relatively constant over the range of operating speeds since the power required for the fans to generate a constant pressure head is also constant.

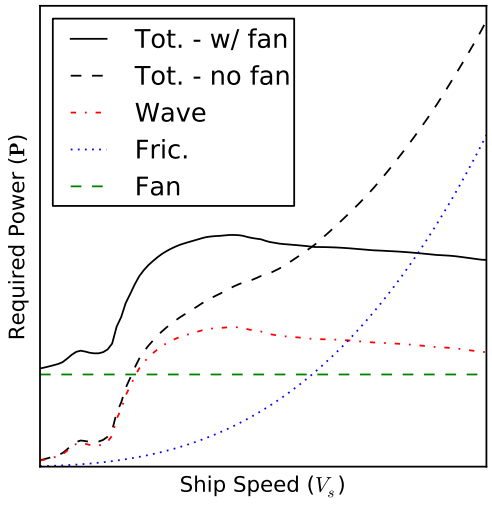

Figure 1.2: Illustration of various power requirements for a notional ACV

In contrast, frictional resistance (R_F) for a traditional displacement vessel is on first-order approximation a function of the square of ship speed (V_s), i.e. $R_F \propto {V_s}^2$. The

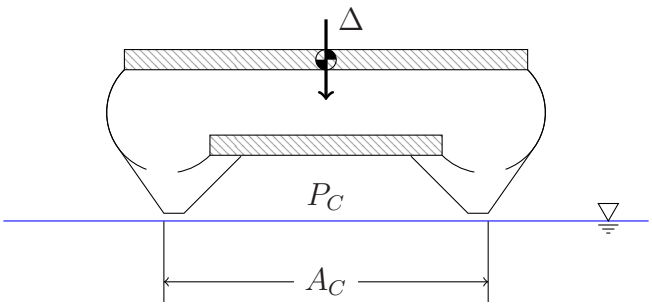

Figure 1.3: Notional ACV showing terminology

required power (P) to overcome the frictional resistance resistance is therefore proportional to the cube of the velocity, i.e. $\mathrm{P}_F \propto {V_s}^3$. By supporting a majority of the weight of the vessel by a pressure cushion, the frictional drag contribution resulting from contact with the water is removed (or at least drastically reduced), although there will still be a resistance contribution due to the frictional and form drag from the air. By significantly reducing the frictional drag contribution due to contact with the water, as long as the intended operating speed is high, the power required to run the lift fan system may be lower than the power that would be required to overcome frictional resistance if the vessel was not air-supported. If the wave resistance is assumed to remain unchanged by the presence of an air cushion, a simple estimate of the total resistance with and without a pressure cushion may be made. As shown in Fig. 1.2, an air-supported craft may require less power at higher speeds (e.g. $30 - 50\,\mathrm{kn}$), enabling the craft to reach higher speeds for the same amount of installed power.

Although the power requirements are difficult to estimate without detailed analyses, and there is no guarantee that an air-supported craft will require less power than a non-air-supported craft, the tradeoff between fan power and power to overcome frictional resistance is essential to the feasibility of the ACV concept. The simple analysis presented in this section is intended as a demonstration of the concept only and should not be taken as a generalized comparison of air-supported and non-air-supported craft. When comparing different types of craft for a given mission, careful consideration must be given to power-

ing requirements, cargo capacity, transport efficiency, and speed capability, among other factors.

1.3 The Surface Effect Ship

1.3.1 Concept

Fully-supported ACVs exhibit inherent performance deficiencies, including poor maneuvering and low payload capabilities, due to the large amounts of air leakage from beneath the perimeter of the craft. To combat these negative effects, the concept of a rigid-sidehull ACV, typically referred to as a Surface Effect Ship (SES), was developed, the idea being that the two immersed sidewalls will prevent leakage from the sides of the vessel and limit pressure losses to the bow and stern regions. A comprehensive review of the technological development history of SESs is given by Butler (1985), however a brief overview will now be given for the unfamiliar reader.

An SES is a type of ACV that is partially supported by a pressurized air cushion while the remaining buoyant force is provided by two rigid sidehulls. In a sense, an SES can be viewed as a hybrid between a hovercraft and a catamaran, taking advantage of both attributes. An illustration of the underside of an SES is shown in Fig. 1.4. The air cushion is contained by the inner walls of the two sidehulls and flexible, rigid, or semi-rigid bow and stern seals. Since the sidehulls are immersed, the amount of air leakage from the cushion is significantly reduced compared to a sidewall-less ACV. The intent of an SES is to combine the drag benefits offered by an ACV with improved maneuvering, seakeeping, low-speed performance, and higher cargo capacity of a catamaran, yielding a more well-rounded vessel that can perform well at both low and high speeds. An additional benefit that should not be overlooked is that traditional marine propulsion options, such as propellers and waterjets, may be used as opposed to less-efficient air fans, which must be used in the absence of sidehulls.

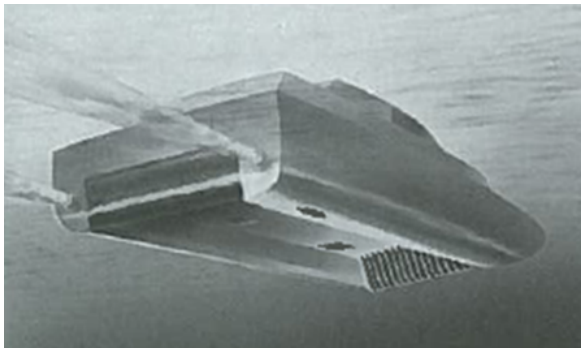

Figure 1.4: Underside view of an SES showing the sidehulls, seals, cushion, and waterjets (from Faltinsen, 2005)

1.3.2 Development History

A majority of SES development took place during the 1960s and '70s to address the US Navy's goal of the "100-knot Navy." During this time period, several test craft were designed and constructed to demonstrate the concept, including two 100-ton test craft, denoted SES-100A and SES-100B, which are shown in Fig. 1.5. Most notably with regards to performance, the SES-100B established a sustained speed record of $91.9\,\mathrm{knots}$ in a low sea state that was described as a "slight chop." A 3000-ton, 80-knot prototype (3K SES) was under development when the program was unfortunately cancelled in 1979, three weeks prior to the initiation of hull construction, due to the lack of a military mission for the prototype vessel (Butler, 1985) and due to a shift in priorities resulting from the fuel crisis of 1974 (Yun and Bliault, 2000, pp. 28). Instead, a shift towards higher-efficiency vessels was made.

More recently, there has been an increased interest in the development of SESs by both the Norwegian and US navies. The Norwegian Navy has developed the Skjold-class patrol boat, shown in Fig. 1.6, which is currently in operation. This craft has an overall length of $47.5\,\mathrm{m}$, and a top speed of $45\,\mathrm{knots}$ in seas and $60\,\mathrm{knots}$ in calm water.

There has been additional interest recently in the development of a Transformable Craft (T-Craft), intended to operate as an SES for long-distance, highly-loaded missions, but with the capability to "transform" into an ACV in the near-shore, littoral region, allow-

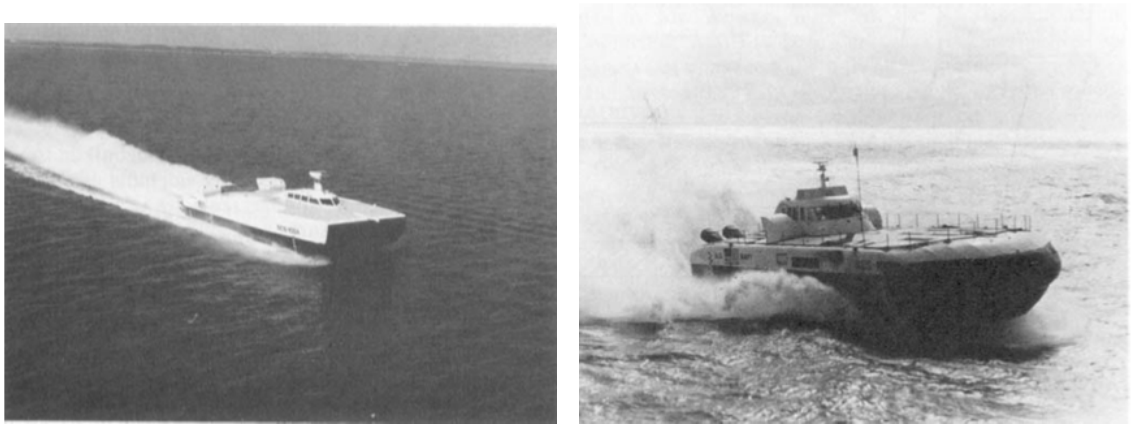

(a) SES-100A (b) SES-100B

Figure 1.5: 1960s-era US Navy SES test craft. The SES-100B established a sustained speed record of 91.9 knots in light seas. (from Butler, 1985)

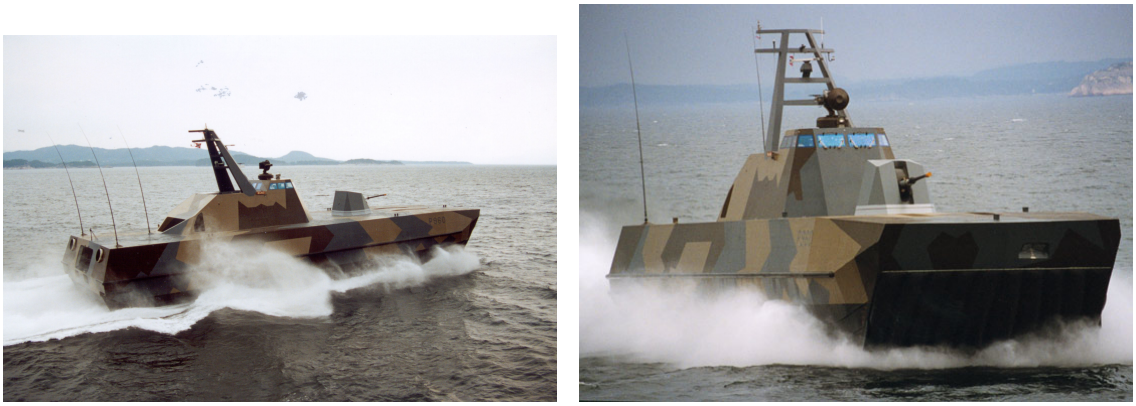

(a) (b)

Figure 1.6: Norwegian Navy Skjold-class patrol boat, having an overall length of $47.5\,\mathrm{m}$ and top speeds of $45\,\mathrm{knots}$ in seas and $60\,\mathrm{knots}$ in calm water (from Naval-Technology.com)

ing for fully-amphibious "feet dry on the beach" operations. One concept design for T-Craft is shown in Fig. 1.7, identifying both the transit SES and amphibious ACV modes. This concept has prompted a renewed interest in the SES concept and helped to highlight some of the unanswered research questions with regards to performance prediction for SESs. In particular, design tools are needed for the accurate prediction of SES seakeeping, maneuvering, and powering performance in order to ensure that the vessel meets all requirements, as well as to yield possibilities for an expanded operating space/regime and performance improvement for the ship designer.

Although the need for accurate design tools is not unique to SESs, traditional design tools must be appropriately used and/or modified in order to handle some of the unique characteristics of SESs. In particular, means for modeling the impact of the air cushion and bow/stern seals must be developed. These characteristics differentiate SESs from other types of vessels, such as monohulls or catamarans, and are found to have a large effect on the vessel performance characteristics. In particular, SES seals have been experimentally-observed to have a large impact on the total resistance (Heber, 1977; Van Dyck, 1972; Van Dyck and Fridsma, 1979), particularly in the low-speed, sub-hump regime, where the physics are still not well-understood and adequate modeling methods still lacking due to the interactions between the flexible seals, air cushion, free-surface waves, and vessel motion. These resistance characteristics are discussed later in this chapter. The content of this thesis aims specifically to address the impact of SES bow and stern seals on the total resistance, identifying possible design constraints, and filling a knowledge gap that has previously been left open.

1.4 SES Performance Characteristics

The performance of an SES may be measured in many ways, including powering, seakeeping, and maneuvering, among others. The work presented herein, however, is associated

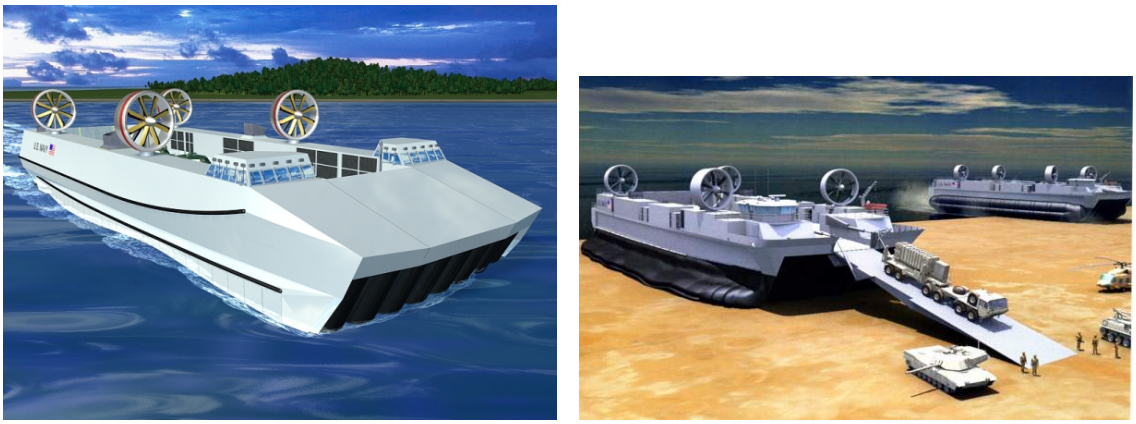

(a) Transit SES Mode (b) Amphibious SES Mode

Figure 1.7: Concept design for US Navy Transformable Craft (T-Craft) (from Wars)

solely with steady-state resistance prediction. Thus, in the context of this thesis, SES performance is associated with steady-state powering and resistance. A broader description of all manners of SES performance may be found in many sources, including but not limited to: Butler (1985); Faltinsen (2005); Yun and Bliault (2000).

The resistance of an SES is characterized by the presence of two or more drag humps, resulting from the effects of interference of the cushion-, sidehull-, and seal-generated wave patterns. These humps are illustrated in Fig. 1.8, which shows the estimated resistance components for the full-scale US Navy SES-100B (Fig. 1.5(b)) in Sea State (SS) 1. Typically, an SES will experience a primary hump at a Froude number of approximately $0.6 - 0.7$ and a secondary hump (a.k.a. subhump) at a Froude number of approximately $0.3 - 0.45$, however the exact values are dependent on a number of factors, including the cushion length-to-beam ratio, seal flexibility, and water depth.

The effects of shallow water are particularly important for vessels that are intended to operate in the near-shore, littoral region, such as the T-Craft. Water depth effects for ACV and SES wave resistance has been studied extensively in the past both experimentally (Van Dyck, 1972), as well as numerically (Doctors, 1993; Doctors and Sharma, 1972). The method presented in the thesis is associated with steady-state, infinite-depth resistance prediction since the primary focus is the prediction of seal effects. However, finite-depth

effects may be added in the future with relatively low effort.

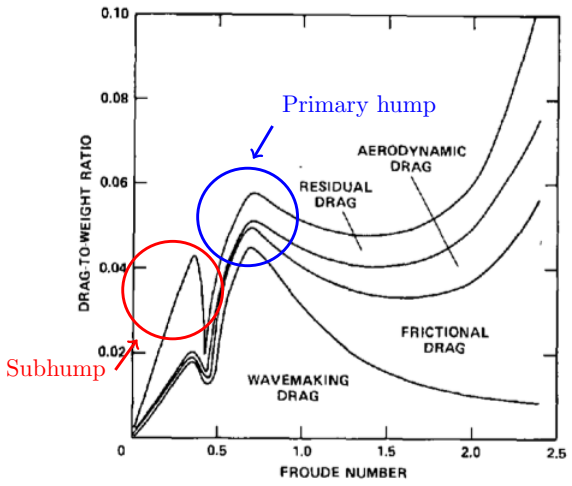

Figure 1.8: Estimated resistance curve for the full-scale US Navy SES-100B in Sea State 1 showing primary and secondary humps (from Wilson et al., 1979)

Although the terminology tends to suggest that the secondary hump (subhump) is of a lower magnitude than the primary hump, this is not true in all cases. In model tests performed for the US Navy XR-1B test craft, the magnitude of the secondary hump was found to be significantly larger than the primary hump (Van Dyck, 1972). In these tests, semi-rigid planing bow and stern seals were used, where the height above the keel (h_{SF} & h_{SA}) was adjustable, as shown in Fig. 1.9. The model-scale dimensions are shown in Table 1.1. In addition to varying the seal heights, the model was tested in both deep and shallow water. The results suggest a strong dependence of the magnitude of the secondary hump on both the water depth and the seal height.

Table 1.1: Principle dimensions of XR-1B scale model

Item	Value
L_C	1.63 m (5.35 ft)
B_C	0.655 m (2.15 ft)
L_C/B_C	2.5
L_{CG}	0.826 m (2.71 ft)
Δ	45.36 kg (100 lb)

The results for deep-water resistance, draft, and trim of the model-scale XR-1B test

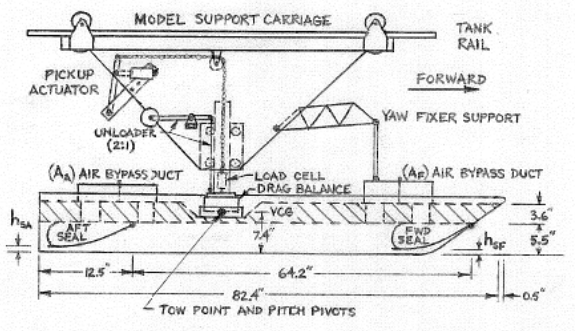

Figure 1.9: Experimental setup with terminology defined for US Navy XR-1B (not to scale) (from Van Dyck, 1972)

craft are presented in Fig. 1.10, where all parameters are held constant except for the seal height. The seal height was varied from $0\,\mathrm{cm}$ $(0\,\mathrm{in})$ to $5.08\,\mathrm{cm}$ $(2\,\mathrm{in})$, and was equal for both the bow and stern seals. The results show that the seal height has a large effect on the resistance and motion characteristics at the secondary drag hump ($Fr_C \approx 0.45$). The magnitude of the drag hump is observed to decrease as the seals are raised higher above the keels, and the secondary drag hump is observed to shift to a lower speed ($Fr_C \approx 0.3$) after the seal heights are raised beyond a certain threshold ($> 2.54\,\mathrm{cm}\,(1.0\,\mathrm{in})$). In addition to changes in resistance, the draft and trim of the model are also found to be largely affected by the seal height. In particular, as the seals are raised, the draft is found to increase and the trim is found to decrease at the secondary drag hump. These effects, and their relation to seal flexibility, will be discussed in further detail in Chapter 8.

The changing behavior at the subhump may be explained by seal-seal wave and body interactions, as will be shown in Chapter 7. These effects are dependent on the type of seal, the height of the seal above the keel, internal seal pressure, cushion pressure, and vessel motion. However, no fundamental theory exists for considering the effects of deformable seals on total resistance and vessel motion. In order to effectively predict the resistance of an SES at low Froude numbers, a method for estimating the contribution of the seals to the total resistance and vessel motion must be developed.

In addition to the experimental study of Van Dyck (1972), several other sources suggest

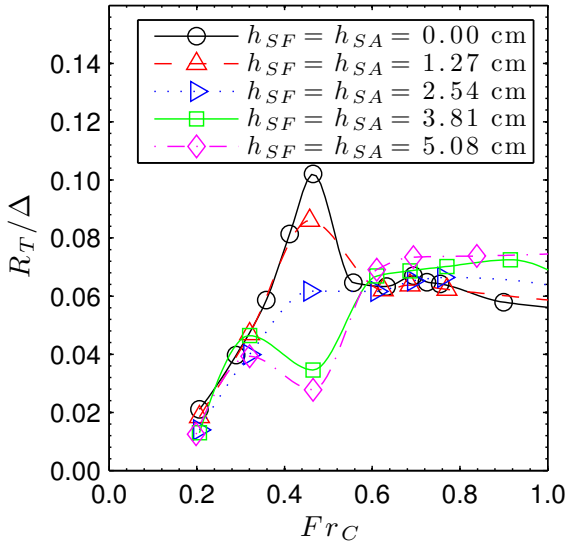

(a) Total Resistance

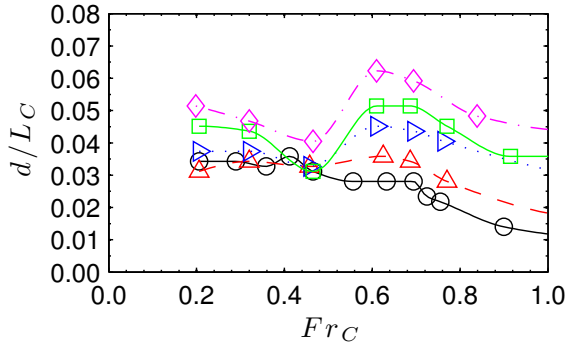

(b) Draft

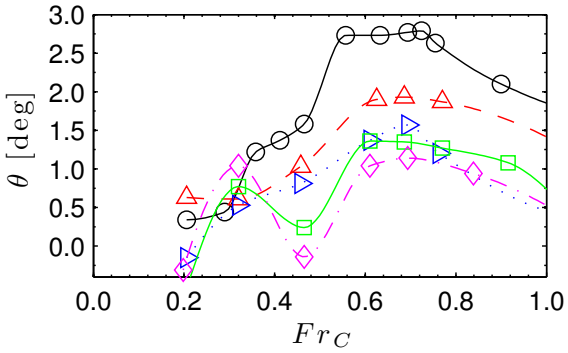

(c) Trim

Figure 1.10: Effect of seal height on response for US Navy XR-1B

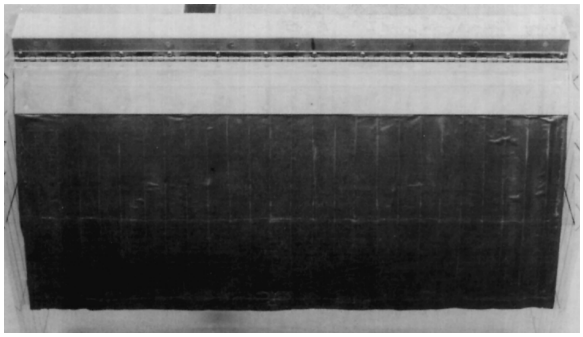

(a) Stay-Stiffened Bag and Membrane (SSBM) seal

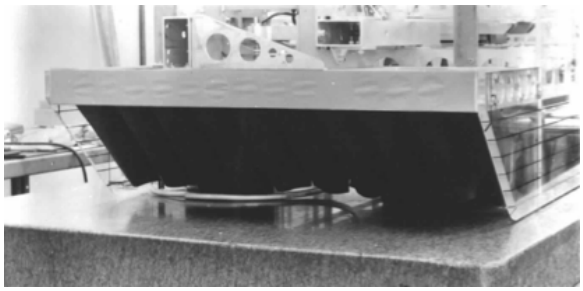

(b) Finger seal

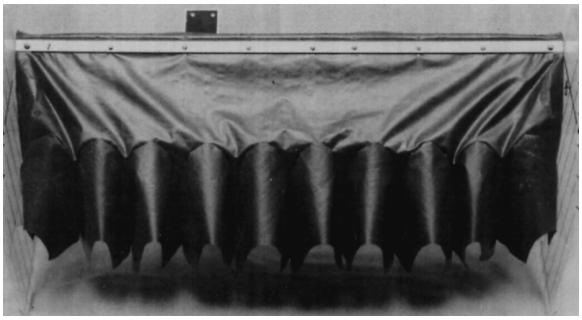

(c) Bag and finger seal

Figure 1.11: Three tested bow seal designs for segmented model tests (from Heber, 1977)

that the secondary hump behavior is caused by rigidity of the seals, including discussions by Butler (1985); Mantle (1973); Wilson et al. (1979); Yun and Bliault (2000). In particular, experiments were performed for a segmented SES model by Heber (1977), where it was observed that a majority of the behavior at the subhump was due to the height of the stern seal. The operating height of the stern seal is directly related to the stern seal flexibility, which is in turn related to the internal seal pressure: a more flexible seal (lower seal pressure) will tend to deform more, operating in a low-load condition at the free surface, whereas a more rigid seal (higher seal pressure) will generally be able to support larger loading, leading to increased drag. The seal positions are also largely affected by coupling between the seals and vessel motions. However, very few results exist where the effects of seal rigidity and/or vessel motions are systematically studied.

In the experimental study of Heber (1977), a segmented model-scale SES was tested by the US Navy with an overall length of roughly $2\,\mathrm{m}$. The seal drag was measured for three different types of bow seals and one stern seal. The bow seals that were tested included Stay-Stiffened Bag and Membrane (SSBM), bag and finger, and full-finger designs. The seal types that were tested are shown in Fig. 1.11. A compartmented model was built such that the resistance on each seal and the sidewalls could be measured independently. The results highlighted the large contribution of the seals to the total resistance at low speeds (in the subhump and primary hump regimes), on the order of 60% or more of the total resistance. However, the nature of the test program was not comprehensive enough to directly study the effect of parametric variations in seal design to be useful for developing a theoretical or empirical model for seal resistance. One set of sample results from these tests is presented in Fig. 1.12, where the resistance was measured at comparable operating conditions for all three seals. In this case, the seals all exhibited similar performance near the subhump ($V_s = 5.2\,\mathrm{ft/s}$, $Fr_C = 0.4$). It should be noted that the large increase in resistance at the highest speed for the bag and finger seal was due to failure of the bow seal, which buckled at this speed. Later in this thesis, the results of this model test are used as a

means for code validation and comparison. Thus, a more thorough review of these tests is given in Chapter 6.

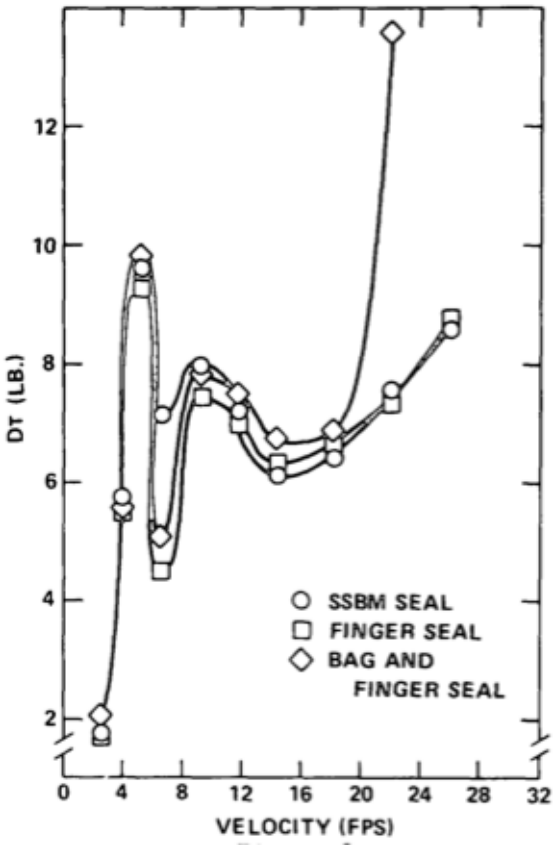

Figure 1.12: Comparison of total resistance for three bow seal configurations of a segmented model-scale SES at comparable conditions (from Heber, 1977)

As a result of the experimental study of Heber (1977), the large effect of the seals on the resistance at the secondary hump compared to the primary hump was found to be due to interaction of the the bow- and stern-seal-generated wave patterns, as illustrated in Fig. 1.13. In particular, at the secondary hump ($Fr_C = 0.4$), the bow seal wave was observed to impact the stern seal, leading to large stern-seal drag, and consequently, total resistance. The magnitude of these waves is dependent on the equilibrium shape and position of the seals, which is naturally related to the effective stiffness of the seals. Hence, it is necessary to be able to predict the deformation of the seals in order to accurately predict the contribution of the seals to the total resistance, and the impact on vessel motions.

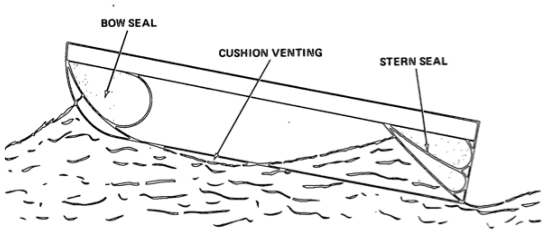

(a) At Secondary Hump ($V_s = 5.2\,\mathrm{ft/s}$, $Fr_C = 0.4$)

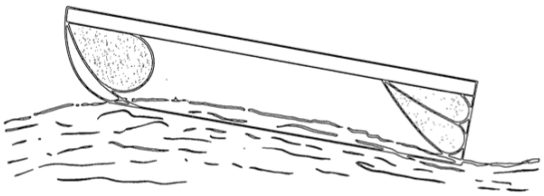

(b) At Primary Hump ($V_s = 9.1\,\mathrm{ft/s}$, $Fr_C = 0.7$)

Figure 1.13: Relation of cushion waves to bow and stern seals at secondary and primary drag humps (from Heber, 1977)

1.5 Review of SES Resistance Prediction Methods

Due to the complex dynamics of the air cushion and flexible seals, the computation of resistance for SESs is more complicated than for traditional mono- or multi-hull vessels. Several models have been developed for calculating SES resistance, which include methods based on linearized potential-flow as well as, more recently, Computational Fluid Dynamics (CFD). Although several methods for SES resistance prediction have been developed over the years, none of these methods have been able to demonstrate the ability to predict the vessel resistance over the entire speed range with acceptable accuracy. Consequently, past designs have consistently relied on experimental model testing.

The first efforts associated with wave resistance prediction for SESs, and ACVs in general, can be traced back to Newman and Poole (1962) and Barratt (1965). In these early works, the air cushion is modeled using linearized potential-flow theory by applying a modified dynamic boundary condition at the free surface to account for the pressure rise in the air cushion. The theory was found to accurately predict the hump speed(s). However, the magnitudes of the resistance humps in the low Froude number regime were largely

overpredicted due to the strong wave interactions due to the sharp drop in pressure at the edges of the pressure cushion.

A means of resolving this overprediction was developed by Doctors and Sharma (1972). In this work, a smoothing function was applied at the edge of the pressure cushion to more accurately model the drop-off from cushion pressure to atmospheric pressure. Using this approximation, it was found that the predicted wave resistance agreed better with experimental results at the primary hump speed and higher. Several studies have suggested that potential-flow methods compare well with experimental results at the primary hump speed and higher, but not at lower speeds (in the subhump regime) due to the significant contribution of the seals to the total resistance (see Doctors, 2009; Doctors and McKesson, 2006; Wilson et al., 1979).

More recently, CFD-based methods have been used for SES resistance prediction. Maki et al. (2013) used a fully-nonlinear Reynolds-Averaged Navier-Stokes (RANS) method to calculate the resistance of an SES in calm water without consideration for the seals. The air cushion was modeled by applying a constant-pressure boundary condition on the free surface, with similar smoothing parameters to Doctors and Sharma (1972). These results were compared to the linearized potential-flow method of Doctors (2009). The RANS results were found to compare well with both the linearized-potential flow and experimental results for the total resistance. It should be noted though that the successful agreement of the linearized potential-flow method with experimental method is in part due to the successful tailoring of hydrodynamic form factors and assumed equilibrium seal shapes based on years of prior experience. For the SES studied by Maki et al. (2013), which had finger bow seals and a lobed stern seal, the seal resistance was found to be small (less than 10%) for $Fr_C > 0.5$.

All of the aforementioned methods represented the air cushion by applying a constant-pressure boundary condition on the free surface. In reality, the air cushion is generated by a set of fans; the pressure within the cushioned space may vary temporally and spatially

due to a ride control system, localized leakage, acoustic wave generation and propagation, and interactions with water waves. To more realistically model the air cushion, previous authors (Donnelly and Neu, 2011; Donnelly, 2010; Young et al., 2011) have used a Volume of Fluid (VOF) method, which solves for the multiphase flow problem by tracking the interface between the air phase and water phase. A momentum source model was used to represent the inflow from the fans. Both inviscid and viscous fluid models were used and the resistance was computed in both calm water (Donnelly and Neu, 2011; Donnelly, 2010; Young et al., 2011) and in regular waves (Donnelly, 2010). The seals were assumed to be rigid, and the height of the seals, along with the fan source strength, were adjusted to avoid excessive seal immersion, which would corrupt both the predicted wave profile and drag computation. The predicted resistance agreed well with the experimental results of Bishop et al. (2009); however, the method requires the cushion pressure and seal height to be known a priori, which is not possible unless experiments are conducted beforehand for that particular SES system at the operating conditions of interest. The proper scaling laws must also be satisfied, which is extremely difficult and often impossible because of the need to satisfy hydrodynamic, aerodynamic, and hydroelastic similarity simultaneously.

A RANS method has also been used by Bhushan et al. (2011), where various simple seal models were tested, including rigid seals, hinged seals, and imaginary seals. In addition, various cushion pressure models were tested, including a fixed-applied pressure and an ideal-gas model with and without leakage. The results were found to compare fairly well with experimental results for the speeds tested, particularly using the hinged seal model and directly-prescribed cushion pressure models, where the cushion pressure was prescribed to be the same as the experimentally-measured value and the seal was assumed to rotate about a hinge at the wetdeck with the restoring moment provided by the seal pressure.

In all cases previously discussed for SES resistance prediction, the seals were either ignored, or very simple models were used in order to prevent the seals from affecting the solution in any major way. One difficulty in predicting SES seal behavior results from

the highly nonlinear structural behavior coupled with nonlinear fluid behavior. SES seals, by their nature, obtain their stiffness by a combination of deformation and internal seal pressure, whereas traditional structures exhibit stiffness through small-scale material deformation, or strain. Consequently, linear beam models have been found to yield poor approximations for seal resistance at lower speeds. Doctors (1977) proposed using a linear beam model coupled with a linearized potential-flow method for the prediction of SES seal drag. While this model may be applicable for more rigid, planar seals, it has been found to yield poor results for more flexible membrane, bag and finger, and full finger seals.

The effects of seal rigidity have been found to be most important in the low-speed regime, which explains why past computational efforts have been very effective at high speeds, while showing poorer prediction accuracy at low speeds (Doctors, 2009; Doctors and McKesson, 2006). The flexibility of the seals drives the need for a model that considers Fluid-Structure Interaction (FSI) effects.

A large test platform was recently constructed to measure the drag and deformation of SES seals (Wiggins et al., 2011; Zalek et al., 2011), the goal being to understand the fundamental physics of the seal-water-air cushion interface, and to provide data for numerical validation studies. The experimental results demonstrated the ability to measure and record the complex dynamics of SES finger bow seals, including folding and flutter patterns, independent seal resistance, and an impressive set of visualization tools. The results also demonstrated the large-deformation behavior of finger seals, which experience very large deformation by "giving way" to hydrodynamic loads. Combined with the experimental observations of Heber (1977), it is expected that, at least for the case of SES subhump resistance, the stern seal is of primary importance due to the fact that the bow seal wave will impact the stern seal in this speed range, with the bow seal contribution being less important due to their low immersion, high deformation, and low loading state. Wiggins et al. (2011) observed that, although the resistance of the bow seals is expected to be relatively low compared to the wave and frictional resistance, the complex buckling patterns and flut-

ter exhibited by the fingers is very important when considering the operating lifetime of the fingers.

In past SES development efforts, the inability to predict low-speed resistance was not thought to be of major consequence since an adequate power margin was typically installed for expected operations at very high speeds (80+ knots). However, for vessels with top speeds around 40 knots (e.g. T-Craft), the prediction of low-speed performance becomes increasingly more important. Consequently, in order to design a vessel intended to operate often in the low-to-moderate speed regime, an improved model for seal resistance that incorporates the FSI response of the seals as well as seal-generated wave interaction must be developed.

1.6 Modeling Challenges

A majority of the previous work for SES resistance prediction has utilized potential-flow techniques, and the methods have been able to accurately predict the resistance, particularly at higher speeds. Owing to increased availability of computing power, a natural extension is to use modern advanced CFD techniques, allowing for increased accuracy and better modeling of the physics with the goal of identifying design issues and improving designs. The use of CFD for SES drag prediction has been explored by many authors (Bhushan et al., 2011; Donnelly and Neu, 2011; Donnelly, 2010; Maki et al., 2013, 2009; Young et al., 2011). However, many issues arise due to the complex interaction of the seals, cushion, and free surface. In this section, some of the issues associated with SES modeling using CFD are discussed.

The main difference between modeling an SES and a non-air-supported vessel such as a catamaran lies in the modeling of the air cushion and the seals needed to contain it. In order to accurately model the cushion lift system, the fan dynamics must be characterized. This requires knowledge of the fan system characteristics, which introduces difficulties,

particularly early in the design stage where the details of the fan system may not be known. Additionally, a control system (which is present in the physical SES) must be included to vary the fan flow rate in order to accommodate leakage and maintain a desired cushion pressure.

The issues of cushion modeling, while introducing complexity, have been addressed successfully in various ways by different authors. Maki et al. (2013) utilized a single-phase level set method where a fixed pressure could be applied to the free surface directly. However, this method is not possible using more popular VOF methods for free surface tracking because the free surface is located in the interior of the computational domain, rather than at a domain boundary. Donnelly (2010) used a two-phase VOF method to capture the free surface along with a momentum source model for the fan, where the volume flow rate was adjusted in order to obtain a target pressure in the cushion volume. In this method, the cushion pressure had to be known a priori, requiring experimental results to perform numerical simulations. This method was also adopted by Young et al. (2011).

A larger difficulty that arises in the modeling of SESs is that of the need to model the deformable seal behavior. The problem of deformable SES seals is a complex FSI problem which includes both hydrodynamically and geometrically nonlinear behavior. Several experimental studies (Besch, 1976; Ryken, 1978) have highlighted the complex physics present for SES bow seals, recently including two large-scale experimental efforts by Zalek and Doctors (2010) and Wiggins et al. (2011). Modeling of this FSI behavior requires modeling of large deformation, inflated structures that may operate in a post-buckled and/or fluttering state subject to fluid pressure and shear forces.

In order to address the issue of SES resistance prediction without the need to fully model the FSI behavior of the seals, some authors have assumed the seals to be rigid in the steady-state condition. As long as the seals are placed in the appropriate equilibrium (deformed) position, this approximation has proven to yield fairly good estimates of total resistance (Donnelly, 2010; Young et al., 2011). The main problem associated with the

practice of using rigid seals is that the seal position must be estimated before the computation is performed and adjusted in order to match the true equilibrium position. If the seal immersion is over-estimated, the seal forces will be drastically over-predicted. If the seal immersion is underestimated, the amount of leakage from beneath the seals will be over-predicted. Hence, it is easy to envision the difficulty of estimating the correct seal height, especially considering cases where the vessel is free to heave and trim. In this case, each change in seal geometry requires re-meshing of both the structural and fluid domains.

Two examples of attempted simulations are shown in Fig. 1.14. In Fig. 1.14(a), the seals are overly-immersed, causing large spray and slamming pressures to be generated at the bow of the vessel. This large spray leads to a dramatic over-prediction in the total resistance. In Fig. 1.14(b), an appropriate seal height has been found, leading to an accurate resistance prediction.

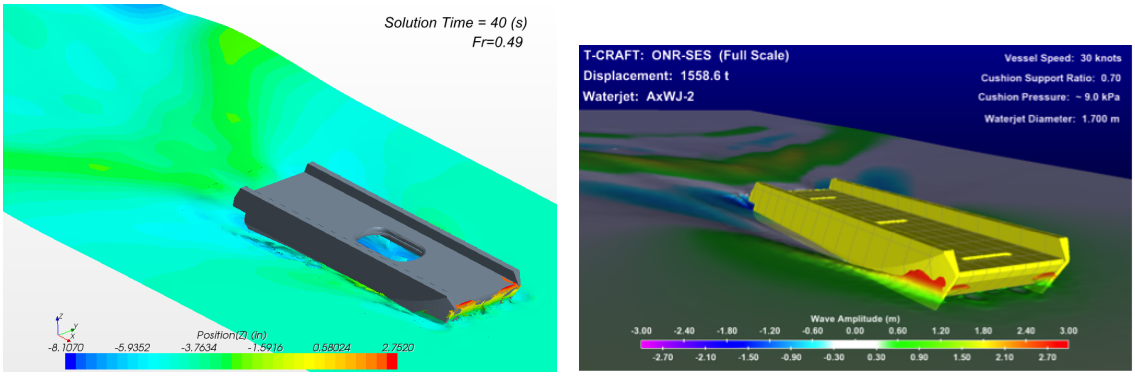

(a) Simulation with overly-immersed seals

(b) Simulation with properly-adjusted seals (Young et al., 2011)

Figure 1.14: Example CFD runs for the US Navy T-Craft model (Bishop et al., 2009) where the seals are (a) too deeply immersed and (b) adjusted correctly

The difficulties associated with the modeling of SESs with seals drive the need for a more systematic means for predicting the running seal position for resistance predictions. In particular, a simplified method for predicting the running seal position before performing expensive CFD computations may reduce the amount of simulations necessary to predict the resistance at a given speed.

1.7 Objectives

The objective of this work is to develop an efficient and accurate numerical model for SES seal resistance that considers the effects of seal interaction with the pressure cushion, free-surface waves, vessel motion, as well as seal flexibility. By predicting the seal resistance, the contribution to the total resistance may be estimated. Through the development of the numerical model, the following research questions are addressed:

1. How can the interaction between flexible seals, air cushion, free-surface waves, and vessel motion be efficiently and effectively captured?

2. How do the seals affect the total resistance (including the subhump and primary hump) and draft/trim for varying Froude number, cushion pressure, and seal pressure?

3. Does seal drag adequately explain the magnitude of the experimentally-observed secondary hump?

4. Can parametric/scaling relationships for the seal/cushion/wave interaction be derived for incorporation into high fidelity CFD models, as well as assist in the design and proper testing of SESs?

5. Can actively-controlled seals be used to improve performance by minimizing resistance over a range of operating speeds?

1.8 Thesis Organization

The numerical model is based in multiple fields of study, including both hydrodynamics and structural mechanics, and as such it is useful to outline the whole problem. An overview of the full problem is described in Chapter 2, along with an description of the layout of the numerical model, physical assumptions, and interaction between the various sub-models.

The details of the fluid and structural models are described in Chapters 3 and 4, respectively, each requiring validation in its respective chapter. The interaction if the fluid and structure models is described in Chapter 5.

After describing the mathematical and physical background, and after validating the hydrodynamic and structural models, the complete numerical model is validated by comparing with experimental results from the segmented SES model tests of Heber (1977). The details of this experiment are described in Chapter 6. The complete numerical model is then validated. The physics of the problem are explored for rigid seals in Chapter 7 in order to explain the primary physical mechanism responsible for the presence of the secondary drag hump. The effects of seal flexibility are then explored in Chapter 8. Finally, conclusions are drawn and opportunities for future work are proposed in Chapter 9.

CHAPTER 2

Problem Description and Overview of Numerical Method

This chapter describes the physical problem for which the numerical model has been developed. It is intended as a relatively general overview of the problem of SES resistance prediction to highlight the work that has been done in this field, the issues and shortcomings that have been encountered, and the ways in which the numerical model proposed in this thesis addresses these issues. After describing the physical problem, an overview of the numerical method is given, detailing in particular the ways in which fluid and structural models interact. In this chapter, the fluid and structural models are treated as "black boxes" in order to maintain a high-level overview. Each model is discussed in detail later in Chapters 3 and 4.

2.1 General Physical Assumptions

The primary objective of this thesis is to efficiently and accurately predict the effects of the bow and stern seals on the total resistance for SESs. The current scope of the model is limited to steady-state, calm-water resistance prediction for both rigid and flexible seals. In addition, the seals are assumed to be Two-Dimensional (2-D), and the total Three-Dimensional (3-D) force values are obtained by multiplying by the seal width. The assumption that the seals behave as two-dimensional lifting bodies is valid in the limit as the

cushion length-to-beam ratio (L_C/B_C) approaches zero (i.e. the vessel is very wide compared to its length), since the wave system within the cushion space becomes more two-dimensional. In order to consider the effects of 3-D waves outside the cushion space for prediction of cushion wavemaking resistance, the standard method of Doctors and Sharma (1972) is used, where the cushion is represented as a 2-D pressure patch on the free surface. Thus, the 2-D assumption is applied for the seals and the waves within the cushion space, but the total resistance prediction is made with consideration for 3-D cushion wavemaking effects.

The primary source of three-dimensional hydrodynamic effects on the seals is due to the wave system within the cushioned space, which becomes more three-dimensional as the speed increases and as the length-to-beam ratio increases. For the case studied in this work, a vessel with a low length-to-beam ratio is studied at low speed and the 2-D model is found to offer reasonable results. The conclusions cannot be said to be general for all speeds and length-to-beam ratios, however. Thus, the work presented in this thesis represents a first step towards a general, 3-D method for considering the interaction effects of SES seals. The assumption of two-dimensionality is discussed in more detail in Appendix A, and future extension of the work to 3-D, time-domain, unsteady response is alluded to in Chapter 9.

Due to the nonlinear behavior of the problem, iterative methods must be used to calculate the equilibrium solution and thus various iteration schemes, some of which require the use of pseudo-time stepping methods, are used. It must be made clear, however, that unless otherwise noted, the solution of interest in this work is the steady-state, equilibrium solution.

Since the numerical model contains elements of both hydrodynamic and structural modeling, several assumptions must be made in order to reduce the complexity of the problem. These assumptions will be covered in detail in the appropriate chapters in order to justify their use. However, it is beneficial for the sake of clarity to introduce beforehand the physical assumptions pertaining generally to the problem, as well as the particular assumptions

for each sub-model (i.e. fluid and structural models). As such, the the following physical assumptions are made throughout this thesis, unless otherwise noted:

- Newtonian physics are assumed, therefore ignoring any relativistic or quantum effects
- Coriolis forces and any other effects caused by the rotation or curvature of the earth are assumed to be negligible
- The vessel is assumed to be operating in a steady, straight-ahead condition
- The reference frame is assumed to be attached to center of rotation of the vessel and moving at a constant forward speed
- The water depth is assumed to be infinite
- Effects of incoming waves are ignored, however steady waves may be developed as a consequence of the moving reference frame
- The wave system within the cushion is assumed to be reasonably approximated by 2-D theory. Therefore, the numerical method is restricted to 2-D.

The fluid model will be covered in detail in Chapter 3, wherein both a potential-flow-based method and a CFD method are compared. For the final results of this work, linearized potential-flow assumptions are made, which can be summarized as follows:

- In all cases, the fluid is assumed to be incompressible
- In all cases, only the steady-state fluid solution is of interest
- Viscosity is ignored in the potential-flow solution, however viscous effects may be included using the ITTC friction line method
- For the potential-flow method, the free-surface and kinematic body boundary conditions are linearized about the undisturbed free surface

- For the potential-flow method, the waves are assumed to be linear, and are thus non-breaking

A brief discussion on the assumption of incompressibility is warranted. In the current study, the fluid solver applies to the water domain only and the air inside the cushion is not directly modeled. Thus, the assumption of incompressible flow is used. For full-scale vessels, it has been observed that compressibility effects of the air cushion can become important, particularly with regards to cobblestone oscillations (see, e.g. Steen, 2004). These oscillations are a dynamic effect caused by the changing volume of air within the air cushion when operating in waves. Due to the compressibility of the air cushion, which behaves as a spring, oscillations can occur that are experienced by the passengers as vibrations much resembling the driving of a car over a cobblestone street. For the current study, air compressibility is not taken into account due the steady-state nature of the solutions, which assume the vessel to be operating in calm water.

One of the objectives of the numerical method is to provide a flexible framework for considering various SES seal models. Therefore, several structural models are presented in Chapter 4 for the modeling of the seals. In addition, the two Degrees of Freedom (DoFs) representing the rigid body motion must be calculated to find the equilibrium draft and trim of the vessel. Within the structural model, the following assumptions are made:

- In all cases, the seal surface is assumed not to fold or buckle
- A hinged-seal model is developed, which assumes that the seal behaves as a rigid structure attached to the SES via a torsional spring
- A large-deformation Finite Element Method (FEM) model is developed, which assumes that the seal membrane structure may be represented as a series of 2-D truss finite elements
- For the FEM method, the material is assumed to be linear elastic

The assumptions of both the fluid and structural methods will be covered in more detail in Chapters 3 and 4, respectively.

2.2 Proposed Modeling Approach

The goal of this work is to develop a simple and efficient method for calculating the influence of rigid and/or flexible seals on the total resistance, running draft, and trim of an SES. Once the method is developed and validated, it may be used to investigate the effects of parametric variations on the vessel performance in order to determine the important design parameters. In order to calculate the total resistance, the various resistance components must first be examined.

For the current study, it is assumed that the total Three-Dimensional (3-D) resistance (R_T) may be broken down linearly into several components in a similar manner to Doctors (2009); Doctors and McKesson (2006):

$$R_T = f_W R_W + f_F R_{F,\mathrm{SW}} + R_H + R_A + R_S + R_a + R_M \tag{2.1}$$

where R_T is the total resistance, f_W is the wave resistance form factor, R_W is the wave resistance, R_H is the transom stern resistance, f_F is the frictional form factor, $R_{F,\mathrm{SW}}$ is the sidewall frictional resistance, R_A is the correlation resistance, R_S is the seal resistance, R_a is the air resistance, and R_M is the momentum resistance.

The topic of pressure cushion modeling and wave resistance prediction is discussed in detail in Doctors (1993). SES wave resistance (R_W) is typically predicted by assuming linearized potential-flow theory and calculating the resistance of a smoothed constant-pressure patch moving along the free surface. This method is fairly simple to implement and has been shown to be accurate for computing the wave resistance (R_W).

The transom stern resistance (R_H) is caused by the pressure loss aft of a blunt transom, and the sidewall frictional resistance ($R_{F,\mathrm{SW}}$) is estimated using an assumed pressure

and frictional drag and an estimation for the wetted area of the sidehulls along with an appropriate friction drag estimation, such as the ITTC or ATTC curve. The correlation resistance (R_A) is fairly straightforward and is used to account for scaling effects between model and full-scale vessels. The last two components, air resistance (R_a) and momentum resistance (R_M) are typically small and may be estimated using experimentally-measured air tares or other empirical methods. The remaining resistance component is the seal resistance (R_S), which contains contributions from both the bow and stern seals.

The prediction of the seal drag is the main objective of this work. The seal resistance is predicted using a 2-D model based on coupling a linearized potential-flow model with a hinged seal model supported by a torsional spring. For higher speeds where the seal drag is negligible, the remaining resistance components are then estimated using a more traditional method, where the cushion wavemaking drag is predicted following Doctors and Sharma (1972). To validate the models, the case of a segmented SES model, presented by Heber (1977) and described in Chapter 6, is simulated because it is the only known experimental study that specifically focused on the bow and stern seal drag for different seal types. This model had very thin sidewalls in order to minimize their effects, and hence the transom stern resistance (R_H) is assumed to be zero. Additionally, the air resistance (R_a), correlation resistance (R_A), momentum resistance (R_M), and the sidewall frictional resistance ($R_{F,\mathrm{SW}}$) resistance are all accounted for based on the results of tare runs that were performed without seals. These components are each found to be relatively small in the subhump regime. The wave resistance form factor (f_W), and frictional form factor (f_F) are assumed to be equal to unity.

Based on these assumptions, the total 3-D resistance of the segmented SES model presented in Heber (1977) may be calculated as

$$R_T = R_W + R_{F,\mathrm{SW}} + R_S \tag{2.2}$$

where the seal resistance (R_S) is obtained based on the 2-D numerical model. The major assumption is that the interaction of the bow and stern seals is due primarily to the longitudinal wave systems and thus may be adequately assumed to be well-approximated as two-dimensional. Although this is a major simplification, it will be shown that the method is able to consider this interaction with a reasonable level of accuracy.

In a general sense, the numerical model for the prediction of seal drag is based on coupling a hydrodynamic model (to obtain fluid forces) with a structural model (to obtain the equilibrium draft, trim, and deflected seal shapes). A general overview of the numerical method is shown in Fig. 2.1. The two models are solved in an iterative manner until all equilibrium conditions are satisfied. The details of both the hydrodynamic and structural models, their interaction, and the FSI iteration scheme and convergence criteria will be discussed in the following three chapters. The goal of the analysis is to estimate R_S for a given vessel geometry as a function of the operating condition, i.e. $R_S = f\left(Fr_C, P_C A_C/\Delta, P_s/\frac{1}{2}\rho_w U^2, L_{CG}/L_C\right)$, where $Fr_C = V_s/\sqrt{gL_C}$ is the Froude number based on the cushion length, $P_C A_C/\Delta$ is the percentage of displacement provided by the pressure cushion, $P_s/\frac{1}{2}\rho_w {V_s}^2$ is the nondimensional internal seal pressure (related to the overall seal stiffness), and L_{CG}/L_C is the relative location of the center of gravity. The effects of internal seal pressure are addressed in this work via a torsional spring hinged seal model, where the stiffness of the torsional spring is intended to be representative of the overall stiffness of the physical seal, which is dependent on the internal seal pressure. The effects of changes in Longitudinal center of gravity (L_{CG}) are not studied directly in this work; however, the effects of changes in L_{CG} were studied experimentally by Heber (1977). These effects are summarized in Appendix C. Due to the complexities associated with modeling the complete physical behavior of the seals, it is desirable to make the model as simple as possible while including all relevant physics.

Although the results presented in this thesis have ignored some resistance components, the drag predictions may be refined in the future by implementing more capability into the

numerical model. Nevertheless, it will be seen that the predictions offered in Chapter 7 yield reasonably accurate results.

2.3 Capabilities of the Numerical Method

Before discussing the details of the numerical method, it is useful to first describe the capabilities of the method in order to put the problem in context. The method presented in this thesis is modeled on a combination of 2-D planing theory with various structural models, including a FEM model, a hinged spring model, and a rigid body motion model.

The method can generally consider multiple bodies connected in tandem, where the rigid body is fixed or free in trim and/or draft (i.e. two Degree of Freedom (DoF) motion). A sample problem layout is shown in Fig. 2.2, which represents an example of an SES with bow- and stern-seal modules. In this case, the vessel is constructed of a wet deck module with a center of rotation (CR) and center of gravity (CG) where the vessel vessel displacement (Δ) acts. Attached to the wet deck module are two seals, which each consist of a torsionally-sprung planing face of stiffness $K_{\delta,i}$ and a bag that is constructed of finite elements. Each seal is provided with an internal seal pressure ($P_{s,i}$), and a cushion pressure (P_C) is located between the two seals. The objective of the numerical method is to find the equilibrium position of the body, which is determined by its draft (d) and trim angle (θ) (defined about CR), as well as the deformed shape of any flexible substructures (in this case δ_1 and δ_2 of the seals). Although this example is intended for illustration, it sufficiently defines the capabilities of the numerical method.

The rigid body may generally be constructed of one or more substructures that may be rigid or flexible in nature, and may be subject to external hydrodynamic loading or a constant internal or external air pressure. The equilibrium solution is defined such that the sum of all forces and moments on each rigid body are zero, where the variable loading is determined from the hydrodynamic solution.

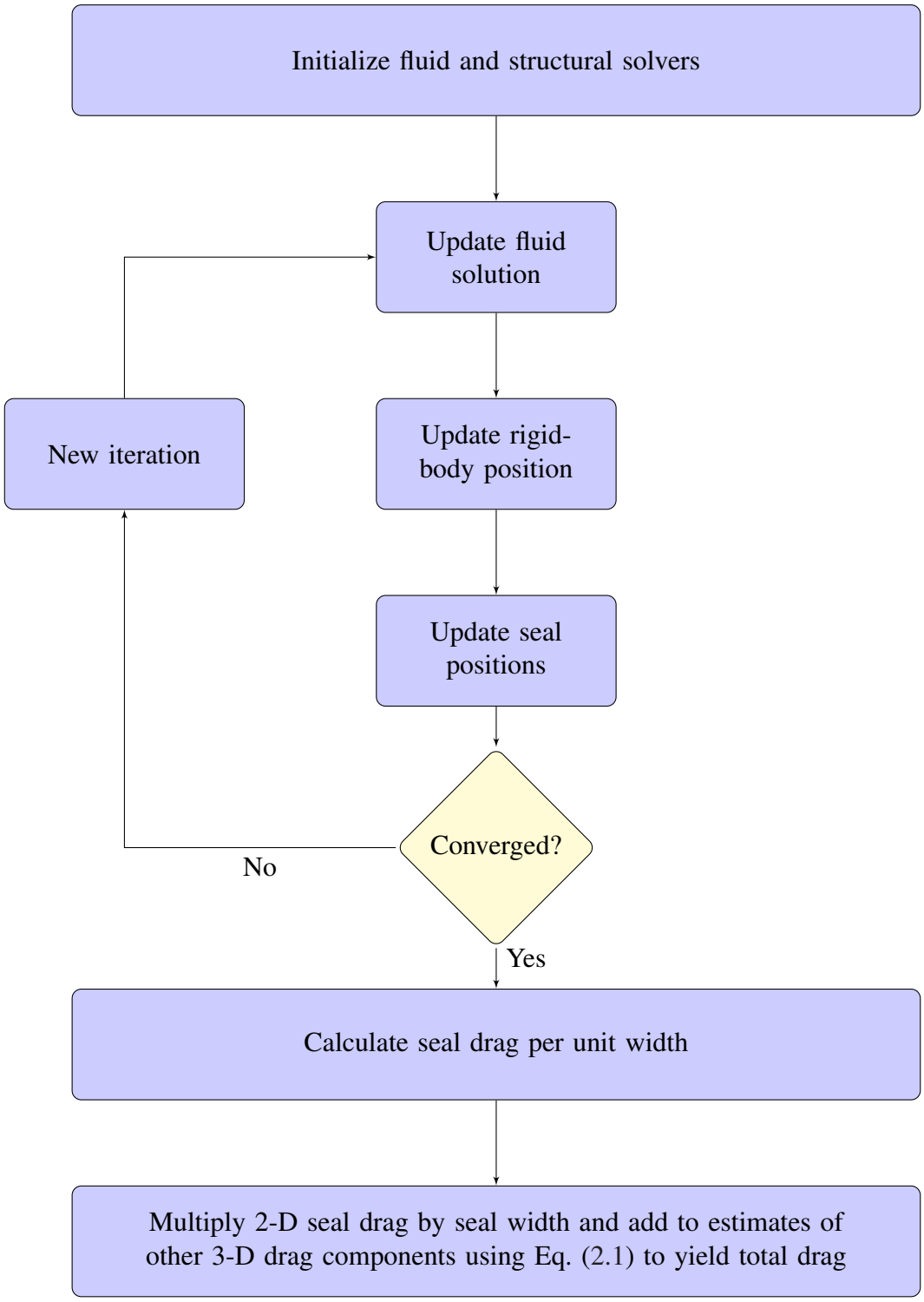

Figure 2.1: Flow chart for calculation of total resistance using 2-D seal drag predicted by proposed numerical model

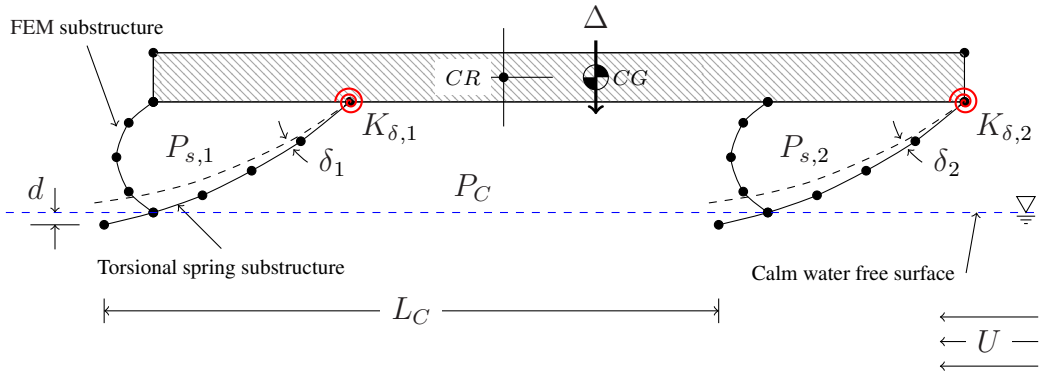

Figure 2.2: Example problem layout with two seals connected to the SES wet deck by torsional springs

In order to better illustrate the concept, one sample output of the equilibrium solution for the segmented model test of Heber (1977) at $Fr_C = 0.38$ is shown in Fig. 2.3. The initial and final center of rotation are shown as a dashed and solid axis system near the center of the vessel, respectively, and the initial and final center of gravity locations are shown as an unfilled square and filled circle, respectively. The substructure surfaces are represented by black curves and there are four separate substructures:

1. Bow seal planing face, shown towards the right of the figure, subject to external hydrodynamic pressure (red), cushion pressure (green), and viscous shear stress (not shown)

2. Stern seal planing face, shown towards the left of the figure, subject to external hydrodynamic pressure (red), cushion pressure (green), and viscous shear stress (not shown)

3. Wetdeck and upper portion of bow seal, subject to cushion air pressure load (green)

4. Rigid substructures representing the sidewalls and upper wet deck structure, which have been included for plotting purposes but are not modeled in the current solution

In Fig. 2.3, the bow seal is assumed to be rigid and the stern seal is assumed to be flexible using a hinged seal model. In general, the seals may be allowed to deform based on

a user-selected structural model (as illustrated in Fig. 2.2). In the current work, the structural deformation models are limited to a nonlinear membrane FEM model and a torsional-spring seal model. The details of the hydrodynamic and structural models will be discussed in detail in Chapters 3 and 4, respectively, and their interaction is discussed in Chapter 5. The results for the case shown in Fig. 2.3 are discussed in more detail in Chapters 7 and 8 using both rigid and flexible seals, respectively. The end result of the numerical method yields the equilibrium trim and draft of the vessel, the deformed shapes of the seals, the hydrodynamic pressure, free-surface profile, and the drag, lift, and moment of each substructure for a given operating condition. The total resistance may be derived by summing the contribution from appropriate substructures.

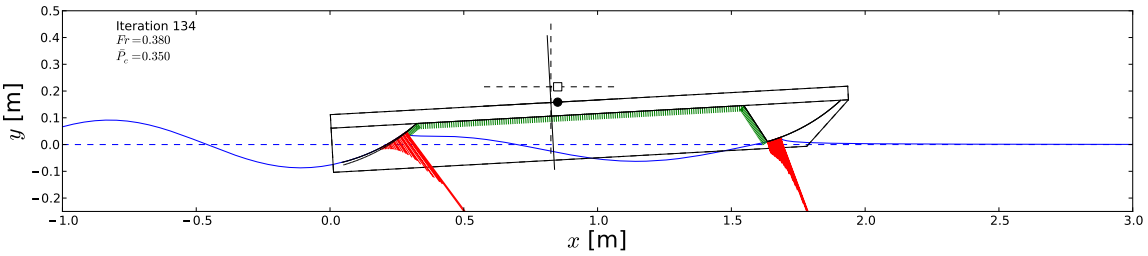

Figure 2.3: A sample of the equilibrium solution for the segmented SES model of Heber (1977) at $Fr_C = 0.38$ with a rigid bow seal and flexible stern seal of stiffness $K_\delta = 5.0\,\mathrm{N.m/deg}$. The deformed and undeformed shape of the stern seal are visible as black lines. The hydrodynamic pressure profiles are shown in red lines, the cushion pressure profile is shown in green, the body geometry is shown in black, and the initial and deformed free-surface profiles are shown as dashed and solid blue lines, respectively. The initial and final center of gravity are shown as a white square and black circle, respectively.

2.4 Summary

In this chapter, a general overview of the layout of the numerical method has been provided. In particular, the way in which the 2-D SES model that is proposed in this thesis is used for total resistance prediction was covered. The 2-D SES model was described as a combination of both a hydrodynamic model and a structural model, however at this point,

each sub-model has been treated as a "black box" and the details of their interaction have not been covered.

In the following three chapters, the details of each portion of the numerical method will be discussed. In Chapter 3, the hydrodynamic model is presented, as well as the results of a computational study for the 2-D planing plate problem comparing the results of a linearized potential-flow based method with a nonlinear CFD method in order to determine the regime where the potential-flow assumptions are valid. As a result of the CFD study, it is expected that the potential-flow method should be valid for the SES cases of interest in this work.

The various structural deformation methods, as well as the rigid body motion solver are then discussed in Chapter 4, followed by a description of the interaction of the two methods in Chapter 5, with particular attention being paid to the methods of interpolation of fluid loads, the iteration scheme, and convergence criteria.

CHAPTER 3

Hydrodynamic Modeling

This chapter describes the hydrodynamic model that is used to calculate the fluid loading on the seals, and on the vessel as a whole. In the first section, two different fluid models are presented, including a fully-nonlinear CFD method and a linearized potential-flow method. The problem of a 2-D planing plate is then studied using both the CFD and the potential-flow method. This problem has been chosen for its similarity to the SES seal problem, as well as the past use of planing plate models for SES seal resistance prediction (Doctors, 1977, 2009; Doctors and McKesson, 2006). The results from the two methods are compared, and the regimes in which the assumptions of the potential-flow method break down are identified. It is found that the potential-flow method is expected to be accurate for the regimes encountered by SESs, thus justifying its use. The linearized potential-flow method is then extended to include the effects of multiple seals and a pressure cushion for its application to the complete SES problem. For each of these extensions, validation studies are performed.

3.1 Model Selection

The objective of the fluid solver is to determine the pressure and shear distributions along the wetted surface of the seals. Although many past studies have made the assumption that viscous effects are negligible or simply approximated with friction coefficients at the speeds of interest and hence enable the use of potential-flow assumptions, it is necessary to

justify this assumption in order to consider it valid for the problem of interest. In order to do so, the similar problem of 2-D flow past a planing flat plate is studied using two methods: (1) a fully-nonlinear, viscous CFD method and (2) an inviscid linearized potential-flow method. The CFD method offers the possibility for more accuracy, since it includes nonlinear effects, such as nonlinear free-surface deformations, jet sprays, wave breaking, and viscous effects. However, it is computationally more expensive and much care must be taken to ensure the numerical accuracy of the solution. In contrast, the linearized potential-flow method, which assumes the fluid to be inviscid and to satisfy linearized free-surface and body boundary conditions, cannot consider the nonlinear free surface conditions or viscous effects.[1] The linearized potential-flow method is, however, much more computationally efficient, offering solutions in a matter of seconds on a single-processor laptop versus multiple days on a multi-core computing cluster for the CFD simulations. It is therefore advantageous to use the linearized potential-flow method for cases in which the assumptions of linear free-surface and kinematic body boundary conditions, and inviscid flow, are valid, and to reserve the use of CFD for cases where the free-surface nonlinearities become important.

In the following sections, both the CFD and linearized potential-flow methods will be described. The problem of a 2-D flat plate is then solved using both methods and the results are compared (Kramer et al., 2012). It is found that at low speeds and large angles of attack, the linearized potential-flow method breaks down due to effects of free-surface nonlinearity as well as unsteady effects due to wave breaking.

3.1.1 Viscous CFD Method

In this section, the governing equations for the CFD method are given. In order to solve the fluid equations of motion, the open source CFD library OpenFOAM (2011) is used. The

[1] It should be noted that there exist potential-flow methods that satisfy the nonlinear free-surface boundary condition, but they are still unable to capture wave breaking effects.

free surface is captured using the VOF method (Hirt and Nichols, 1981). In this formulation, the complete domain is represented as a single fluid with spatially- and temporally-varying density and viscosity. The air and water phases are represented using the volume fraction (α), where $\alpha = 1$ corresponds to water and $\alpha = 0$ corresponds to air, and the fluid density (ρ) and fluid dynamic viscosity (μ) of the mixture are taken to be a volume-weighted average of the two phases, i.e.

$$\rho(\mathbf{x}, t) = \alpha(\mathbf{x}, t) \cdot \rho_w + (1 - \alpha(\mathbf{x}, t)) \cdot \rho_a \tag{3.1}$$

$$\mu(\mathbf{x}, t) = \alpha(\mathbf{x}, t) \cdot \mu_w + (1 - \alpha(\mathbf{x}, t)) \cdot \mu_a \tag{3.2}$$

where $\mathbf{x}$ is the spatial location vector, t is the time variable, ρ_w and ρ_a are the density of water and air, respectively, and $\mu_w = \rho_w \nu_w$ and $\mu_a = \rho_a \nu_a$ are the dynamic viscosity of water and air, respectively.

The volume fraction satisfies the advection equation:

$$\frac{\partial \alpha}{\partial t} + \nabla \cdot (\alpha \mathbf{u}) = 0 \tag{3.3}$$

where $\mathbf{u} = \mathbf{u}(\mathbf{x}, t)$ is the fluid velocity vector.

The flow velocity and pressure satisfy the incompressible Navier-Stokes equations, which may be written as:

$$\frac{\partial}{\partial t}(\rho \mathbf{u}) + \nabla \cdot (\rho \mathbf{u}\mathbf{u}) = -\nabla p^* - \mathbf{g} \cdot \mathbf{x} \nabla \rho + \nabla \cdot \left(\mu \left(\nabla \mathbf{u} + \nabla \mathbf{u}^T\right)\right) \tag{3.4}$$

$$\nabla \cdot \mathbf{u} = 0 \tag{3.5}$$

where $p^* = p^*(\mathbf{x}, t) = p - \rho \mathbf{g} \cdot \mathbf{x}$ is the dynamic pressure, p is the total pressure, and $\mathbf{g}$ is the gravitational acceleration vector. The results of the current study show minimal differences between inviscid and laminar-flow simulations; however, a laminar-flow model is used in order to facilitate calculation of the wetted length, which depends on the identification of

the stagnation point. A turbulence model is not used because it is not expected that viscous effects are very important for this problem, and to minimize possible sources of uncertainty in the CFD solutions.

The equations are discretized using a finite-volume discretization such that all spatial terms are second-order. Since the quasi-steady solution is desired for the problem of interest, first-order time discretization is used to minimize computational time. The free-surface location is determined by the fixed-value contour of the volume fraction at $\alpha = 0.5$.

3.1.2 Potential-Flow Method

3.1.2.1 Governing Equations

The potential-flow method selected is based on the work of Sedov (1965) and the numerical implementation is very similar to Doctors (1974, 1977), though a small modification to the latter method has been made. The problem will first be posed as presented by Sedov (1965) and then the numerical implementation will be discussed.

The fluid is assumed to be incompressible, inviscid, and irrotational, thus satisfying Laplace's equation for the velocity potential in an earth-fixed reference frame (Φ):

$$\nabla^2 \Phi = 0 \tag{3.6}$$

defined such that the fluid velocity vector $\mathbf{u} = \nabla\Phi$. We introduce the perturbation potential ϕ to account for a steadily-moving body-fixed reference frame such that

$$\Phi = \phi - Ux \tag{3.7}$$

where U is the forward speed traveling in the x-direction. Taking the Laplacian of both sides of Eq. (3.7) demonstrates that Laplace's equation is satisfied for the perturbation

potential as well:

$$\nabla^2\Phi = \nabla^2\left(\phi - Ux\right) = 0 \longrightarrow \nabla^2\phi = 0 \tag{3.8}$$

The dynamic free-surface boundary condition may be derived using the steady-state Bernoulli equation to relate a point far upstream with any other point in the fluid:

$$p_\infty + \tfrac{1}{2}\rho U^2 = \tfrac{1}{2}\rho\nabla\Phi\cdot\nabla\Phi + \rho g y + p \tag{3.9}$$

where p is the total pressure, p_∞ is the far-field pressure, ρ is the fluid density, g is the gravitational acceleration, and y is the vertical component of the position vector.

Substituting Eq. (3.7) into Bernoulli's equation and rearranging yields:

$$\begin{aligned} p - p_\infty &= \tfrac{1}{2}\rho\left[U^2 - \nabla\Phi\cdot\nabla\Phi\right] - \rho g y \\ &= \tfrac{1}{2}\rho\left[U^2 - \left(\frac{\partial\phi}{\partial x} - U\right)^2 - \left(\frac{\partial\phi}{\partial y}\right)^2\right] - \rho g y \\ &= \rho U\frac{\partial\phi}{\partial x} - \tfrac{1}{2}\rho\nabla\phi\cdot\nabla\phi - \rho g y \end{aligned} \tag{3.10}$$

Assuming $p_\infty = 0$ (thus defining p to be the relative instead of absolute pressure), after linearization of Eq. (3.10), the dynamic free-surface boundary condition may be written as:

$$p + \rho g\eta - \rho U\frac{\partial\phi}{\partial x} = 0 \quad \text{on}\, y = 0 \tag{3.11}$$

where η is the free surface elevation above the reference height $y = 0$.

The kinematic (non-penetration) free-surface boundary condition requires that the ma-

terial derivative of the quantity $y - \eta$ vanishes on the free surface:

$$\frac{D}{Dt}(y - \eta) = 0 \quad \text{on } y = \eta \tag{3.12}$$

where

$$\frac{D}{Dt}() = \frac{\partial()}{\partial t} + \frac{\partial \Phi}{\partial x}\frac{\partial()}{\partial x} + \frac{\partial \Phi}{\partial y}\frac{\partial()}{\partial y} \tag{3.13}$$

is the material derivative.

Evaluating Eq. (3.12) for steady-state conditions ($\frac{\partial}{\partial t} = 0$), substituting Eq. (3.7), and linearizing about $y = 0$ yields the linearized kinematic free-surface boundary condition:

$$\begin{aligned} \frac{\partial \Phi}{\partial y} - \frac{\partial \Phi}{\partial x}\frac{\partial \eta}{\partial x} - \frac{\partial \Phi}{\partial y}\frac{\partial \eta}{\partial y} &= 0 \\ \frac{\partial \phi}{\partial y} - \frac{\partial \phi}{\partial x}\frac{\partial \eta}{\partial x} - \frac{\partial \phi}{\partial y}\frac{\partial \eta}{\partial y} + U\frac{\partial \eta}{\partial x} &= 0 \\ \frac{\partial \phi}{\partial y} + U\frac{\partial \eta}{\partial x} &= 0 \quad \text{on } y = 0 \end{aligned} \tag{3.14}$$

The combined free-surface boundary condition is obtained by eliminating η by combining Eqs. (3.11) and (3.14):

$$\begin{aligned} \frac{\partial p}{\partial x} + \rho g\frac{\partial \eta}{\partial x} - \rho U\frac{\partial^2 \phi}{\partial x^2} &= 0 \\ \frac{\partial p}{\partial x} - \frac{\rho g}{U}\frac{\partial \phi}{\partial y} - \rho U\frac{\partial^2 \phi}{\partial x^2} &= 0 \\ \frac{1}{\rho U}\frac{\partial p}{\partial x} = k_0\frac{\partial \phi}{\partial y} + \frac{\partial^2 \phi}{\partial x^2} &\quad \text{on } y = 0 \end{aligned} \tag{3.15}$$

where $k_0 = g/U^2$ is the fundamental wave number.

3.1.2.2 Constructing a Numerical Solution

Using the boundary conditions from the previous section, the solution to the linearized potential-flow problem may be found and solutions are known for simple pressure distributions. The principle of the numerical method is that, given a pressure distribution $p(x)$ applied to the free surface, the free-surface elevation may be calculated, or vice versa. Due to the linearization of the problem, any number of pressure distributions may be combined by the principle of linear superposition. Thus, a complete solution for the hydrodynamic response may be constructed by summing the effects of any number of fundamental pressure distributions, where the free-surface elevation due to each element is analytically known. In essence, the numerical method represents the presence of a planing body by the pressure distribution that it applies to the free surface.

In order to solve for the unknown pressure distribution along the free surface, which represents the presence of the body, the free surface must be discretized in the x-direction into N separate pressure distributions. The complete hydrodynamic solution may be formulated by summing the influence of any number of known and unknown pressure elements and applying a kinematic boundary condition for the body surface. In this section, the way in which the pressure elements combine to form a complete solution is discussed. The exact form of the various pressure distributions is described in the next section.

Consider a planing surface that is discretized into N discrete pressure elements of arbitrary form. At any point along the free surface, the principle of superposition implies that the free surface elevation is

$$\eta\left(x\right) = \frac{1}{\rho g}\sum_{i=1}^{N} C_i\left(x\right) p_i \tag{3.16}$$

where $C_i = \rho g \eta / p_o$ is the influence coefficient of pressure element i, the form of which is chosen from the appropriate formula given in the next section. The influence coefficient is a function that is proportional to the free-surface elevation that is generated when a given

pressure distribution is applied to the free surface. The kinematic body boundary condition requires that the free-surface height is equal to the height of the submerged surface of the body, i.e.

$$\eta\left(x\right) = y\left(x\right) \quad \text{on the body} \tag{3.17}$$

Since each pressure element represents the pressure along the planing surface, Eq. (3.16) may be written at the location of each pressure element and the following system of equations may be constructed:

$$\eta_j = \frac{1}{\rho g} \sum_{i=1}^{N} C_{ij} p_i = y_{B,j} \tag{3.18}$$

where $\eta_j = \eta(x_j)$ and $y_{B,j} = y_B(x_j)$ are the free-surface height and submerged body height at the location x_j of pressure element j, and $C_{ij} = C_i(x_j)$ is the influence coefficient at point j due to element i. Thus, a system of N equations may be constructed for N unknown pressures (p_i's) and may be solved using a linear matrix solver to solve Eq. (3.18).

More generally, the solution may also have known pressure distributions applied to the free surface. For example, an SES pressure cushion may be represented by a known pressure distribution. Thus, a more general expression for the free-surface elevation is:

$$\eta(x) = \frac{1}{\rho g} \left[\sum_{i=1}^{N} C_i p_i + \sum_{k=1}^{M} \tilde{C}_k \tilde{p}_k \right] \tag{3.19}$$

where k is the index of the source element, a tilde represents a known quantity, and N and M are the number of unknown elements and source elements, respectively. In a similar manner, the kinematic boundary condition may be applied at all unknown pressure

elements and a linear system of equations may be constructed:

$$\frac{1}{\rho g}\sum_{i=1}^{N} C_{ij}p_i = y_{B,j} - \frac{1}{\rho g}\sum_{k=1}^{M} \tilde{C}_{kj}\tilde{p}_k \tag{3.20}$$

By using this method of constructing a numerical solution, the pressure distribution along any arbitrary body shape may be calculated with consideration to additional pressure source terms.

3.1.2.3 Fundamental Pressure Distributions

In order to construct a numerical solution, fundamental pressure distributions must be used. These are relatively simply-defined pressure distributions that are known to satisfy the governing equations given in Section 3.1.2. The fundamental building blocks of the method are based on the results of Lamb (1945) for semi-infinite pressure distributions. Triangular pressure elements are then derived from these fundamental distributions, which enable a linear approximation of any pressure distribution to be constructed. These fundamental pressure distributions have been previously provided by Doctors (1977), and they are included here for completeness.

Semi-Infinite Pressure Bands The most fundamental pressure distributions are the forward and aft semi-infinite pressure bands, which are defined by a sharp pressure "jump" at the location x_o. The first variation is the forward semi-infinite pressure band, which is defined as follows:

$$p = \begin{cases} p_o & x >= x_o \\ 0 & x < x_o \end{cases} \tag{3.21}$$

where p_o is the pressure element strength and x_o is the pressure element location.

The influence coefficient for the forward semi-infinite pressure band is

$$\frac{\rho g \eta}{p_o} = \Gamma_3 \left(\lambda_0 \right) \tag{3.22}$$

where $\lambda_0 = \left(x - x_o \right) k_0$ is the nondimensional x-location and

$$\Gamma_3(\lambda) \equiv -\frac{1}{\pi} \mathrm{sgn} \left(\lambda \right) f \left(\lambda \right) - 2H \left(-\lambda \right) \cos \left(\lambda \right) - H \left(\lambda \right) \tag{3.23}$$

is the form of the influence coefficient, which is proportional to the free-surface height. Here, $\mathrm{sgn}\left(\right)$ is the sign function, $H\left(\right)$ is the Heaviside step function, λ is a the independent variable in the form of the x-location non-dimensionalized by the fundamental wave length, and f and g are the auxiliary sine and cosine integral functions, defined by Abrahamowitz and Stegun (1965) as

$$f \left(\lambda \right) = \int_0^\infty \frac{\sin(t)}{\lambda + t} \, dt \tag{3.24}$$

$$g \left(\lambda \right) = \int_0^\infty \frac{\cos(t)}{\lambda + t} \, dt \tag{3.25}$$

where t is the working variable inside the integrals. In the current work, these integrals are solved using the `SciPy` scientific computing package.

The second variation is the aft semi-infinite pressure band, which is the same as the forward semi-infinite pressure band but reflected across the point x_o. This pressure distribution is defined as follows:

$$p = \begin{cases} 0 & x >= x_o \\ p_o & x < x_o \end{cases} \tag{3.26}$$

The influence coefficient for the aft semi-infinite pressure distribution is

$$\frac{\rho g \eta}{p_o} = \Gamma_2 \left(\lambda_0 \right) \tag{3.27}$$

where

$$\Gamma_2(\lambda) \equiv \frac{1}{\pi} \mathrm{sgn} \left(\lambda \right) f \left(\lambda \right) + H \left(-\lambda \right) \left(2 \cos \left(\lambda \right) - 1 \right) \tag{3.28}$$

The pressure distributions and influence coefficients for both the aft and forward semi-infinite pressure bands are shown in Fig. 3.1. The presence of a jump in pressure is found to cause a disturbance to the free surface both upstream (right) and, to a greater extent, downstream (left). Hence, pressure disturbances upstream greatly affect the response downstream.

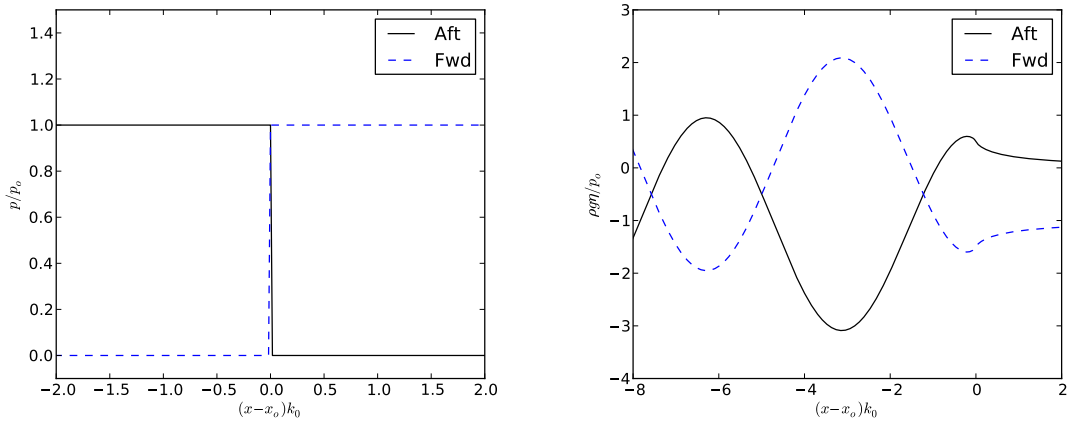

(a) Pressure Distribution

(b) Influence Coefficient

Figure 3.1: Pressure distributions and influence coefficients (proportional to the free-surface height) for forward and aft semi-infinite pressure bands

Forward Half-Triangular Pressure Element By integrating a continuous distribution of semi-infinite pressure bands, triangular pressure elements may be constructed. The derivation of these integrals is given by Doctors (1977), however the definitions and influence

coefficients for these elements will now be given for completeness.

The forward half-triangular pressure element is defined as follows:

$$p = \begin{cases} 0 & x >= x_o + b \\ p_o \left(1 - \frac{x - x_o}{b}\right) & x_o < x < x_o + b \\ 0 & x < x_o \end{cases} \tag{3.29}$$

where b is the pressure element width, and the influence coefficient for this pressure distribution is

$$\frac{\rho g \eta}{p_o} = \frac{1}{b k_0} \left[\Gamma_1 (\lambda_0) - \Gamma_1 (\lambda_1)\right] - \Gamma_2 (\lambda_0) \tag{3.30}$$

where $\lambda_1 = (x - x_o - b)k_0$. The function $\Gamma_1 (\lambda)$ is related to the integration of $\Gamma_2 (\lambda)$ and has the following form:

$$\Gamma_1(\lambda) \equiv \frac{1}{\pi} \left[g (\lambda) + \ln \lambda\right] + H (-\lambda) \left[2 \sin (\lambda) - \lambda\right] \tag{3.31}$$

The pressure distribution and influence coefficient for this pressure element is shown in Fig. 3.2 for various element widths.

Aft Half-Triangular Element This pressure distribution is the reflected version of the forward half-triangular element and is defined as follows:

$$p = \begin{cases} 0 & x >= x_o \\ p_o \left(1 + \frac{x - x_o}{b}\right) & x_o - b < x < x_o \\ 0 & x < x_o - b \end{cases} \tag{3.32}$$

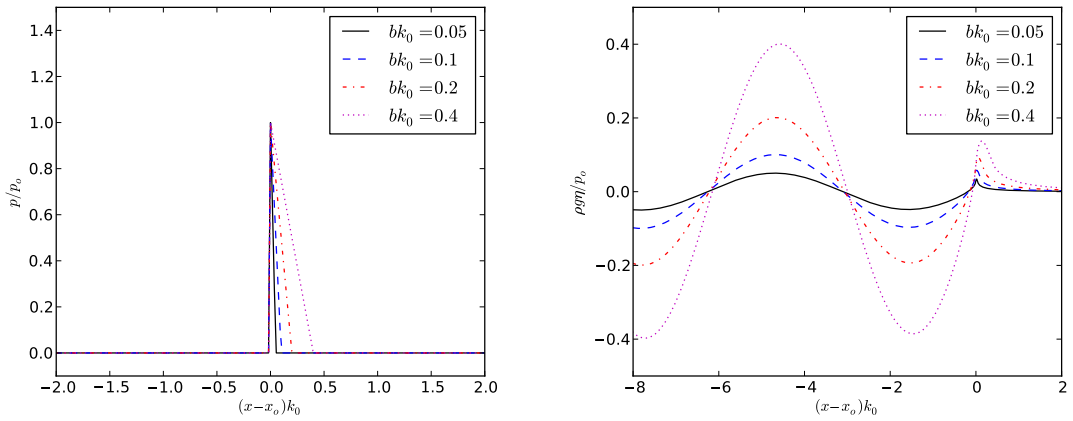

(a) Pressure Distribution (b) Influence Coefficient

Figure 3.2: Pressure distributions and influence coefficients (proportional to the free-surface height) for forward half-triangular pressure element for a range of element widths

The influence coefficient for this pressure distribution is

$$\frac{\rho g \eta}{p_o} = \frac{1}{bk_0} \left[\Gamma_1 \left(\lambda_0 \right) - \Gamma_1 \left(\lambda_2 \right) \right] + \Gamma_2 \left(\lambda_0 \right) \tag{3.33}$$

where $\lambda_2 = (x - x_o + b)k_0$.

The pressure distribution and influence coefficient for this pressure element is shown in Fig. 3.3 for a range of element widths.

3.1.2.4 Compound Pressure Elements

Using the fundamental pressure elements that have been described in the previous section, compound pressure elements may be constructed by combining them in useful configurations via the principle of superposition. It is useful to define a few compound elements for convenience.

Complete Triangular Pressure Element A complete triangular pressure element may be constructed by placing a forward and aft half-triangular pressure element at the same location. Generally, the influence coefficient of the complete triangular pressure element

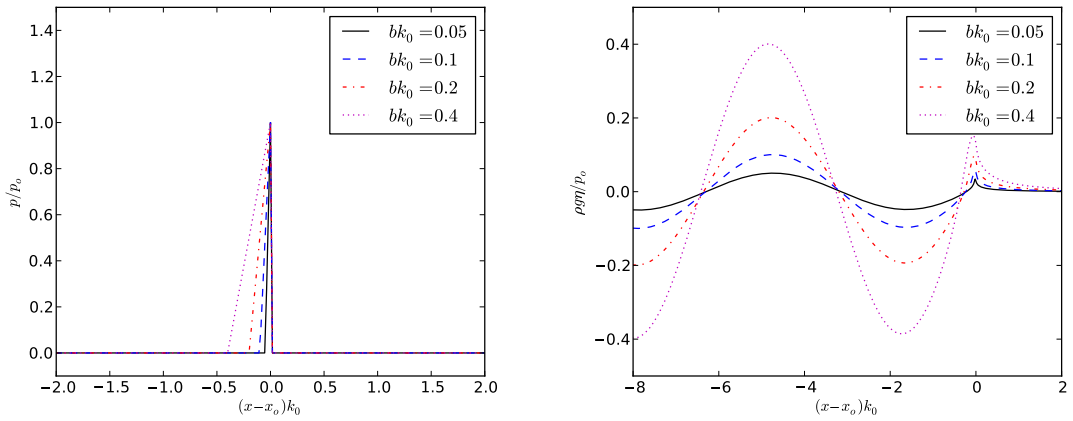

(a) Pressure Distribution (b) Influence Coefficient

Figure 3.3: Pressure distributions and influence coefficients (proportional to the free-surface height) for aft half-triangular pressure element for a range of element widths

may be written by adding Eqs. (3.30) and (3.33), which yields

$$\frac{\rho g\eta}{p_o} = \frac{1}{k_0}\left[\left(\frac{1}{b_a}+\frac{1}{b_f}\right)\Gamma_1(\lambda_0) - \frac{1}{b_a}\Gamma_1(\lambda_2) - \frac{1}{b_f}\Gamma_1(\lambda_1)\right] \tag{3.34}$$

where b_a and b_f are the widths of the aft and forward half-triangular pressure elements, respectively. The pressure distributions and influence coefficients for this pressure element are shown in Fig. 3.4 for cases where the aft and forward half-triangular elements are the same width.

In the special case where the two half-triangular elements are the same width, the influence coefficient may be simplified:

$$\frac{\rho g\eta}{p_o} = \frac{1}{bk_0}\left[2\Gamma_1(\lambda_0) - \Gamma_1(\lambda_2) - \Gamma_1(\lambda_1)\right] \tag{3.35}$$

Finite Pressure Band A finite pressure band may be constructed by subtracting an aft semi-infinite pressure band placed at the downstream side of the element from an aft semi-

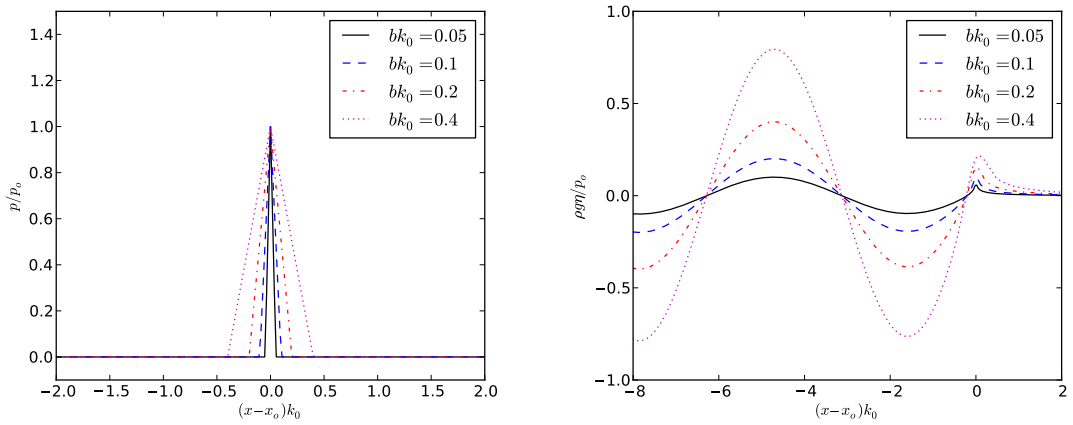

(a) Pressure Distribution

(b) Influence Coefficient

Figure 3.4: Pressure distributions and influence coefficients (proportional to the free-surface height) for complete triangle pressure element for a range of element widths

infinite pressure band placed at the upstream side of the element.

$$\frac{\rho g \eta}{p_o} = \Gamma_3 \left(\lambda_{\text{bow}}\right) - \Gamma_3 \left(\lambda_{\text{stern}}\right) \tag{3.36}$$

where $\lambda_{\text{bow}} = (x - x_{\text{bow}})k_0$ and $\lambda_{\text{stern}} = (x - x_{\text{stern}})k_0$.

The pressure distributions and influence coefficients for this pressure element are shown in Fig. 3.5 for varying element Froude number, defined as $Fr_b = U/\sqrt{gb}$ is the Froude number based on the element width, and in this case, $b = x_{\text{bow}} - x_{\text{stern}}$. A finite pressure band was used in the early development of SESs for wave resistance prediction. By changing the Froude number based on the element width, which is representative of the Froude number based on the cushion length (Fr_C) if one element is used to model the cushion, the bow and stern wave systems interact, causing cancellation effects. These effects may be seen in Fig. 3.5(b).

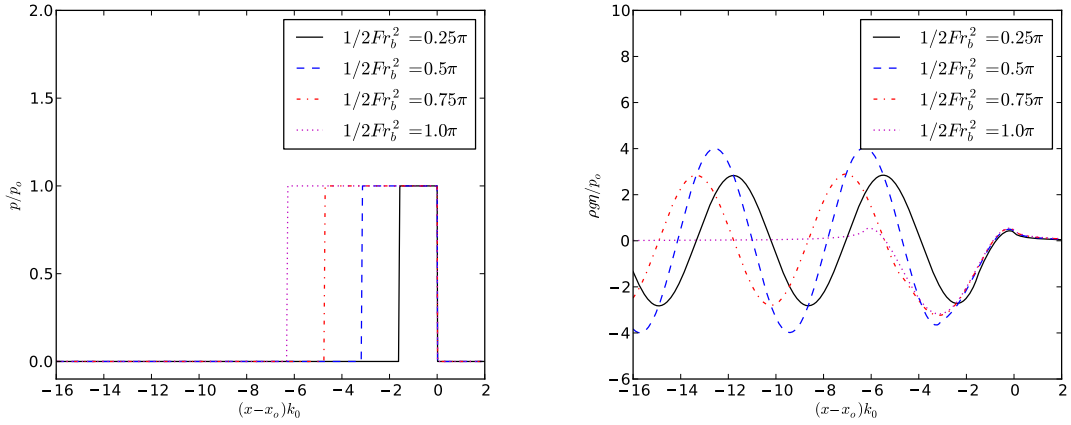

(a) Pressure Distribution

(b) Influence Coefficient

Figure 3.5: Pressure distributions and influence coefficients (proportional to the free-surface height) for finite pressure bands for a range of element widths. It should be noted that at certain Fr_b, the waves cancel. This is the direct driver of the humps and hollows in the 2-D ACV/SES wave resistance curve.

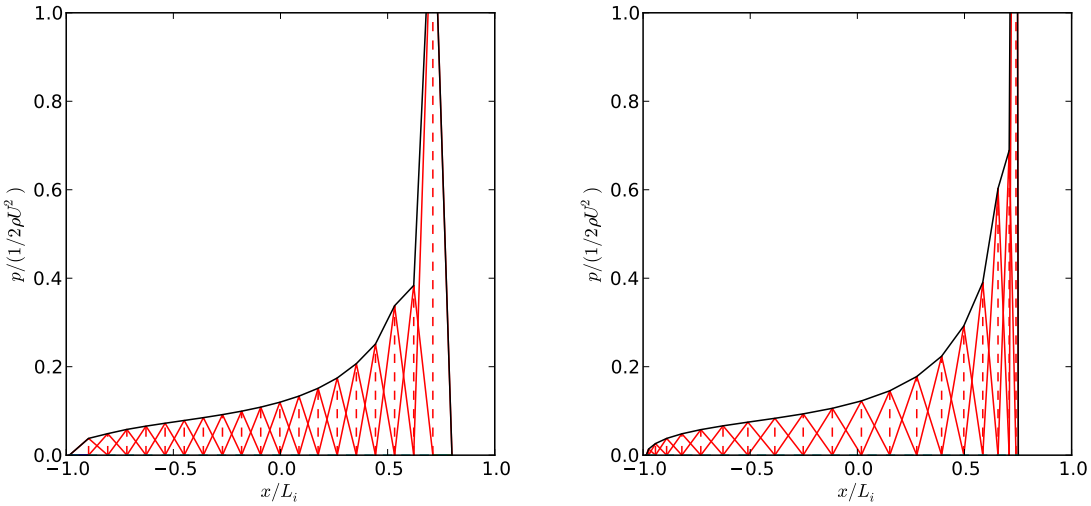

(a) Linear spacing

(b) Cosine spacing

Figure 3.6: Example discretization of single planing flat plate problem using two discretization schemes. In both cases, 19 complete-triangular elements are used with one forward half-triangle element at the trailing edge (20 elements in total), the pressure of which is driven to zero by the wetted-length solver. It should be noted that these cases are not converged, but are instead provided for illustration.

3.2 Example Discretization: Planing Flat Plate

For the simplest case of a planing plate without a pressure cushion behind it, the plate may be represented by a collection of $N-1$ complete triangular pressure elements with one forward half-triangular pressure element at the trailing edge, as illustrated in Fig. 3.6, where two options for the discretization scheme are shown. For the case of linear spacing, all elements are located an equal distance away from each other, whereas the cosine spacing concentrates more elements near the trailing edge and stagnation point, where the pressure gradient is largest.

The pressure element locations for the linear spacing are defined as:

$$x_i = x_{\mathrm{TE}} + L_w \frac{i-1}{N-1} \quad \text{for } i = 1...N \tag{3.37}$$

and the pressure element locations for the cosine spacing are defined as:

$$x_i = x_{\mathrm{TE}} + \frac{L_w}{2}\left[\cos\left(\frac{(i-1)\,\pi}{N-1}\right) + 1\right] \quad \text{for } i = 1...N \tag{3.38}$$

where x_{TE} is the x-location of the trailing edge and L_w is the wetted length of the planing surface.

The benefit of the cosine spacing versus linear spacing is that fewer elements are needed to obtain an accurate solution by concentrating elements at regions of high pressure gradient at the leading and trailing edges. A convergence study will be shown to demonstrate this case in Section 3.3.4.

One of the characteristics of the problem is that the wetted length of the planing surface (L_w) must be assumed prior to solving the linear system for the pressure of each element in order to distribute the pressure elements. There must then be an additional unknown parameter as part of the solution in order to force the dynamic wetted length to be equal to the guessed wetted length. In the case of Doctors (1974), and most other solutions

for the planing plate problem (e.g. Fridman and Tuck, 2006; Sedov, 1965), the height of the trailing edge is left as an unknown, to be solved for in conjunction with the pressure along the planing surface, and the trailing edge pressure is assumed to be zero (i.e. atmospheric, or any other fixed value). In essence, these methods solve for the immersion depth that must be attained in order to match the assumed wetted length. The wetted length of the planing surface can be varied using a nonlinear solver in order to match the immersion depth from the solution with the true immersion depth of the fixed geometry.

In the current case, however, a slightly different approach is taken. In both the traditional and the current formulations, the dynamic wetted length must be assumed in order to distribute pressure elements and calculate the pressure profile along the plate. The difference lies in the treatment of the trailing edge condition. For the current formulation, the trailing edge height is considered to be fixed and the pressure at the trailing edge is taken as part of the total pressure solution by placing an unknown forward half-triangular pressure element at the trailing edge. In both cases, a nonlinear solver must be used to find the dynamic wetted length that satisfies the appropriate trailing edge condition, and the results of both methods are ultimately identical. This approach is chosen due to the ambiguity associated with solving for two unknown trailing edge heights when more than one planing surface is present. Instead, by formulating the problem in such a way that the trailing edge pressure is an unknown, multiple trailing edge pressure conditions may be simultaneously satisfied relatively easily. This point is discussed further in Section 3.4.

The complete solution for the single planing flat problem may thus be stated as: find the wetted length (L_w) such that

$$\mathcal{R}(L_w) \equiv p_{TE}(L_w) - p_{\text{kutta}} = 0 \tag{3.39}$$

where p_{TE} is the pressure of trailing edge element after solving Eq. (3.18), p_{kutta} is the assumed (desired) trailing edge pressure, and L_w is the wetted length. For the case of a

single planing surface, the Secant method is found to be appropriate, typically converging in less than 10 iterations. In general, a tolerance of 1.0×10^{-6} is used.

3.3 Flat Plate Study

3.3.1 Problem Description

In order to compare the two fluid models, the problem of a two-dimensional, infinitely thin flat plate planing on the free surface between water and air is considered, as shown in Fig. 3.7. The plate has an immersed length (L_i) and is oriented at an angle of attack (β) from the calm-water free-surface. The transom submergence depth (h) is geometrically related to the immersed length and angle of attack via the following relation: $h = L_i \sin\beta$. The plate is traveling at a constant forward speed (U) on the water surface, which is assumed to be an incompressible fluid of density ρ_w and kinematic viscosity ν_w. A steady, body-fixed reference frame ($x - y$) is placed at the intersection of the plate face with the calm-water free surface. A local reference frame (s) is placed along the plate with the origin at the trailing edge, from which the pressure distribution is referenced. Gravity is assumed to act in the negative y-direction with gravitational acceleration (g). The wetted length (L_w) is defined as the distance from the plate trailing edge to the stagnation point. The velocity is made dimensionless using the Froude number based on twice the immersed length $Fr_i = U/\sqrt{2gL_i}$. The immersion-depth-based Froude number is also found to be an important parameter, defined as $Fr_h = U/\sqrt{gh}$.

A brief note must be made to explain the factor of two that has been used in the reference length in the definition of Fr_i. In typical potential-flow results from the literature, the Froude number is defined using an assumed wetted length as the reference length and the height of the trailing edge is part of the solution. In the current formulation, the trailing edge height is fixed and the wetted length is part of the solution. Thus, the wetted length varies as a function of U and β. A factor of two was chosen after observing that the wetted

length tends to be roughly twice the immersed length for most of the cases studied in this paper. Although the correspondence is not exact, this brings the current definition of Froude number closer to that which is found in the literature.

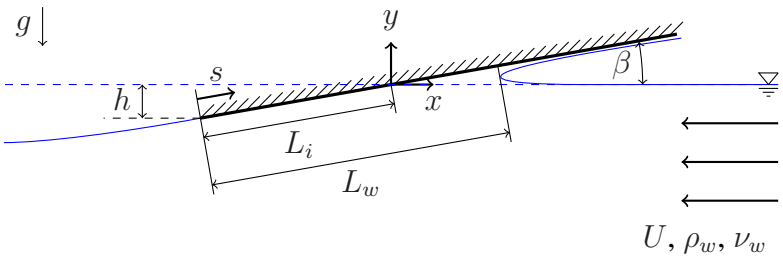

Figure 3.7: Definition of 2-D planing flat plate problem

For the results shown in this section, the flow speed U and angle of attack β are varied while the remaining parameters are held constant, as tabulated in Table 3.1. For reference, based on this definition, $Fr_i = 1.0$ corresponds to a flow speed of $3.13\,\mathrm{m/s}$ for $L_i = 0.5\,\mathrm{m}$ and $U = 6.26$ and $9.90\,\mathrm{m/s}$ for $L_i = 2$ and $5\,\mathrm{m}$, respectively.

Table 3.1: Fixed geometric and fluid properties for flat plate calculations

Item	Symbol	Value
Water density	ρ_w	$998.2\,\mathrm{kg/m^3}$
Air density	ρ_a	$1.225\,\mathrm{kg/m^3}$
Water kinematic viscosity	ν_w	$1.0048 \times 10^{-6}\,\mathrm{m^2/s}$
Air kinematic viscosity	ν_a	$1.4604 \times 10^{-5}\,\mathrm{m^2/s}$
Immersed length	L_i	$0.5\,\mathrm{m}$
Gravitational acceleration	g	$9.81\,\mathrm{m/s^2}$

3.3.2 CFD Mesh Topology

Due to the simple geometry, a structured mesh is used; care is taken to minimize potential sources of error due to grid non-orthogonality. The domain is decomposed into several regions, as shown in Fig. 3.8, to ensure adequate mesh refinement while minimizing the total number of cells. The mesh is refined in three key locations:

1. near the stagnation point (to capture the large pressure gradient)

2. along the plate surface (to capture the large velocity gradient and shear stress)

3. near the free surface (to resolve the free surface profile)

The chosen mesh is shown in Fig. 3.9 and consists of approximately 125,000 cells with 325 faces along the plate surface. The near-wall resolution has approximately 5 cells within the boundary layer at the origin for $\beta = 10°$ and $Fr_i = 1.0$.

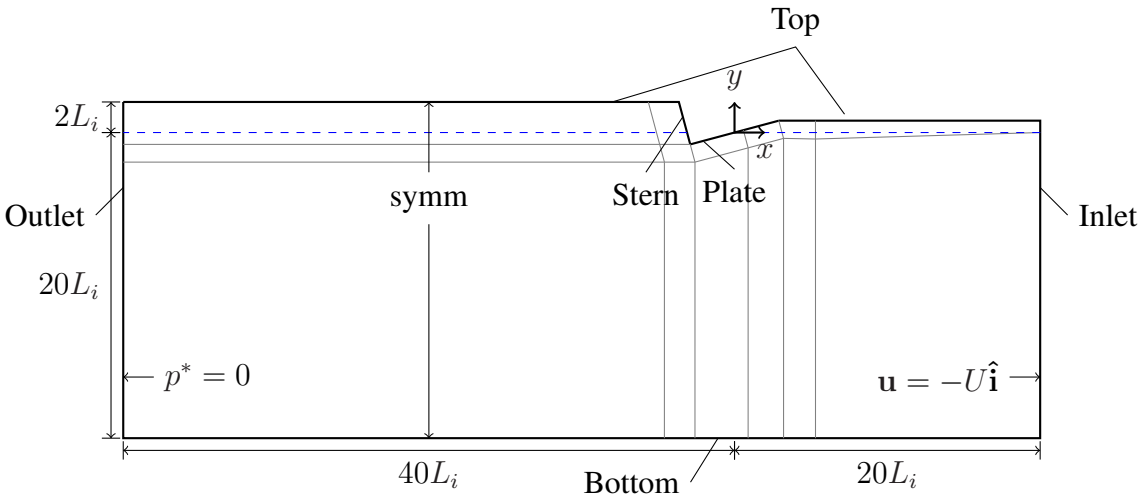

Figure 3.8: Diagram of computational domain for CFD simulations showing mesh topology, boundaries, and dimensions (not to scale)

3.3.3 Boundary Conditions

The boundary conditions for the simulations are listed in Table 3.2. The inlet boundary conditions are consistent with a velocity inlet and the outlet is consistent with a pressure outlet. For all plate surfaces (including the stern), a no-slip wall boundary condition is used.

3.3.3.1 Upstream Pressure Outlet

For the planing plate problem, the stagnation point causes the flow to split. The majority of the fluid continues to flow beneath the plate, but a small volume of fluid is redirected

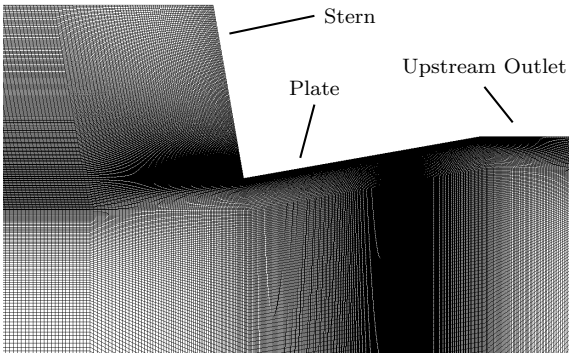

(a) Near-field view

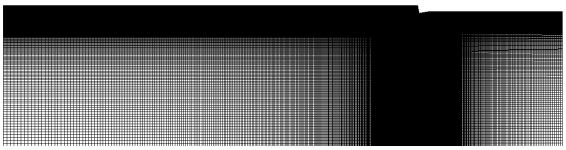

(b) Far-field view

Figure 3.9: Near- and far-field views of the computational (CFD) grid for $\beta = 10°$

Table 3.2: Boundary conditions for flat plate CFD simulations ($\partial_n(\cdot) \equiv \partial(\cdot)/\partial n$)

Boundary	Variable		
	$\mathbf{u}$	p^*	α
Inlet Water	$\mathbf{u} = -U\hat{\imath}$	$\partial_n p^* = 0$	$\alpha = 1$
Inlet Air	$\mathbf{u} = -U\hat{\imath}$	$\partial_n p^* = 0$	$\alpha = 0$
Outlet	$\partial_n \mathbf{u} = 0$	$p^* = 0$	$\partial_n \alpha = 0$
Plate & Stern	$\mathbf{u} = \mathbf{0}$	$\partial_n p^* = 0$	$\partial_n \alpha = 0$
Top & Bottom	— symmetry —		
Upstream Outlet	$\partial_n \mathbf{u} = \mathbf{0}$	$p^* = 0$	$\partial_n \alpha = 0$

upstream, known as the "jet," "spray," or "planing splash." Gravitational forces eventually cause the jet to fall and impact the upstream free surface. The effects of the jet impinging on the free surface are typically assumed to be negligible (Fridman and Tuck, 2006; Sedov, 1965), based on experimental observations.

In order to compare the potential-flow theory with the CFD method, the handling of the jet must be carefully considered. Although the VOF method being employed can capture the unsteady effects of the falling jet, the temporal and spatial discretization requirements necessary to accurately capture this effect are deemed prohibitive for the current study. The effects of the falling jet are thus ignored by introducing a pressure outlet upstream of the stagnation point. This approach was also used by Garland and Maki (2012). This point is illustrated in Fig. 3.10, where the jet region for $\beta = 10°$ at $Fr_i = 1.0$ is shown. The pressure outlet location is chosen to be far enough upstream to have negligible impact on the plate forces, but far enough downstream to prevent the jet from impinging on the upstream free surface.

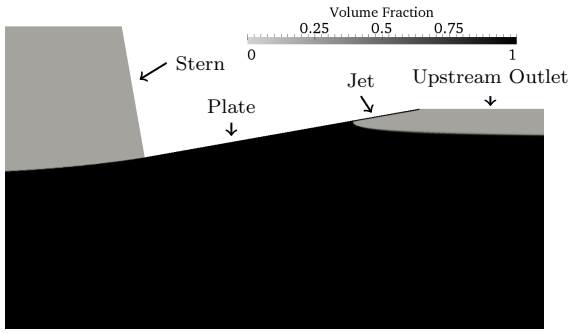

Figure 3.10: Close-up view of jet region for $\beta = 10°$, $Fr_i = 1.0$ showing contours of the volume fraction, α. The fluid is flowing from right-to-left. A pressure outlet is placed upstream of the stagnation point to prevent the jet from impinging on the free surface, which has the effect of corrupting the steady-state solution.

3.3.4 Convergence Study

The grid resolution is varied at $\beta = 10°$ and $Fr_i = 1.0$ in order to ensure adequate mesh refinement to accurately predict the forces and pressure distribution along the plate. In this

condition, the Reynolds number based on twice the immersed length (i.e. $Re_i = 2UL_i/\nu_w$) is approximately 3.1 million. Inviscid and laminar simulations are found to yield similar results with negligible differences. A laminar-flow model is chosen as the basis for this study to facilitate calculation of the stagnation point, which determines the wetted length. Turbulence models were not utilized due to the added complexity, ambiguity associated with the validity of turbulence models for free-surface flows (particularly in 2-D), as well as the expectation that the viscous effects would be negligible compared to the pressure drag.

The results for the pressure distributions and free-surface profiles for four meshes of varying levels of refinement are shown in Fig. 3.11 and compared with the linearized potential-flow theory described in Section 3.1.2, which yields the the same results as those presented in Doctors (1974). The results are found to compare fairly well in terms of the pressure profile, wetted length, and free surface profile. The potential-flow method predicts a pressure singularity at the stagnation point due to the linearization process; for the CFD simulations, the stagnation pressure based on the Bernoulli equation is also used as a measure of convergence.

Table 3.3: Convergence of lift, drag, and moment coefficients, and wetted length for various levels of mesh refinement at $\beta = 10°$, $Fr_i = 1.0$

Mesh	# Cells	Faces on Plate	C_l	C_d	C_m	$L_w/2L_i$
Coarse	45k	195	0.1673	0.0299	0.0280	0.948
Medium	80k	260	0.1680	0.0301	0.0293	0.966
Fine	125k	325	0.1685	0.0302	0.0311	0.971
Finest	180k	390	0.1684	0.0303	0.0308	0.982

In addition to convergence of the pressure and free-surface profiles, it is important to examine the convergence of the lift, drag, moment, and wetted length. Since the simulations are performed in the time domain, the steady-state forces and moments are obtained by computing a time-average over 20+ cycles after the initial transient oscillations have subsided. The results of the convergence study for lift, drag, moment, and wetted length

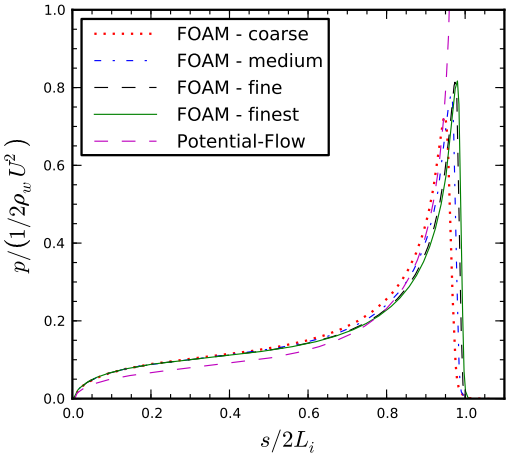

(a) Total pressure coefficient

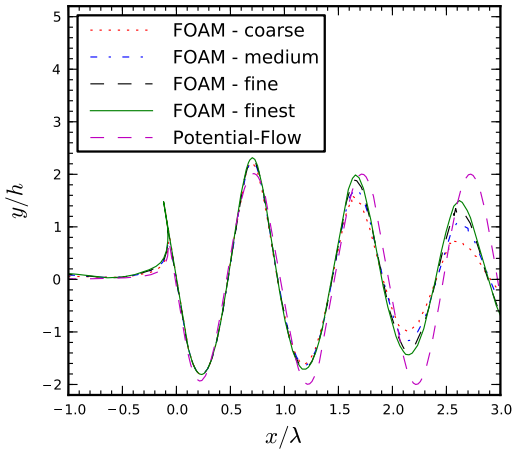

(b) Free-surface profile

Figure 3.11: Convergence of pressure distribution on the plate and the free-surface profile for various levels of mesh refinement at $\beta = 10°$, $Fr_i = 1.0$. Here, $\lambda = 2\pi U^2/g$ is the linear potential-flow theory estimate of the far-field wavelength and $h = L_i \sin\beta$ is the draft at the plate trailing edge.

are shown in Table 3.3. The lift, drag, and moment are nondimensionalized as follows:

$$C_l = \frac{\mathcal{L}}{1/2\rho_w U^2 \cdot 2L_i} \tag{3.40}$$

$$C_d = \frac{\mathcal{D}}{1/2\rho_w U^2 \cdot 2L_i} \tag{3.41}$$

$$C_m = \frac{\mathcal{M}}{1/2\rho_w U^2 \cdot (2L_i)^2} \tag{3.42}$$

where $\mathcal{L}$, $\mathcal{D}$, and $\mathcal{M}$ are the lift, drag, and moment, respectively, obtained by integrating the pressure and shear stress distributions along the plate. The moment is taken as positive in the counterclockwise direction about the origin. It should be noted that the trend is found to be non-monotonic for the lift and moment coefficients for the Finest mesh, most likely due to accumulation of small round-off errors in the pressure and shear stress integrals. The accuracy of the Fine mesh is deemed to be sufficient and is elected for the remainder of the CFD computations.

In addition to the convergence study for the CFD solutions, it is necessary to determine the number of required elements for the linearized potential-flow simulations. In Fig. 3.12, the normalized error of the lift coefficient and wetted length are shown versus the number of elements for both linear and cosine spacing. The normalized error is defined as $\varepsilon = |f - f_0| / f_0$, where f is the solution of interest (i.e. lift or wetted length) and f_0 is the "true" solution, which is taken as the potential-flow solution with 170 elements. The cosine spacing is found to converge much faster than the linear spacing, due to the increased resolution near the trailing edge and stagnation point. Consequently, fewer elements may be used with the cosine spacing than for the linear spacing. For the flat-plate study, 150 elements were used with cosine spacing.

3.3.5 Effects of Angle of Attack on Pressure Distribution

In order to independently investigate the effects of angle of attack, the hydrodynamic response is calculated for a range of angle of attack, β at a fixed Froude number, $Fr_i = 1.1$.

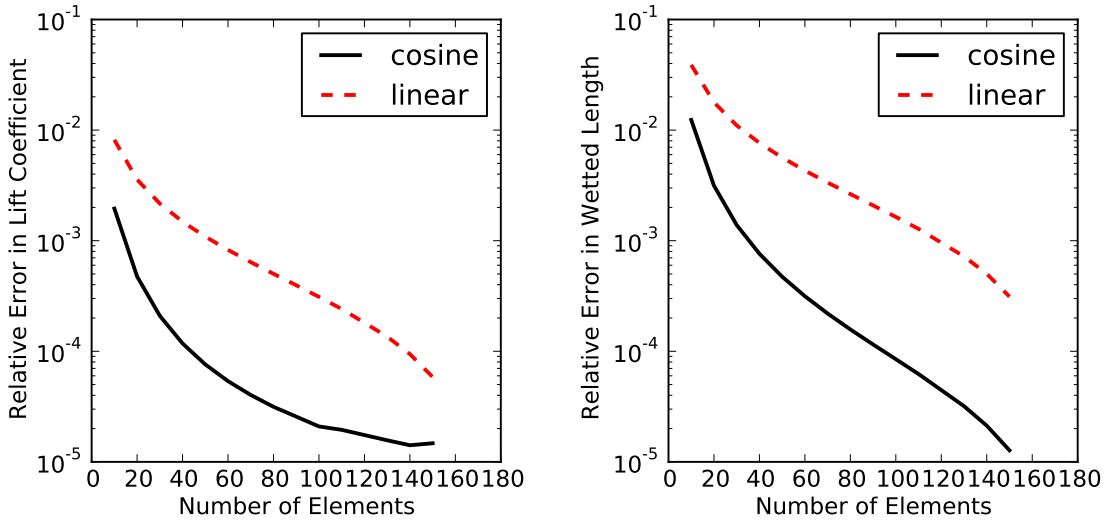

(a) Normalized Error in Lift

(b) Normalized Error in Wetted Length

Figure 3.12: Normalized error of lift and wetted length for linearized potential-flow method. The cosine element spacing is found to exhibit a much faster convergence rate than the linear element spacing.

The pressure and free-surface profiles for each case are shown in Fig. 3.13. In addition to the CFD results, which are shown as solid curves, the linearized potential-flow results are shown as dashed lines. In all cases at this flow speed, the results were found to reach steady-state. Good agreement is observed between the CFD and potential-flow solutions for $\beta \leq 10°$; however, at larger angles of attack, nonlinear effects are shown to be increasingly important. In particular, the wave profiles are found to become more nonlinear as β increases. These trends are generally found to be true at other Froude numbers as well, but unsteady effects caused by breaking waves are found to become dominant at lower speeds.

It should be noted that, as β increases, the center of pressure moves towards the trailing edge, the pressure becomes more evenly distributed, and the pressure gradient near the leading edge is reduced. Conversely, the pressure gradient near the trailing edge is increased.

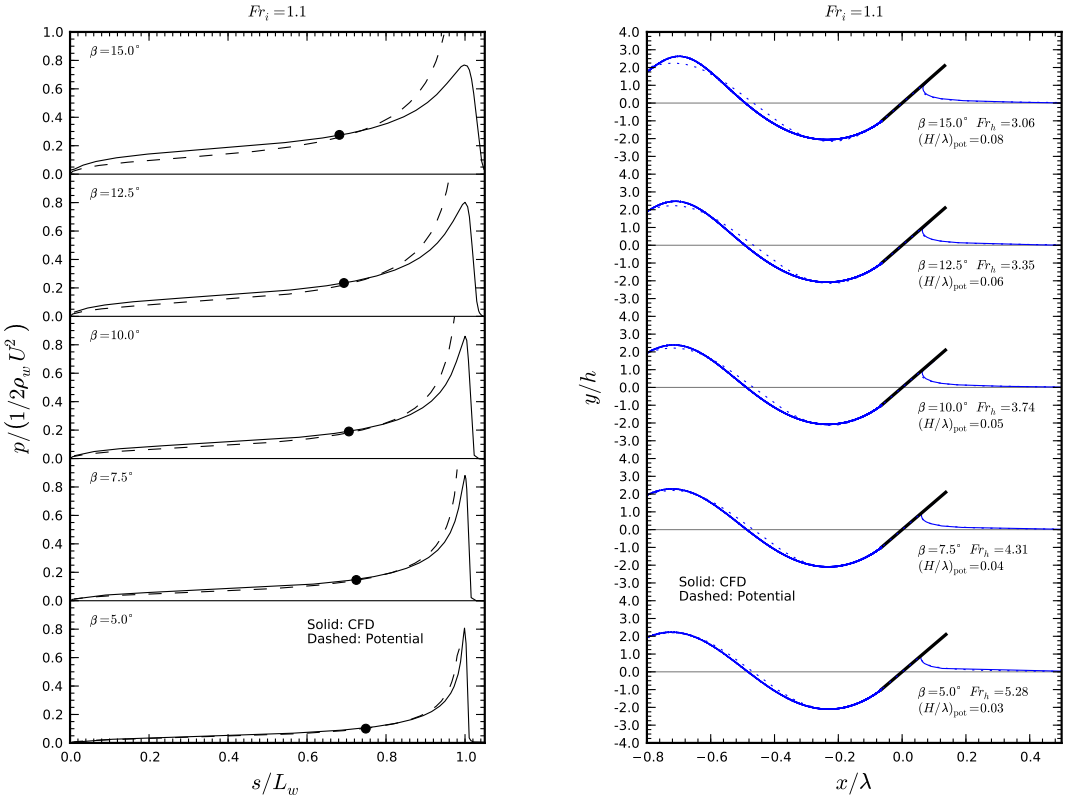

(a) Pressure Profile

(b) Free-Surface Profile

Figure 3.13: Plots of total pressure coefficient and free-surface profile at fixed Froude number $Fr_i = 1.1$ for varying angle of attack, β. Solid lines correspond to CFD results and dashed lines correspond to linearized potential-flow results. In subfigure (a), the symbols are located at the center of pressure on the abscissa and spatially-averaged pressure on the ordinate. In subfigure (b), $\lambda = 2\pi U^2/g$ is the linear potential-flow theory estimate of the far-field wavelength and $h = L_i \sin\beta$ is the draft at the plate trailing edge.

3.3.6 Effects of Froude Number on Pressure Distribution

The pressure and free surface profiles for a range of Froude number, Fr_i, at fixed angle of attack, $\beta = 7.5°$, are shown in Fig. 3.14. The linearized potential-flow results are found to compare well with the CFD results for high Froude numbers. However, at lower speeds ($Fr_i < 0.8$), differences due to nonlinearity become more important. For this angle of attack, the results become unsteady due to wave breaking at $Fr_i = 0.5$, and hence the pressure profile shown is a snap-shot at the final simulation time.

In general, it was found that as Fr_i decreases, the waves become more nonlinear and the relative center of pressure moves towards the middle of the plate. Additionally, the pressure gradient at the trailing edge increases until the waves begin to break. This trend is especially apparent for $Fr_i < 0.8$. Once the waves begin to break, the mean trailing edge pressure is not zero, as expected. This is due to the breaking of the downstream waves, which causes a slight periodic re-wetting of the transom, leading to an increase in hydrostatic pressure at the trailing edge. The increase in pressure at the trailing edge is found to increase as Fr_i decreases, leading to increasing differences between the linearized potential-flow and CFD results. This effect is discussed in the next section.

3.3.7 Effects of Unsteadiness and Nonlinearity on the Hydrodynamic Response

The lift, drag, and moment coefficients are shown as functions of the Froude number Fr_i for a range of angle of attack β in Fig. 3.15. The linear potential-flow results are shown as curves and the CFD results are shown as symbols.

The results show that the CFD and linear potential-flow results compare fairly well for $Fr_i \geq 0.8$. In this speed range, the potential-flow method should be chosen for its computational efficiency. However, at lower Froude numbers, the time-averaged force and moment coefficients differ largely due to nonlinear effects. Due to the effects of wave

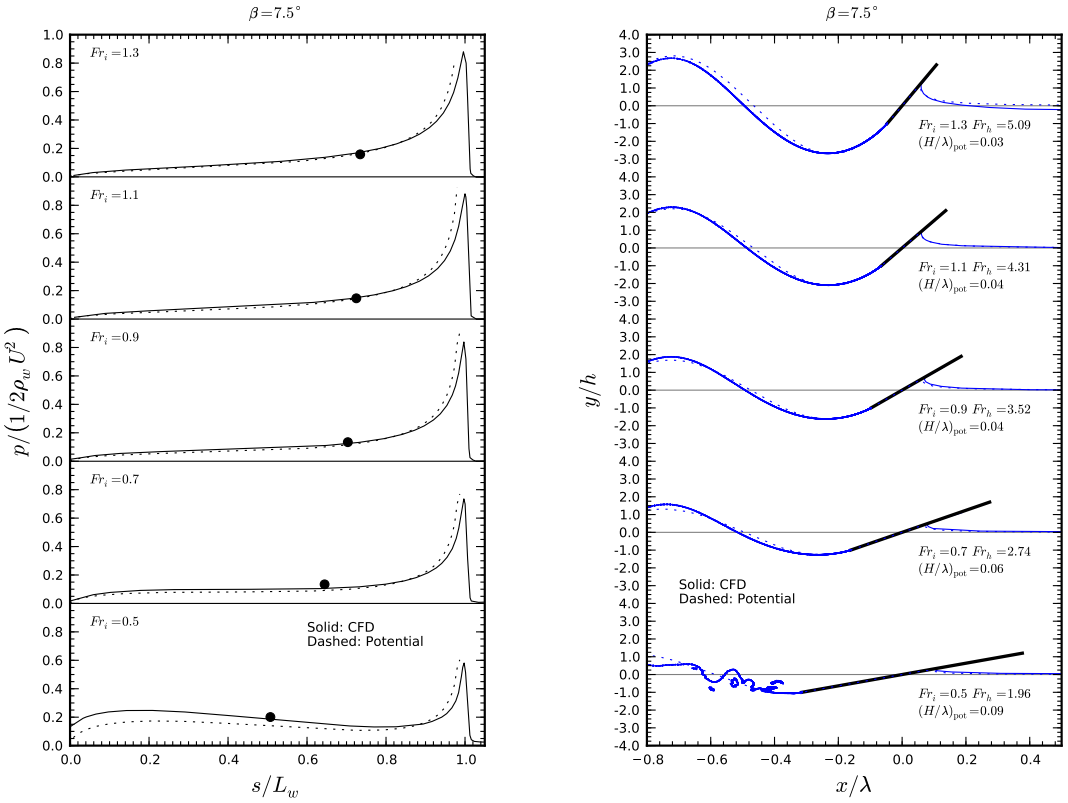

(a) Pressure Profile

(b) Free-Surface Profile

Figure 3.14: Plots of total pressure coefficient and free-surface profile at fixed angle attack $\beta = 7.5°$ for varying Froude number, Fr_i. Solid lines correspond to CFD results and dashed lines correspond to linearized potential-flow results. In subfigure (a), the symbols are located at the center of pressure on the abscissa and spatially averaged pressure on the ordinate. In subfigure (b), $\lambda = 2\pi U^2/g$ is the linear potential-flow theory estimate of the far-field wavelength and $h = L_i \sin\beta$ is the draft at the plate trailing edge. It should be noted that the plates are of identical geometry, but appear not to be so due to the nondimensionalization of the x variable.

breaking, the differences between the linear potential-flow and CFD results are seen to increase as Fr_i decreases.

Contours of the absolute difference in the lift and drag coefficients predicted by the CFD and linear potential-flow methods and normalized by the CFD result are shown in Fig. 3.16. The two methods are found to compare well for $Fr_i \geq 0.8$ and $\beta < 10°$ (error $\leq 5\%$). For $Fr_i < 0.8$, the difference increases as Fr_i is reduced and β is increased due to nonlinear effects. In addition to the effects of wave nonlinearity, some differences between the two methods at larger Froude numbers may be due to insufficient domain size, which was optimized for $Fr_i \leq 1.0$.

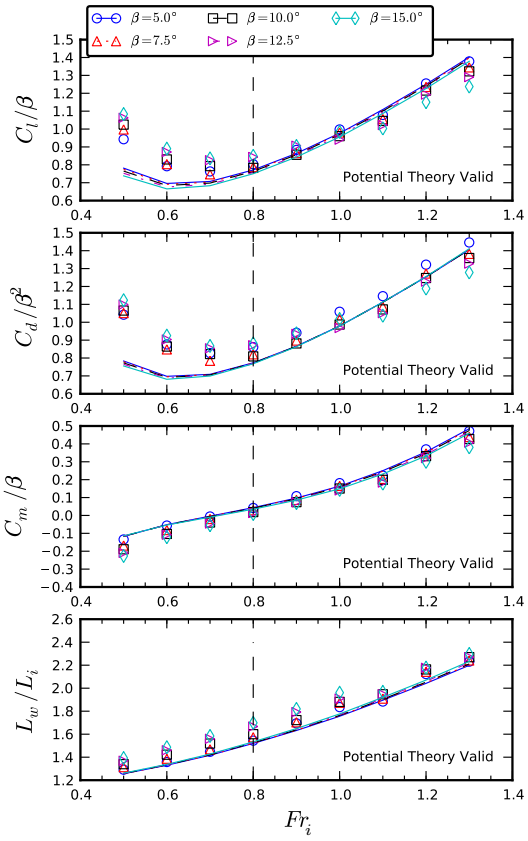

Figure 3.15: Curves of lift, drag, and moment coefficients and wetted length as a function of Froude number Fr_i for various angle of attack, β. The potential-flow results are plotted as curves while the time-averaged CFD results are shown as symbols.

It is useful to determine the operating boundaries where unsteadiness due to wave

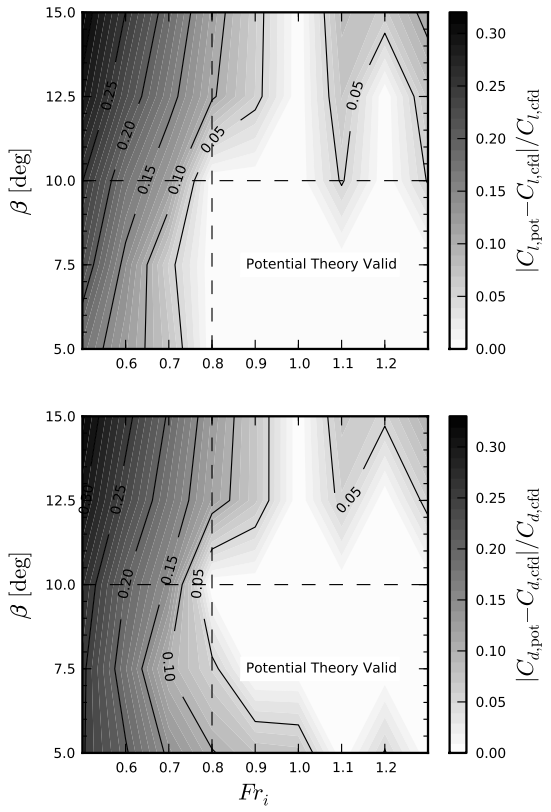

Figure 3.16: Contours of normalized difference in lift and drag coefficient between CFD and linear potential results for a range of β and Fr_i

breaking becomes important. In order to do so, a contour of the standard deviation of the lift and drag coefficient time histories, denoted C_l' and C_d', respectively, normalized by the time-averaged value is shown in Fig. 3.17. In addition to the filled contours, black contour curves are shown at constant immersion-based Froude number, defined as $Fr_h = U/\sqrt{gh}$, where $h = L_i \sin\beta$ is the draft of the trailing edge. The results show that the large increase in unsteadiness is fairly well characterized by the contour at $Fr_h \approx 2.75$. This value is quite close to the results found numerically and experimentally by Maki (2006) for two-dimensional transom-stern flows.

The results show a distinct region at low Fr_i and high β where unsteady wave breaking effects become important. It can be seen that, as the Froude number decreases, the waves break first for larger angle of attack. This observation is consistent with the fact that wave breaking is in large part governed by the slope of the waves. In Fig. 3.18, the free surface profiles are shown for $\beta = 10^\circ$ and $\beta = 15^\circ$ for varying Fr_i. The free surface waves are seen to become more nonlinear as the Froude number decreases and as the angle of attack increases. Eventually, the nonlinear effects cause the waves to break, as shown in Fig. 3.18. The increased level of unsteadiness due to wave breaking is also apparent from the lift coefficient time histories of these runs, which are shown in Fig. 3.19. In these cases, a clear distinction between nominally steady and unsteady cases is observed. It should be noted that although the drag coefficient time histories are not shown, they are characteristically identical to the lift coefficient time histories and have simply been omitted for conciseness.

3.3.8 Conclusions of Flat Plate Study

The classical problem of a two-dimensional planing flat plate has been investigated using a nonlinear CFD method for a range of angle of attack and Froude number. The results are compared to a linearized potential-flow model in order to determine the effects of nonlinearity and wave breaking. The CFD and potential-flow methods are found to agree well for

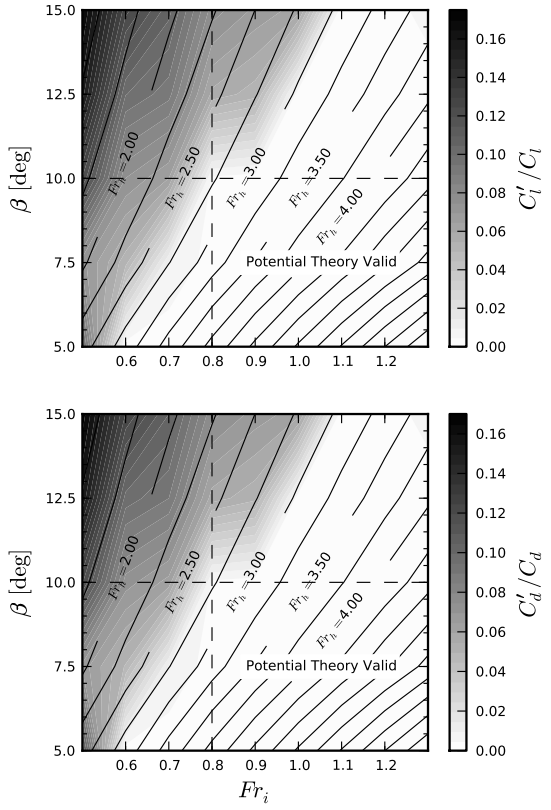

Figure 3.17: Contours of standard deviation of time histories of lift and drag coefficients normalized by the time-averaged values for a range of β and Fr_i. Areas of large standard deviation correspond to regions of large unsteadiness caused by wave breaking effects.

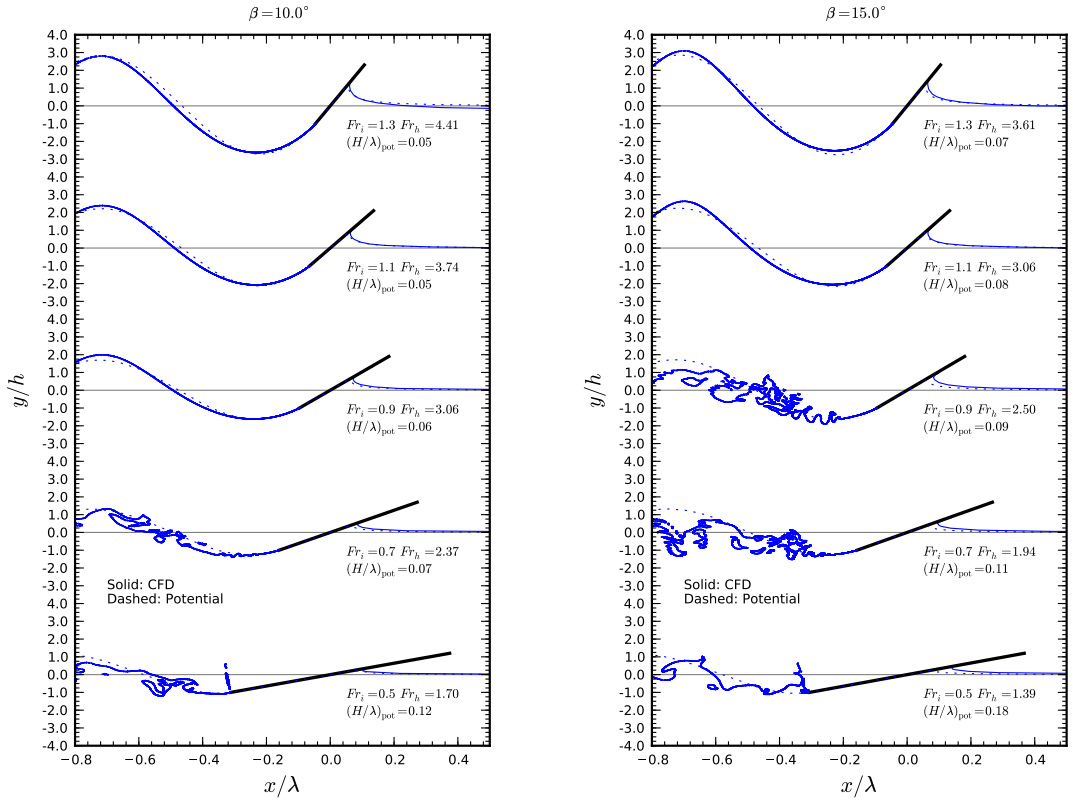

(a) $\beta = 10^\circ$ (b) $\beta = 15^\circ$

Figure 3.18: Plots of free-surface profile at $\beta = 10^\circ$ and $\beta = 15^\circ$ for varying Froude number, Fr_i. Solid lines correspond to CFD results and dashed lines correspond to linearized potential-flow results. Here, $\lambda = 2\pi U^2/g$ is the linear potential-flow theory estimate of the far-field wavelength and $h = L_i \sin\beta$ is the draft at the plate trailing edge. It should be noted that the plates are of identical geometry, but appear not to be so due to the nondimensionalization of the x variable.

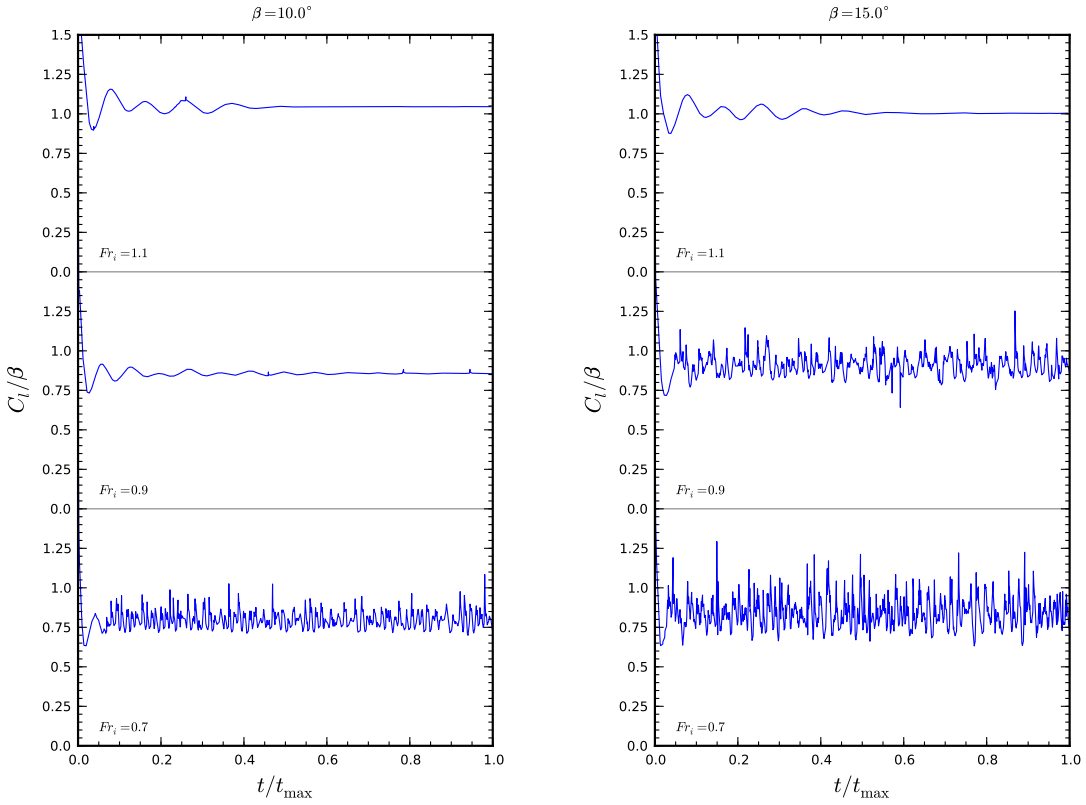

(a) $\beta = 10^\circ$ (b) $\beta = 15^\circ$

Figure 3.19: Complete time histories of lift coefficient from CFD simulations at $\beta = 10^\circ$ and $\beta = 15^\circ$ for varying Froude number, Fr_i, corresponding to the free surface profiles shown in Fig. 3.18. Time averages referenced throughout this section were taken over the last 20% of simulated time, after transient effects became negligible. For all cases, the simulations were run for $t_{\max} = 100\,\mathrm{s}$.

high Froude number. However, at low Froude number and large angle of attack, nonlinear effects become important. Two types of nonlinearity are found to be important: (1) nonlinear, non-breaking free-surface waves, which occur first as the angle of attack increases and Froude number decreases and (2) breaking waves, as the angle of attack is increased and Froude number are decreased further. Based on the results of the current study, it is determined that potential-flow methods offer sufficient accuracy for $Fr_i \geq 0.8$ and $\beta \leq 10°$, and should be chosen for their computational efficiency. At lower speeds ($Fr_i < 0.8$) and larger angles of attack ($\beta > 10°$), the results of the potential-flow method are found to under-predict the time-averaged lift and drag coefficients, where the difference can be as much as 35% at $Fr_i = 0.5$ and $\beta = 15°$.

The boundary where the transom waves begin to break down is found to be closely related to the immersion-based Froude number, defined as $Fr_h = U/\sqrt{gh} \approx 2.75$. The results of the current study are found to be fairly close to the results for two-dimensional transom stern flows, owing to similarity between the two flows.

Based on the results of the flat plate study, it is possible to determine whether the linearized potential-flow method is appropriate to use for SES seal simulations. Using the definitions for the Froude number based on the cushion length (Fr_C) and Froude number based on twice the immersed length (Fr_i), the following scaling relation may be derived by eliminating the forward speed (U) and gravitational acceleration (g):

$$\frac{Fr_i}{Fr_C} = \sqrt{\frac{L_C}{2L_i}} \tag{3.43}$$

The numerical method is found to be of use for speeds for approximately $Fr_C > 0.3$, which corresponds to $Fr_i > 0.8$ for $L_i/L_C < 7\%$. As long as the immersed length of each seal is lower than this value, the potential-flow method can be considered valid. Although it is difficult to calculate the initial immersed length for cases where both seals are included in the simulation, it is expected that the potential-flow method should be valid for the cases

of interest due to the low-immersion nature of SES seals. Nevertheless, it is acknowledged that the curvature of SES seals will probably reduce the zone where potential-flow assumptions are valid. The aim of the current work is to develop an efficient FSI solver to predict the response with consideration for seal-seal interaction using a linearized potential-flow solver coupled with a 1-DoF structural model. Future work should consider the use of higher-fidelity models to systematically study the influence of viscous FSI effects.

3.4 Potential-Flow Method for Multiple Planing Surfaces

In the previous section, the problem of a single planing flat plate was studied using both a CFD and potential-flow-based method. It was determined that at high Froude number and low angle of attack, the potential-flow method was sufficiently accurate. In order to study the problem of SES seals, however, the method must be extended in order to be able to consider multiple planing surfaces.

Using the single-planing-surface formulation presented in Section 3.1.2, the extension of the problem to multiple planing surfaces is fairly straightforward owing to the placement of a pressure element at the trailing edge. In the following discussion, the number of planing surfaces will be limited to two. However, in principle, the method should be able to consider any number of planing surfaces. An unvalidated example of a quadruple-stepped planing flat plate is shown in Appendix B as an illustration of the flexibility of the method.

In the case of two planing surfaces in tandem, there are two unknown wetted lengths that must be solved-for. Therefore, a multidimensional nonlinear root finder must be used to satisfy a number of residual equations equal to the number of planing surfaces, i.e.

$$\mathcal{R}_i(L_{w,j}) \equiv p_{TE,i}(L_{w,j}) - p_{\mathrm{kutta},i} = 0 \tag{3.44}$$

where the subscripts i and j refer to the index of the planing surface. Therefore, for the case of two planing surfaces, there are two residual equations that must be driven to zero, each of

which are functions of the wetted length of both planing surfaces. Broyden's root-finding method (Broyden, 1965) has been found to be effective in solving this type of system of equations.

The unknown pressure of each element may be found by solving the linear system shown in Eq. (3.18), while taking care to note that all pressure elements must be considered simultaneously for all planing surfaces.

3.5 Potential-Flow Shear Stress Correction

Since the potential-flow method assumes the fluid to be inviscid, it ignores the shear stress along the planing surface. Although this assumption has been shown to be valid at higher speeds for the planing flat plate problem, it is useful to include a frictional correction term in the current study to consider the relative magnitude of the frictional drag.

The flat-plate friction coefficient is used to predict the shear stress along the planing surface, where the shear stress is assumed to act between the stagnation point and the trailing edge. Although the model currently ignores curvature effects, these effects may be added in the future. The Reynolds number of each planing surface is based on the wetted length and is calculated as

$$Re_w = \frac{U \cdot L_w}{\nu_w} \tag{3.45}$$

in order to determine whether the flow is expected to be laminar or turbulent. Turbulent flow is assumed when $Re_w > 5 \times 10^5$. Otherwise, laminar flow is assumed.

The laminar shear stress is calculated as:

$$\tau(s) = 0.332 \rho_w U^2 {Re_s}^{-0.5} \tag{3.46}$$

where τ is the fluid shear stress at the wall, s is the arc-length coordinate, and Re_s is the

Reynolds number based on wetted arc length (from the stagnation point to the pressure element), defined as:

$$Re_s = \frac{U \cdot (s_{\text{stag}} - s)}{\nu_w} \tag{3.47}$$

The turbulent shear stress is calculated using the 1/7 power law, i.e.:

$$\tau(s) = 0.0576 \rho_w U^2 {Re_s}^{-1/5} \tag{3.48}$$

The shear stress is integrated along with the pressure in order to obtain the lift and drag forces, and the moment on the body. For all cases considered in this thesis, the frictional drag was found to be at least two orders of magnitude lower than the pressure drag, and hence the viscous correction term is not included.

3.6 Validation Studies

The problem of a single planing plate has been studied in the past by several authors and hence, in conjunction with the CFD study presented in Section 3.3, the solution to that problem can be considered validated. For the purposes of the simulation of an SES with a pressure cushion and bow and stern seals, two capabilities must be added to the method in order to ensure its validity. The first addition is the consideration of multiple planing surfaces, which was described in Section 3.4. This addition is validated in Section 3.6.1 by considering the flow past a 2-D stepped planing flat plate. The second addition is use of a pressure source term to model the influence of the pressure cushion, which is validated in Section 3.6.2 by comparing the code with past efforts associated with wave resistance prediction for 2-D ACVs.

3.6.1 Stepped Planing Flat Plate

The problem of a stepped planing flat plate is chosen in order to demonstrate the ability of the potential-flow method to consider multiple planing surfaces. This problem has been studied by Garland and Maki (2012), who used a similar CFD model to the one presented in Section 3.1.1. The geometry for this problem is shown in Fig. 3.20. The plate has an initial immersed length (L_i) of $1.0\,\mathrm{m}$ and an afterbody length of $L_a = 0.9L_i$. It is oriented at an angle of attack $\beta = 5°$ to the calm-water free surface. The step height (h_{step}) is varied from $h_{\mathrm{step}}/L_i = 0.0$ (unstepped) to $h_{\mathrm{step}}/L_i = 0.025$ at a flow speed of $5.0\,\mathrm{m/s}$, yielding a Froude number based on twice the immersed length (Fr_i) of 1.129 and a Reynolds number based on twice the immersed length (Re_i) of ten million.

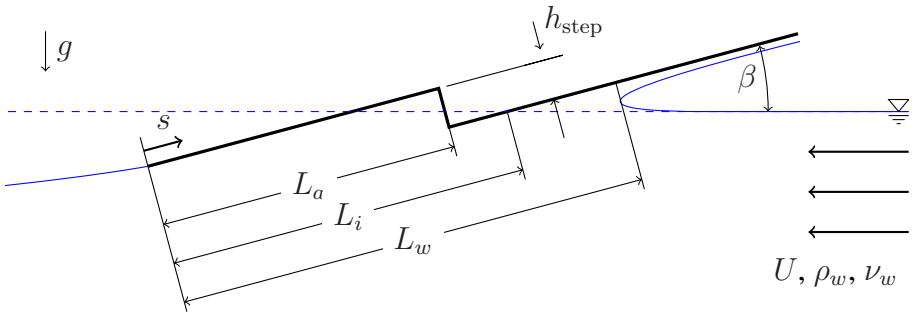

Figure 3.20: Geometry for stepped planing plate (not to scale)

The free-surface profile for a single step height of $h_{\mathrm{step}}/L_i = 0.10$ is shown in Fig. 3.21 to illustrate the successful satisfaction of the kinematic boundary condition on both the fore- and aft-body planing surfaces. For all cases, 50 elements per planing surface are used with cosine spacing.

The pressure profiles for six values of the step height are plotted in Fig. 3.22 compared to the CFD results of Garland and Maki (2012). The results are found to compare well with the CFD results. A drastic increase in computational efficiency is obtained using the potential-flow method, which can solve each case in a matter of seconds on a single-core processor laptop, versus days on a multi-core computing cluster for the CFD simulations.

The integrated lift forces are shown in Fig. 3.23. The total lift is found to decrease as

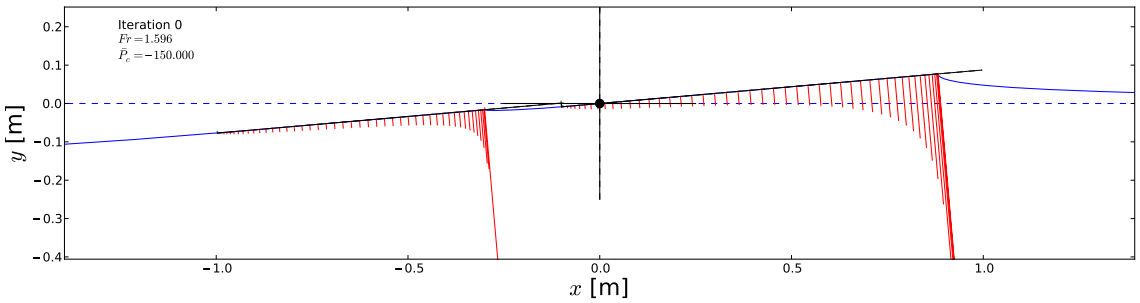

Figure 3.21: Potential-flow solution for stepped planing plate for $h_{\text{step}}/L_i = 0.10$. The free-surface profile is shown as a solid blue line while the undeformed free surface is shown in a dashed blue line. The body profile is shown in black and the pressure profiles are shown as red lines.

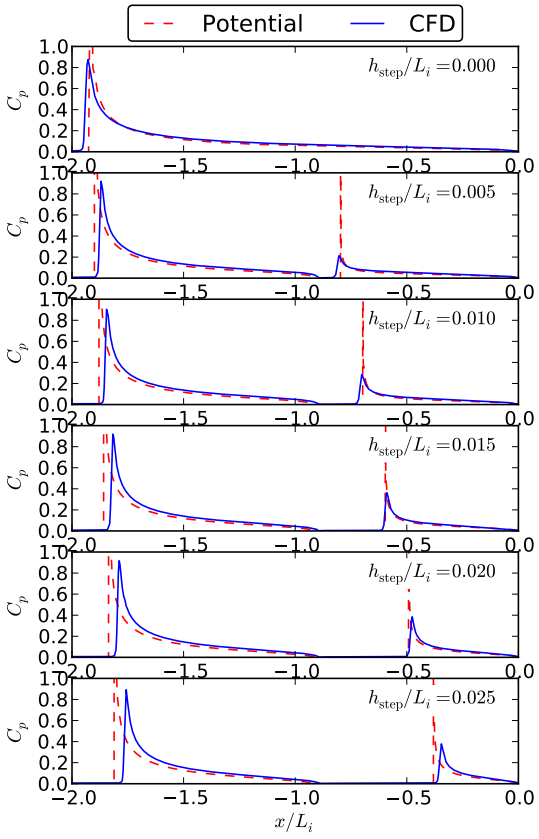

Figure 3.22: Comparison of pressure profiles for stepped planing plate with varying step height for $Fr_i = 1.129$, $\beta = 5°$, $L_i = 1.0\,\text{m}$, and $L_a = 0.9L_i$.

the step height decreases, however there is also a corresponding drop in wetted length and hence frictional drag. The goal of the inclusion of the step is to increase the lift-to-drag ratio of the plate by reducing the frictional drag more than the generated lift. The potential-flow method is found to under-predict the lift predicted by the CFD method at low step heights. The under-prediction is exhibited solely for the afterbody, as the forebody lift is found to agree very well with the CFD results. Although the exact cause of this discrepancy is unknown, it might be attributed to either insufficient grid resolution to capture the afterbody jet (which becomes important especially for small step heights) or possible differences in the pressure between the forebody and afterbody due to a small region of recirculation just aft of the step. The discrepancy warrants future investigation. In any case, the comparisons of the trends are found to be accurate between the two methods.

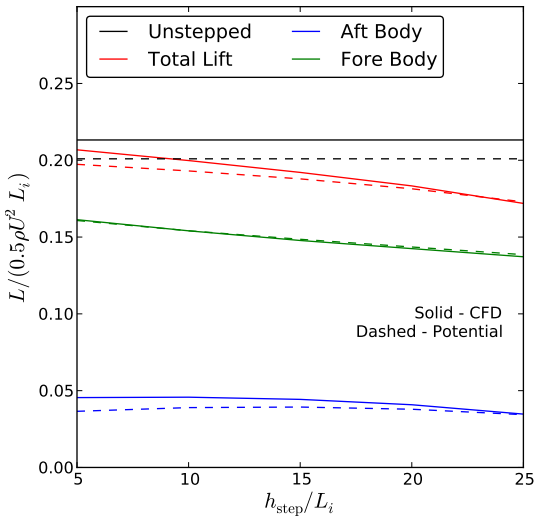

Figure 3.23: Comparison of lift coefficient for stepped planing plate with varying step height

3.6.2 Known Pressure Patch on the Free Surface

The final addition which must be implemented in order to model an SES is the pressure cushion, which is located between the bow and stern seals. Since the cushion pressure is

assumed to be fixed, it is included as a source term in the pressure equation (Eq. (3.20)).

In order to validate the source terms used for the pressure cushion, the 2-D smoothed pressure distribution of Doctors and Sharma (1972) was modeled and the free surface elevation was calculated. The total free surface elevation as a function of x may be calculated using Eq. (3.19).

A simple function minimizer may be used to find the maximum and minimum of the free surface elevation at a location far downstream. The wave resistance per unit width is then calculated as

$$R_W = \frac{1}{4}\rho g A^2 \tag{3.49}$$

where $A = \eta_{\max} - \eta_{\min}$ is the wave amplitude.

The wave resistance was calculated for the 2-D smoothed pressure distributions of Doctors and Sharma (1972) for three values of the smoothing parameter. The pressure distribution is defined as

$$p\left(x\right) = \frac{1}{2}P_C\left[\tanh\alpha_s\left(x + \frac{1}{2}L_C\right) - \tanh\alpha_s\left(x - \frac{1}{2}L_C\right)\right] \tag{3.50}$$

where α_s is the longitudinal smoothing factor. In order to apply this pressure distribution using the previously-defined pressure distributions, the pressure distribution was discretized into multiple complete triangular pressure elements, where 50 elements are placed in each smoothing region. The discretized smoothed pressure distribution is shown in Fig. 3.24. This contrasts with the method of Doctors and Sharma (1972), which considers Eq. (3.50) directly. However, since both methods are solving the same problem the results should agree. It can be viewed as a good test that the linear approximation of Eq. (3.50), which is what is obtained using the triangular pressure distributions, should match the exact form of the pressure distribution. The results for the resistance coefficient as a function of Froude number based on the cushion length (Fr_C) are shown in Fig. 3.25 for three different

values for the longitudinal smoothing factor (α_s). The numerical results from the current study are shown as curves, while the peaks from Doctors and Sharma (1972) are plotted as red circles. The results between the two methods match very well, and it can be seen that the effects of the pressure smoothing are captured.

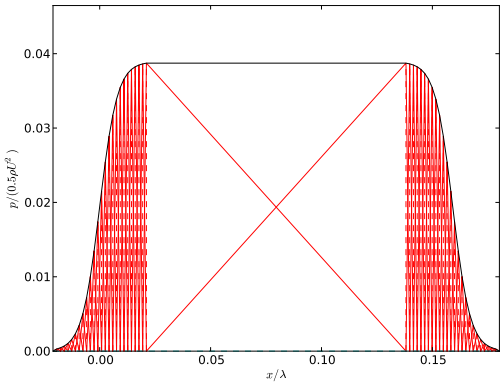

Figure 3.24: Discretization of Eq. (3.50) for $\alpha_s = 10$ using triangular pressure elements. Each pressure element is plotted as a red triangle while the total applied pressure is plotted in black. There are 50 elements distributed throughout each smoothing region while two half-triangular elements represent the constant pressure patch.

3.7 Summary

In this chapter, the fluid model has been described. First, the potential-flow method was compared to a CFD method for the 2-D planing flat plate problem and it was found that the potential-flow method was sufficiently accurate at high speeds and low angles of attack. Based on this study, it was determined that the potential-flow method should be of sufficient accuracy for the SES seal problem. It should be noted that, while the current study applies the assumptions of linearized potential-flow, the effects of nonlinearity have recently been studied for both the planing plate problem and the smoothed pressure distribution problem by Kramer et al. (2013) and Maki et al. (2012), respectively. In Maki et al. (2012), it was observed that the waves can become nonlinear as the cushion pressure increases. In the scope of the current study, the linearized potential-flow method is used for its simplicity;

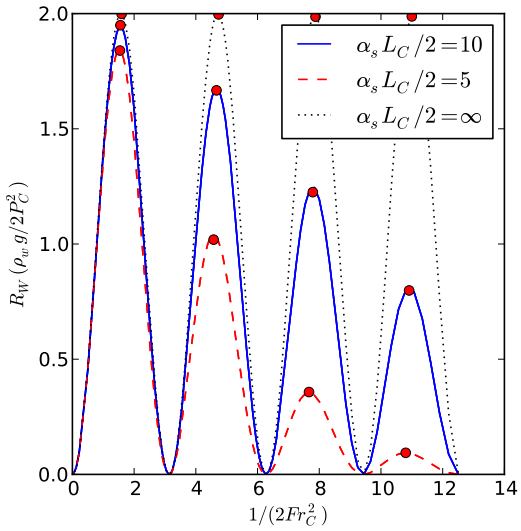

Figure 3.25: Resistance coefficient for the smoothed pressure distribution of Doctors and Sharma (1972) for varying smoothing factors. The humps from Doctors and Sharma (1972) are shown as red circles and compare well to the current method, shown as curves.

however, future studies are warranted to investigate the influence of nonlinearity for the problem of an SES with both a pressure cushion and multiple planing seals.

The potential-flow method, which is based on the work of Doctors (1974, 1977), was then extended to include consideration for multiple planing surfaces and source terms for modeling the pressure cushion. Both of these extensions were validated against existing published results and were found to compare well. Now that both of these extensions to the classical planing plate problem have been implemented and validated, the method may be used to model the flow past a 2-D SES with bow and stern seals, and a pressure cushion between the two. The structural and FSI methods will now be discussed. The fluid model is next implemented in Chapter 7 for an SES with rigid bow and stern seals with consideration for two Degree of Freedom (DoF) rigid body motion.

CHAPTER 4

Structural Modeling

The objective of the structural modeling is two-fold. First, the rigid body motion must be considered in order to find the running trim and draft of the vessel. Without this consideration, the forces and moments on the vessel will be incorrectly predicted due to excessive or too little immersion, and due to different angles of attack. The numerical model must additionally be able to consider cases where one or both of these degrees of freedom are fixed.

The second objective of the structural model is to determine the deformed equilibrium shapes of the bow and stern seals in order to be able to study the effects of seal flexibility on the seal resistance. For this aspect of the structural modeling, it is beneficial to formulate the problem in a modular manner such that various seal models may be interchanged and tested.

In this chapter, each of these problems are addressed, first separately, and then in combination. The structural portion assumes as an input the availability of fluid pressure and shear stress, which was detailed in the previous chapter on the fluid model.

4.1 Structural Layout

The complete structure is represented as a rigid body oriented along the free surface, as shown in Fig. 4.1. The rigid body consists of any number of substructures, which are

located along the boundaries of the body. Each substructure may be rigid or flexible depending on the user input, the selection of which governs whether the boundary will be able to move or remain rigid with respect to a body-fixed coordinate system. The rigid body has the properties of weight (Δ), which acts at the center of gravity located at (x_{CG}, y_{CG}), and a center of rotation located at (x_{CR}, y_{CR}). The substructures are treated generally and contain their own properties. In the example shown in Fig. 4.1, the bow and stern seals each have the additional properties of torsional spring stiffness (K_δ) and seal pressure (P_s). All of the equations of motion are written about the center of rotation, where the forces are obtained by integrating the pressure and shear profiles along all substructures. For the purposes of this section, the availability of force and moment calculations is assumed. The specifics associated with force and moment calculation are given later in Section 4.3.1.

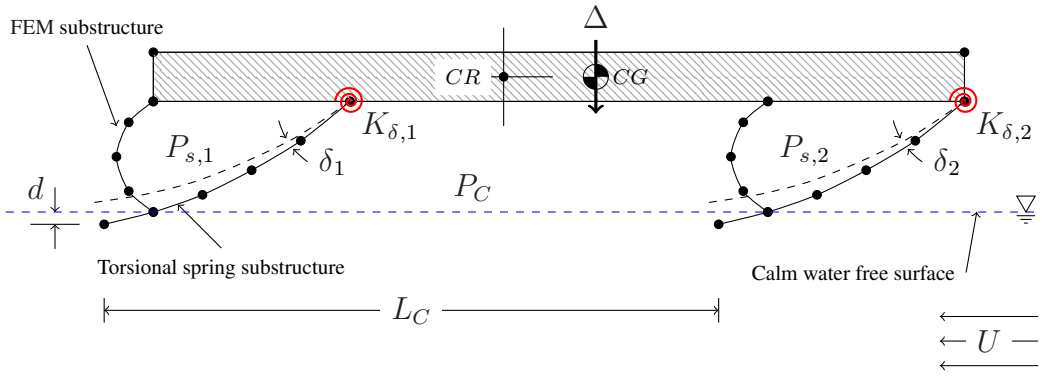

Figure 4.1: Definition of structural layout showing rigid body made up of several substructures, which may be rigid or flexible

4.2 Rigid Body Motion Solver

The objective of the rigid body motion solver is to determine the running trim (θ) and draft (d) of the vessel at a given operating condition. The physical forces are determined by hydrodynamic forces (pressure and/or shear), applied air pressure forces, and gravitational forces. The total lift and drag forces for each rigid body are calculated as the sum of the

forces from each substructure associated with the rigid body, i.e.

$$\mathcal{L}_{\text{tot}} = \sum_{ss} F_{ss,y} \tag{4.1}$$

$$\mathcal{D}_{\text{tot}} = -\sum_{ss} F_{ss,x} \tag{4.2}$$

$$\mathcal{M}_{\text{tot}} = \sum_{ss} M_{ss} \tag{4.3}$$

where $F_{ss,x}$ and $F_{ss,y}$ are the total force along the surface of substructure ss in the x- and y-directions, respectively, and M_{ss} is the total moment along substructure ss about the center of rotation (CR), counter-clockwise being positive. A free body diagram of a representative rigid body is shown in Fig. 4.2.

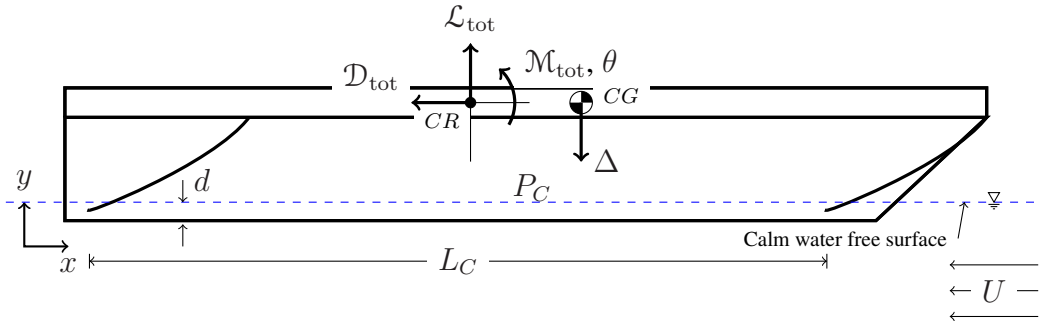

Figure 4.2: Free body diagram for rigid body vessel motion

Although the intent is to calculate the steady equilibrium solution, it is useful first to consider the fully-unsteady equations of motion. The steady-state equations of motion may then be simplified when necessary later by dropping the unsteady terms. The unsteady equations of motion, written about the center of rotation, are:

$$m\ddot{d} + C_d\dot{d} = \Delta - \mathcal{L}_{\text{tot}}\left(d, \theta, \dot{d}, \dot{\theta}, \ddot{d}, \ddot{\theta}\right) = 0 \tag{4.4}$$

$$I_z\ddot{\theta} + C_\theta\dot{\theta} = \mathcal{M}_{\text{tot}}\left(d, \theta, \dot{d}, \dot{\theta}, \ddot{d}, \ddot{\theta}\right) - \Delta \cdot (x_{CG} - x_{CR}) = 0 \tag{4.5}$$

where m is the mass of the rigid body, I_z is the mass-moment of inertia about the center of rotation, Δ is the vessel displacement, d is the draft, θ is the trim angle, and C_d &

C_θ are numerical or physical damping coefficients which may be used to help maintain numerical stability and improve convergence speed. It should be noted that the draft (d) is defined as positive downwards, which accounts for the sign of the forces on the right-hand side of Eq. (4.4). The trim angle (θ) is defined positive bow-up, or counter-clockwise. It should be noted that currently there are no restoring force terms on the right-hand-side of Eqs. (4.4) and (4.5) since all hydrodynamic forces are obtained directly from the fluid solver. However, additional restoring force terms may be included fairly easily in the future if necessary.

The objective of the steady-state rigid body motion solver is to determine d and θ such that Eqs. (4.4) and (4.5) are satisfied when $\ddot{d} = \dot{d} = \ddot{\theta} = \dot{\theta} = 0$.

4.2.1 Broyden's Method

The method for calculating the steady-state equilibrium that has been implemented is based on Broyden's method (Broyden, 1965), which is a general method for solving a system of nonlinear equations. Broyden's method can be viewed as a multidimensional extension of the secant method, which uses an approximated Jacobian matrix that is updated at each iteration to prevent the need to re-evaluate the Jacobian at each iteration. It is a root-finding algorithm, and as such the equations must be written in the form of residuals. By using this method, the steady equations of motion may be solved quickly and accurately. Equations (4.4) and (4.5) may be rewritten in a residual form, dropping all unsteady terms:

$$\mathcal{R}_1(d,\theta) \equiv \mathcal{L}_{\text{tot}}(d,\theta) - \Delta = 0 \tag{4.6}$$

$$\mathcal{R}_2(d,\theta) \equiv \mathcal{M}_{\text{tot}}(d,\theta) - \Delta \cdot (x_{CG} - x_{CR}) = 0 \tag{4.7}$$

Using this method, it is necessary to set strict limits on the allowable step size, since steps that are too large can place the vessel in a position where the hydrodynamic solver cannot obtain a solution. The major benefit of using Broyden's method is that, provided

that a hydrodynamic solution can always be found, it can converge in as little as 10 iterations. The downside to this method is that, since it is gradient-based, it relies heavily on a smooth prediction of the forces and moment as a function of body position and tends not to converge if any of the seals leaves the free surface, causing an abrupt change in forces and moments on the body. This method is most appropriate for cases where the seals are expected to be highly wetted and are not anticipated to leave the free surface during the solution procedure.

4.2.2 Validation of Broyden's Method for Motion Calculation

In order to test the rigid body motion method, a test case was constructed for an SES without hydrodynamic or air loading. In this case, a fixed-value pressure cushion is placed between the two seals, and consequently the free-surface profile is determined a priori since there are no unknown pressure elements. The fluid lift force is replaced by stiff numerical springs intended to drive the seal tips to the fixed free surface. The total lift force then takes the form:

$$\mathcal{L}_{\mathrm{tot}} = F_{s,\mathrm{bow}} + F_{s,\mathrm{stern}} \tag{4.8}$$

where $F_{s,\mathrm{bow}}$ and $F_{s,\mathrm{stern}}$ are the vertical numerical spring force for the bow and stern seals, respectively. The spring force takes the form $F_s = -K_s\left(y_{\mathrm{tip},i} - \eta\left(x_{\mathrm{tip},i}\right)\right)$, where η is the free surface elevation, $K_s = 10^5\,\mathrm{N/m}$ is the linear spring stiffness, and $x_{\mathrm{tip},i}$ and $y_{\mathrm{tip},i}$ are the coordinates of each respective seal tip.

The case is constructed to ensure that the rigid body motion solver can handle solving for both the equilibrium draft and trim angle simultaneously, and that the method converges to the known value, which may be calculated analytically. The body is initialized with a draft $d = 0.0\,\mathrm{cm}$ and trim angle of $\theta = 5.0^\circ$. The initial and final rigid body positions are shown In Fig. 4.3 for $Fr_C = 0.4$ and with a cushion pressure $\bar{P_C} = P_C A_C/\Delta = 0.7$.

The body geometry and mass properties are the same as those that will be given for the segmented model of Heber (1977) in Chapter 6.

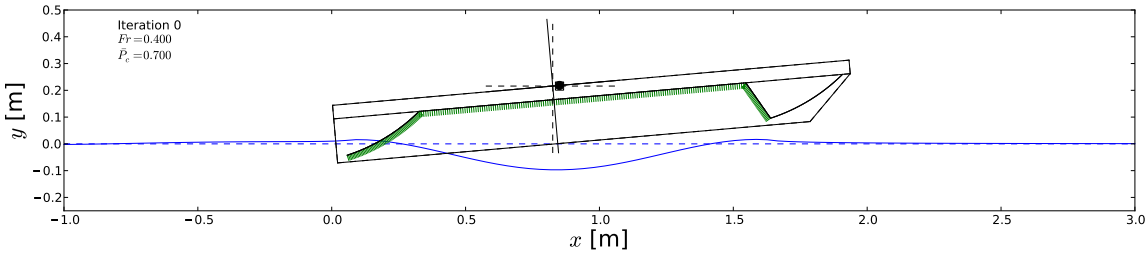

(a) Initial body position

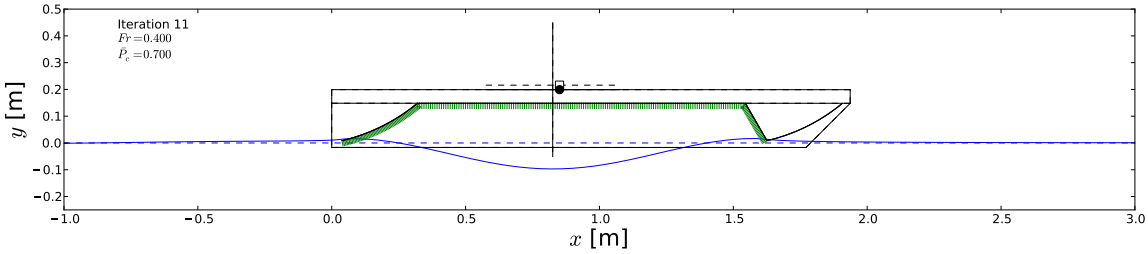

(b) Final body position

Figure 4.3: Initial and final body positions for an SES with rigid seals and numerical springs placed at the seal trailing edges in order to drive the seal tips to the fixed free-surface position. $Fr_C = 0.4$, $\bar{P_C} = P_C A_C / \Delta = 0.7$.

The residual histories for the lift and moment are shown in Fig. 4.4. The simulations are run until the absolute value of the lift and moment residuals (Eqs. (4.6) and (4.7)) are below 1.0×10^{-6}. The method is found to converge to the known solution of $d = 1.677\,\mathrm{cm}$ and $\theta = 0.0064°$ in 11 iterations. This highlights the major benefit of Broyden's method compared to methods which rely on integrating the unsteady equations of motion in time.

4.3 Substructure Models

As was described in Section 4.2, the rigid body is constructed of one or more substructures, which may be rigid or flexible in nature. All substructures share the characteristics of being

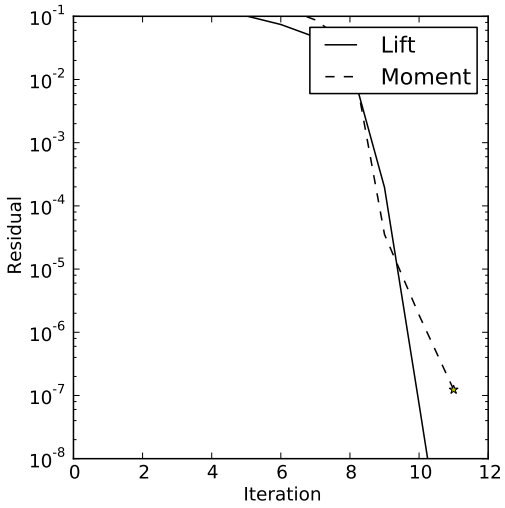

Figure 4.4: Iteration histories of the lift and moment residuals. The simulations are run until both residuals (Eqs. (4.6) and (4.7)) are below 1.0×10^{-6}. $Fr_C = 0.4$, $\bar{P_C} = P_C A_C / \Delta = 0.7$.

able to calculate the total forces to apply to the rigid body, however specialized flexible substructures also contain methods to calculate the deformation based on the loads applied to that particular substructure. In this subsection, the details of force calculation for the steady-state rigid body motion calculation are discussed, as well as the details of particular flexible models, which are used to calculate the deformed shape.

4.3.1 Rigid Substructures

The most basic type of substructure is the rigid substructure, upon which all of the flexible types are built. Each substructure is represented by a series of nodes, connected by elements. These nodes and elements are collectively referred to as the "mesh". An example substructure mesh is shown in Fig. 4.5.

The total force on the substructure is calculated by summing the force and moment

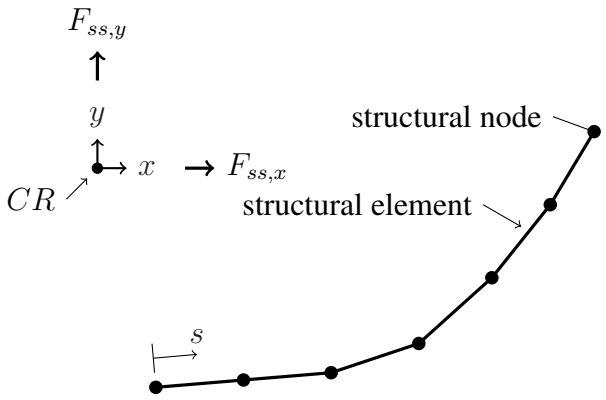

Figure 4.5: Example mesh for rigid substructure

contribution from each element, i.e.

$$\mathbf{F_{ss}} = \sum_{i}^{N_{el}} \mathbf{F}_i \tag{4.9}$$

$$M_{ss} = \sum_{i}^{N_{el}} M_i \tag{4.10}$$

where N_{el} is the number of elements in the substructure and the moments (M_i) are taken to be positive counter-clockwise about the rigid body center of rotation (CR).

The force and moment along each element are obtained by integrating the pressure and shear stress distributions from the `FSIInterpolator`, which will be described in the next chapter. For the purposes of the current discussion, it is sufficient to say that the `FSIInterpolator` returns a discrete number of pressure and shear stresses located between the element's two end nodes as well as the interpolated pressure at the nodes as a function of the arc length coordinate (s). The interpolated pressure is illustrated in Fig. 4.6. The pressure and shear stresses are numerically integrated in order to calculate the total force and moment of the element. Trapezoidal integration was chosen due to the linear

nature of the fluid solver as well as the much finer fluid mesh resolution compared to the structural mesh, however other integration schemes could be implemented easily.

The force and moment along element i are calculated using the following equations:

$$\mathbf{F}_i = \int_{s_0}^{s_1} -p \cdot \hat{\mathbf{n}} - \tau \cdot \hat{\mathbf{t}}\, ds \tag{4.11}$$

$$M_i = \int_{s_0}^{s_1} \left(-p \cdot \hat{\mathbf{n}} - \tau \cdot \hat{\mathbf{t}}\right) \times \mathbf{r}\, ds \tag{4.12}$$

where $\mathbf{r} = \mathbf{x}_B(s) - \mathbf{x}_{CR}$ is the moment arm about the center of rotation and s_1 and s_2 are the value of the arc length coordinate at the two nodes.

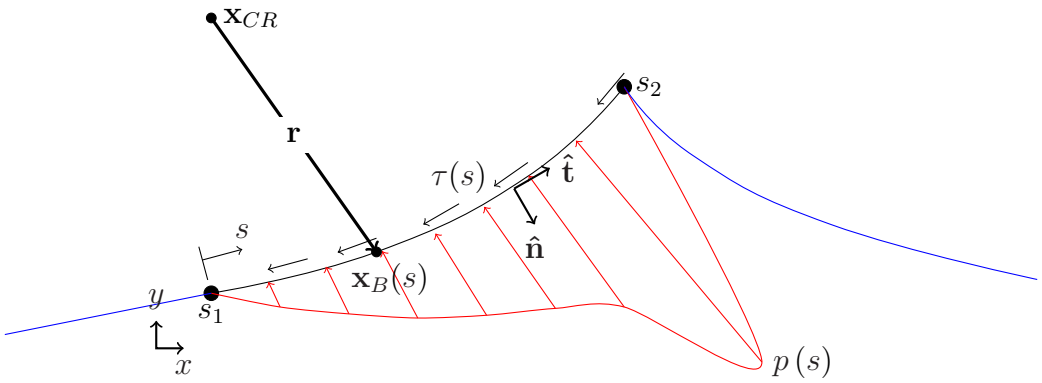

Figure 4.6: Example of discretized pressure and shear stress as a function of the arc length coordinate (s) showing nomenclature for force integrals

Using these equations, the total force and moment for each element may be calculated for each substructure. The sum of these may be applied to each rigid body in order to find the equilibrium position.

4.3.2 Finite Element Method (FEM) for Thin Membranes

It is also useful to consider various flexible substructure models, particularly for problems such as SES seals. SES seals are generally constructed of very flexible, thin rubber membranes that are reinforced by fibers. Although the material properties have been shown to

be important for localized effects, such as flutter and buckling (see, e.g. Besch, 1976; Wiggins et al., 2011), the overall deformation pattern is governed more by the nonlinear large deformation behavior, rather than small-scale material strain. As such, large inflated structures such as SES bag seals have been modeled assuming the material to be inextensible in the past (Jabbarizadeh, 2012; Jabbarizadeh and Karr, 2013). For these types of structures, it is generally assumed that the bending stiffness of the material is negligible and that the restoring force is obtained by large deformation behavior.

In the works of Jabbarizadeh (2012) and Jabbarizadeh and Karr (2013), the membrane is represented by constant-length arc and quadratic Bézier curve finite elements, which may be extensible or inextensible. Using these specialized curved elements, the membrane structure can be represented using a small number of elements, as opposed to traditional methods using flat truss or shell elements, which must use many more elements to represent the curved membrane. For the current study, 2-D nonlinear truss elements were chosen for their simple nature, however the results of Jabbarizadeh (2012) and Jabbarizadeh and Karr (2013) are encouraging and offer the possibility for representing the seal surface with much fewer elements in the future, which can help to increase computational speed. As a consequence of using truss elements, a body-exact geometry cannot be modeled and an appropriate interpolation scheme must be used for transfer of hydrodynamic loading between the fluid and structural models. The interpolation scheme is described in the next chapter.

The truss elements are straight and have four degrees of freedom (two translational degrees of freedom at each end of the element), as shown in Fig. 4.7. Since truss elements only allow axial loads, the influence of bending rigidity is ignored. The elements are assumed to be extensible (allowing axial deformation), but for the cases of SES seals the axial stiffness is set to be large enough that the elements are practically inextensible. For a traditional, small-deformation truss structure, the truss elements are assumed to yield a restoring force for displacements in the 1 and 3 degrees of freedom only, however for large

deformation structures, and for transverse loading, a nonlinear formulation must be used.

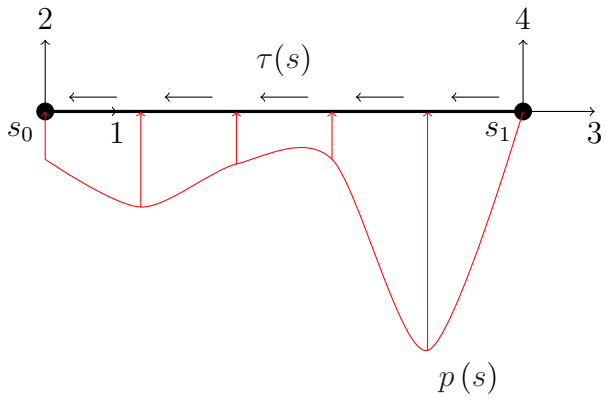

Figure 4.7: Diagram of nonlinear truss element showing the degrees of freedom, applied pressure, and shear loading

The nonlinear FEM formulation is provided by Bathe (1982). The local stiffness matrix is split into two components, a linear component and a nonlinear component, the total stiffness being the sum of the two:

$$\mathbf{K}_{\text{lin}} = \frac{EA}{\ell} \begin{bmatrix} 1 & 0 & -1 & 0 \\ 0 & 0 & 0 & 0 \\ -1 & 0 & 1 & 0 \\ 0 & 0 & 0 & 0 \end{bmatrix} \tag{4.13}$$

$$\mathbf{K}_{\text{nonlin}} = \frac{F_{\text{int}}}{\ell} \begin{bmatrix} 1 & 0 & -1 & 0 \\ 0 & 1 & 0 & -1 \\ -1 & 0 & 1 & 0 \\ 0 & -1 & 0 & 1 \end{bmatrix} \tag{4.14}$$

$$\mathbf{K}_{\text{tot}} = \mathbf{K}_{\text{lin}} + \mathbf{K}_{\text{nonlin}} \tag{4.15}$$

and the local force vector is split in a similar manner:

$$\mathbf{F}_{\text{lin}} = \begin{bmatrix} f_1 \\ f_2 \\ f_3 \\ f_4 \end{bmatrix} \tag{4.16}$$

$$\mathbf{F}_{\text{nonlin}} = F_{\text{int}} \begin{bmatrix} 1 \\ 0 \\ -1 \\ 0 \end{bmatrix} \tag{4.17}$$

$$\mathbf{F}_{\text{tot}} = \mathbf{F}_{\text{lin}} + \mathbf{F}_{\text{nonlin}} \tag{4.18}$$

where E is the circumferential Young's modulus, A is the cross-sectional area of the membrane, ℓ is the initial length of the truss element, and F_{int} is the internal tensile force in the truss element. For small-deformation formulations, $F_{\text{int}} = 0$ since only one structural update is performed. On the other hand, for cases of large deformations, $F_{\text{int}} = EA\varepsilon$, where $\varepsilon = (\ell_{\text{new}} - \ell)/\ell$ is the axial strain, and is updated each time the end node positions are updated. It should be noted that the material is assumed to behave as linear elastic in the current model.

The global stiffness and force vectors are constructed in the traditional manner by assembling the individual element matrices. As such, the details will not be covered in the scope of this thesis. Once the global stiffness and force matrices are constructed, the nodal displacements may be calculated by solving the following linear equation for the vector of nodal displacements (w):

$$\mathbf{K}_g \mathbf{w} = \mathbf{F}_g \tag{4.19}$$

where $\mathbf{K}_g$ and $\mathbf{F}_g$ are the global stiffness matrix and force vector, respectively. After the

displacement vector has been calculated, the nodes are moved and the stiffness and force matrices are updated. The solution is iterated on until the nodal displacement update is below a user-defined tolerance. The solution is considered to be converged when:

$$\max |\mathbf{w}| \leq \varepsilon_{\text{fem}} \tag{4.20}$$

where ε_{fem} is the specified tolerance. In general, the tolerance is set to 1.0×10^{-6} for the FEM solver.

All of the terms f_i in the linear force vector are obtained by integrating the pressure profile and shear stress along the element face and applying the equivalent nodal loading. The terms of the force vector are calculated in a similar manner to the previous subsection where the pressure and shear stress are integrated. For the case of truss finite elements, an additional integration must be performed in order to appropriately apply the integrated loads to the finite element nodes. The nodal forces may be calculated as follows:

$$f_1 = \frac{s_{cp} - s_0}{s_1 - s_0} \int_{s_0}^{s_1} p \, ds \tag{4.21}$$

$$f_3 = \frac{s_1 - s_{cp}}{s_1 - s_0} \int_{s_0}^{s_1} p \, ds \tag{4.22}$$

$$f_2 = \frac{s_{c\tau} - s_0}{s_1 - s_0} \int_{s_0}^{s_1} -\tau \, ds \tag{4.23}$$

$$f_4 = \frac{s_1 - s_{c\tau}}{s_1 - s_0} \int_{s_0}^{s_1} -\tau \, ds \tag{4.24}$$

where s_{cp} and $s_{c\tau}$ are the center of pressure and shear stress, respectively, calculated as

$$s_{cp} = \frac{\int_{s_0}^{s_1} p \cdot s \, ds}{\int_{s_0}^{s_1} p \, ds} \tag{4.25}$$

$$s_{cp} = \frac{\int_{s_0}^{s_1} \tau \cdot s \, ds}{\int_{s_0}^{s_1} \tau \, ds} \tag{4.26}$$

By discretizing a long membrane by several truss elements, the deformation may be

calculated. Due to the nonlinear nature of the method, and since the stiffness and force matrices shown above are linearized at the current position, the nodal positions must be updated in an iterative manner until the convergence criteria are met. To maintain numerical stability, it was found that an under-relaxation factor had to be used for the nodal displacements and the structure had to be incrementally-loaded. The update equation for the nodal position is thus:

$$\mathbf{x}_{i+1} = \mathbf{x}_i + \beta_r \mathbf{K}_{g,i}^{-1} \mathbf{F}_{g,i} \tag{4.27}$$

where β_r is the under-relaxation factor. In general, $\beta_r = 0.3$ was found to generally yield good results, however the exact value depends on the problem.

4.3.3 Validation of FEM Model: Inflated Membrane Dam

In order to validate the nonlinear truss elements, an example problem from the literature was chosen for a large-deformation membrane structure subject to a varying pressure load. In this section, the nonlinear truss FEM is compared to the analytical results of Ghavanloo and Daneshmand (2010) and experimental results of Hsieh et al. (1989) for an inflated membrane dam subject to hydrostatic loading. For the current validation study, only internal hydrodynamic loading is considered. Although the SES problem has both internal and external loading, the truss FEM model is only dependent on the net pressure distribution on the structure, and thus it is expected that the method will work just as well for externally-loaded structures as for internally-loaded structures.

In this problem, a flexible 2-D membrane is filled with water and the internal pressure is specified by the pressure at the base of the dam (P_{base}). The atmospheric pressure (P_{atm}) is assumed to be zero. The problem definition is shown in Fig. 4.8. The pressure varies

linearly with submergence depth:

$$p\left(y\right) = P_{\text{base}} - \rho_w g y \tag{4.28}$$

where ρ_w is the water density and g is the gravitational acceleration. The geometry is specified by the chord length at the base (B) and initial arc length of the membrane (ℓ). The stiffness of the membrane material is represented by the Young's modulus (E) of the material.

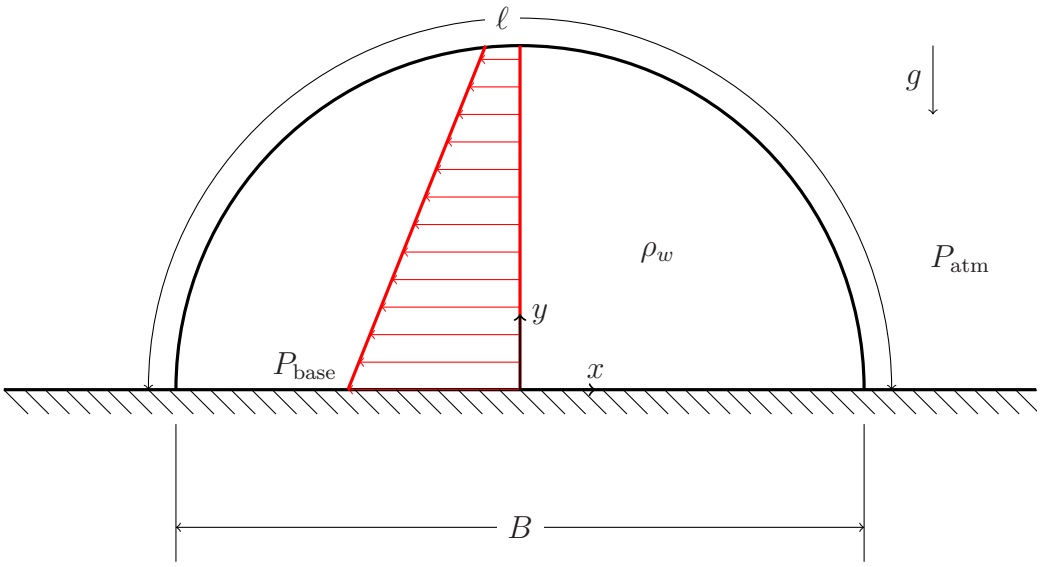

Figure 4.8: Problem definition for 2-D fluid-filled inflated membrane dam

Due to the simple nature of the problem, it may be nondimensionalized fairly easily. The nondimensional parameters are represented in this section by using an over-bar. All of the length scales are nondimensionalized by the base length, B, i.e. $\bar{x} = x/B$, $\bar{y} = y/B$, and $\bar{\ell} = \ell/B$ are the nondimensional x and y-coordinates, and initial arc length of the membrane. The pressure at the base is represented using the pressure head at the base of the dam (h_{base}), which is made nondimensional by the base length, i.e. $\bar{h}_{\text{base}} = h_{\text{base}}/(\rho_w g) = P_{\text{base}}/(\rho_w g B)$. The Young's modulus is nondimensionalized as $\bar{E} = EA/(\rho_w g B^2)$ is the non dimensional Young's modulus, where A is the cross-sectional area of the membrane

per unit width, i.e. the membrane thickness.

In order to test the accuracy of the nonlinear truss FEM analysis, several of the test cases presented in the original paper were replicated. In all of the cases, the fluid used was water with a $\rho_w = 1000\,\mathrm{kg/m^3}$ subject to $g = 9.81\,\mathrm{m/s^2}$. In the following sections, the arc length (ℓ), internal pressure head (h_{base}), and Young's modulus (E) are varied in order test the ability of the FEM model to consider large deformations, as well as element extensibility (for low values of Young's modulus). The results for each case that was compared will now be presented. It should be noted that for all comparisons, the length of the membrane was discretized into 200 truss elements.

4.3.3.1 Comparison with Experimental and Analytical Results for Fluid-filled Inextensible Membrane

The first case that was simulated was for a geometry that was tested by Hsieh et al. (1989) for an inextensible water-filled membrane of base length $B = 17.8\,\mathrm{cm}$, membrane length of $\ell = 78\,\mathrm{cm}$. The internal pressure head of the water at the base of the dam, h_{base}, was varied from $46.7\,\mathrm{cm}$ to $88.4\,\mathrm{cm}$, and the maximum height of the membrane was used as a measure of comparison. The FEM results for this case are shown in Table 4.1 along with the experimental results of Hsieh et al. (1989) and the analytical method of Ghavanloo and Daneshmand (2010), and are found to be within the presented accuracy of the analytical method.

Table 4.1: Comparison of maximum height of membrane ($y_{\max}$) with $\ell = 78\,\mathrm{cm}$, $B = 17.8\,\mathrm{cm}$ versus pressure head at the base of the dam (h_{base}) between current Finite Element Method, analytical method of Ghavanloo and Daneshmand (2010), and experimental results of Hsieh et al. (1989).

h_{base} (cm)	$y_{\max}$ (cm)			Error %
	FEM	Analytical	Experimental	
46.7	24.8	24.8	25.1	1.353
68.1	26.2	26.2	25.9	1.030
88.4	26.7	26.7	26.7	0.084

4.3.3.2 Inextensible, Fluid-filled Membrane of Varying Arc Length and Internal Pressure

The membrane shape was calculated for cases of constant internal pressure, where the pressure is specified nondimensionally as $\bar{h}_{\text{base}} = 2.66$. The arc length is varied, and the resulting membrane shapes are shown in Fig. 4.9 along with the analytical results of Ghavanloo and Daneshmand (2010). The membranes are found to become "flatter" as the arc length increases, with shorter dams more resembling the infinite-pressure limit of a constant-arc-length curve. The results are found to agree well with those presented in the paper for the analytical method.

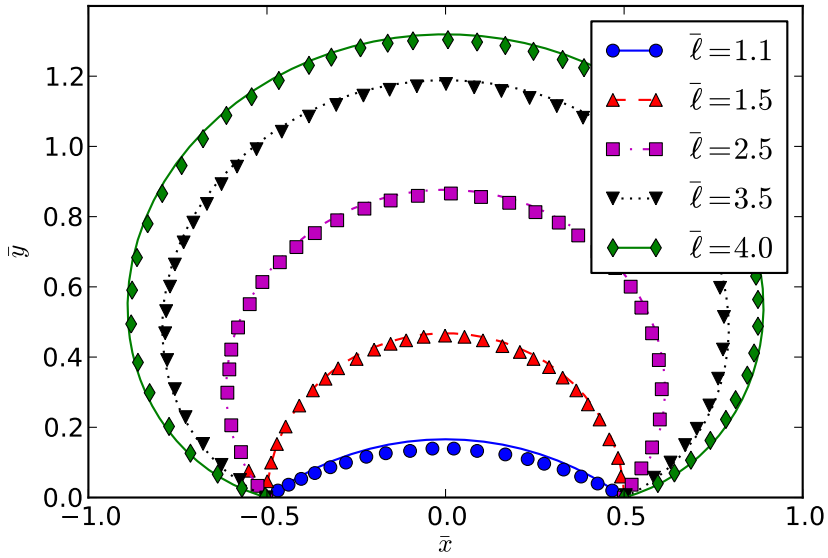

Figure 4.9: Equilibrium shapes for inextensible membrane dam for varying arc length and a fixed base pressure head of $\bar{h}_{\text{base}} = 2.66$. Lines are results from current FEM method, symbols are points transcribed from Ghavanloo and Daneshmand (2010).

Cases were also considered where the nondimensional arc length was held constant at a value of $\bar{\ell} = 3.0$ and the internal base pressure head was varied. These results are shown in Fig. 4.10. The results were found to compare well with the analytical results of Ghavanloo and Daneshmand (2010). It is found that the larger the internal pressure, the more "round" the membrane becomes, and the lower the pressure, the more "flattened" it becomes.

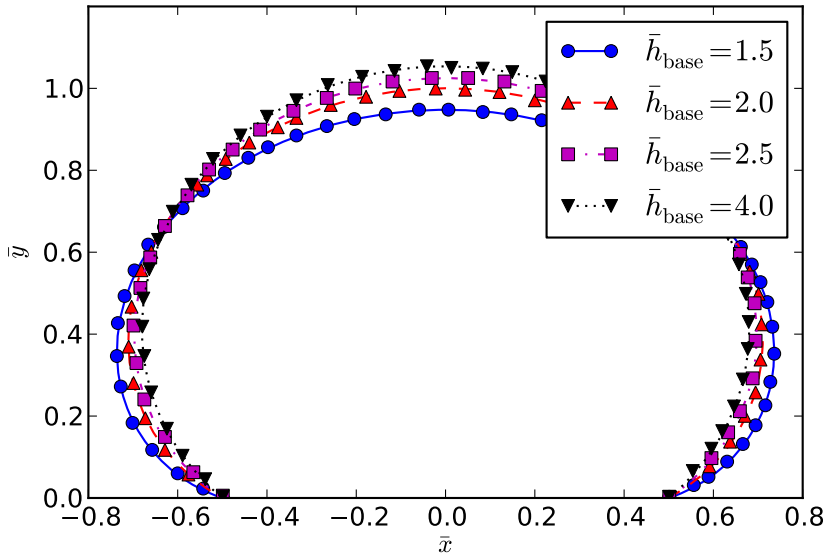

Figure 4.10: Equilibrium shapes for inextensible membrane dam for varying internal base pressure head and a fixed arc length of $\bar{\ell} = 3.0$. Lines are results from current FEM method, symbols are points transcribed from Ghavanloo and Daneshmand (2010).

Combining both variations in arc length and internal pressure, the results for the maximum height of the membrane versus internal pressure for three membrane lengths are shown in Fig. 4.11. Based on a comparison of the analytical results and the current numerical results, the results are found to compare well between the theoretical results of Ghavanloo and Daneshmand (2010) and the current numerical FEM model.

4.3.3.3 Extensible, Fluid-filled Membrane of Varying Young's Modulus

Finally, the impact of extensibility of the membrane was tested. Although for the case of SES seals, the effects of extension of the membrane material are often ignored (Jabbarizadeh, 2012; Karr and Jabbarizadeh, 2010), it is useful to assure the accurate modeling of this effect in order to ensure that the chosen circumferential Young's modulus is large enough to be considered effectively inextensible.

The results for the extensible, fluid-filled membrane are shown in Fig. 4.12. In this case, the initial nondimensional arc length of the dam was fixed at $\bar{\ell} = 1.5$ and the internal base

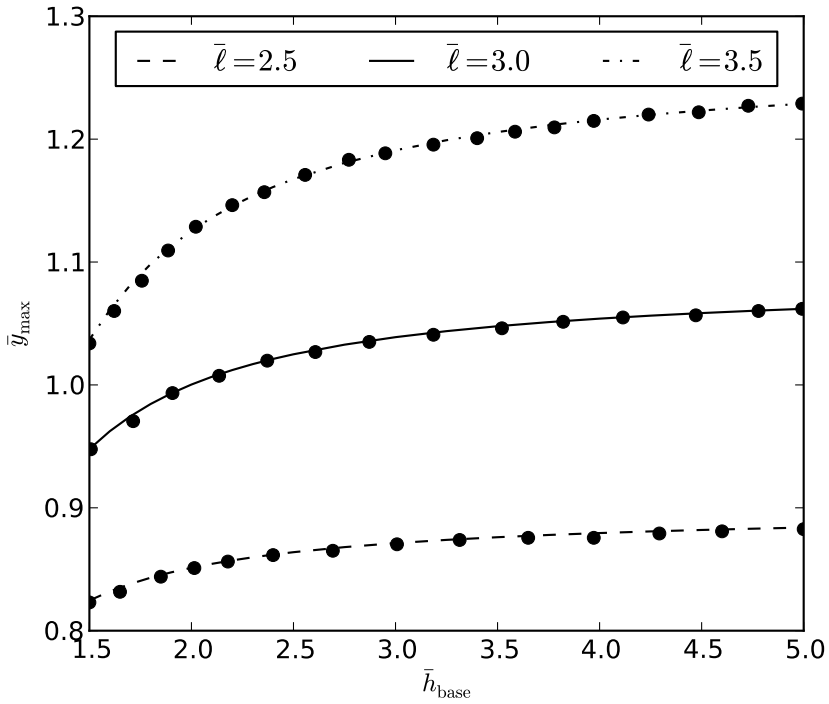

Figure 4.11: Maximum height of inextensible membrane dam as a function of internal base pressure head for varying arc length. Lines are results from current FEM method, symbols are points transcribed from Ghavanloo and Daneshmand (2010).

pressure head was fixed at $\bar{h}_{\text{base}} = 2.66$. The non-dimensional Young's modulus ($\bar{E}$) was varied from 6.2 to 10^5, where the latter was taken to represent the inextensible case. The results are found to compare well with the analytical results, and the membrane is found to stretch more as the Young's modulus decreases, much like a balloon would. The results for the maximum membrane height for this case are tabulated in Table 4.2 and are found to agree with the analytical results of Ghavanloo and Daneshmand (2010) to the published level of accuracy.

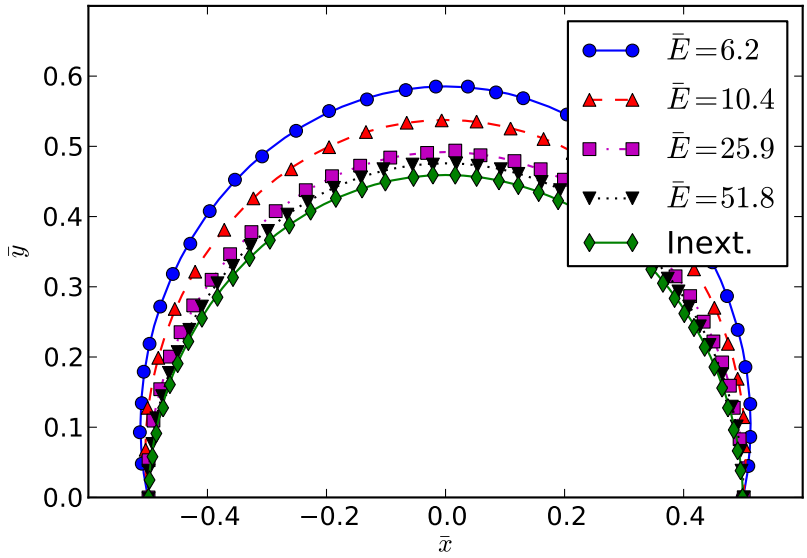

Figure 4.12: Equilibrium shapes for extensible membrane dam for varying non-dimensional Young's modulus ($\bar{E}$). The non-dimensional pressure head at the base of the dam is fixed at $\bar{h}_{\text{base}} = 2.66$, and the non-dimensional initial arc length of the membrane is $\bar{\ell} = 1.5$. Lines are results from current FEM method, symbols are points transcribed from Ghavanloo and Daneshmand (2010).

4.3.4 Single Degree of Freedom (DoF) Seal Model

A hinged planing seal model has also been developed in order to facilitate comparisons with the segmented model test of Heber (1977). These types of seals were often used in the early days of SES development. The planing portion of these seals was constructed of a rubber laminate which was internally reinforced by metal stays. Consequently, the planing face

Table 4.2: Comparison of maximum non-dimensional height of membrane dam ($\bar{y}_{\max}$) for varying non-dimensional Young's modulus ($\bar{E}$) between current Finite Element Method and analytical method of Ghavanloo and Daneshmand (2010)

Young's Modulus ($\bar{E}$)	$\bar{y}_{\max}$	
	FEM	Analytical
Inextensible (10^5)	0.4592	0.4592
51.80	0.4758	0.4758
25.90	0.4919	0.4919
10.36	0.5375	0.5375
6.216	0.5853	0.5853

was quite stiff locally compared to the previously-discussed membrane structures. The seal was internally supported by air pressure which was contained by a bag-shaped membrane on the back (dry) side of the planing face. A sample drawing of the bow seal tested in the segmented SES model tests and simulated in Section 8.1 is shown in Fig. 4.13.

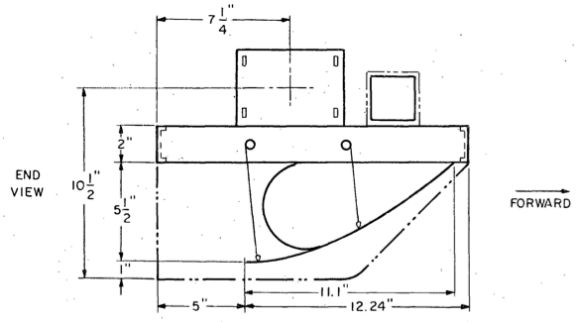

Figure 4.13: Diagram of experimentally-tested hinged SSBM planing seal module (from Heber, 1977)

The planing face of the seal was attached to the model using a piano hinge. Thus, due to the stiffness of the planing surface, the structure behaved as a torsionally-sprung structure, where the spring stiffness was derived from the internal air pressure. The model assumes that the bending rigidity of the planing face is large enough such that bending deformation is negligible. Instead, the structure obtains its stiffness by the pressure inside the bag, which is typically larger than the cushion pressure, and the deformation is measured by the rotational rigid body motion of the planing face about the hinge point. Further details of the validity of this assumption are given in Chapter 6, where a static load test was performed

for the segmented seal models. It suffices to say that, for the segmented model validation studies shown in this work, approximating the bow and stern seals using a linear torsional spring at the planing surface attachment point to represent the stiffness provided by the internal seal over-pressure is found to be a good assumption. Thus, a seal model based on this principle was developed.

The seal model is quite simple, as it only contains a single DoF, the seal deformation angle (δ), as shown in Fig. 4.14. The equilibrium equation for the seal angle is:

$$K_\delta \delta = -\mathcal{M}_o \tag{4.29}$$

where $\mathcal{M}_o$ is the moment about the hinge point, K_δ is the torsional spring stiffness, and δ is defined as positive in the clockwise direction (hence the negative sign on the moment).

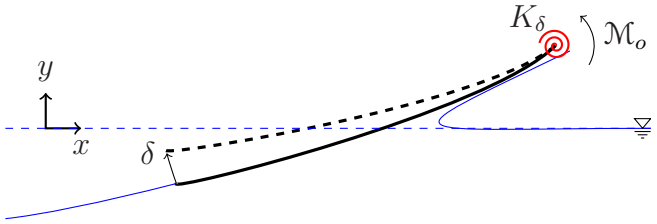

Figure 4.14: Diagram of numerical model for hinged seal with torsional spring

The moment ($\mathcal{M}_o$) is obtained by integrating the pressure distribution along the planing face of the seal. Since the rigid body motion and seal deformations are calculated simultaneously, it was found to be beneficial to apply an under-relaxation factor (β_r) on the deformation angle in order to maintain stability and improve convergence properties. The angular update equation may be written as:

$$\delta_{i+1} = (1 - \beta_r)\, \delta_i - \beta_r \frac{\mathcal{M}_{o,i}}{K_\delta} \tag{4.30}$$

The validation for the torsionally-hinged substructure model will be shown in Section 6.4, where the numerical model is used to compare with experimentally-performed

static load tests for the segmented model of Heber (1977).

4.4 Summary

In this chapter, the details of the structural solver were covered. A rigid body motion solver for calculating the steady-state equilibrium position of the vessel (i.e. draft and trim) based on Broyden's method was developed. For a sample problem with simple assumed linear spring loading of the seals, the rigid body motion method was found to yield an accurate solution in very few iterations. Although the fully-coupled FSI problem will require more iterations, since the fluid loading is more complicated than the assumed linear spring loading and the seal deformations must be calculated, it is found that a gradient-based root finder, such as Broyden's method, is much more computationally efficient compared to methods that rely on integrating the transient equations of motion.

In addition to the rigid body motion solver, details of the various substructure models were discussed, including a nonlinear truss-based Finite Element Method (FEM) and a simple hinged seal supported by a torsional spring. The FEM was validated by comparing with published results for a 2-D membrane dam subject to internal hydrostatic loading. This method was implemented as a means for future work, as well as to provide a fairly complex structural solver for validation of the FSI model, which is discussed in the next chapter.

The various fluid and hydrodynamic methods considered in this thesis are tabulated in Fig. 4.15. In general, there is a tradeoff between complexity/accuracy and computational efficiency. The increase in computational speed cannot be overlooked, and hence it is useful to use the potential-flow in combination with the 1-DoF hinged seal model when possible. For more advance performance predictions, where viscous effects are important, or where localized structural deformation of the seal material is anticipated to be large, more advanced methods such as CFD or FEM must be used.

Fluid:	CFD solver	Potential-flow solver
Solid:	FEM	1DoF solver (torsional spring)

← Complexity →
← Computational Efficiency →
← Accuracy →

Figure 4.15: Comparison of different fluid and structural models

The case studies performed in Chapters 6 through 8 are associated with drag prediction for the experimentally-tested segmented SES model of Heber (1977). In this case, semi-rigid bow and stern seals were considered and hence the hinged seal model is used to consider the effects of seal flexibility. The validation of the hinged seal model for that problem will be shown in Chapter 6.

CHAPTER 5

Modeling of Fluid-Structure Interaction

The previous two chapters described the fluid and structural solvers in detail. The fluid solver assumed the availability of the position of all wetted structural surfaces as an input, and the structural solver assumed the availability of the fluid pressure and shear stress as inputs. In this chapter, the interaction of the two solvers is discussed. The overall code architecture is first described in order to illustrate the functional interaction between the various code modules. Next, the interpolation scheme is described, which is responsible for transferring fluid loads and structural surface positions between the two solvers. Finally, the iteration scheme is discussed and some sample simulations are shown.

5.1 Solution Overview / FSI Modeling

The objective of the FSI model is to facilitate the transfer of hydrodynamic loading from the fluid solver to the structural solver, and to transfer the updated solid position (including both seal deformation and rigid body motion) from the structural solver to the fluid solver. By iterating between the hydrodynamic and structural solvers, an equilibrium solution may be found.

The code architecture is structured in a modular way in order to facilitate testing of various fluid and structural models. A general overview of the code hierarchy is shown in Fig. 5.1. The outermost class, `FSIIterator`, controls the overall iteration scheme,

determining when to update the fluid and solid solutions and when the solution has converged. Each `RigidBody` consists of any number of substructures (`FESubstructure`), which may be rigid or flexible. These structures may exist with or without planing surfaces attached.

The total fluid solution (`PotPlaningProblem`) consists of any number of `PlaningSurface` and `PressurePatch` objects, which are constructed in order to solve the complete potential-flow problem presented in Chapter 3. Each `PlaningSurface` object is tied to an `FESubstructure` object through an `FSIInterpolator` object, which transfers loads and deformations between the fluid and structural solvers.

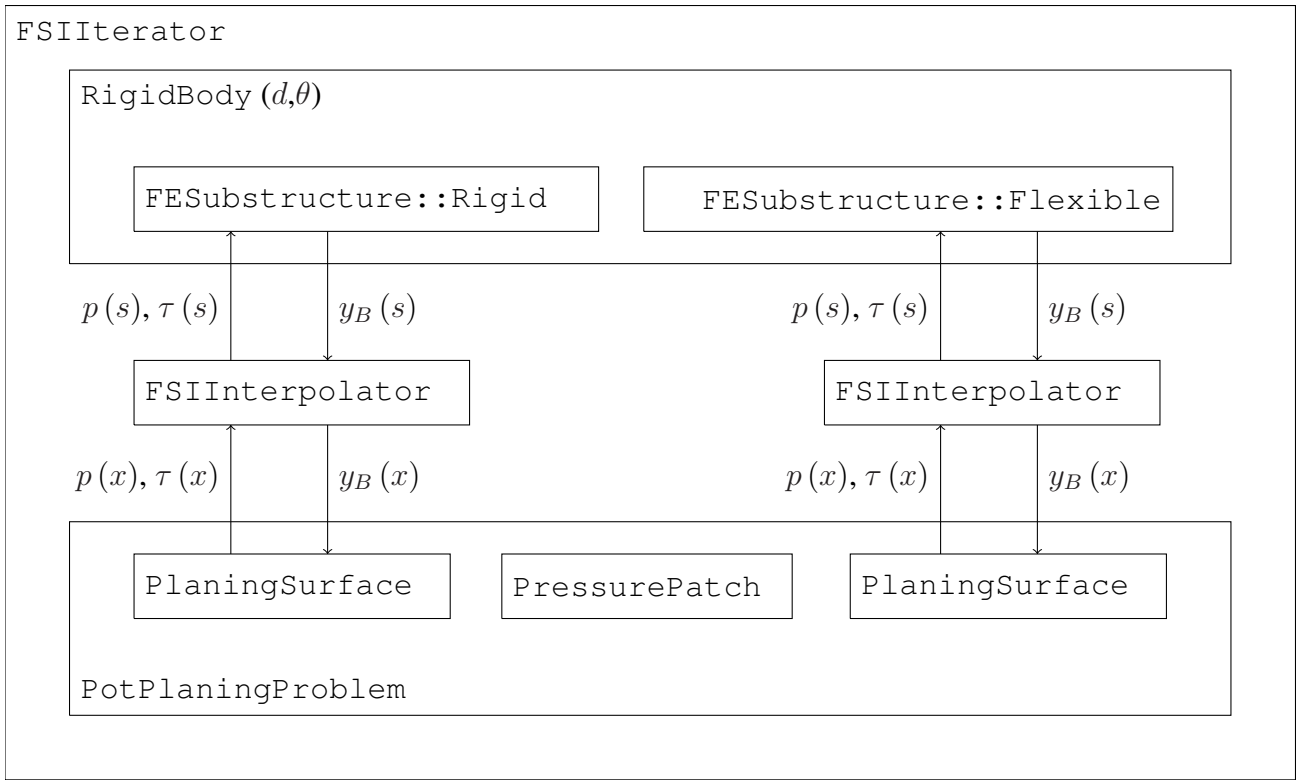

Figure 5.1: General overview of the code layout for the FSI scheme. Taking the right side to be the bow of the vessel, this figure corresponds to a simulation with a flexible bow seal, rigid stern seal, and a pressure cushion between the two.

As far as the `FSIIterator` is concerned, at a given operating condition, the `PotPlaningProblem` object yields as an output the pressure distribution as a function of the

x-location, $p(x)$, given an input of body height, $y_B\,(x)$, and the `FESubstructure` object yields an updated body position given a pressure and shear stress loading. The `FSIInterpolator` object, which handles interpolation and data transfer between the fluid and solid models must be detailed first in order to close the problem.

5.2 Interpolation Scheme

In the case of SES seals, each seal must be represented by a minimum of three objects:

1. An `FESubstructure` object, which determines the deformed shape and rigid body motion of the seal surface for a given pressure and shear loading

2. A `PlaningSurface` object, which determines the hydrodynamic pressure and shear stress along a fixed surface geometry, and the resulting free-surface profile

3. An `FSIInterpolator` object, which passes the interpolated pressure/shear loading, rigid body position, and substructure shapes between the two models

The details of the `FSIInterpolator` object are the main focus of this section. Therefore, for the purposes of this discussion, the fluid solver is assumed to know the body height y_B for all x-locations, and the solid solver is assumed to know the pressure and shear stress along the entire surface of the seal ($p\,(s)$ & $\tau\,(s)$). The objective of the `FSIInterpolator` object is to ensure that both the kinematic (no penetration) and dynamic (equal and opposite surface traction) boundary conditions are satisfied on the seal surface.

A diagram of a notional seal surface is shown in Fig. 5.2. The seal is parameterized by the arc length coordinate (s). Each seal surface is represented by a series of nodes, which are connected by an interpolated surface. The surface between the nodes may be linear, quadratic, or cubic in shape. Therefore, the seal surface coordinates $\mathbf{x}_B$ can be represented

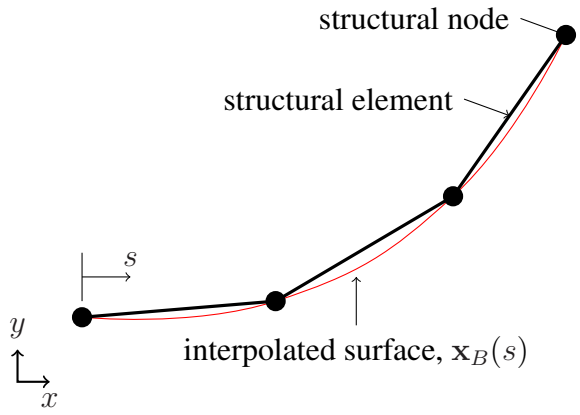

Figure 5.2: Diagram of seal surface denoting the nomenclature and showing structural elements (black curve), structural nodes (black dots), and the interpolated surface (red curve)

as:

$$\mathbf{x}_B(s) = \left\{ \begin{array}{c} x_B(s) \\ y_B(s) \end{array} \right\} \tag{5.1}$$

where $x_B(s)$ and $y_B(s)$ are determined by interpolating the nodes along the surface.

In order to calculate the hydrodynamic solution, the fluid solver must know the body height as a function of x, i.e. $y_B(x)$. In order to calculate the height of the body at a given x-coordinate, the corresponding value for s must first be calculated numerically by driving the following residual equation to zero using a simple root finder:

$$\mathcal{R} \equiv x - x_B(s) = 0 \tag{5.2}$$

The body height may then be calculated using the function $y_B(s)$. The body height is utilized by the fluid solver in order to ensure that the kinematic (no penetration) boundary condition is satisfied on the wetted surface, as in Eq. (3.20).

In a similar manner, the structural solver must be able to determine the pressure and shear stress (if included) along the entire arc length of the seal, i.e. $p(s)$ and $\tau(s)$. Since the hydrodynamic solution is given as a function of x, an interpolation procedure must be used. This interpolation is obtained by using the function $x_B(s)$ to transfer from s to x and then linearly interpolating the functions $p(x)$ and $\tau(x)$ to find the pressure along the entire seal, i.e. $p\,(s)$ and $\tau(s)$. It should be noted that the interpolation method is currently unable to consider cases where the x-coordinate of the wetted surface does not increase monotonically, e.g. such as when the seal surface folds or buckles. However, this is not found to be an issue because the potential-flow solver is not appropriate for these cases since viscous effects may not be negligible due to the formation of vortices in regions of large curvature, which cannot be modeled using a potential-flow method. Thus, the current method is only valid for cases where the wetted surface height is single-valued in x.

Through this simple interpolation scheme, which is generalized and may use any assumed shape between the structural nodes, the pressure, shear, and body location may be efficiently transferred between the fluid and structural solver. As a consequence, the fluid and solid grids are not required to be identical, which is a necessary property for the fluid solver since the pressure element locations must be changed as the wetted length is solved-for.

5.3 Iteration Scheme

Since the problem is steady, many of the stability issues associated with performing time-accurate FSI simulations may be avoided. The iteration scheme is summarized in Fig. 5.3. In its current state, the rigid body motion and substructure deformation are applied simultaneously, however in future applications it may be beneficial to include inner iterations for updating the substructure deformation between updates of the rigid body positon. This is particularly important for cases where the rigid body motion is solved in combination

with the FEM model, since the shape of the membrane must be solved iteratively. For the current cases which involve the 1-DoF hinged seal model, it has been found that simultaneous updating of the structural positions is sufficient as long as the structural steps are limited using prescribed maximum step sizes (in trim, draft, nodal deformation, etc.) as well as under-relaxation factors. The maximum step sizes are chosen manually in order to prevent numerical divergence and vary on a case-to-case basis. In all cases, the solutions were converged to a residual of 1.0×10^{-5} for the trailing edge pressure residuals, rigid body motion residuals, and nodal-deformation residuals.

5.4 Numerical Issues

Although the use of a potential-flow method for calculating the hydrodynamic solution is beneficial for reasons relating to simplicity and computational efficiency, it does not come without its own numerical difficulties. Due to the steady nature of the fluid solver, the fluid solution is solely dependent on the position of the wetted planing surfaces and may be calculated in a single function call. Numerical difficulties arise, however, when the planing surface is too lightly-immersed, i.e. the draft is too low. For these cases, there is no solution to the planing plate problem, or in other words, the wetted length required drops to zero for one or more of the planing surfaces.

This issue has been recognized by Wu and Whitney (1972) and is a consequence of the linearized potential-flow theory relating to the assumption that the flow splits at the stagnation point. Although a workaround to this issue may be developed for cases of single planing surfaces, it is difficult to do so for cases with multiple planing surfaces due to the interaction of the two planing surfaces, as well as the need to use a multi-dimensional root finder to find the wetted lengths of the planing surfaces. Therefore, in order to prevent numerical issues, it was found to be necessary to place strict limits on the draft and trim step sizes to prevent either the bow or stern seal from achieving an immersion that is too

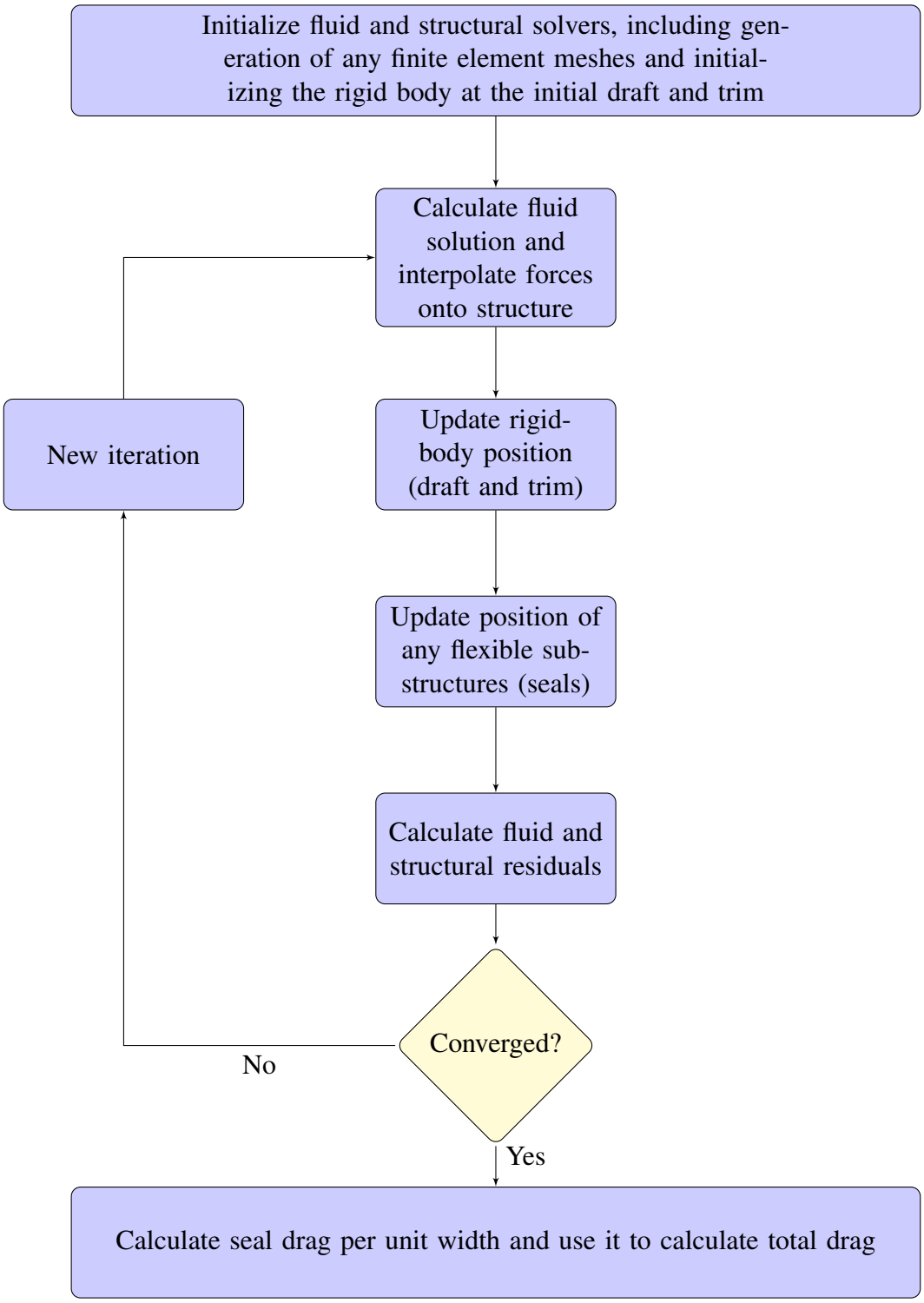

Figure 5.3: Flow chart for FSI simulation

low. This issue is exacerbated at higher Fr_C, where the fixed-lift condition of the seals causes the required immersion to be very low. Consequently, for most cases which will be shown in the following chapters, a solution cannot be obtained for Froude numbers higher than roughly 0.45 for the two seals with an air cushion cases. Fortunately for the problem of SES drag prediction, the seal component of the resistance is very small for $Fr_C > 0.45$ since the seals are only barely touching the free surface, and just a simple constant-pressure cushion model (as described in Section 3.6.2) without the seal drag is sufficient. Hence, in this work, a hybrid approach is used. For the regime where seal drag is important ($Fr_C < 0.45$), the coupled seal-cushion wave model is employed. For the region where the seals are barely touching the free surface ($Fr_C > 0.45$), the constant pressure patch method as described in Section 3.6.2 is applied. The model details and validation studies are shown in Chapters 7 and 8 for rigid and flexible seals, respectively.

In general, for the results shown in Chapters 7 and 8, the trim step is limited to $7.5 \times 10^{-3}\,\mathrm{deg}$ and the draft step is limited to $0.02 d_{\mathrm{design}}$, where $d_{\mathrm{design}} = 2.54\,\mathrm{cm}\,(1.0\,\mathrm{in})$ is the design draft of the sidewalls. These limits enable the code to solve the problem, however they can slow the convergence speed drastically. Future work to improve the stability of the solver in the low-immersion cases is recommended to improve the convergence speed.

5.5 Example: Inflated Membrane Subject to Planing Flow

In order to test the validity of the FSI model, a sample case was generated for an inflated membrane seal subject to planing flow. The intent of this example is not to provide physical validation, since experiments for these types of seals have not been performed. Instead, the intent is to examine the performance of the FSI model, to verify that the fluid and structural models are interacting appropriately, and to ensure that the solution will converge.

An inflated membrane seal was constructed, similar to the case of Ghavanloo and Daneshmand (2010), except inverted and subject to external hydrodynamic pressure in-

stead of internal hydrostatic pressure. The structure is roughly intended to model a flexible membrane seal, similar to lobed stern seals. The wave profiles for varying seal pressure are shown in Fig. 5.4.

The seal surface was discretized into 50 truss finite elements and the boundary condition at the two end nodes was a pinned connection. The pressure distribution along the wetted surface is discretized into 100 pressure elements. Since the separation point is difficult to identify (as opposed to the planing plate, which has a sharp trailing edge), the separation point is assumed to be located at the lowest point on the seal surface. The model was fixed in draft and in trim.

The initial geometry was a constant-radius arc with an arc length $\ell_s = 12.5\,\mathrm{m}$ and the end nodes were placed at a distance $1.5\,\mathrm{m}$ above the undisturbed free surface. The chord length between the end points is $10\,\mathrm{m}$. The seal is subject to planing flow on water of density $\rho_w = 1000\,\mathrm{kg/m^3}$ and a flow speed of $5\,\mathrm{m/s}$.

The predicted wave profiles for varying seal pressure are shown in Fig. 5.4. The undeformed seal shapes are shown as dashed black curves. As expected, the amount of deformation for the seal surface is found to increase as the internal seal pressure decreases. The stagnation point is found to cause a large indentation in the seal surface. The drag coefficient (C_D), lift coefficient (C_L), and minimum seal height ($y_{\min}$) is shown in Fig. 5.5, where the lift and drag coefficient are defined as

$$C_D = \frac{\mathcal{D}}{\frac{1}{2}\rho_w U^2 \ell_s} \tag{5.3}$$

$$C_L = \frac{\mathcal{L}}{\frac{1}{2}\rho_w U^2 \ell_s} \tag{5.4}$$

where $\mathcal{D}$ and $\mathcal{L}$ are the 2-D drag and lift per unit width, respectively, and ℓ_s is the total arc length of the seal. Additionally, the y-location of the minimum point on the membrane is shown.

The drag coefficient is generally found to decrease as the internal seal pressure is de-

creased, which makes the seal more flexible. The lift coefficient is found to vary slightly as the seal pressure is changed, but this effect is fairly small. Additionally, the minimum seal height is found to rise as the pressure is decreased and the seal is made more flexible. The minimum point then drops again at the smallest seal pressure due to the "kink" in the membrane. It is unclear whether this effect is physical and unfortunately experimental data do not exist for this case to verify. It should be noted that the shear stress correction described in Section 3.5 was included, however the frictional drag was two orders of magnitude below the pressure drag and hence did not have much of an effect.

5.6 Summary

In this chapter, the interaction of the fluid and structural solvers was discussed, with a particular focus on the interpolation and iteration methods. The way in which the numerical method transfers the pressures, shear stresses, and body surface locations between the two independent solvers were identified. In the end, a relatively simple interpolation scheme was developed that is able to handle non-matching grids between the fluid and structural solutions.

In the final section of this chapter, a validation study was performed for a notional membrane seal subject to planing flow. However, this case was constructed as a purely numerical investigation to ensure that the interaction of the fluid and structural solvers was captured accurately. Further validation of the interaction between the FEM and potential-flow methods must rely on experimental studies, which are currently unavailable. Should data become available in the future, it is recommended that the method is used to compare with the experimental results in order to test the validity of the coupled FEM-potential-flow method for the physical problem.

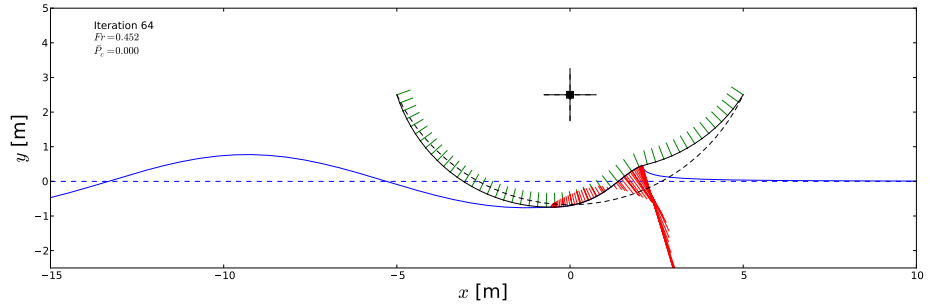

(a) $P_s/\frac{1}{2}\rho_w U^2 = 0.4$, $C_D = 3.434 \times 10^{-2}$, $C_L = 5.219 \times 10^{-2}$

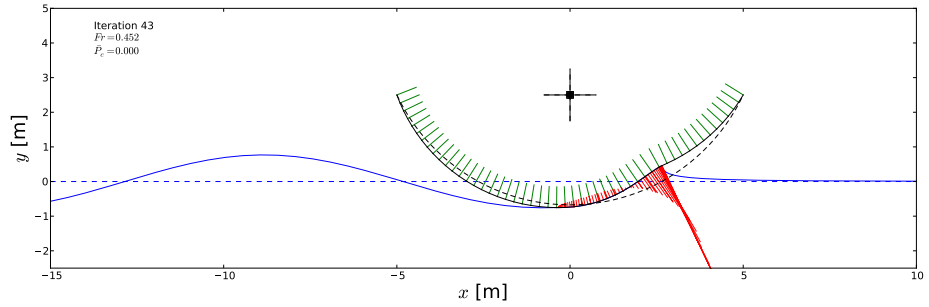

(b) $P_s/\frac{1}{2}\rho_w U^2 = 0.6$, $C_D = 3.949 \times 10^{-2}$, $C_L = 5.250 \times 10^{-2}$

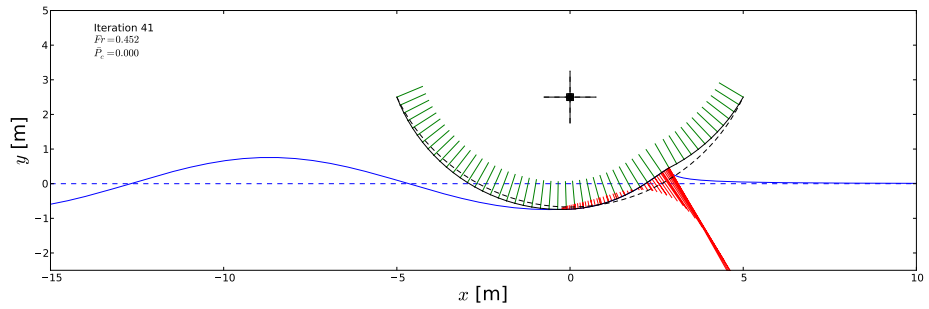

(c) $P_s/\frac{1}{2}\rho_w U^2 = 0.8$, $C_D = 4.193 \times 10^{-2}$, $C_L = 5.205 \times 10^{-2}$

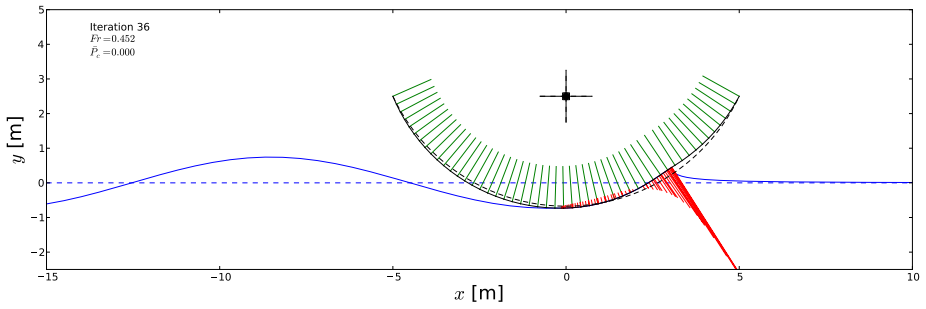

(d) $P_s/\frac{1}{2}\rho_w U^2 = 1.2$, $C_D = 4.252 \times 10^{-2}$, $C_L = 5.188 \times 10^{-2}$

Figure 5.4: Inflated membrane seal shapes for varying seal pressure. Flow speed $U = 5.0\,\mathrm{m/s}$, seal arc length $\ell_s = 12.5\,\mathrm{m}$, distance between end points $= 10\,\mathrm{m}$, end point height above free surface $= 1.5\,\mathrm{m}$. The initial and deformed membrane positions are shown as dashed and solid black curves, respectively. The undeformed and deformed free-surface profile is shown as a dashed and solid blue line, respectively. The external hydrodynamic and internal air pressure are shown as red and green lines, respectively.

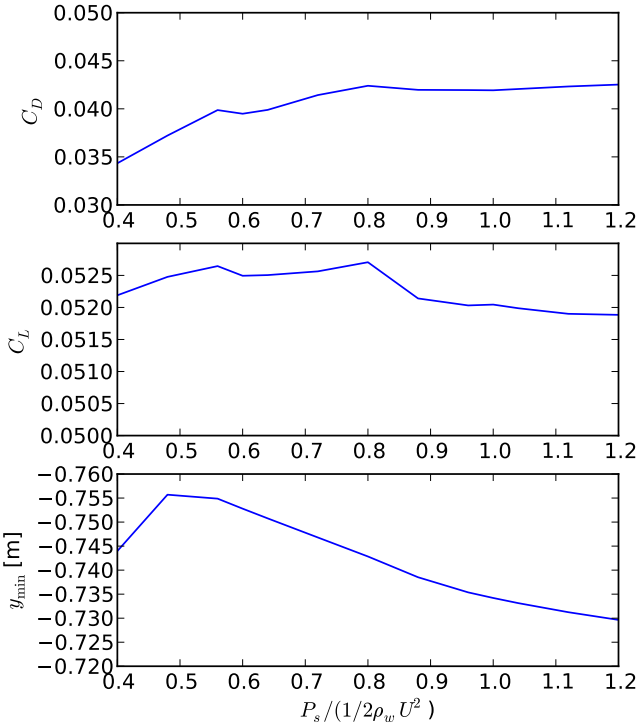

Figure 5.5: Calculated force coefficients and minimum height of the inflated membrane seal for varying seal pressure. Flow speed $U = 5.0\,\mathrm{m/s}$, seal arc length $\ell_s = 12.5\,\mathrm{m}$, distance between end points $= 10\,\mathrm{m}$, end point height above free surface $= 1.5\,\mathrm{m}$.

CHAPTER 6

Segmented Surface Effect Ship Model Tests

"These interactions suggest that good seal designs should potentially involve not only optimization of the individual bow and stern seals but also an optimization of the bow/stern seal system. It appears from interactions ... that a designer could take advantage of proper bow seal contouring and attitude to create lower wave profiles on the stern seal at critical conditions." – Heber (1977)

A wide range of experimental investigations were performed in the 1970s by the US Navy Surface Effect Ship Program Office (SESPO) in order to generally characterize the performance of SESs. Many of these tests focused on identifying overall parametric trends to aid in design decisions. Examples of variables that were tested include length-to-beam ratio, seal configuration, propulsion system, percent displacement supported by air cushion, and a variety of appendage types. These studies focused on the overall performance of model-scale SESs, some of which were built as full-scale prototypes. In most cases, the experimental studies investigated measures of performance such as total resistance, trim/heave stability, maneuvering, propulsion system performance, and seakeeping. Since these experiments were primarily designed to assess the overall SES characteristics, the detailed effects of the seals were not studied in the majority of cases.

Stemming from the need to accurately predict SES total resistance, several model test studies were performed for resistance characteristics in particular. In many of these studies, it was determined that the seals had a large effect on the total resistance, particularly in the low-to-moderate speed range (e.g. Van Dyck, 1972). It is, however, difficult to isolate

the effects of seals for a complete SES due to the inherent interaction of the lift system, sidehulls, seals, and free-surface waves. In order to quantify the effects of the seal drag on the total resistance, an experimental study (Heber, 1977) was undertaken in 1975, being carefully designed to isolate the effects of the seals as much as possible from the sidewalls, and to allow the independent measurement of bow and stern seal forces. This experimental study provides one of the only openly published studies where the drag of the bow and stern seal were independently measured, and thus provides a useful means for validation of the seal drag model proposed in the previous chapters.

The quote at the beginning of this chapter is taken from the report for the segmented SES model test performed by the US Navy (Heber, 1977), and highlights the importance of the interactions of the bow/stern seal system. Based on the findings of that report, as well as the simplicity of the model that was tested, it was decided that the segmented SES model geometry would be used as a means for validation of the numerical model by comparing with the experimental results. Additionally, it is the only known model test where the effects of the seals were isolated from the remaining resistance components. In addition, the model serves as a good test case in order to investigate the bow/stern seal wave interaction effects, as well as the effects of seal flexibility and seal height on the total system response. These effects are investigated in Chapters 7 and 8.

In order to compare the numerical model with the experimental results, it is necessary to adapt the segmented SES model geometry. The complete details of this experimental study are given in Heber (1977) and Van Dyck and Fridsma (1979). However, a descriptive summary of the experimental setup and major physical findings will now be given to provide the necessary background knowledge for comparisons between the numerical model and experimental results, which are shown in the following chapters. The numerical adaptation of the geometry is then described and the torsional-spring seal model, the theory of which was previously described in Section 4.3.4, is validated by comparing with a static load test performed by Heber (1977). The effects of bow/stern seal wave interaction and

seal flexibility are then studied in detail in the following two chapters for both rigid and flexible seals with an air cushion.

6.1 Experimental Setup

6.1.1 Model Dimensions and Properties

The model was designed to be similar to the US Navy XR-1C test craft with a cushion length-to-beam ratio of approximately 2.5. A photograph of the model is provided in Fig. 6.1 and a dimensioned drawing is shown in Fig. 6.2. The dimensions of the model are also very similar to the XR-1B model tested by Van Dyck (1972), which was described in Chapter 1. The principle dimensions of the model are shown in Table 6.1.

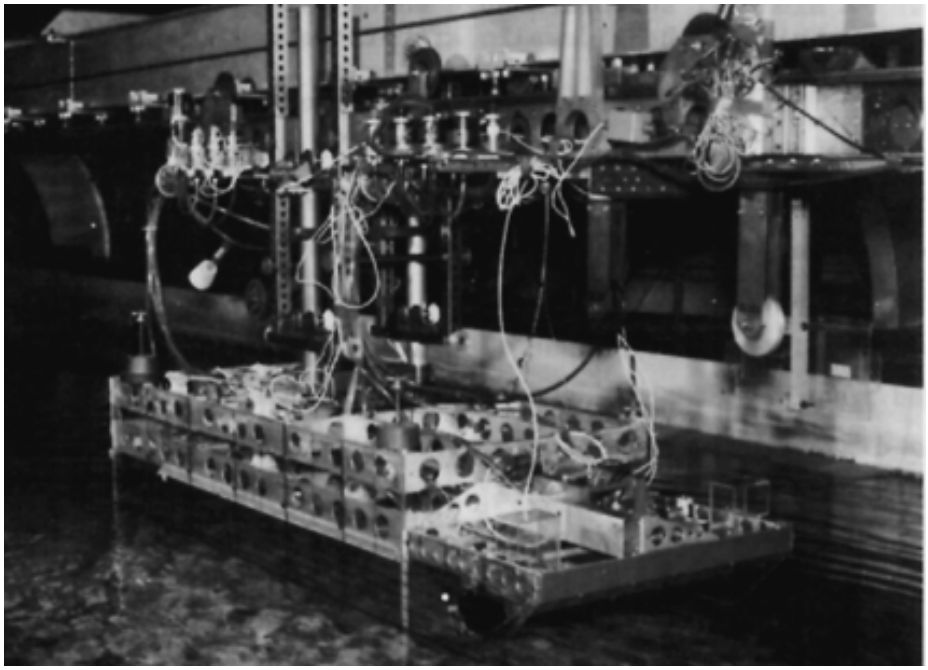

Figure 6.1: Photograph showing segmented model test setup in tank 3 at Stevens Institute of Technology (SIT) (from Heber, 1977)

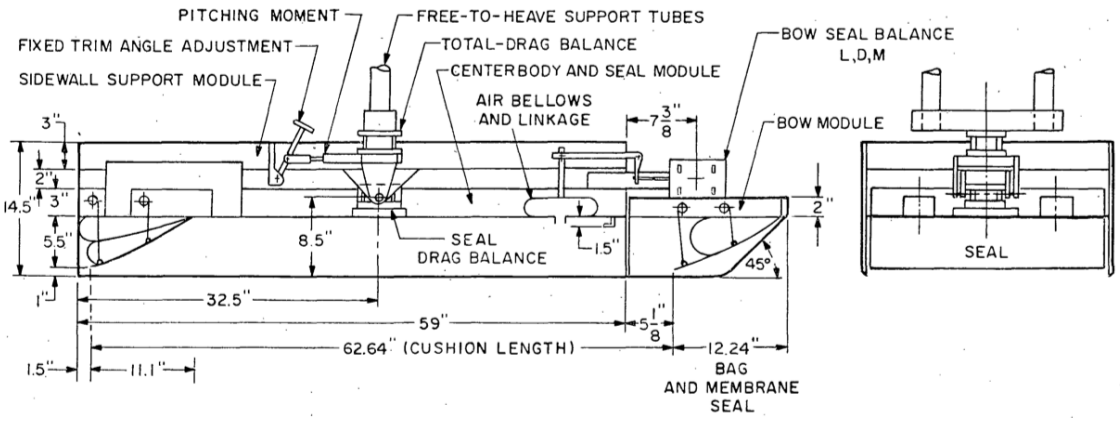

Figure 6.2: Layout of experimentally-tested segmented model including dimensions (from Van Dyck and Fridsma, 1979)

Table 6.1: Principle dimensions for segmented SES model

Dimension	Symbol	Value
Displacement	Δ	$45.36\,\mathrm{kg}\,(100\,\mathrm{lb})$
Cushion Length	L_C	$1.591\,\mathrm{m}\,(62.64\,\mathrm{in})$
Cushion Beam	B_C	$0.6541\,\mathrm{m}\,(25.75\,\mathrm{in})$
Length-to-Beam Ratio	L_C/B_C	2.45
Design Draft	d	$0.0254\,\mathrm{m}\,(1.0\,\mathrm{in})$

6.1.2 Segmentation of Model

The model was designed with the goal of physically isolating the bow and stern seals from the remainder of the SES structure. The sidewalls were constructed of 3/8-inch $(9.5\,\mathrm{mm})$ thick clear acrylic material in order to minimize sidewall effects as well as to allow the inside of the cushion to be visible. In order to allow for the independent measurement of the seal loads, the model consisted of three independent sections, which were connected by force balances. The three main sections are shown in Fig. 6.3 and include a sidewall module, a centerbody/stern seal module, and a bow seal module. As a result of the model segmentation, the total resistance, as well as the bow and stern seal loads could be measured independently using a total of three force balances. By estimating the contribution of the pressure cushion on the bow and stern seal loads, as well as the sidewall loads, which were obtained using experimentally-measured tares with no seals, the hydrodynamic drag and lift components of the bow and stern seals could be isolated.

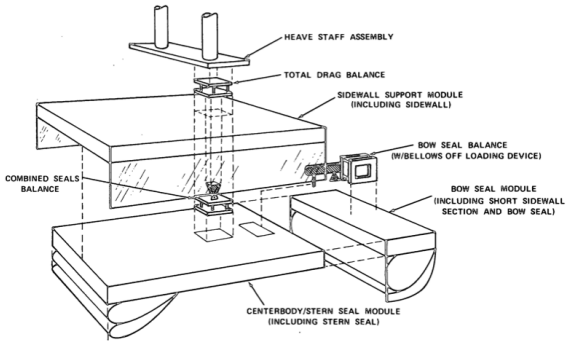

Figure 6.3: Schematic of segmented model showing three independent sections (not to scale) (from Heber, 1977)

6.1.3 Bow Seal Modules

In order to facilitate the comparison of different types of bow seals, three interchangeable bow seal modules were designed. In this manner, the type of bow seal being tested could be changed relatively quickly and easily. The three types of seals tested consisted of:

- **Finger Seal**, consisting of 10 semi-cylindrical "fingers," supported by cushion pressure (not supported by internal seal pressure)
- **Bag and Finger Seal**, consisting of an upper bag supported by internal seal pressure and ten lower "fingers"
- **SSBM Seal**, consisting of a single inflated membrane supported by internal seal pressure and stiffened with wire stays on the upstream (planing) face

The best available photographs for the three types of bow seals tested are shown in Fig. 6.4. Due to the simplicity provided by the 2-D nature of the SSBM seal, as well as its increased stiffness, the comparisons presented in the following two chapters will be shown for this seal only. The measured total resistance, draft, and trim are shown in Fig. 6.5 for similar operating conditions for the three different bow seal modules. The results are shown to be fairly consistent for all three bow seals, particularly at the secondary drag hump ($V_s = 5.2\,\mathrm{ft/s},\ Fr_C = 0.4$). The trends were also similar for other measured variables (see

Appendix C for further details). As a result, the SSBM comparisons are deemed to be sufficient in order to identify the physical cause of the secondary drag hump. The results also suggest that, in the subhump regime, the stern seal is of major importance, since a change in bow seal does not change the response significantly. It should be noted that at the highest speed for the bag and finger seal, the seal failed, causing a loss in bow seal lift support and consequently bow-down motion. This loss in lift led to an increase in the resistance and draft, and a decrease in trim. Unfortunately, the details of the bow seal failure were not reported by Heber (1977).

A transverse dimensional drawing of the SSBM seal module is shown in Fig. 6.6 for reference. The SSBM seal was designed to operate primarily as a planing surface and was consequently much stiffer than the other two seals. The wetted (upstream) face of the SSBM seal was constructed of two sheets of rubber material surrounding stiffening wire in order to form a laminate. The seal was attached to the wet deck by a hinge where the planing face meets the wet deck. The trailing edge of the SSBM seal was fitted with a downstop to prevent the seal from operating below a designated level, as shown in Fig. 6.6. The default downstop position was located one inch above the keel, corresponding to a downstop height of $h_{SF} = 0.0\,\mathrm{cm}\,(0.0\,\mathrm{in})$, as shown in Fig. 6.6. The downstop height was left as a configuration variable and runs were also performed with the downstop position set to $h_{SF} = 2.54\,\mathrm{cm}\,(1.0\,\mathrm{in})$ and $5.08\,\mathrm{cm}\,(2.0\,\mathrm{in})$ above the default position.

6.1.4 Stern Seal Module

Only one stern seal was tested during the experiment. The stern seal was similar in construction to the SSBM bow seal, but consisted of two pressurized lobes. A photograph showing the laminated construction of the planing face of the stern seal is shown in Fig. 6.7 and a cross-sectional diagram showing dimensions as well as defining the stern seal height (h_{SA}) is shown in Fig. 6.8. The stern seal was similarly fitted with downstop wires to prevent the seal from operating below a specified level.

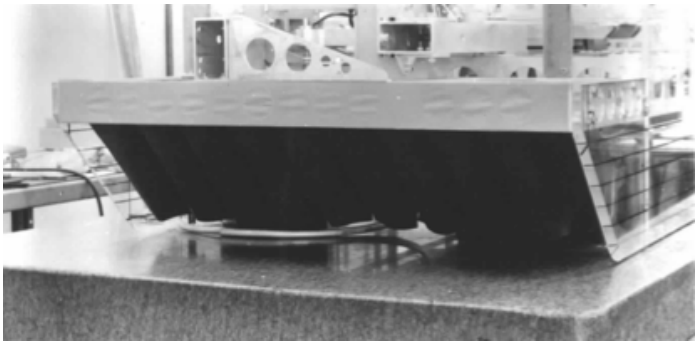

(a) Finger Bow Seal

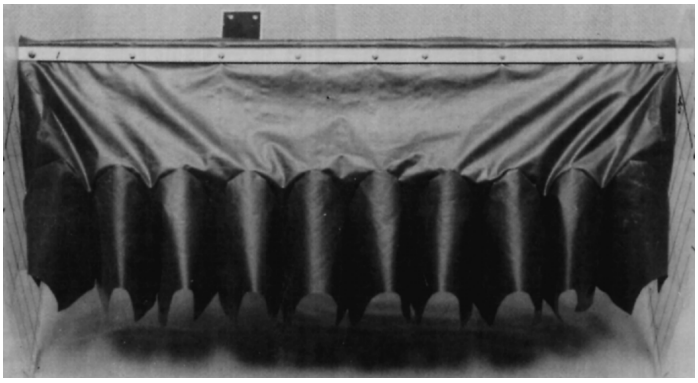

(b) Bag & Finger Bow Seal

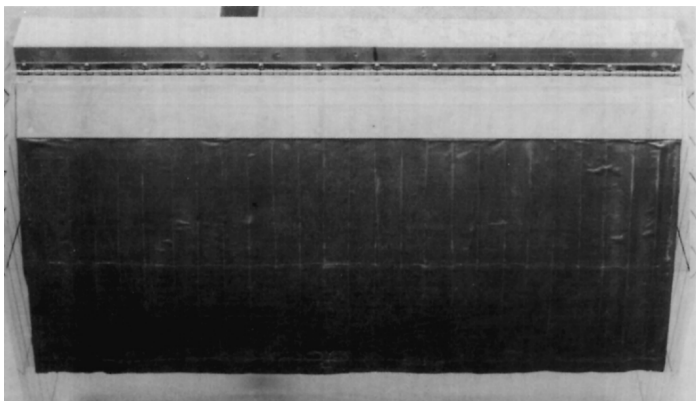

(c) SSBM Bow Seal

Figure 6.4: Photographs of various bow seals tested (from Van Dyck and Fridsma, 1979)

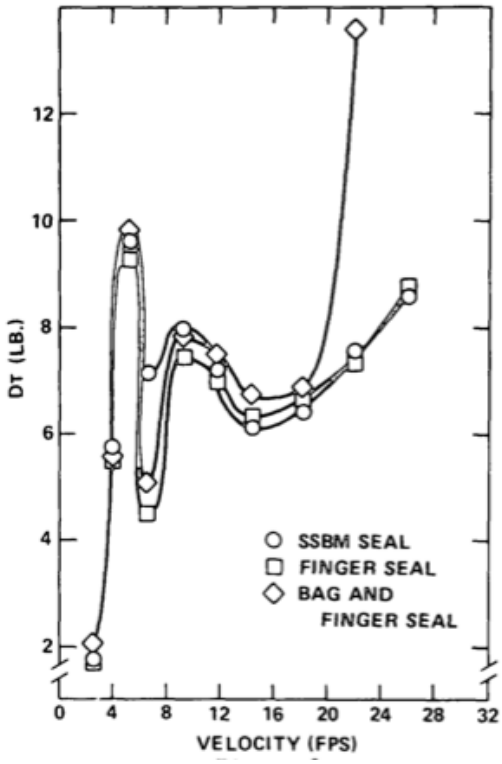

(a) Total resistance

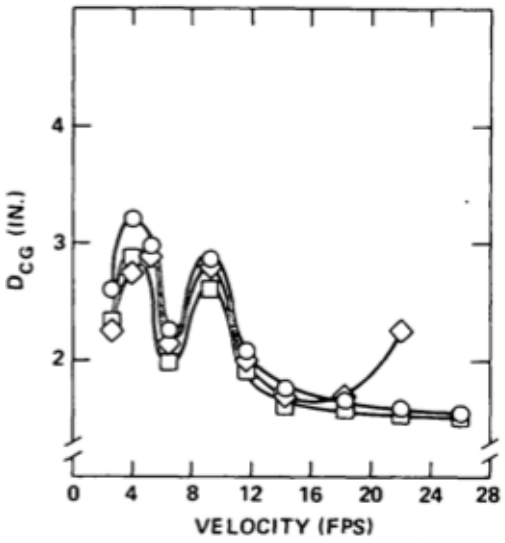

(b) Draft

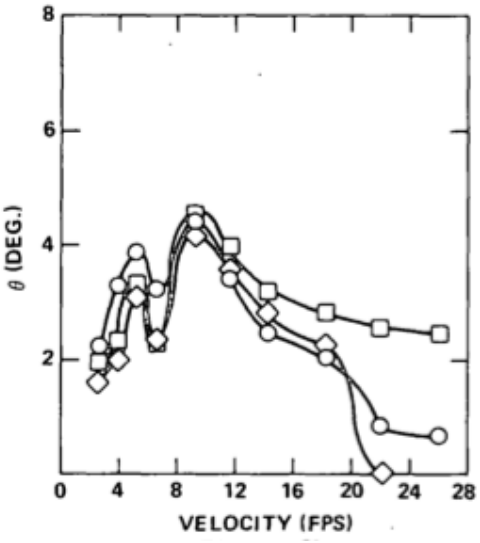

(c) Trim

Figure 6.5: Comparison of total resistance, draft, and trim for three bow seal configurations at comparable conditions. The model is free to heave and trim with $\Delta = 45.36\,\mathrm{kg}\,(100\,\mathrm{lb})$, $h_{SF} = h_{SA} = 0.0\,\mathrm{cm}\,(0.0\,\mathrm{in})$. At the highest speed for the bag and finger seal, the bow seal failed, causing a loss in bow seal lift support and consequently bow-down motion. This loss in lift led to an increase in resistance and draft, and a decrease in trim. (from Heber, 1977)

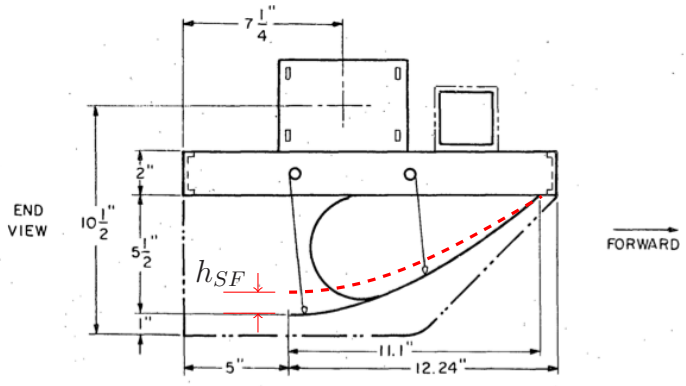

Figure 6.6: Diagram of SSBM bow seal module showing dimensions, as well as defining the bow seal height (h_{SF}) (from Van Dyck and Fridsma, 1979)

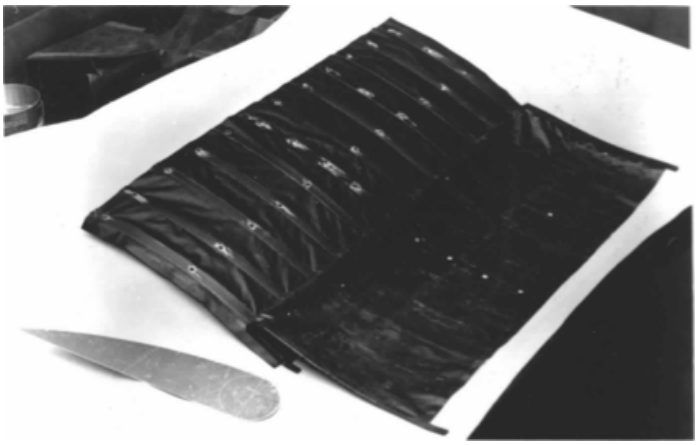

Figure 6.7: Photograph of stern seal showing laminated construction and internal stiffeners (from Van Dyck and Fridsma, 1979)

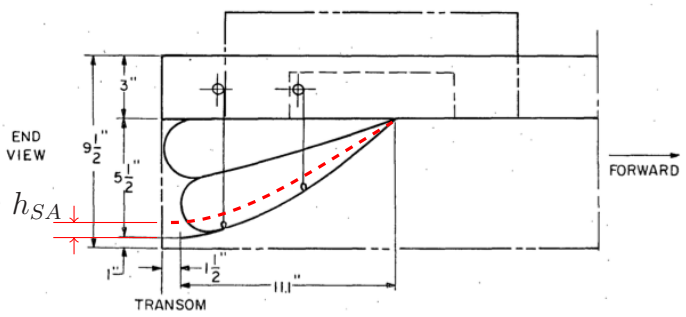

Figure 6.8: Diagram of stern seal module showing dimensions, double-lobed construction, and defining the stern seal height (h_{SA}) (from Van Dyck and Fridsma, 1979)

6.2 Test Program and Measured Data

The model tests were conducted in Tank 3 of the Davidson Laboratory at SIT. The tank was roughly $45.7\,\mathrm{m}\,(150\,\mathrm{ft})$ long and $1.52\,\mathrm{m}\,(5\,\mathrm{ft})$ deep. The test plan was designed to test each of the three bow seal modules for a wide number of parametric variations. The model was free-to-heave in all cases, but both free-to-trim and fixed-in-trim runs were performed.

For the free-to-trim cases, the parametric variations were allowed in seal downstop height, cushion fan system flow rate (by varying the number of fans), pressure ratio (P_s/P_C), Longitudinal center of gravity (L_{CG}), and vessel displacement (Δ). For the fixed-in-trim cases, parametric variations were allowed in the pitch angle and the seal-to-cushion pressure ratio (P_s/P_C).

Table 6.2: Experimentally-tested parametric relations for segmented SES model

Dimension	Symbol	Value
Displacement	Δ	$36.29,\ 45.36\,\mathrm{kg}\,(80,\ 100\,\mathrm{lb})$
Longitudinal center of gravity	L_{CG}	$82.55,\ 85.09\,\mathrm{cm}\,(32.5,\ 33.5\,\mathrm{in})$
Seal Pressure/Cushion Pressure	P_s/P_C	$1.05 - 1.30$
Number of cushion fans		$0 - 8$
Number of seal fans		$0 - 3$

Three force balances were used to measure loads between the three independent modules, as shown in Fig. 6.3. In addition to these channels, the trim angle (θ) and draft (d) were measured to determine the attitude of the model. The trailing edge height of the stern seal was measured at three transverse locations, and the SSBM bow seal trailing edge was measured at one location. Finally, a wide array of pressure sensors were used to measure the cushion pressure, internal seal pressures, and stern seal face pressures along the centerline. Details of the test setup and results can be found in Heber (1977) and Van Dyck and Fridsma (1979), and are summarized further in Appendix C.

6.3 Numerical Adaptation of Geometry

The dimensions for the overall vessel, the SSBM bow seal, and the stern seal (shown in Figs. 6.3, 6.6, and 6.8, respectively) were replicated numerically in order to yield the best accuracy possible. The numerical mesh is shown in Fig. 6.9, where the location of the major points used to designate the geometry are shown as red circles (labeled with point ID numbers). Unfortunately, due to the age and scope of the experimental study, some details are not available and must be inferred from drawings. In particular, the shape of the seal planing face had to be estimated.

The geometry is defined in a body-fixed coordinate system, as shown in Fig. 6.9. The main parameters defining the geometry are the cushion length L_C, the coordinates of the center of gravity and rotation, (x_{CG}, y_{CG}) and (x_{CR}, y_{CR}), respectively, and the geometry of the seals and their attachment points.

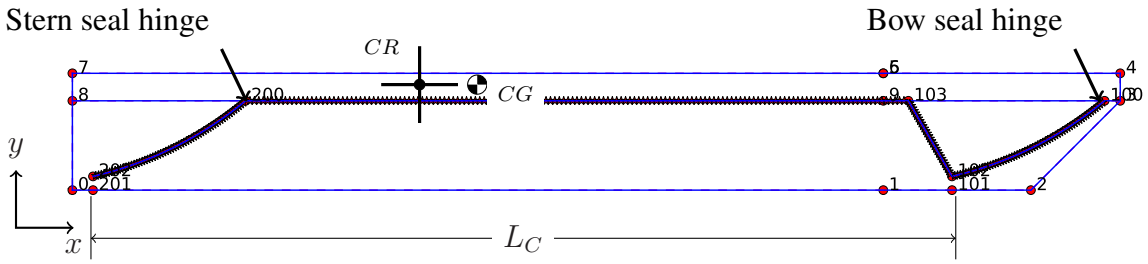

Figure 6.9: Geometry of segmented model, adapted for numerical drag prediction. The substructure faces are represented by blue lines and the control points are represented by red circles. The large number of star symbols across the seals and wet deck area represent the structural nodes, which are used to discretize the portion of the structure subject to possible pressure and shear loading. The center of gravity (CG) and center of rotation (CR) are denoted by a plus sign and a circle with two quadrants filled, respectively. Note that the CG and CR are not plotted to scale, but instead are placed to illustrate their general locations.

The seal geometry is constructed based on the drawings shown in Figs. 6.6 and 6.8. Both of these seals were stiffened membranes, and as such they were assumed to be fairly rigid on the planing face. Due to a lack of details, the planing faces were assumed to be sufficiently represented by constant-radius arcs. It was found that a radius of $12.5\,\mathrm{in}$ was

sufficient to match the shape of the seals provided in the experimental drawings for both the bow and stern seals.

The height of the trailing edge of the seals was adjustable during the model test using downstops. Due to the rigidity of the planing faces, it is assumed that the seals behave as rigid members that rotate about the hinge that attaches the seal to the wet deck. Hence, in order to match the downstop height specified in the experiment, each seal is correspondingly rotated about its hinge point until the seal height matches the specified downstop height.

6.4 Static Load Test Comparison

Due to the rigid nature of the seals, which were both constructed with planing faces consisting of metal stiffeners laminated by rubber membranes, the seals are assumed to behave as rotating bodies attached to the wet deck by a torsional spring. In order to test this assumption, the torsional-spring seal deformation model (described in Section 4.3.4) is compared with the results of a static deformation test.

In order to measure the deformation behavior of the seals, the segmented SES model was placed on a rigid surface, as shown in Fig. 6.10. The model was supported by a fulcrum, placed in the cushion area, and the seal. A series of weights was placed above the seal and the tip deflection (Δh_{tip}) of the seal was measured. Numerically, the seal is modeled by applying a fixed vertical tip force (F_{tip}) and recording the tip deflection, as shown in Fig. 6.11.

The stiffness of the torsional spring was chosen to match the measured stiffness of the seal from the experimental results. The tip load was varied for both the bow and stern seals, and the deformation was calculated. The results are shown in Fig. 6.12 for both the bow and stern seal. The torsional-spring model is found to be fairly well-representative of the experimental results. The torsional spring stiffness of the seals that was found to match the

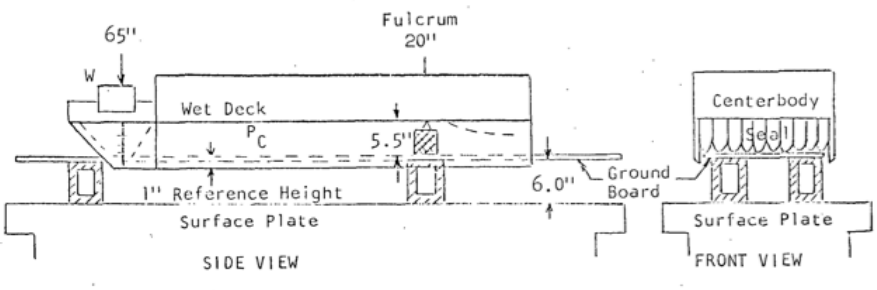

Figure 6.10: Diagram of experimental static load tests (from Van Dyck and Fridsma, 1979)

experimental results well was $K_\delta = 63.0\,\mathrm{N.m/deg}$ and $535.8\,\mathrm{N.m/deg}$ for the bow and stern seal, respectively. The stern seal was found to be much stiffer than the SSBM bow seal. The internal seal pressure of the seals was not varied during the experimental static load tests for the SSBM and stern seal tested, however it was varied for the finger bow seal. The finger bow seal was found to exhibit fairly linear behavior as well for both seal pressures tested.

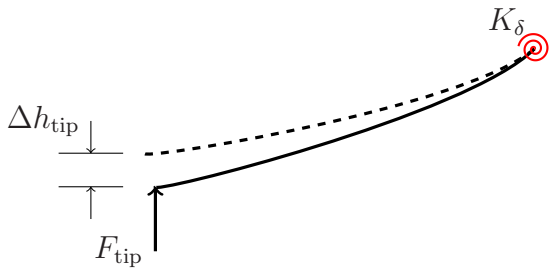

Figure 6.11: Diagram of loading and nomenclature for numerical static load tests

6.5 Relationship Between Torsional Spring Stiffness and Internal Seal Pressure

In the previous section, it was shown that the hinged seal model provides a good estimate for the deformation behavior of the stiffened bag and membrane bow and stern seals that were experimentally tested for the segmented SES model. Essentially, this model assumes that the bending stiffness of the planing faces of the seals is large enough that the bending

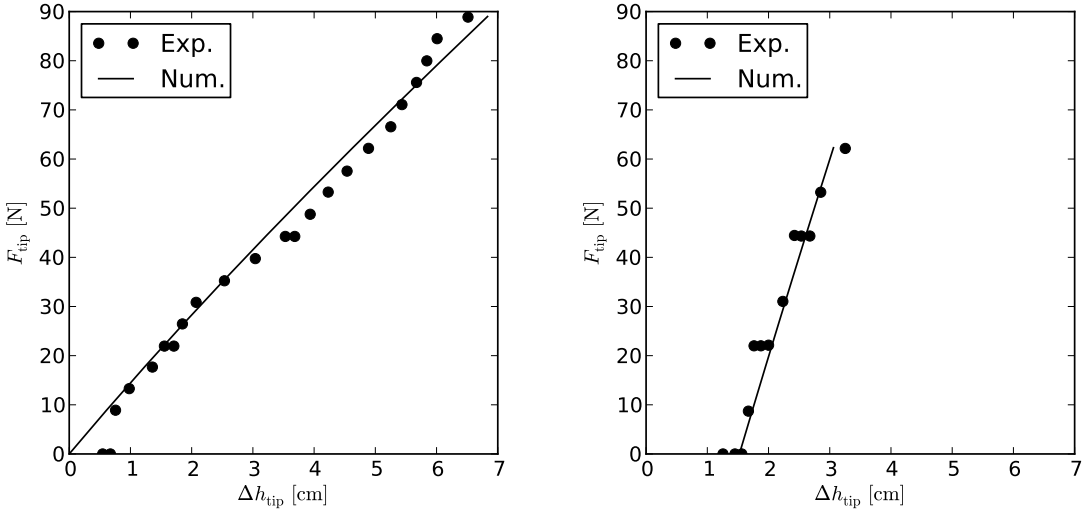

(a) Bow Seal ($K_\delta = 63.0\,\mathrm{N.m/deg}$)

(b) Stern Seal ($K_\delta = 535.8\,\mathrm{N.m/deg}$)

Figure 6.12: Comparison of numerical torsional-spring hinged seal model with experimental static load tests for seal tip deflection for bow and stern seals

deformations can be assumed to be negligible, and that the planing face behaves as a rotating rigid member. The torsional spring is included in order to represent the action of the internal seal pressure.

Although it is difficult to directly relate the internal seal pressure and the torsional spring stiffness due to a lack of details on the internal structure of the seals and material properties, the general behavior of the seals may be compared qualitatively by combining the truss finite elements with the hinged seal model for the stern seal. In this section, the behavior of the stern seal alone is examined for a single forward speed to examine the relationship between the torsional spring stiffness and internal seal pressure.

The stern seal was modeled using a rigid planing surface, as in the hinged seal model, connected to truss finite elements for the internal seal structure, as shown in Fig. 6.13. The seal is subject to a varying internal seal pressure, which exerts a restoring moment. The seal is initially placed with the trailing edge at $2.54\,\mathrm{cm}$ $(1.0\,\mathrm{in})$ below the initial free surface and the Froude number is $Fr_C = 0.35$, where the cushion length is based on the segmented SES model discussed previously in this chapter.

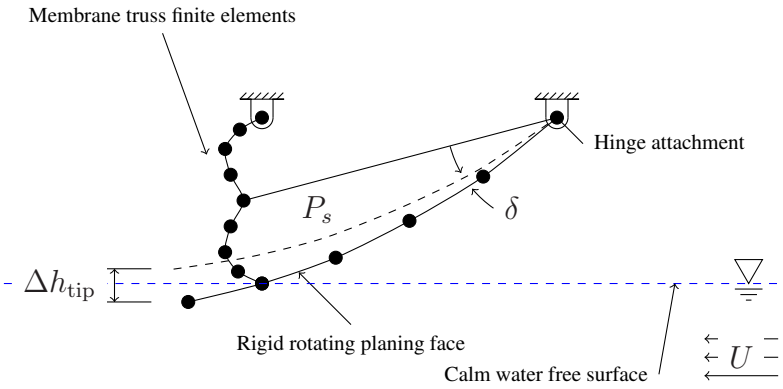

Figure 6.13: Diagram of the structural layout for stern seal calculations. The planing face is represented as a rotating rigid member with no bending deformation while the internal seal structure is modeled as a large deformation membrane using nonlinear truss finite elements.

The steady-state results for several internal seal pressures are shown in Fig. 6.14. The results qualitatively show the effect of internal seal pressure on the response. For the highest seal pressure, the seal planing face rotates very little, which is representative of a very stiff seal with large torsional stiffness. As the seal pressure is reduced, the deformation increases significantly. The seal tip deformation Δh_{tip} (as defined in Fig. 6.11) is shown in Fig. 6.15 as a function of the internal seal pressure. The response is found to be practically linear for relatively high seal pressure. The results qualitatively match the behavior of the torsional spring model. As the seal pressure is reduced, the seal becomes less "stiff" and exhibits a larger deformation. At very large seal pressures ($P_s > 300\,\text{Pa}$), the seal tip rests at the downstop and the seal is essentially rigid. Thus, for stiffened bag and membrane seals, the torsional spring hinged seal model is found to be representative of the deformation behavior of the physical seals, where the stiffness is derived from the internal seal pressure. Further investigation of each seal may yield a more quantitative correlation between the internal seal pressure and the torsional spring stiffness, which allows the simple hinged seal model to be used to efficiently model more complex structures without the need to directly simulate the membrane structure.

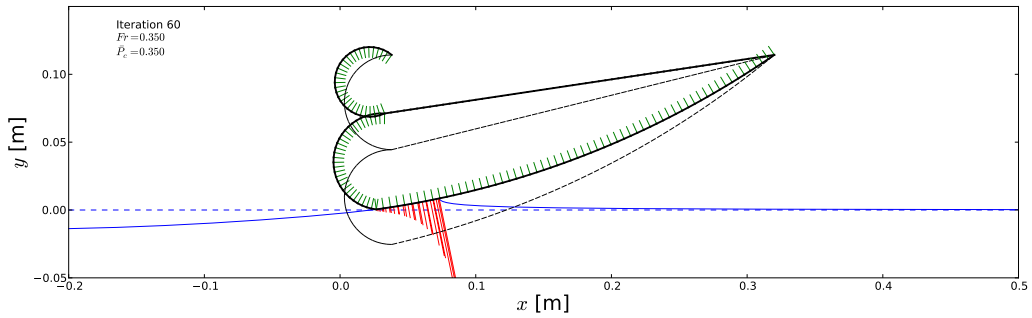

(a) $P_s = 110\,\mathrm{Pa}$

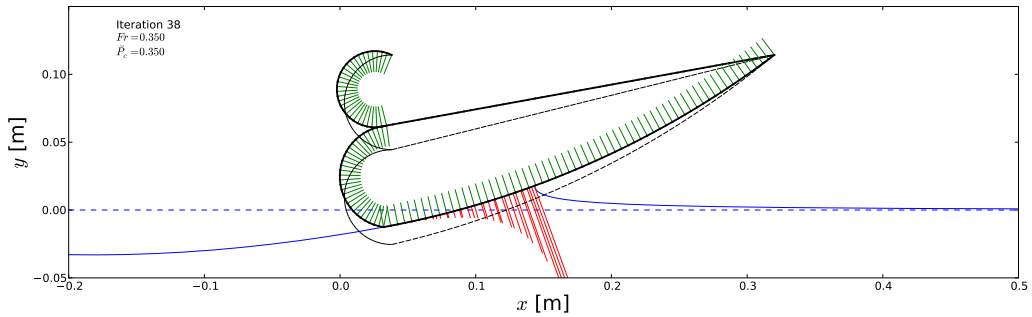

(b) $P_s = 220\,\mathrm{Pa}$

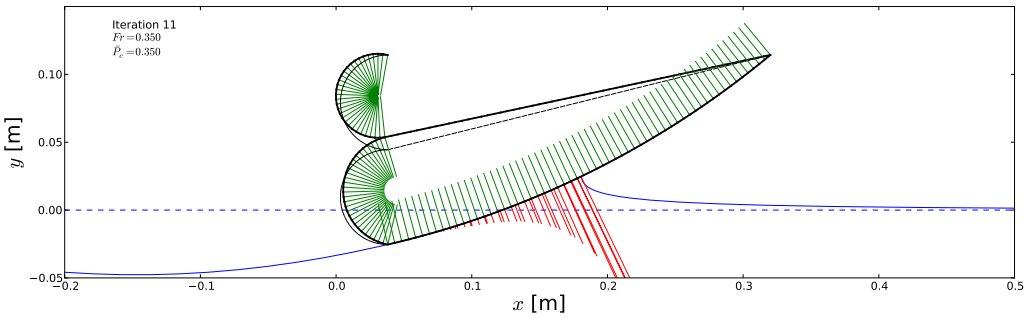

(c) $P_s = 450\,\mathrm{Pa}$

Figure 6.14: Free-surface profiles and deformed geometry for varying internal seal pressure. The seal pressure is shown in green lines while the hydrodynamic pressure is shown in red. The final and initial seal shapes are shown as a solid and dashed black curves. The free-surface profile is shown as a blue curve. The seal angular deformation is found to increase as the internal seal pressure decreases, which corresponds to a decrease in the torsional spring stiffness.

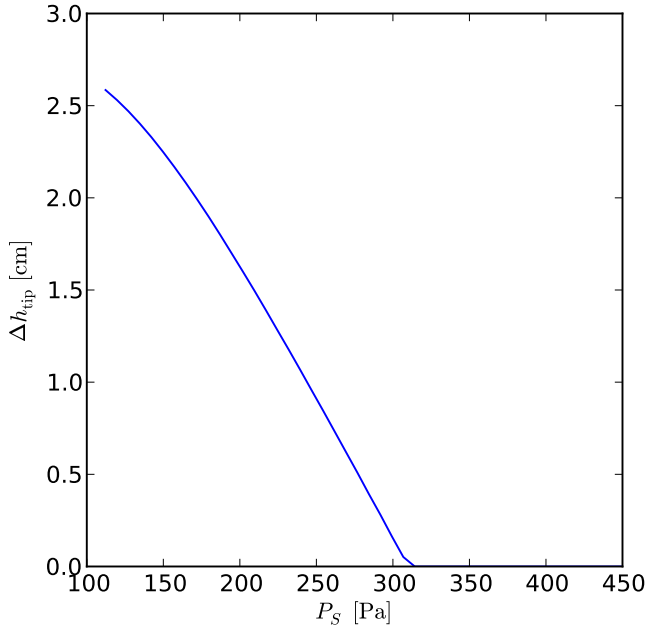

Figure 6.15: Tip deformation as a function of internal seal pressure

CHAPTER 7

Results: Rigid Seals

The results of the segmented SES model test of Heber (1977) described in Chapter 6 showed that the interaction of the bow and stern seal wave systems had a large effect on the total resistance at the secondary and primary drag humps. One of the primary objectives of this thesis is to investigate the physical cause of the increase in seal resistance, and to accurately predict the influence of the seals on the vessel motions and total drag. In this chapter, the segmented SES is modeled using a rigid-seal approximation. In doing so, the importance of including body motion in the model is identified and the cause of the increase in seal resistance at the secondary hump is determined. Due to the rigidity of the experimental seals that were employed, the rigid seal approximation is found to yield a fairly good comparison. The influence of seal flexibility is studied in Chapter 8.

7.1 Total Resistance and Vessel Motion Predictions

The geometry of the segmented SES model of Heber (1977) was described in the previous chapter. The 2-D numerical geometry is chosen to match the centerline geometry of the experimentally-tested model as closely as possible to avoid end effects. The major fixed operating parameters used for the current study are defined in Table 7.1. For the results of the current section, the only major variable that was changed is the Froude number based on the cushion length ($Fr_C = V_s/\sqrt{gL_C}$). The bow and stern seal heights, (h_{SF} and h_{SA}, respectively) were both set to their baseline configuration, i.e. $h_{SF} = h_{SA} =$

$0.0\,\mathrm{cm}\,(0.0\,\mathrm{in})$, which places the tips of the seals one inch $(2.54\,\mathrm{cm})$ above the keels, since the seals are assumed to be rigid. The seals are chosen to match the geometry of the stiffened stern seal and SSBM bow seal from the experiments, which were fairly rigid with a torsional stiffness of $K_\delta = 535.8\,\mathrm{N.m/deg}$ and $63.0\,\mathrm{N.m/deg}$, respectively. Dimensional drawings of these two seals are shown in Figs. 6.6 and 6.8, respectively.

Table 7.1: Fixed geometric and physical properties for simulations of the segmented SES model of Heber (1977)

Item	Symbol	Value
Water density	ρ_w	$1000.0\,\mathrm{kg/m^3}$
Gravitational acceleration	g	$9.81\,\mathrm{m/s^2}$
Cushion length	L_C	$1.591\,\mathrm{m}\,(62.64\,\mathrm{in})$
Cushion width	B_C	$0.6541\,\mathrm{m}\,(25.75\,\mathrm{in})$
Displacement	Δ	$45.36\,\mathrm{kg}\,(100\,\mathrm{lb})$
Nondimensional Cushion Pressure	$\bar{P_C} = P_C L_C B_C / \Delta$	0.7
x-location of center of rotation	x_{CR}	$0.8255\,\mathrm{m}\,(32.5\,\mathrm{in})$
x-location of center of gravity	x_{CG}	$0.8509\,\mathrm{m}\,(33.5\,\mathrm{in})$
y-location of center of rotation	y_{CR}	$0.1905\,\mathrm{m}\,(7.5\,\mathrm{in})$
y-location of center of gravity	y_{CG}	$0.1905\,\mathrm{m}\,(7.5\,\mathrm{in})$

For all cases, fifty pressure elements were used for each seal with cosine spacing, and one constant-pressure finite pressure band was placed between the trailing edge of the bow seal and the stagnation point of the stern seal to represent the pressure cushion. Since the objective is to compare the numerical predictions with experimental measurements for the segmented model given in Heber (1977), the total measured lift of the bow and stern seals is applied to the seals as the vessel weight. The restoring force is assumed to be generated by the hydrodynamic pressure and shear stress forces on the seals only, i.e. the thin sidehulls are assumed to have negligible contribution to the restoring force. The measured total lift and breakdown into the bow seal lift and stern seal lift are shown in Fig. 7.1 as curves, along with the values predicted by the numerical method, shown as symbols. The numerical method is found to accurately solve for the fixed-seal-lift case, where the lift is assumed to match the experiments. It should be noted that the total seal-provided lift is specified, however the fraction of the lift provided by each seal and the resultant seal motion are

solved as part of the solution. As shown in Fig. 7.1, the distribution of lift between the bow and stern seals is predicted fairly well, although there are some differences between the experimental and numerical lift distributions.

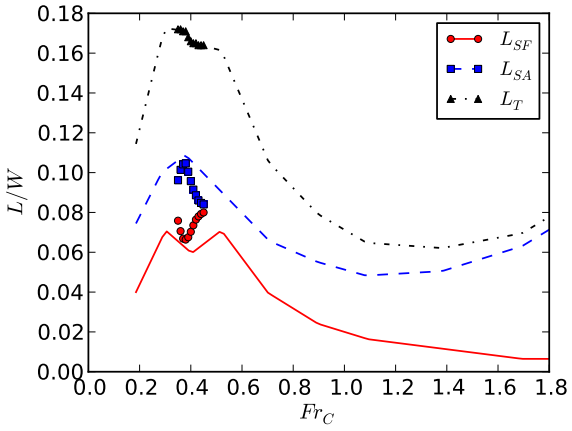

Figure 7.1: Experimentally-measured (curves) and numerically-calculated (symbols) seal lift fractions for the segmented model of Heber (1977) with $h_{SF} = h_{SA} = 0.0\,\mathrm{cm}\,(0.0\,\mathrm{in})$. The total seal-provided lift is prescribed numerically, while the bow- and stern-seal contributions are solved for.

The simulations for the seal resistance calculation are limited to Fr_C between $0.35 - 0.45$. In all cases, the frictional resistance of the seals is not included since it was observed to be at least two orders of magnitude lower than the pressure drag in early-stage simulations. For $Fr_C > 0.45$, the wetted length of both seals is less than 15% of the total arc length of the seal, i.e. the seals were barely touching the surface of the water. This implies that the seal drag is relatively negligible in this speed range. In addition to the 2-D seal resistance model, the resistance was estimated using a more traditional method, where the 3-D cushion wave making drag ($R_{W,\mathrm{3d}}$), computed by applying a constant pressure patch on the free surface (as described in Section 3.6.2) without consideration for the seal resistance, is used. To compute the total resistance over the full range of Froude numbers, both methods are used in conjunction with an estimate for the sidewall frictional drag.

The sidewall friction drag is approximated using Eq. (7.1) and tare runs performed experimentally by Heber (1977). The sidewall frictional resistance ($R_{F,\mathrm{SW}}$) is calculated

as:

$$R_{F,\mathrm{SW}} = C_{f_o} {V_s}^2 + C_f \cdot \frac{1}{2} \rho_w S {V_s}^2 \tag{7.1}$$

where S is the computed wetted surface area of the sidehulls, C_f is the ITTC friction coefficient based on Reynolds number based on the sidewall wetted length, and $C_{f_o} = 4.356 \times 10^{-3}\,\mathrm{Ns}^2/\mathrm{m}^2$ is a constant dimensional friction factor measured from experimental runs with no seals present. The wetted area is estimated for the speed range by integrating the computed wave profile, as illustrated in Fig. 7.2. Since the sidewalls were simply thin plates, the area was multiplied by four to account for both the inside and outside of the two sidewalls. The wetted area is plotted versus Fr_C in Fig. 7.3. The wetted area is shown to decrease as Fr_C increases because of the increase in wave length.

The seal resistance of the numerical model was calculated by integrating the hydrodynamic pressure over both seals and multiplying by the cushion beam (B_C). The sidewall drag was then added to yield the total resistance, i.e.:

$$R_{T,\mathrm{curr}} = R_{SF} + R_{SA} + R_{F,\mathrm{SW}} \tag{7.2}$$

where R_{SF} and R_{SA} are the bow and stern seal resistance, respectively, and $R_{F,\mathrm{SW}}$ is the sidehull frictional drag, calculated via Eq. (7.1).

The results for the total resistance (R_T), bow and stern seal resistance (R_{SF} and R_{SA}), draft (d), trim angle (θ), and wetted length of the seals (L_w) are shown in Fig. 7.4. In Fig. 7.4(a), the total seal resistance ($R_{T,\mathrm{curr}}$) from the numerical model is shown as a solid black curve, the sidewall frictional resistance ($R_{F,\mathrm{SW}}$) is shown as a dash-dot green curve, and the wave resistance based on the moving smoothed pressure distribution of Doctors and Sharma (1972) ($R_{W,\mathrm{3d}}$) is shown as a dashed red line. The method employed for 3-D wave resistance estimation is similar to the 2-D smoothed pressure patch method shown and validated in Section 3.6.2 but expanded to three dimensions. The details of the calculation

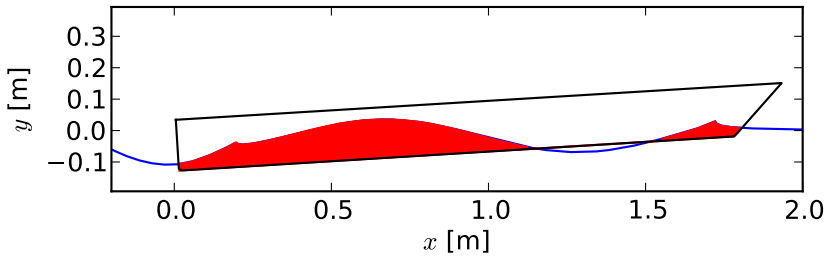

(a) $Fr_C = 0.35$

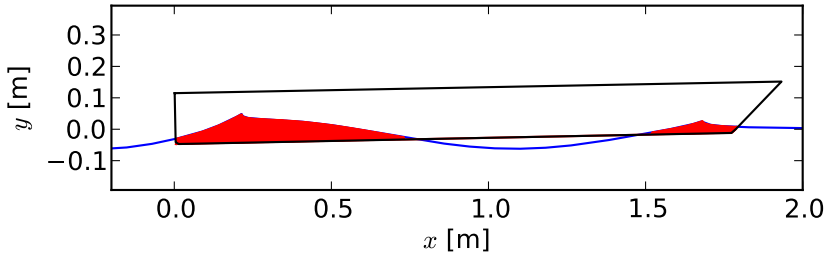

(b) $Fr_C = 0.4$

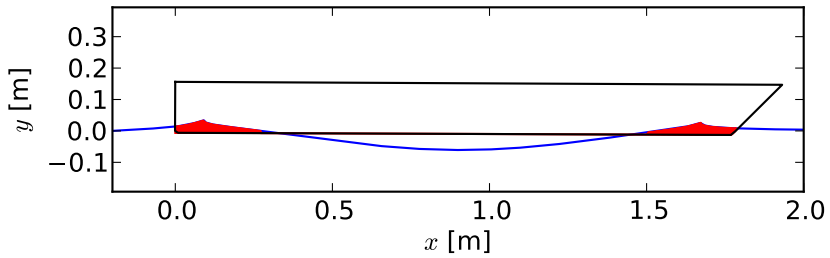

(c) $Fr_C = 0.45$

Figure 7.2: Calculated wetted area (red) for sidehull frictional drag predictions for different Froude number based on the cushion length (Fr_C)

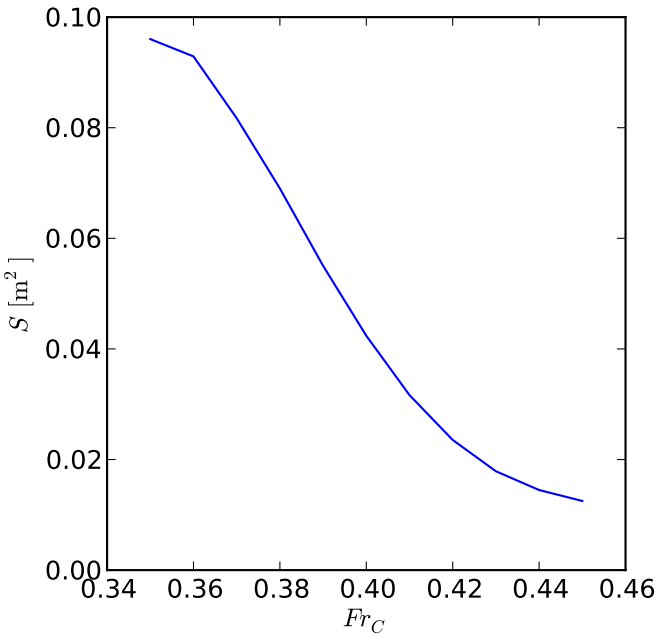

Figure 7.3: Computed wetted area of the segmented SES model versus Froude number based on the cushion length (Fr_C)

of the 3-D cushion wavemaking drag are given in Appendix D. The total resistance based on the traditional method ($R_{T,\text{trad}} = R_W + R_{F,\text{SW}}$) (the sum of 3-D wave making and sidewall frictional drag) is shown as a dotted black curve. The results from the hybrid approach, which utilizes the seal-cushion-wave interaction model for $0.35 < Fr_C < 0.45$ ($R_{T,\text{curr}} = R_W + R_{F,\text{SW}} + R_S$), and the 3-D wave cushion model for $Fr_C > 0.45$, are found to offer a reasonable estimate of the measured total resistance, which are shown as symbols. Error bars are included for the experimental results, corresponding to the estimated accuracy from Van Dyck and Fridsma (1979), which was reported to be $\pm 0.09\,\text{kg}\,(0.2\,\text{lb})$ for resistance measurements, which corresponds to an error in resistance-to-weight ratio of ± 0.002.

In particular, the total resistance predicted by the current method, $R_{T,\text{curr}}$, is able to capture the large increase in the total resistance at the subhump ($Fr_C = 0.37$) due to the seal drag. The traditional 3-D wave drag, $R_{T,\text{trad}}$, significantly under-predicts the total resistance at the subhump because the seal drags are ignored in the traditional pressure patch method. The traditional 3-D wave drag, when combined with an estimation of the sidewall

frictional resistance, $R_{F,\mathrm{SW}}$, is found to be sufficient for predicting the total resistance for $Fr_C > 0.45$, when the seal contributions are practically negligible.

Although the current 2-D numerical method for seal drag prediction is able to capture the secondary drag hump, it is unable to capture the primary hump directly. This is due to the fact that the numerical model currently relies on integrating the near-field pressure distribution along the wetted surface to obtain the hydrodynamic forces, whereas the cushion wavemaking drag is primarily a far-field effect. In reality, the vessel experiences the effects of cushion wavemaking drag through a changing pressure distribution of the air within the pressure cavity, which is discussed in Yun and Bliault (2000, pp. 203). The effects of cushion wavemaking drag are also expected to be influenced by compressibility and 3-D effects of the waves inside the cushioned space, where 3-D focusing of the wave at the stern may occur in reality (see e.g. the CFD simulations of Donnelly (2010)). However, these complex effects are currently not captured in the numerical model for the seal resistance due to the assumption of a constant pressure cushion as well as the assumption of 2-D flow, which necessarily ignores the 3-D variation of the pressure within the cushioned space, as well as the 3-D wave system generated by the pressure cushion. Hence, for accurate predictions of the total resistance over the entire speed range, a combination of the two methods (2-D seal drag model + 3-D cushion wavemaking drag model) is recommended, where the 2-D seal drag model is used in the subhump regime ($Fr_C = 0.35 - 0.45$) and the traditional 3-D cushion wavemaking drag model is used at higher speeds ($Fr_C > 0.45$). It should be noted that, although 3-D effects are not accounted for in the seal resistance predictions, they are considered in the 3-D cushion wavemaking drag prediction, as detailed in Appendix D.

By examining the frictional drag component in Fig. 7.4, it is apparent that the frictional drag from the sidewalls is relatively small in the $Fr_C = 0.35 - 0.45$ range, where the seal drag dominates. Hence, changes in wetted area were minimally effective at these speeds.

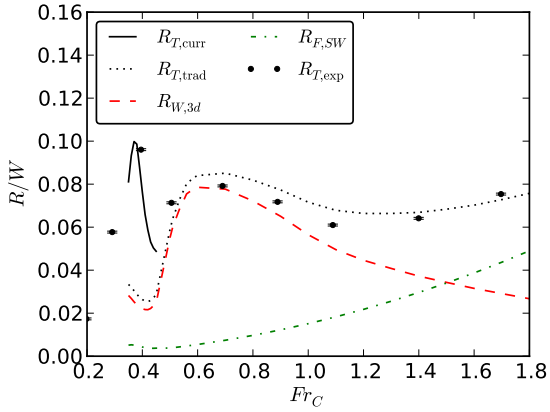

(a) Total Resistance

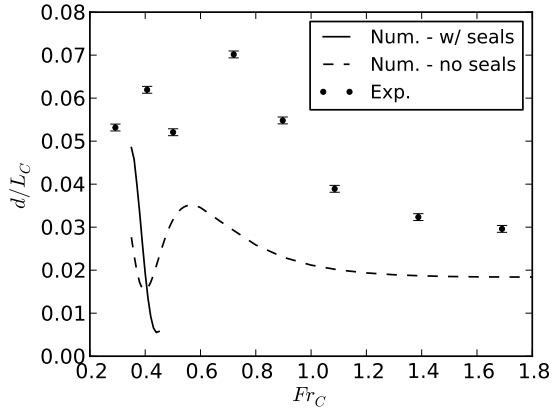

(b) Draft

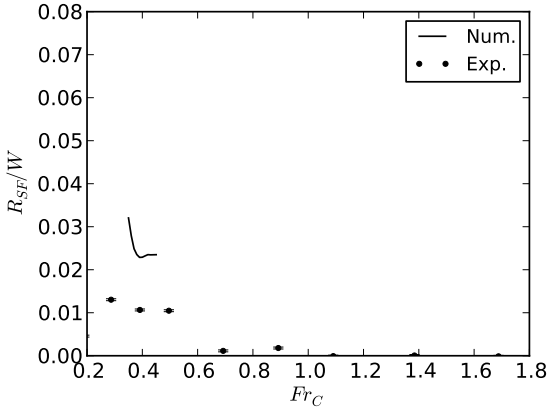

(c) Bow Seal Resistance

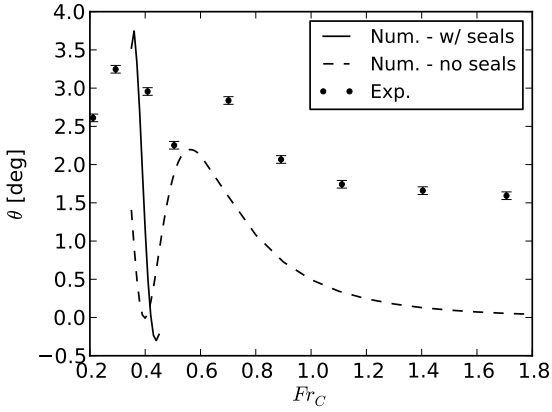

(d) Trim

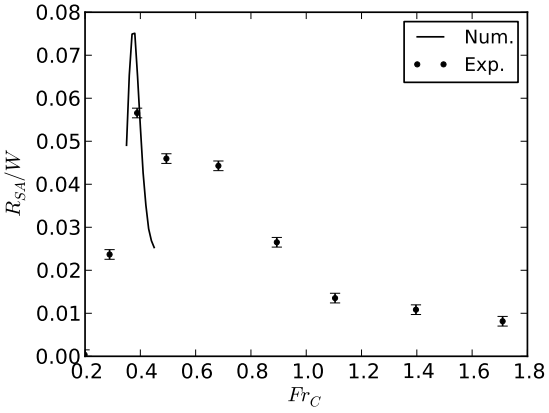

(e) Stern Seal Resistance

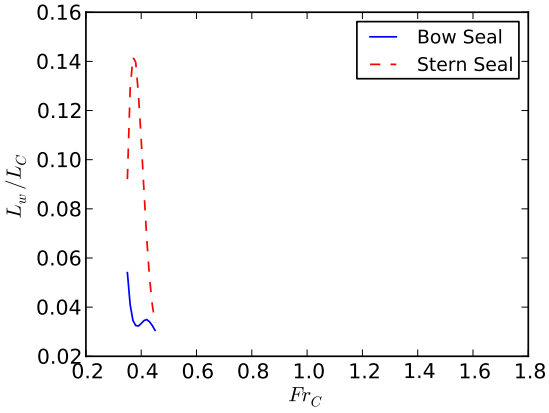

(f) Wetted Length

Figure 7.4: Results for rigid seal simulations with $h_{SF} = h_{SA} = 0.0\,\mathrm{cm}\,(0.0\,\mathrm{in})$

7.2 Bow/Stern Seal Interaction

The results for the total resistance (Fig. 7.4(a)) show a large drag hump at $Fr_C \approx 0.37$ that is primarily due to stern seal drag. The cause of this is readily observed by investigating the predicted wave profiles, which are shown in Fig. 7.5. As the Froude number increases, the location of the first wave crest of the bow-seal wave moves aft. This crest impacts the stern seal, which affects the wetted length of the stern seal. It is seen that at the secondary hump ($Fr \approx 0.37$), this increased wetted length causes a dramatic increase in pressure drag of the stern seal. This effect was observed experimentally by Heber (1977), as is illustrated in Fig. 7.6. Although the wetted length, and consequently the drag of the bow seal, did vary as a function of Froude number, the effect was much less drastic due to the fact that there were no waves being generated upstream of the bow seal. Both the experimental and numerical results shown in Fig. 7.4 also suggest that the contribution of the bow seal drag is much smaller than the stern seal drag across the range of Froude numbers, and the contribution of both seal drags are small for $Fr_C > 0.45$.

The phasing of the wave pattern is also observed to have a large effect on the running draft and trim of the vessel. This effect is due to the location of the first wave crest. In the subhump regime, the wave height at the stern seal is found to either raise or lower the effective submergence at the stern seal. For $Fr_C > 0.6$, which corresponds to speeds above the primary hump, the wave crest is located aft of the stern seal, and the model begins to level off. At these higher speeds, the model is found to trim with the slope of the cushion wave and barely touches the water surface, which is consistent with good agreements observed between past prediction efforts in which the seals were ignored and experimental measurements for $Fr_C > 0.6$.

The vessel motions are compared between the numerical model and the experimental results in Figs. 7.4(b) and 7.4(d). The numerical results are shown as a solid black line and the experimental results are shown as dots with error bars corresponding to the estimates from Heber (1977). The reported values for estimated error in draft and trim are

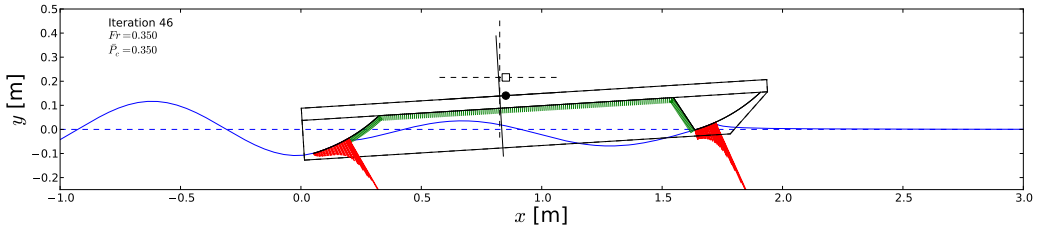

(a) $Fr_C = 0.35$

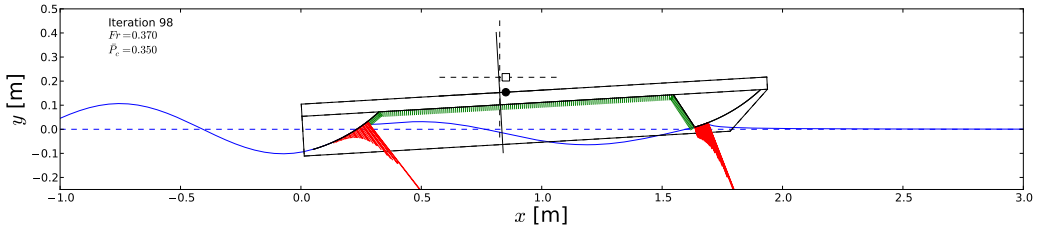

(b) $Fr_C = 0.37$

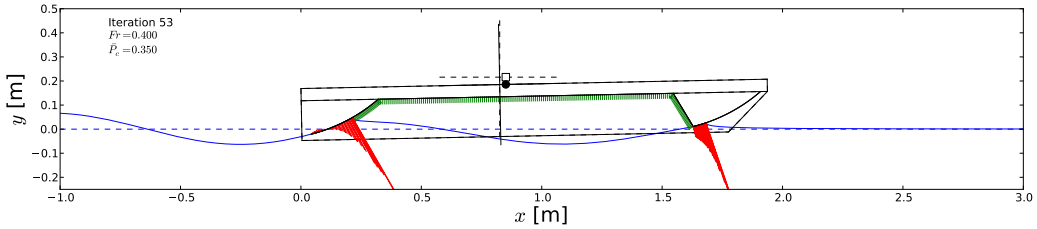

(c) $Fr_C = 0.4$

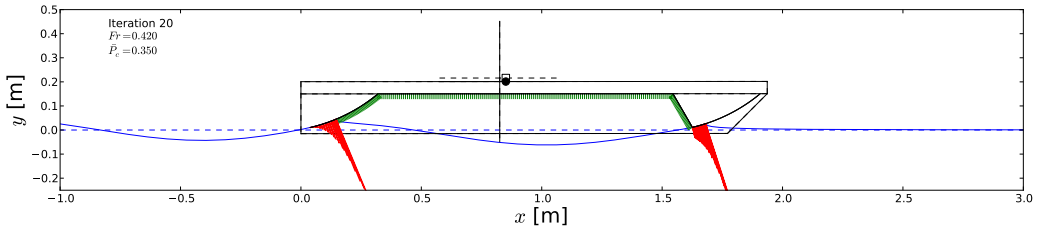

(d) $Fr_C = 0.42$

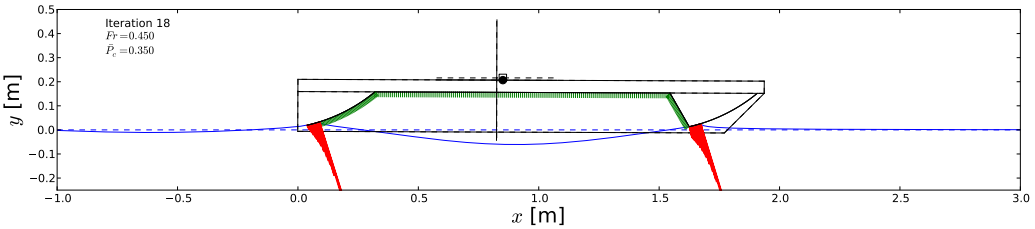

(e) $Fr_C = 0.45$

Figure 7.5: Equilibrium solutions for a segmented SES with rigid seals for a range of Froude numbers with $h_{SF} = h_{SA} = 0.0\,\mathrm{cm}\,(0.0\,\mathrm{in})$ showing the passing of the bow seal wave aft as Froude number increases. The deformed and undeformed free-surface profiles are shown as solid and dashed blue lines, respectively. The hydrodynamic pressure profiles are illustrated as red lines and the cushion pressure is shown as green lines. The initial center of rotation is shown as a dashed set of axes, while the final center of rotation is shown as a solid set of axes. The initial and final center of gravity are shown as a white square and black circle, respectively.

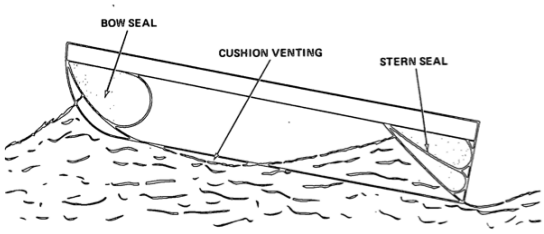

(a) At secondary hump

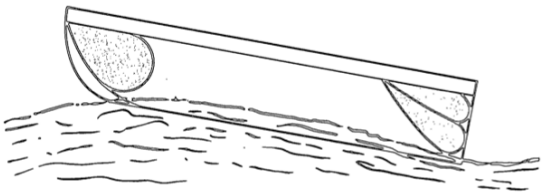

(b) At primary hump

Figure 7.6: Relation of cushion waves to bow and stern seals (from Heber, 1977)

$\pm 0.127\,\mathrm{cm}\,(0.05\,\mathrm{in})$ and $\pm 0.05°$, respectively. The numerical method is found to under predict both the draft and trim for this case, however the trend is similar.

At speeds of $Fr_C > 0.45$, the wetted length of both of the seals is found to be very small compared to the cushion length (i.e. less than 5%). Hence, the seals ride with the tip very close to the free surface and the seals do not disturb the free surface very much. In order to investigate the motions at higher speeds, the equilibrium draft and trim were calculated assuming that the seals do not affect the hydrodynamic solution and that the tips of the seals ride at the surface of the cushion-generated wave (similar to Section 4.2.2). It should be noted that in this speed range, the seal resistance is assumed to be negligible.

The results for draft and trim without consideration for the effects of the seals on the hydrodynamic solution are shown as dashed lines in Figs. 7.4(b) and 7.4(d). The numerical results without consideration for the seals are found to significantly under-predict the experimentally-measured values for $Fr_C < 0.45$, however the agreements in trend are good for $Fr_C > 0.45$. The predicted wave profiles for the simulations without considering the hydrodynamic effects of the seals are shown in Fig. 7.7, where the vessel motions are seen to be governed primarily by the cushion-generated wave. Comparison of the results

shown in Figs. 7.5 and 7.7 suggests two things: (1) the vessel motions (running trim and draft) are highly dependent on the shape of the free surface (determined by the cushion- and seal-generated wave patterns), and (2) the vessel trim and draft should also be highly dependent on the seal height above the keels.

By comparing the predicted wave profiles for $Fr_C = 0.35$, 0.40, and 0.45 for the case with and without consideration for the hydrodynamic effects of the seals (Figs. 7.5 and 7.7, respectively), several observations can be made. First, the presence of the seals acts to move the first wave trough forward, influencing the speed at which the first wave crest will impact the stern seal. Second, the bow seal is seen to increase the magnitude of the waves inside the pressure cushion by forcing the trough down and the crest up toward the stern seal, which may have a large impact on ventilation of cushion air, stern seal drag, and vessel motion (as evidenced by the higher predicted draft and trim for the model prediction with the seals in Figs. 7.4(b) and 7.4(d)). The effects of cushion ventilation are expected to be a 3-D phenomenon, however. Hence, although it may appear as though the cushion would vent, it is not necessarily true since the 2-D model is expected to offer a wave elevation prediction more in line with the centerline wave profile rather than at the sidewalls, where ventilation is most likely to occur. It is perceivable that the amplified wave system caused by the presence of the seals may promote a 3-D wave pattern in the cushioned space, and hence lead to 3-D effects that cannot be captured with the current 2-D model. In any case, the 2-D numerical model is found to be useful for examining the physics of the interaction of the bow and stern seal waves.

Investigation of the free-surface wave profiles at low Fr_C shows that the waves can become very steep (e.g. $H/\lambda = 0.18$ at $Fr_C = 0.35$, where H is the wave height and λ is the wavelength) and consequently the waves may begin to break. Hence, further investigation is necessary in order to determine the effects of nonlinearity and wave breaking on the free-surface response, in a similar manner to the single planing plate problem (which was shown in Section 3.3) and the work of Maki et al. (2012), who studied the effects of

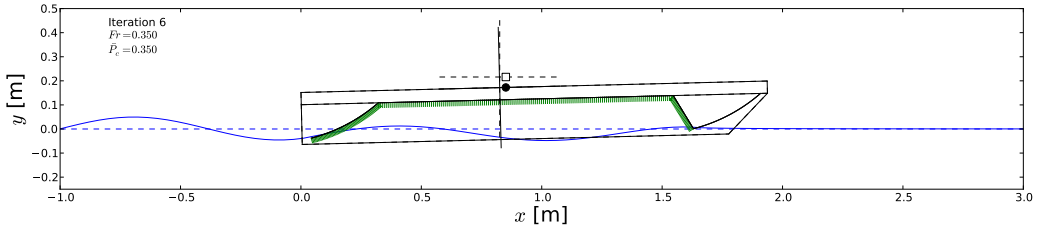

(a) $Fr_C = 0.35$

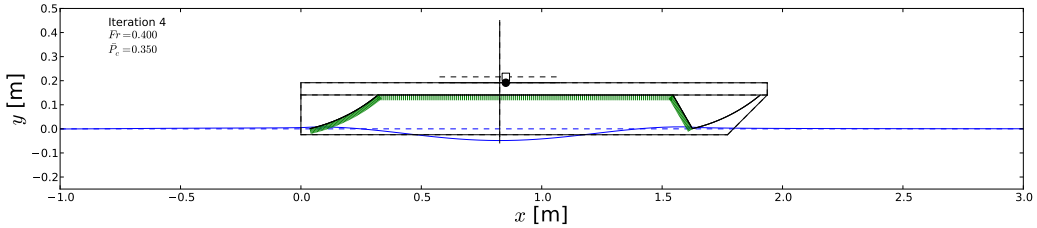

(b) $Fr_C = 0.4$

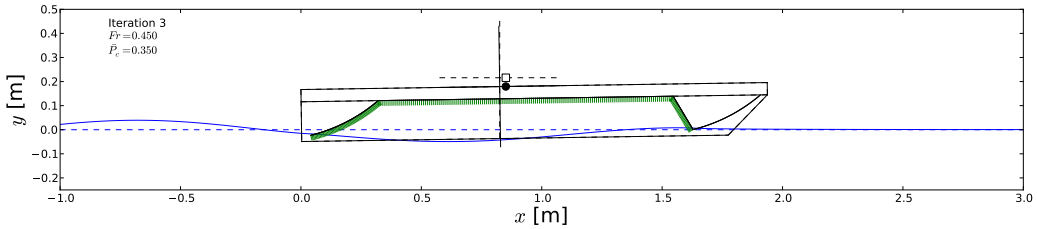

(c) $Fr_C = 0.45$

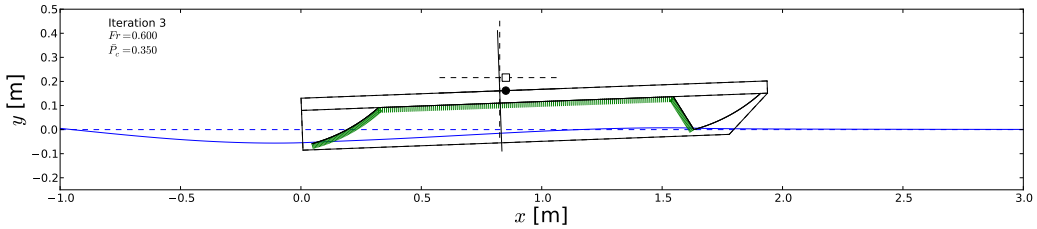

(d) $Fr_C = 0.6$

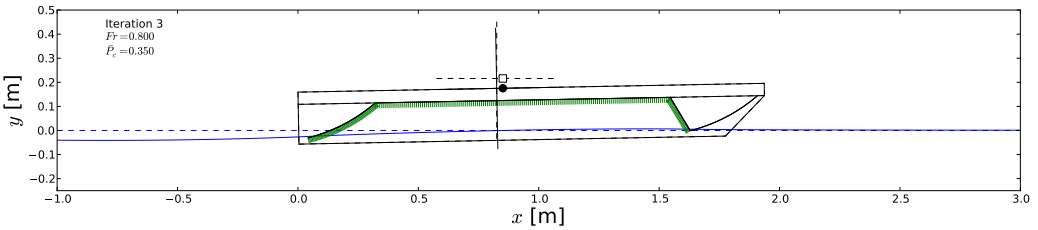

(e) $Fr_C = 0.8$

Figure 7.7: Equilibrium solutions for a segmented SES with rigid seals for a range of Froude numbers with $h_{SF} = h_{SA} = 0.0\,\mathrm{cm}\,(0.0\,\mathrm{in})$ where the seals are assumed to operate with the tip on the cushion-generated free surface and the effects of the seals on the hydrodynamic solution are ignored

nonlinearity and wave breaking for the 2-D moving pressure patch. In any case, the current work represents a first step towards investigating the interaction of the bow and stern seal wave systems and was able to offer reasonable predictions for the contribution of the seals to the total resistance for the segmented SES model.

7.3 Summary

In this chapter, the experimentally-tested segmented SES model of Heber (1977) was simulated for one model configuration over a range of speeds and the seals were assumed to be rigid. The total resistance was predicted using a hybrid approach, where the 2-D numerical model, which considers the interaction of the bow and stern seals, pressure cushion, free-surface waves, and vessel motion, is used for $Fr_C < 0.45$, and the more traditional method based on the wave resistance of a moving smoothed pressure distribution without consideration of the seal drag (as developed by Doctors and Sharma (1972)) is used for $Fr_C > 0.45$. The traditional method was found to offer accurate predictions of the total resistance at high speeds ($Fr_C > 0.45$) when the added frictional resistance of the sidewalls was considered. However, at lower speeds ($Fr_C = 0.35 - 0.45$), the resistance is under-predicted since the effects of the seals are not included. The 2-D numerical method is found to offer accurate predictions of the total resistance in the subhump regime ($Fr_C = 0.35 - 0.45$) by accounting for the interaction of the bow and stern seal wave systems. The 2-D model is unable to offer predictions for $Fr_C > 0.45$, however, since the seals are very lightly immersed, and hence have negligible effects. Therefore, in order to predict the total resistance over the entire range of Froude numbers, it is recommended that a combination of the two methods be used.

In addition to predicting the total resistance, the wave profiles were predicted using the 2-D method and the physical cause of the large subhump resistance was identified. The bow-seal wave was found to impact the stern seal at the subhump ($Fr_C = 0.37$), causing a

drastic increase in resistance. This numerically-derived explanation is in accordance with the experimental observations of Heber (1977). The influence of the seals was also found to have a large impact on the vessel motion for $Fr_C < 0.45$, where the higher submergence and trim angle for the case with consideration for the seals leads to higher total resistance.

In the next chapter, the same segmented SES model of Heber (1977) is simulated, but the stern seal is allowed to be flexible using the 1-DoF hinged seal model described in Section 4.3.4. In doing so, the effects of stern seal rigidity are investigated.

CHAPTER 8

Results: Flexible Seals

In the previous chapter, the segmented SES model from Heber (1977) was simulated for a range of operating conditions using a rigid-seal approximation. In doing so, the secondary drag hump was identified as being caused by the interaction of the bow seal wave with the stern seal, leading to increased stern seal wetting, higher submergence and trim, and larger drag/lift forces. The results of the numerical model with rigid seals were found to agree reasonably well with the experimental results, likely owing to the rigidity of the Stay-Stiffened Bag and Membrane (SSBM) seals that were tested. In this chapter, the effects of seal flexibility are examined for the same vessel by performing numerical simulations with flexible seals that are attached to the model by torsional springs.

8.1 Effects of Flexibility for a Single Seal

In Fig. 7.1 (previous chapter), it was observed that the amount of lift provided by each seal was relatively constant in the $0.35 < Fr_C < 0.45$ range. This is due to the fact that the cushion pressure is assumed to be constant, thus leading to the total lift contribution from the air being fairly constant as well. In reality, the cushion pressure is a function of the lift fan system properties and air leakage, which is dependent on the seal deformation, draft, and trim of the vessel. All of these properties determine how much of the vessel weight is supported by the seals versus the air cushion, sidehulls, etc. Hence, the overall vessel behavior can become quite complex and is beyond the scope of the current work.

Given that the amount of lift provided by each seal is relatively constant in the simulated speed range, it is therefore useful first to study the effects of seal stiffness on the seal performance for a single (bow) seal without accounting for the rest of the vessel. In doing so, the general effects of stiffness may be investigated without the complication of the bow-stern seal interaction effects.

In order to investigate the effects of seal stiffness for the bow seal alone, the SSBM seal from Heber (1977) was tested at $Fr_C = 0.4$, where the Froude number is still defined based on the cushion length (L_C) to provide an adequate frame of reference. The reference hinge point is located at $16.5\,\mathrm{cm}\,(6.5\,\mathrm{in})$ above the calm-water free surface (which corresponds to the wetdeck height for the reference draft of the complete SES model), from which the draft is defined as positive downwards, as shown in Fig. 8.1. Simulations are performed for both prescribed-draft and fixed-lift cases in order to compare their effects on the performance. In all cases, the seal surface is allowed to deform by rotating about the hinge point and shear stress is not included (because the contribution of the shear on the total lift and moment is very small compared to the pressure effect). For the prescribed-draft simulations, the hinge point is fixed, whereas for the fixed-lift cases, the hinge point is allowed to translate in the vertical direction (i.e. to move with the wetdeck according to the vessel motion) until the equilibrium condition (lift = weight) is satisfied. The seal stiffness of the torsional-spring seal (K_δ) is varied and the seal deformation angle (δ) is determined. The nomenclature is shown in Fig. 8.1.

8.1.1 Prescribed-Draft Case

The seal was set at a prescribed draft of $\Delta d = 5.08\,\mathrm{cm}\,(2.0\,\mathrm{in})$ while the torsional stiffness was varied. For the case of a single seal with a prescribed draft, the response is fairly intuitive. The predicted response as a function of the seal stiffness, K_δ, are shown in Fig. 8.2. The corresponding undeformed (thin black line) and deformed (thick black line) seal shapes are shown in Fig. 8.3 for varying K_δ. The results show that, for very stiff seals

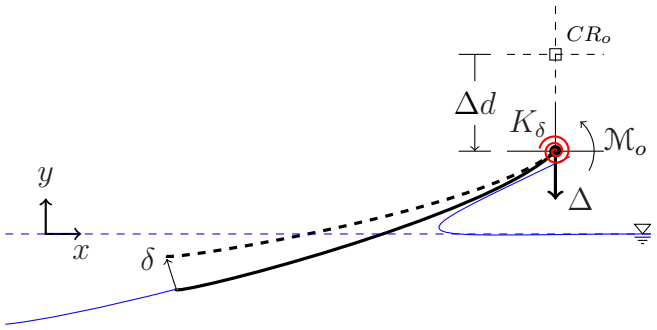

Figure 8.1: Diagram of numerical model for hinged seal with torsional spring showing definitions of the reference center of rotation (CR_o), change in draft (Δd), seal deformation angle (δ), hydrodynamic moment about the hinge point ($\mathcal{M}_o$), and torsional spring stiffness (K_δ)

(high K_δ), the solution approaches the rigid case, where the seal deformation angle (δ) approaches 0 as $K_\delta \to \infty$. As the stiffness decreases, the deformation angle will gradually increase until the tip of the seal is riding on the free surface. Since the change in seal draft (Δd) is prescribed, i.e. the hinge is held fixed in place, the lift drops as K_δ is reduced due to a decrease in both the wetted length and effective angle of attack, as shown in Figs. 8.2 and 8.3. The measured stiffness of the SSBM bow seal in Heber (1977) ($K_\delta = 63.0\,\mathrm{N.m/deg}$) is also shown in Fig. 8.2, and it is observed that it corresponds to the location where the effects of flexibility have just begun to be important. This effect is likely the reason that the rigid-seal approximation provided reasonably good results in Chapter 7.

8.1.2 Fixed-Lift Case

The fixed-lift case requires the lift to be constant in accordance with the rigid body equations of motion. For this case, the body displacement is assumed to be $\Delta = 4.1\,\mathrm{kg}\,(9.0\,\mathrm{lb})$, which is close to the measured lift of the bow seal that was shown in Fig. 7.1. This case is more similar to the true operating conditions of the model-scale seals, at least in the context of the complete-SES simulations presented in the previous chapter. The results for this case are shown in Fig. 8.4 and the seal shapes are shown in Fig. 8.5 for varying K_δ. As

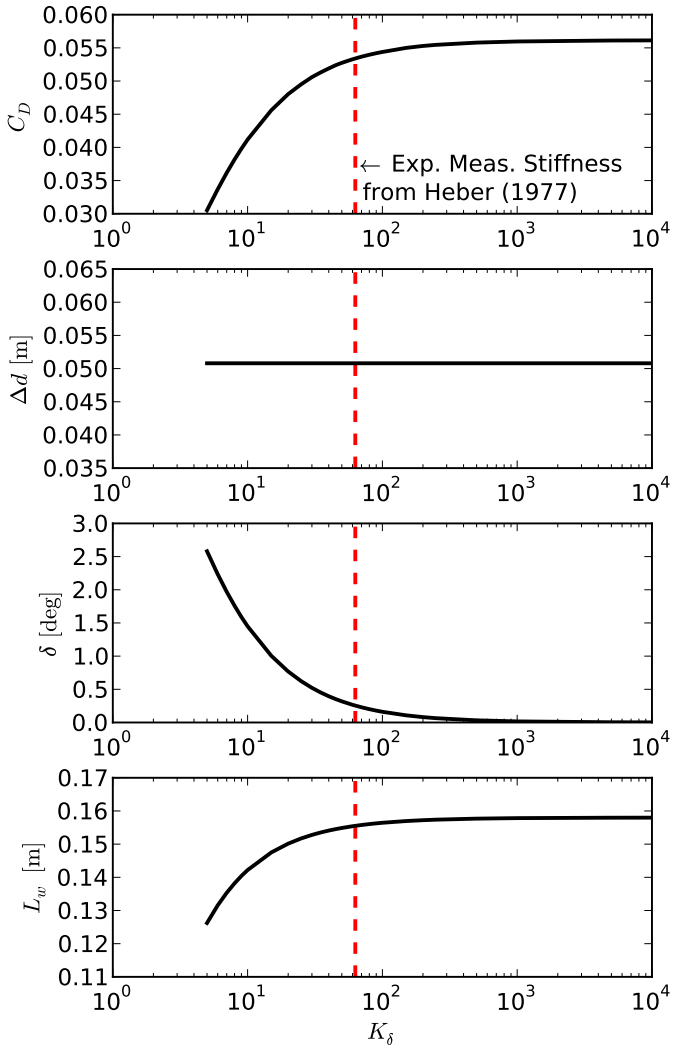

Figure 8.2: Results for a single (bow) seal at $Fr_C = 0.4$ and prescribed draft of $\Delta d = 5.08\,\mathrm{cm}\,(2.0\,\mathrm{in})$. The effects of seal flexibility are apparent at low K_δ and the results asymptote to the rigid case as $K_\delta \to \infty$.

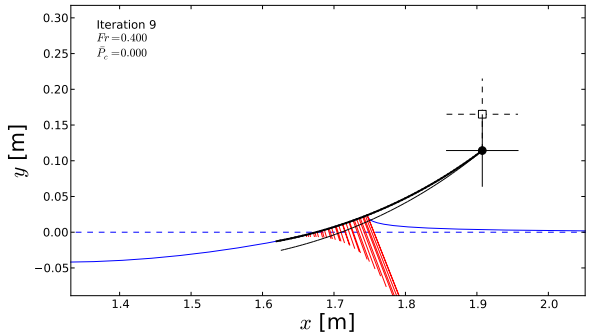

(a) $K_\delta = 5\,\mathrm{N.m/deg}$

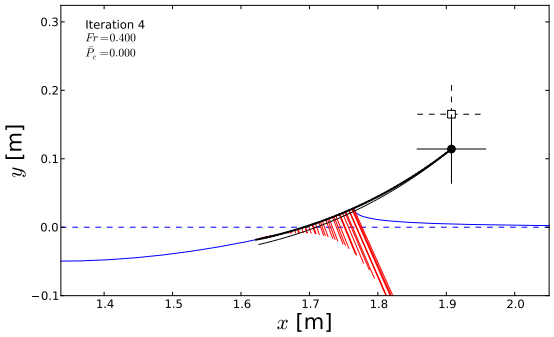

(b) $K_\delta = 10\,\mathrm{N.m/deg}$

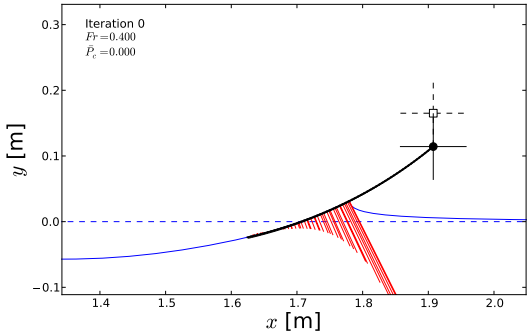

(c) $K_\delta = 50\,\mathrm{N.m/deg}$

Figure 8.3: Equilibrium solutions for a single (bow) seal at $Fr_C = 0.4$ and prescribed draft of $\Delta d = 5.08\,\mathrm{cm}\,(2.0\,\mathrm{in})$. The deformed and undeformed seal shapes are shown as a thick and thin solid black lines, respectively. The deformed and undeformed free-surface profiles are shown as solid and dashed blue lines, respectively. The hydrodynamic pressure profiles are illustrated as red lines. The reference center of rotation is shown as a dashed set of axes, while the final center of rotation is shown as a solid set of axes. The initial and final center of gravity are shown as a white squares and black circles, respectively.

the results show, the seal is found to exhibit a fairly-constant drag over the tested range of stiffnesses. This is due to the fact that the lift remains constant over the range of stiffnesses. As the stiffness decreases, the deformation angle gradually increases (decreasing the effective angle of attack), which decreases the lift coefficient. In order to compensate for the loss of lift due to the reduced effective angle of attack, the draft must be increased. The change in drag throughout this process is relatively minor until the effective seal stiffness is decreased below a certain threshold ($K_\delta \approx 50\,\mathrm{N.m/deg}$). At this point, the increase in draft required to maintain the required lift leads to a dramatic increase in wetted length and the drag is seen to increase, albeit only slightly. Hence, the trends are opposite in the low-stiffness regime for the wetted length and drag for the prescribed-draft (Fig. 8.2) and fixed-lift (Fig. 8.4) cases.

Along with the results of the single-seal fixed-lift simulation, the stiffness of the SSBM bow seal that was actually used in the segmented model tests (Heber, 1977) is shown. Based on the results of this single-seal simulation, it can be seen that the stiffness of the experimental seal was relatively large, being higher than the range in which the stiffness of the seal becomes important. This likely explains why the rigid seal approximation used in the previous chapter was able to deliver fairly accurate results for the seal contribution to the total resistance.

8.2 Effects of Stern Seal Flexibility for a Complete SES

In performing the simulations for the SES with rigid seals, it was determined that the secondary drag hump was primarily caused by the bow seal wave impacting the stern seal. The bow seal tended to skim on top of the free surface at a low level of immersion for the majority of the speed range while the stern seal behavior was much less consistent, owing to the fact that the bow-seal wave crest location moved fore or aft as a function of the Froude number based on the cushion length. The shape of the bow seal surface, the height of the

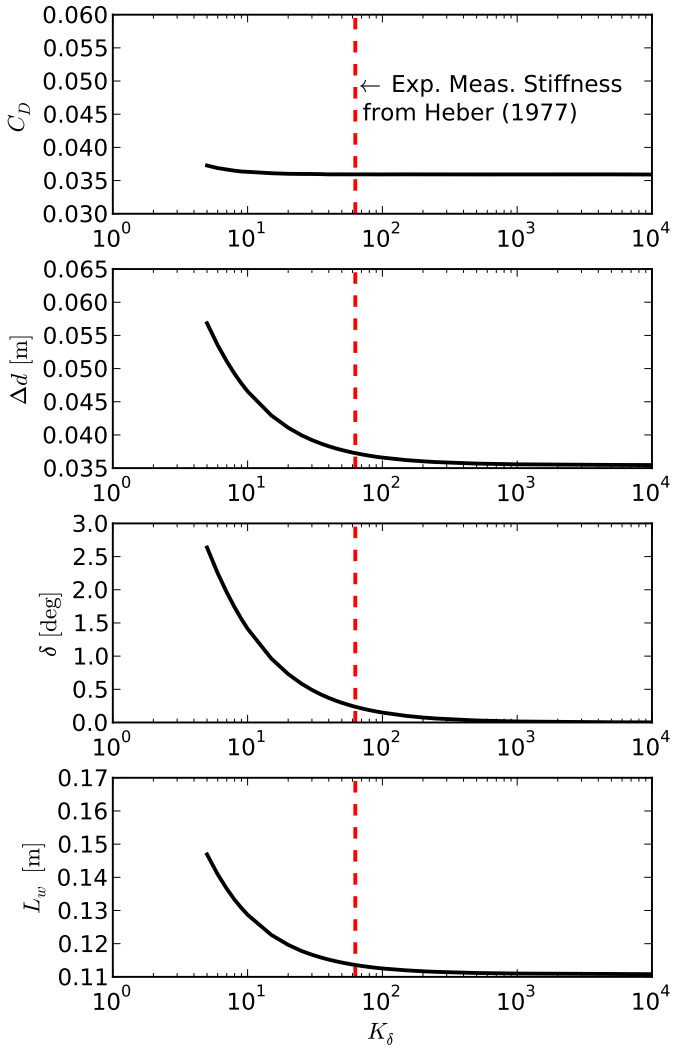

Figure 8.4: Results for a single (bow) seal at $Fr_C = 0.4$ in a fixed-lift condition with an assumed displacement of $\Delta = 4.1\,\mathrm{kg}\,(9.0\,\mathrm{lb})$. The effects of seal flexibility are apparent at low K_δ and the results asymptote to the rigid case as $K_\delta \to \infty$.

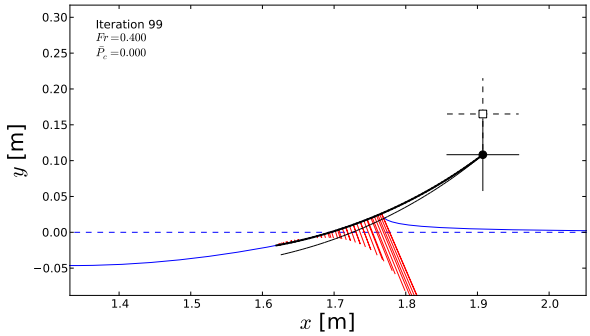

(a) $K_\delta = 5\,\mathrm{N.m/deg}$

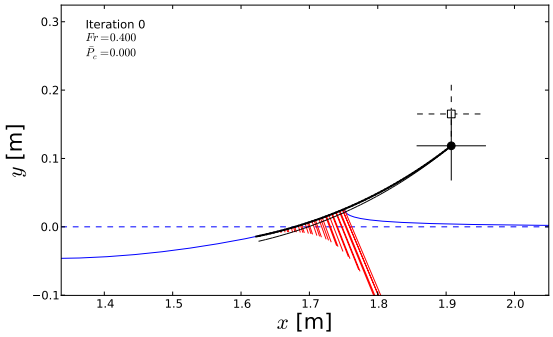

(b) $K_\delta = 10\,\mathrm{N.m/deg}$

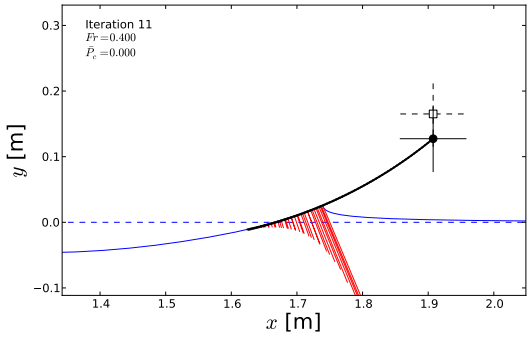

(c) $K_\delta = 50\,\mathrm{N.m/deg}$

Figure 8.5: Equilibrium solutions for a single (bow) seal at $Fr_C = 0.4$ in a fixed-lift condition with an assumed displacement of $\Delta = 4.1\,\mathrm{kg}\,(9.0\,\mathrm{lb})$. The deformed and undeformed seal shapes are shown as a thick and thin solid black lines, respectively. The deformed and undeformed free-surface profiles are shown as solid and dashed blue lines, respectively. The hydrodynamic pressure profiles are illustrated as red lines. The reference center of rotation is shown as a dashed set of axes, while the final center of rotation is shown as a solid set of axes. The initial and final center of gravity are shown as a white squares and black circles, respectively.

bow seal trailing edge above the keel, and the lift percentage provided by the bow seal were all observed have a large impact on the characteristics of the bow seal wave, which in turn affects the stern seal. However, since the bow seal is subject to a calm free-surface inflow, the effects of Froude number for the bow seal are observed to be less important than for the stern seal. Since the behavior of the stern seal was found to be more interesting, the segmented SES was simulated with a flexible stern seal. The goal is to eventually be able to consider both flexible bow and stern seals simultaneously. However, the very low levels of immersion by the bow seal leads to numerical issues which must be resolved first.

The stiffness of the stern seal was varied to three different values, one of them being the stiffness of the stern seal tested by Heber (1977) ($K_\delta = 535.8\,\mathrm{N.m/deg}$). The other two values ($K_\delta = 5.0$ and $10.0\,\mathrm{N.m/deg}$) were chosen to yield results that were expected to be much more highly-deformed. Due to the numerical difficulties inherent in performing simulations at high Froude numbers where the seals are very lightly-immersed, the simulations were only run for a Froude number range of $Fr_C = 0.35 - 0.45$ to examine the stiffness effects near the secondary drag hump. It is expected that at higher speeds ($Fr_C > 0.45$), the seal effects will become very small and eventually negligible. For all cases, the total seal-provided lift was assumed to be equal to the measured values, which were shown in Fig. 7.1.

Within this section, two sets of simulations will be presented. In the first case, 2-DoF body motion is allowed and the total seal-provided lift is assumed to be fixed to the appropriate value from Fig. 7.1 at each speed (as in Chapter 7). In the second case, the body motion is prescribed at the equilibrium draft and trim for the rigid-seal case that was shown in Chapter 7. The reason for performing both sets of simulations will be made clear in following sections.

8.2.1 Simulations with 2-DoF Motion

In this section, the results will be presented with both the heave and trim degrees of freedom. This case corresponds roughly to the fixed-lift case for the single-seal simulations presented in Section 8.1.2. The results for the four different stern seal stiffnesses are shown in Fig. 8.6, where results from the traditional method for total resistance prediction ($R_{T,\mathrm{trad}}$) are also shown. In a similar manner to the single-seal results, the drag ($R_{T,\mathrm{curr}}$) is found to vary by very little as the stiffness is varied. Since the lift must be the same for all the cases, the lift-to-drag ratio of the seal is relatively unchanged with varying stiffness. Therefore, since the lift is assumed not to be a function of the stiffness, the drag also remains mostly constant. The flexibility of the stern seal does influence the equilibrium position of the vessel though. As the stiffness decreases, the seal will deform more, leading to a decrease in the effective angle of attack. Thus, in order to maintain the required lift for the rigid-body equilibrium, the stern of the vessel must become more immersed. The bow of the vessel, however, remains relatively in the same position. This corresponds to an increase in both the draft and the trim as the stiffness is decreased. The wave profiles for $K_\delta = 5\,\mathrm{N.m/deg}$ and $535.8\,\mathrm{N.m/deg}$ are shown in Figs. 8.7 and 8.8, respectively, along with the undeformed and deformed seal shapes. The results for the lower stiffness are seen to exhibit a visually-identifiable amount of deformation, while the higher stiffness barely exhibits any. The results for the experimentally-tested stiffness are found to be very similar to the rigid-seal results.

8.2.2 Simulations with Prescribed Draft and Trim Based on Rigid Seal Simulations

Although the results of the previous section suggest that the stiffness of the stern seal does not have a large effect on the secondary hump drag of the vessel, this may not necessarily be the case. It was observed that the flexibility of the stern seal had an impact on the trim and

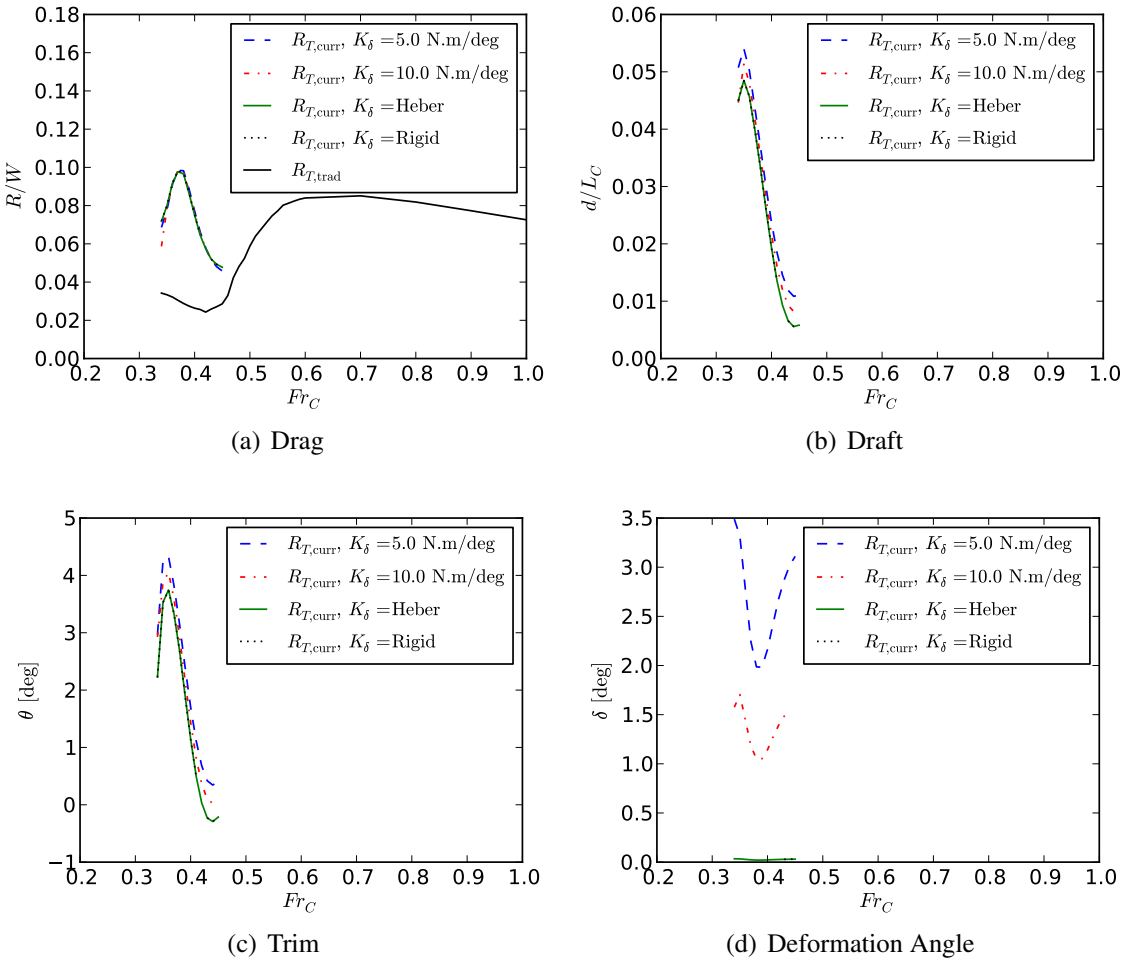

(a) Drag

(b) Draft

(c) Trim

(d) Deformation Angle

Figure 8.6: Results for flexible stern seal simulations for varying stern seal torsional stiffness with 2-DoF motion

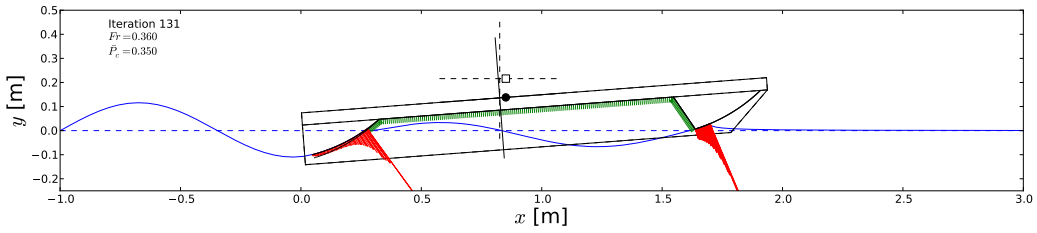

(a) $Fr_C = 0.36$

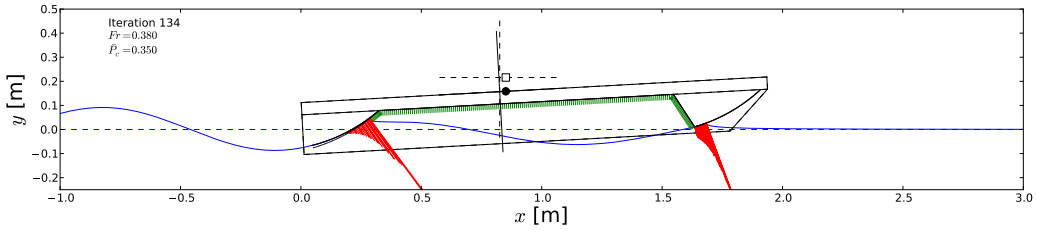

(b) $Fr_C = 0.38$

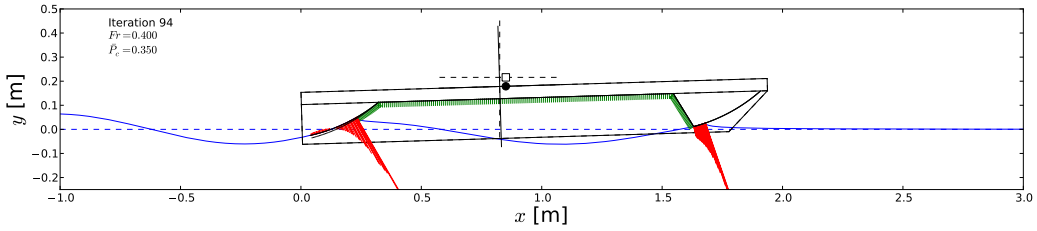

(c) $Fr_C = 0.4$

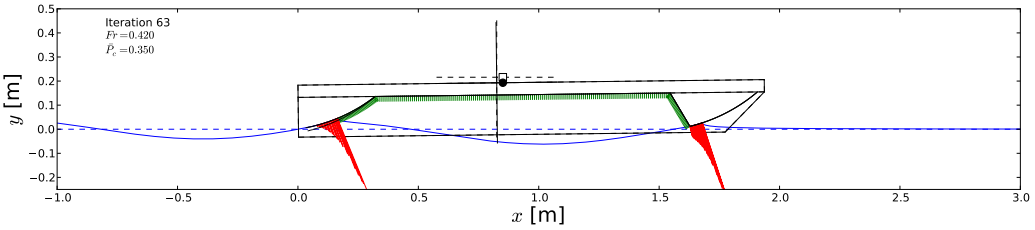

(d) $Fr_C = 0.42$

Figure 8.7: Equilibrium solutions for flexible stern seal simulations with 2-DoF motion for a range of Froude numbers with $K_\delta = 5.0\,\mathrm{N.m/deg}$, $h_{SF} = h_{SA} = 0.0\,\mathrm{cm}\,(0.0\,\mathrm{in})$ showing the passing of the bow seal wave aft as Froude number increases. The deformed and undeformed seal surfaces are shown as black curves. The deformed and undeformed free-surface profiles are shown as solid and dashed blue lines, respectively. The hydrodynamic pressure profiles are illustrated as red lines and the cushion pressure is shown as green lines. The initial center of rotation is shown as a dashed set of axes, while the final center of rotation is shown as a solid set of axes. The initial and final center of gravity are shown as a white square and black circle, respectively.

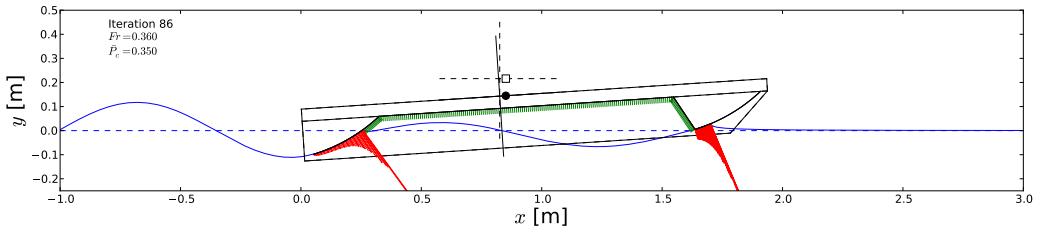

(a) $Fr_C = 0.36$

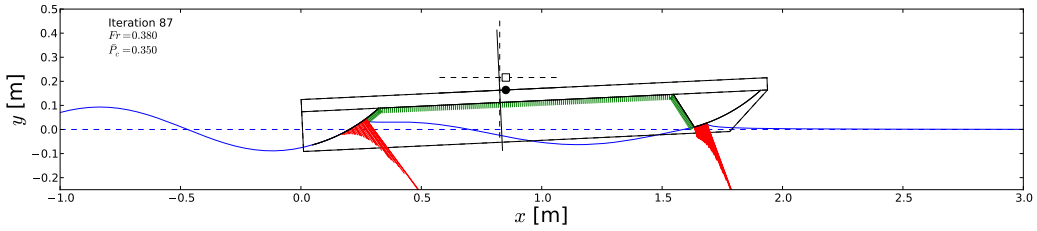

(b) $Fr_C = 0.38$

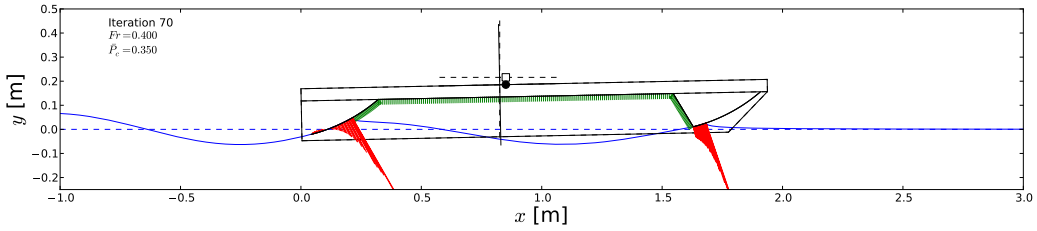

(c) $Fr_C = 0.4$

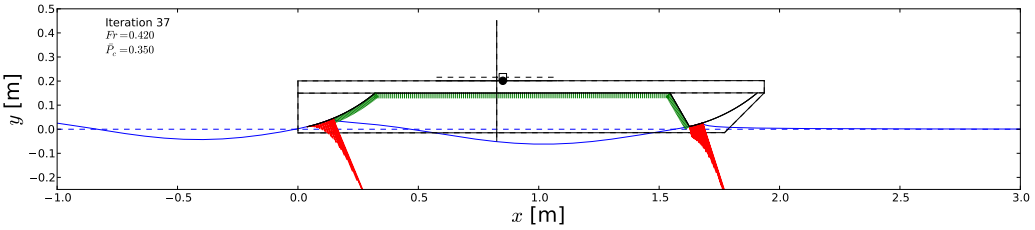

(d) $Fr_C = 0.42$

Figure 8.8: Equilibrium solutions for flexible stern seal simulations with 2-DoF motion for a range of Froude numbers with $K_\delta = 535.8\,\mathrm{N.m/deg}$, $h_{SF} = h_{SA} = 0.0\,\mathrm{cm}\,(0.0\,\mathrm{in})$ showing the passing of the bow seal wave aft as Froude number increases. The deformed and undeformed seal surfaces are shown as black curves. The deformed and undeformed free-surface profiles are shown as solid and dashed blue lines, respectively. The hydrodynamic pressure profiles are illustrated as red lines and the cushion pressure is shown as green lines. The initial center of rotation is shown as a dashed set of axes, while the final center of rotation is shown as a solid set of axes. The initial and final center of gravity are shown as a white square and black circle, respectively.

draft of the vessel. For the case of a 2-D SES with a constant applied cushion pressure, the results of the previous section are true. However, in practice, for a "real" SES, the effects of the sidehulls as well as the characteristics of the lift-fan system and possible leakage effects must be integrated and considered for a more accurate prediction. Unfortunately, these effects are not currently considered in the numerical model. The trends can, however, be investigated by performing fixed-body simulations with a flexible stern seal, where the draft and trim are prescribed to be equivalent to the equilibrium draft and trim of the rigid-seal simulations. These effects will now be demonstrated.

Consider the introduction of stern-seal flexibility, as compared to a completely rigid stern seal. When the seal begins to deform, the effective angle of attack will decrease, leading to a decrease in the lift provided by the stern seal (see, e.g. Fig. 8.3). Consequently, the vessel will no longer be in equilibrium. In the case of the simulations with 2-DoF motion, equilibrium is maintained by increasing the effective submergence of the stern seal, which in turn leads to an increase in trim and draft.

In more "real-life" situations, however, the lift contribution by the seals should be small compared to the cushion pressure and restoring force of the sidehulls. In addition, the lift reduction exhibited by the stern seal may be made-up-for by other sources, e.g. increasing cushion or seal pressure. It is useful, therefore, to consider the limiting case where all of the lift lost due to deformation of the stern seal is taken up by other sources without changes in trim or draft. Although this case is not fully-realistic, it may still offer beneficial insight into the flexibility effects for a more realistic vessel.

The simulations were run for a prescribed draft and trim at the equilibrium position of the rigid-seal simulations. The stiffness of the stern seal was varied in the same manner as in the previous section. The results are shown in Fig. 8.9. As shown in Figs. 8.9(b) and 8.9(c), the draft and trim of the vessel are unchanged compared to the rigid-seal results since the draft and trim are prescribed. The rigid body motion is not solved, and hence the body is not in equilibrium (i.e. Eqs. (4.6) and (4.7) are not satisfied) for the flexible-

seal cases. In contrast to the results shown in Fig. 8.6(a), the subhump resistance is seen to decrease as the stiffness of the stern seal is reduced for the simulations based on the rigid-seal draft and trim motions, i.e. when the flexible seal deformation is assumed to have negligible impact on the vessel motion, as shown in Fig. 8.9(a). The wave profiles for $K_\delta = 5\,\mathrm{N.m/deg}$ and $535.8\,\mathrm{N.m/deg}$ are shown in Figs. 8.10 and 8.11, respectively, along with the undeformed and deformed seal shapes. The results for the lower stiffness are seen to exhibit a visually-identifiable amount of deformation, while the higher stiffness barely exhibits any. The results for the experimentally-tested stiffness are found to be very similar to the rigid-seal results.

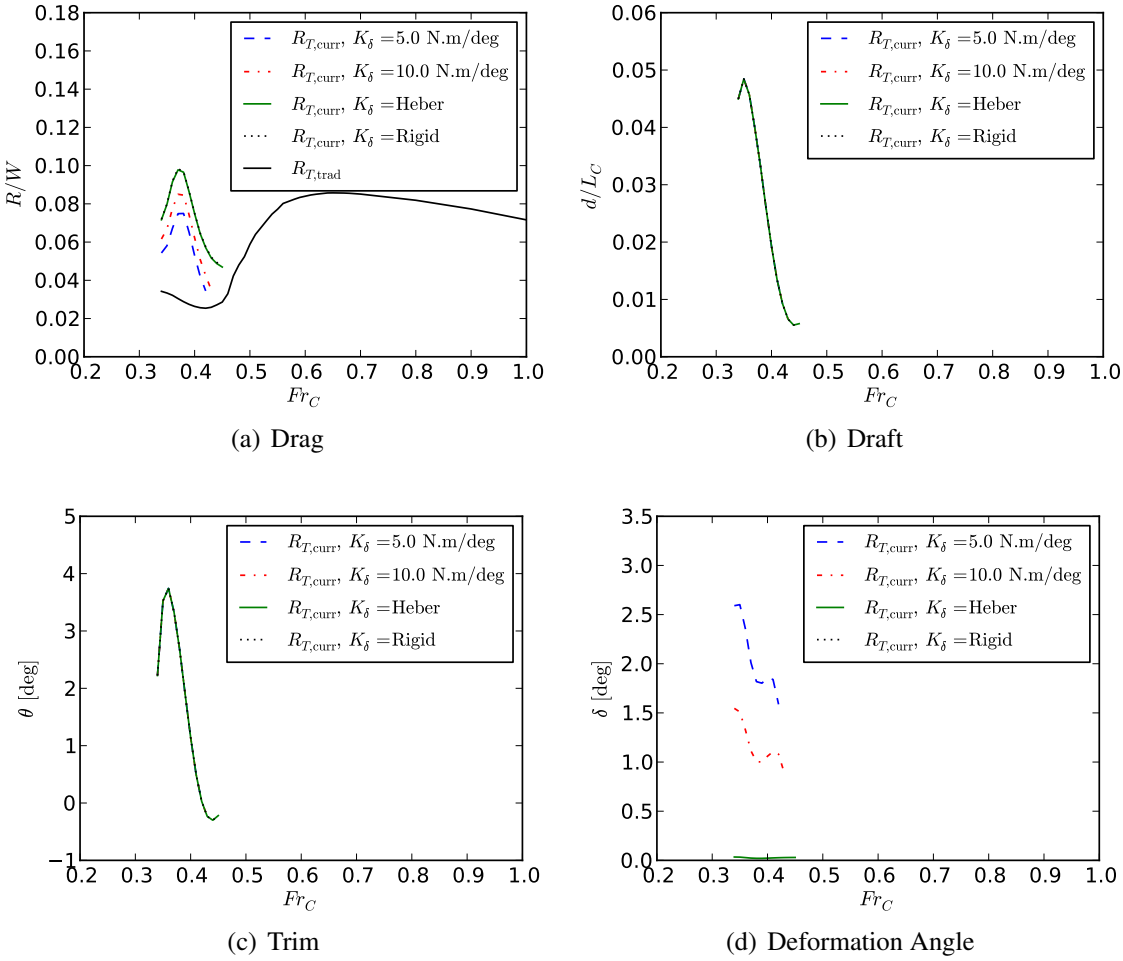

(a) Drag (b) Draft

(c) Trim (d) Deformation Angle

Figure 8.9: Results for flexible stern seal simulations for varying stern seal torsional stiffness with prescribed vessel motion at the rigid-seal equilibrium draft and trim

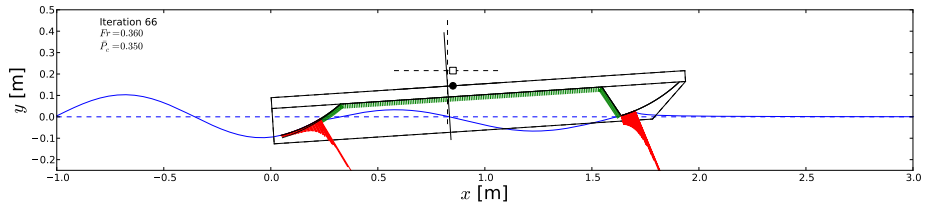

(a) $Fr_C = 0.36$

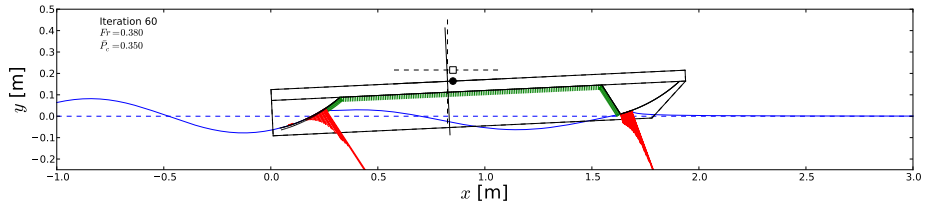

(b) $Fr_C = 0.38$

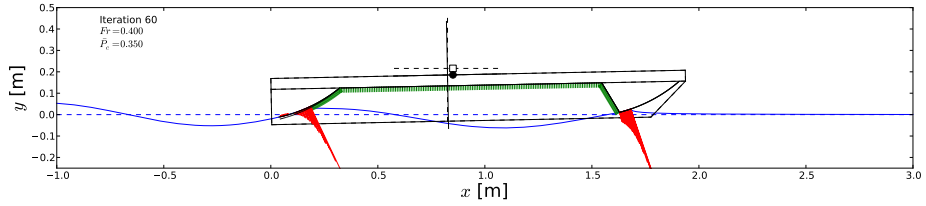

(c) $Fr_C = 0.4$

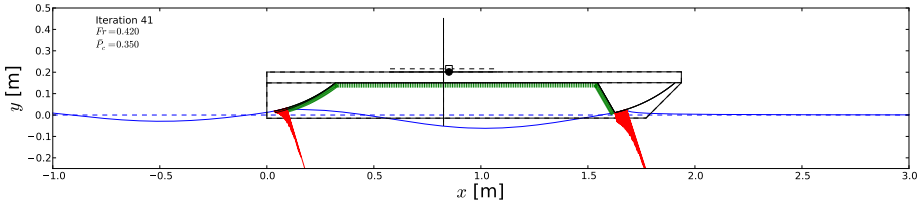

(d) $Fr_C = 0.42$

Figure 8.10: Equilibrium solutions for flexible stern seal simulations with prescribed vessel motion at the rigid-seal equilibrium draft and trim for a range of Froude numbers with $K_\delta = 5.0\,\mathrm{N.m/deg}$, $h_{SF} = h_{SA} = 0.0\,\mathrm{cm}\,(0.0\,\mathrm{in})$ showing the passing of the bow seal wave aft as Froude number increases. The deformed and undeformed seal surfaces are shown as black curves. The deformed and undeformed free-surface profiles are shown as solid and dashed blue lines, respectively. The hydrodynamic pressure profiles are illustrated as red lines and the cushion pressure is shown as green lines. The initial center of rotation is shown as a dashed set of axes, while the final center of rotation is shown as a solid set of axes. The initial and final center of gravity are shown as a white square and black circle, respectively.

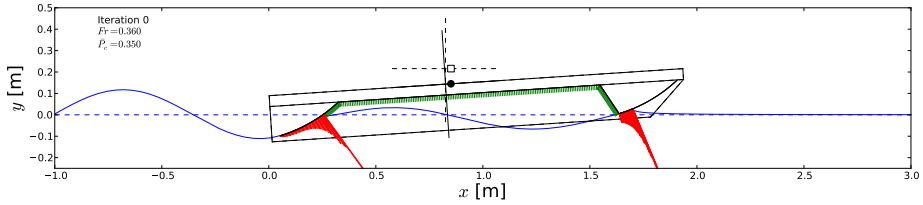

(a) $Fr_C = 0.36$

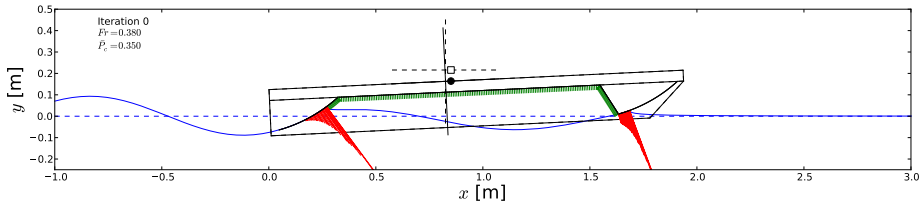

(b) $Fr_C = 0.38$

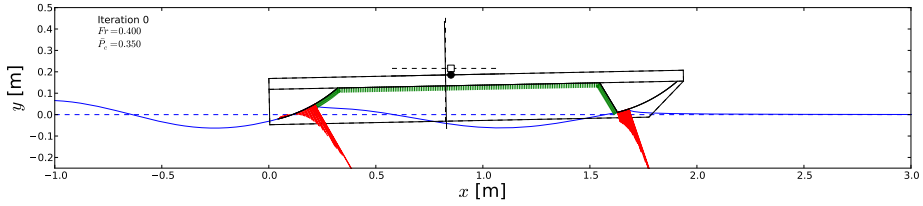

(c) $Fr_C = 0.4$

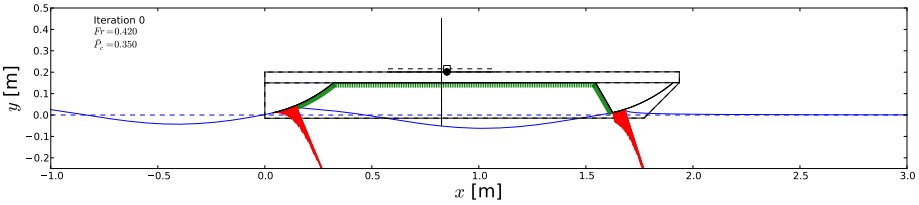

(d) $Fr_C = 0.42$

Figure 8.11: Equilibrium solutions for flexible stern seal simulations with prescribed vessel motion at the rigid-seal equilibrium draft and trim for a range of Froude numbers with $K_\delta = 535.8\,\mathrm{N.m/deg}$, $h_{SF} = h_{SA} = 0.0\,\mathrm{cm}\,(0.0\,\mathrm{in})$ showing the passing of the bow seal wave aft as Froude number increases. The deformed and undeformed seal surfaces are shown as black curves. The deformed and undeformed free-surface profiles are shown as solid and dashed blue lines, respectively. The hydrodynamic pressure profiles are illustrated as red lines and the cushion pressure is shown as green lines. The initial center of rotation is shown as a dashed set of axes, while the final center of rotation is shown as a solid set of axes. The initial and final center of gravity are shown as a white square and black circle, respectively.

8.3 Relationship Between Seal Flexibility and Seal Height

Physically-speaking, these results highlight an important experimental trend that is not captured when performing the free-body simulations for a 2-D SES with an assumed constant cushion pressure.

Due to the nature of the hinged-seal model, the deformation angle is directly related to the height of the seal tip above the keel. In essence, as the deformation angle increases, so does the height of the seal trailing edge. Although both the segmented model (Heber, 1977) and the XR-1B model (Van Dyck, 1972) had nearly-identical stern seals, which were both relatively stiff, they also both considered the effects of seal height on the total resistance. These results are reproduced in Figs. 8.12 and 8.13.

In both of these tests, it was observed that the magnitude of the secondary drag hump ($Fr_C = 0.45$ and $Fr_C = 0.4$ for the XR-1B and segmented SES model, respectively) was observed to decrease as the seal height increased (see e.g. Fig. 8.12 for the XR-1B and Fig. 8.13 for the segmented SES model). Additionally, the draft was observed to increase as the seal height was increased in both cases. The effects of the trim were opposite for both cases, where the XR-1B was found to exhibit a decrease in the trim and the segmented SES models was found to exhibit an increase in trim as the seal heights were increased. The effects of the seal height on trim in particular are anticipated to be highly affected by the effects of the pressure cushion and the sidewalls, which were different for the two experimental studies.

The numerical results for the total resistance from the previous section (with prescribed motion) showed that the total resistance at the secondary drag hump decreased as the seal stiffness decreased, which corresponds to a larger deformation angle and hence a higher seal height. This effect is in accordance with both experimental studies, although in the experiments, the seal height was adjusted manually through the use of downstops. In addition, for the fixed-lift case, the numerical model predicted an increase in both draft and trim as the seal stiffness was reduced. In this case, the more flexible seals operate at a higher

seal height above the keel, which causes the stern of the vessel to ride lower, leading to an increase in both the draft and the trim. This trend is also apparent from the segmented SES model results, shown in Figs. 8.13(b) and 8.13(c).

In order to accurately predict the effects of the seals on the resistance and motions, the impact of the sidehulls and the pressure cushion on the resistance and vessel motions must be more accurately modeled. The effects of the sidehulls are expected to be important for the case of the XR-1B (Fig. 8.12) in particular, since the model contained sidehulls that provided roughly 20% of the lift. For the XR-1B study, the secondary drag hump becomes a hollow for the larger seal heights. It is likely that, in these cases, the loss in lift from the stern seal is taken up by the sidehulls or the lift fan system and thus the stern seal is no longer wetted. Instead, a drag hump is observed at a lower $Fr_C = 0.3$, which is more consistent with the drag hump predicted for a pressure patch without seals, as in Doctors and Sharma (1972).

8.4 Applications for Different Seal Types

The results presented in this chapter were associated with the effects of seal flexibility for a stiffened membrane stern seal. Due to the rigidity of the planing face and the high seal pressure of this stern seal, the seal was found to behave generally as a rotating rigid member connected to the vessel via a hinged attachment. While these types of stern seals were used early on in the development of SESs, more recent designs have favored inflated membrane seals constructed of two or more lobes, as shown in Fig. 8.14. These seals are designed such that there is a small leakage gap beneath the seal and are typically constructed of very flexible membrane materials. Due to the flexible nature of the membrane materials, seals of this type are likely unable to support the amount of lift provided by the stiffened stern seal used for the segmented SES model test. For these seals, the localized bending and membrane stretching deformations are not negligible and large deformation membrane

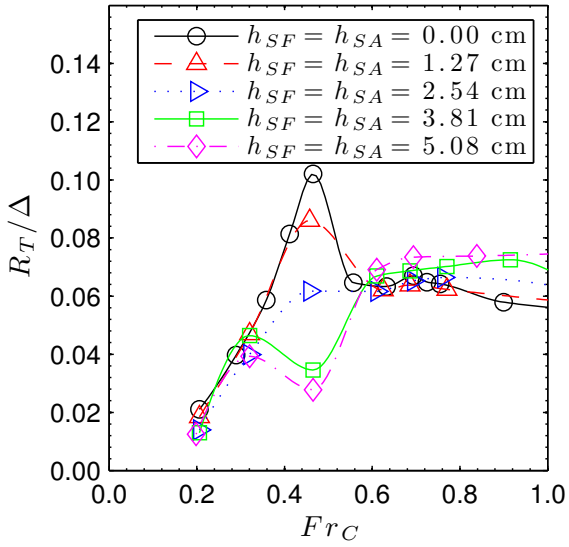

(a) Total Resistance

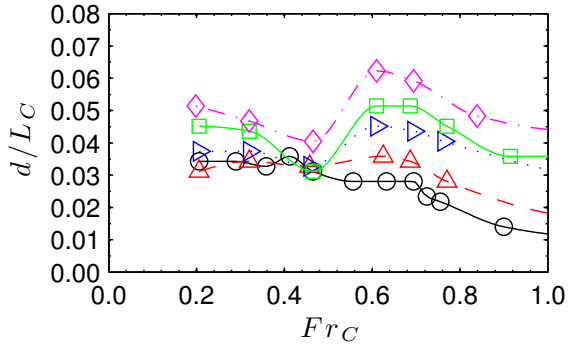

(b) Draft

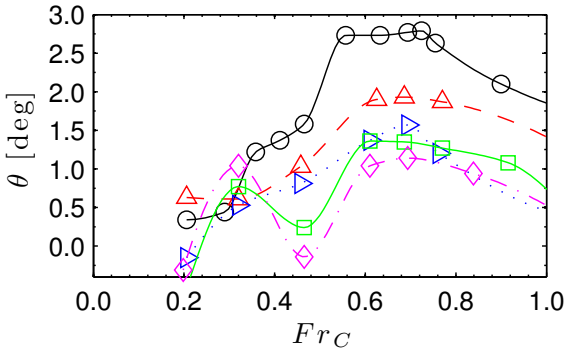

(c) Trim

Figure 8.12: Effect of seal height on response for US Navy XR-1B (from Van Dyck, 1972)

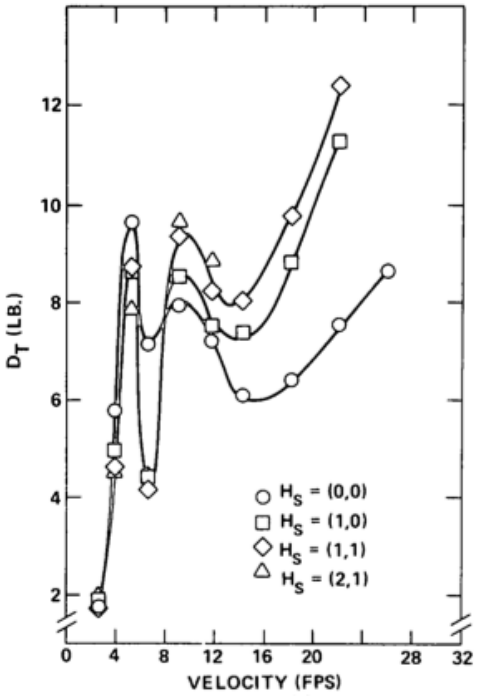

(a) Segmented Model

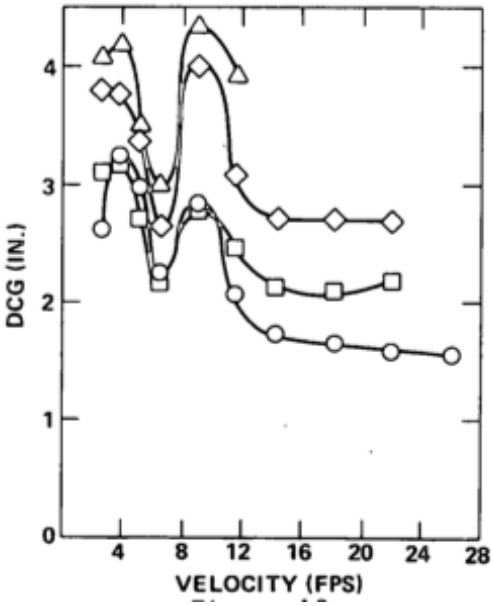

(b) Segmented Model

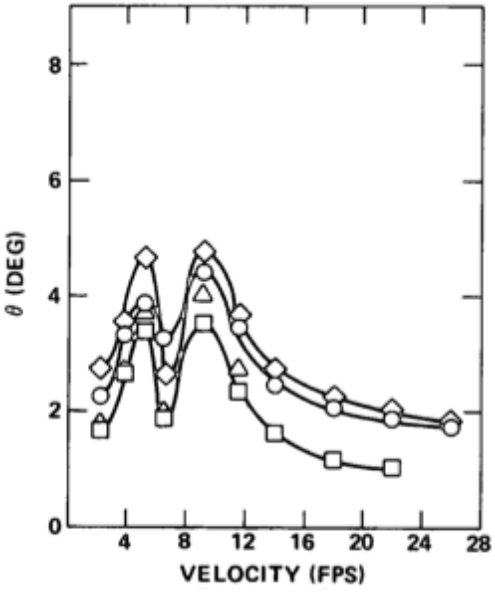

(c) Segmented Model

Figure 8.13: Effect of seal height on response segmented model tests (from Heber, 1977)

structural models must be used. Consequently, it is likely that for full-scale SESs with lobed membrane seals, the contribution of the stern seals to the total drag at the subhump will likely be lower than for the stiffened membrane seal. The relative locations of the wave crests will likely not change much, however, since the wavelength follows Froude scaling. As such, consideration for the interaction of the bow and stern seal waves may still be important for more modern, full-scale SESs, particularly at low Froude number regimes. However, further analysis is required to quantify these effects.

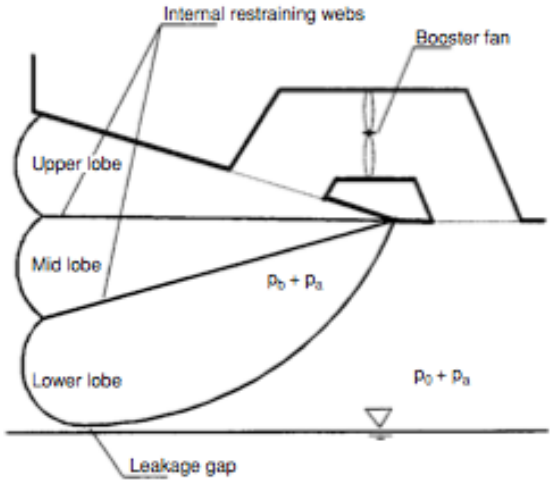

Figure 8.14: Example of a three-lobed SES stern seal (from Faltinsen, 2005)

The results from the segmented SES model test identified the large impact of the stern seal on the resistance at the subhump. The contributions of the bow seal to the total resistance were observed to be fairly small over the range of speeds, since the bow seal is designed to skim on top of the free surface with as little drag as possible. Consequently, the bow seal drag is typically small, especially for more modern finger-type bow seals which are designed to be very flexible and to conform to the free surface as well as possible. Instead, the effects of the seals on the total resistance are likely most important when considering the interaction of the bow seal wave with the stern seal in the low Froude number regime.

8.5 Summary

In this chapter, the effects of seal flexibility were explored for both the single-seal case as well as for the case of an SES with flexible stern seal. For both of these configurations, simulations were performed for both fixed-lift and prescribed-motion cases. The effects of body motion were found to be important for the characteristics of the response due to an inherent difference between the fixed-lift and prescribed-motion cases. It is anticipated that, for the problem of real SES seals, the seals will operate in a case somewhere between the two limiting cases due to the effects of the pressure cushion, restoring forces of the sidehulls, and possible venting beneath the cushion and/or the seals. For all cases, the torsional spring stiffness of the seal was varied and the effects were compared.

For the single-seal simulations, it was found that the trends in the resistance characteristics were opposite for the fixed-lift and prescribed-draft cases. The fixed-lift cases were found to predict a fairly constant drag as the seal stiffness was varied. This was due to the fact that, for any reduction in lift coefficient due to angular deformation, a corresponding increase in draft had to be made to satisfy the equilibrium condition such that the weight equals the lift. For the prescribed-draft case, the seal was allowed to deform freely, and the drag was found to be reduced as the stiffness of the seal was reduced.

A similar trend was observed for the case of a complete SES with flexible stern seal. For the case of the 2-DoF motion simulations, the total resistance was found to vary very little as a function of the seal stiffness due to the lift being required by the rigid body equilibrium conditions to be relatively constant for each simulated speed. As the seal stiffness was reduced, the stern of the vessel was found to ride at a lower level of immersion to account for the loss in lift coefficient due to a decrease in the effective angle of attack of the flexible stern seal. The corresponding reduction in lift coefficient was made up for by increasing the trim and the draft, which in turn led to higher drag. For the cases where the draft and trim were prescribed to be equal to the draft and trim of the rigid-seal simulations, the resistance of the vessel was found to decrease as the seal stiffness decreased, since the seals would

more easily “give way” to the incoming wave.

For fully-physical cases with sidehulls that support a fairly large percentage of the weight, such as for the US Navy XR-1B, the response is likely a combination of the free-motion case and the prescribed motion case, since the losses in lift provided by the stern seal may be taken up by additional sources, such as the pressure cushion, the sidehulls, or changes in flow rate to the fans. In order to more accurately predict the effects of the sidehulls, the numerical model must be expanded to include these the effects of sidehull lift as well as an appropriate air-cushion model that can consider changes in the pressure in the cushion to account for possible ventilation due to vessel motions, and to account for the fan control system.

CHAPTER 9

Conclusions

In this thesis, the problem of calm-water resistance prediction for Surface Effect Ships (SESs) was studied with consideration for interactions between the bow and stern seals, pressure cushion, free-surface waves, and vessel motions. Although the bow and stern seal drag have been experimentally-observed to be dominant in some cases in the low-speed regime, existing methods for SES resistance prediction have been unable to accurately predict these effects. The accurate prediction of the total resistance in the low-speed regime was not of concern for past SESs where the design speed was in the range of $80-100\,\mathrm{knots}$. However, the prediction of the total resistance in the low-speed regime is of particular importance for vessels intended to operate in a top speed range near $40 - 50\,\mathrm{knots}$ to ensure adequate propulsion power is installed to surpass the secondary and/or primary drag humps.

The primary objective of this work has been to study the effects of bow/stern seal wave interaction on SES total resistance and motions in steady-state operations. This objective was met by developing a simple, effective, Two-Dimensional (2-D) numerical model based on coupling a linearized potential-flow solver with a single-degree-of-freedom seal model and rigid body vessel motion model to predict the vessel performance for $Fr_C < 0.45$, and using a 3-D moving pressure patch model coupled with the rigid body vessel motion model to predict the vessel performance for $Fr_C > 0.45$. The numerical model was used to predict the resistance of a model-scale SES with both rigid and flexible seals to determine

the influence of seal flexibility. The predicted seal resistance and vessel motion, as well as surface wave patterns, were compared with published experimental measurements and observations.

The seal-wave-cushion model was found to offer accurate predictions for the low-speed ($Fr_C < 0.45$) total resistance of the segmented SES model of Heber (1977) by accounting for the interaction of the seals, pressure cushion, free-surface waves, and vessel motions. In this speed range, a drag subhump was found to occur at $Fr_C \approx 0.37$, due to the bow-seal wave impacting the stern seal. A more traditional method was also used and found to offer accurate predictions of the total resistance at higher speeds ($Fr_C > 0.45$) by accounting for the cushion wavemaking drag and sidewall drag only (i.e. no seal effects). By using a combination of the two methods, an accurate prediction of the total resistance was obtained over the entire range of operating speeds.

In this final chapter, the objectives of the work are reiterated, and the ways in which the results of this work address each objective are described. The main contributions of the work are then summarized, along with the major findings. Finally, several opportunities for future work are identified and recommended.

9.1 Objectives

The primary objective of this work was to develop an efficient and accurate numerical model for SES seal resistance prediction with consideration for the interaction of the bow and stern seals, pressure cushion, free-surface waves, vessel motions, and seal flexibility. Through the development of the numerical model, several research questions were addressed. These questions were first posed in Chapter 1, and they are repeated below along with the findings based on the results of this work. Further explanation of these findings will be given in Section 9.2.

1. How can the interaction between flexible seals, air cushion, free-surface waves, and

vessel motion be efficiently and effectively captured?

- It was found that the interaction between flexible seals, air cushion and waves can be efficiently and effectively captured by coupling a linearized potential-flow model with a rigid body vessel motion and hinged seal model. For the segmented SES model of Heber (1977), the effects of seal-seal interaction were found to be due to the bow-seal wave impacting the stern seal wave at the sub-hump ($Fr_C \approx 0.37$), leading to a large increase in the total resistance, as well as resulting in higher equilibrium draft and trim. At higher speeds ($Fr_C > 0.45$), this interaction is negligible since the bow-seal wave crest is aft of the stern seal and a more traditional approach for resistance prediction should be used, based on predicting the various resistance components without consideration for the seal drags.

2. How do the seals affect the total resistance (including the subhump and primary hump) and draft/trim for varying Froude number, cushion pressure, and seal pressure?

    - The seals were found to have a large effect on the total resistance, draft, and trim, primarily at the secondary drag hump due to interaction of the bow seal wave with the stern seal. Since the seal drag was found to be strongly dependent on the amount of lift provided by the seals, the influence of the seals on the total resistance is likely to decrease as the cushion pressure (and resulting cushion-provided lift) increases, which causes a decrease in seal-provided lift and drag. The effects of varying cushion pressure are expected to become more important once consideration for leakage, changing cushion pressure, and sidehull contributions are included into the model. For the stay-stiffened bag and membrane seals considered in this study, the effects of internal seal over-pressure were examined by varying the torsional spring stiffness using a hinged seal model.

The results showed that, at least for the case of stay-stiffened membrane bow and stern seals, the effects of seal over-pressure can be well-represented by using a hinged spring seal model. Based on the results of Chapter 8, the effects of torsional spring stiffness (i.e. seal over-pressure) on the vessel response are expected to be important, particularly in the subhump regime. At higher speeds ($Fr_C > 0.45$) the effects of seal pressure are anticipated to be smaller since the seal drag is negligible in this regime. The knowledge that the seal performance varies depending on the operating speeds suggests that actively-controlled contouring/morphing or varying-stiffness seals might be used to optimize the vessel performance over the entire range of operating speeds.

3. Does seal drag adequately explain the magnitude of the experimentally-observed secondary hump?

   - The seal drag was found to explain both the magnitude and the speed of the experimentally-observed secondary hump. This effect was primarily due to the bow seal wave impacting the stern seal at those speeds.

4. Can parametric/scaling relationships for the seal/cushion/wave interaction be derived for incorporation into high fidelity CFD models, as well as assist in the design and proper testing of SESs?

   - The results have identified the likely possibility of fairly-simple parametric/scaling relationships for seal/cushion/wave interaction effects; however, a more comprehensive model must be developed to account for varying cushion pressure, possible air leakage, and sidehull effects. The method is anticipated to be useful for predicting the response of an SES prior to performing CFD computations in order to predict the running draft, trim, and deformed seal shapes. By incorporating the results of the 2-D model into the CFD simulation as an initial condition, it may be possible to minimize the number of manual iterations

necessary to find the appropriate seal height, thus enabling improvements in computational speed.

5. Can actively-controlled seals be used to improve performance by minimizing resistance over a range of operating speeds?

    - The results of the simulations for the response of the segmented SES model identified strong interaction effects for the bow/stern seal system. In addition, the results of the flexible seal computations for the total resistance with prescribed trim and draft showed that the resistance characteristics at the subhump can change as the flexibility of the seals is changed. A similar, related trend was observed for experimental studies for both the segmented SES model and the XR-1B model by varying the seal downstop heights. It is therefore conceivable to design actively-controlled contouring/morphing seals in order to take advantage of this interaction to minimize the secondary hump resistance. By doing so, it may be possible to minimize the amount of required propulsion power, which can reduce the weight, increase top speeds, and improve the fuel efficiency.

9.2 Contributions and Major Findings

The primary contribution of this work is the development and validation of the numerical model, which is designed to be flexible in terms of architecture, being able to solve complex FSI problems for rigid or flexible structures subjected to 2-D planing flow. The fluid model is based on linearized potential-flow and has been adapted from past computational efforts for the planing plate problem (Doctors, 1974, 1977). Several major additions have been made, however, allowing for the considering of multiple planing surfaces, the inclusion of a known pressure cushion, and the incorporation if rigid body vessel motion and deformable seals. The fluid model was validated by considering the problems of a 2-D planing plate, a

2-D stepped planing plate, and a moving smoothed pressure distribution (for ACV and SES cushion modeling). The structural models were validated by comparing the Finite Element Method with analytical and experimental results of Ghavanloo and Daneshmand (2010) for an inflated membrane dam subject to internal hydrostatic pressure. The 1-DoF hinged seal model was validated by comparing with experimentally-measured static load tests of Heber (1977) for a segmented SES model with Stay-Stiffened Bag and Membrane bow and stern seals.

The numerical model allows for the simulation of complex FSI problems for free-surface flows with consideration for multiple planing surfaces, pressure cushions, free-surface wave interaction, rigid body motion, and localized deformation. Due to the simple and efficient nature of the method, it is beneficial in terms of computational cost compared to high-fidelity tools, especially considering the need to capture the free surface, vessel motion, and seal deformation with re-meshing and numerical stability issues. Hence, the tools developed in this work may be used for early-stage design, analysis, and optimization, where the computational cost of high-fidelity models is prohibitive, provided the assumptions of the model are valid.

Additionally, through the application of the numerical model to the problem of steady-state drag prediction for SESs, several contributions to the physical understanding of the problem have been made. First, it was determined that the interaction between the bow and stern seals (both rigid and flexible), air cushion, and free-surface waves may be efficiently and accurately captured using a computationally-efficient potential-flow-based model coupled with an appropriate structural model for $Fr_C < 0.45$. Previous prediction methods for SES drag have been unable to predict the seal drag in the subhump regime since they ignore seal-seal interaction effects. The prediction of resistance in the subhump regime is particularly important in order to ensure that the vessel has adequate installed propulsion to reach the designed top speeds. By including the effects of seal interaction in the current study, it was found that the seal contribution to the total drag can be predicted with reasonable

accuracy. For $Fr_C > 0.45$, traditional 3-D wave drag calculations of a moving pressure distribution coupled with frictional corrections for the sidewalls were found to be adequate because the contribution of the seals to the total resistance are negligible in this regime because they barely touch the free surface, and hence act to contain the cushion pressure only. The seals were found to have a large impact on the total resistance and vessel motion, particularly at the secondary drag hump and possibly at the primary hump (although it was not captured by the numerical model due to the the assumption that the pressure in the cushion is constant). This finding is in agreement with experimental observations (Heber, 1977; Van Dyck, 1972; Van Dyck and Fridsma, 1979), as well as observations by other authors (e.g. Yun and Bliault, 2000).

By careful investigation of the wave patterns, the physical cause of the secondary drag hump was identified as being related to the interaction of the bow-seal wave with the stern seal. Consequently, the stern seal was found to have a greater impact on the vessel performance at the subhump and hence warrants further study. Additionally, the effects of stern seal flexibility were investigated and the possibility for drag reduction at the subhump via actively-controlled morphing/contouring seals was identified. The seal drag contribution was found to be of primary importance at the subhump, with negligible effects at higher speeds ($Fr_C > 0.45$). A major contribution of this work is the better understanding of the root cause of the SES subhump resistance, particularly for very rigid seals, and to illustrate the importance of the interaction of the seals, pressure cushion, free-surface waves, and vessel motions on the total resistance. By understanding this cause, possible solutions may be envisioned.

The rigid-seal simulations showed that the secondary drag hump is primarily caused by the bow-seal wave impacting the stern seal. Additionally, coupling between the seal-generated wave profiles, vessel motions, and their relationship to the lift and drag was examined. These effect have been observed to be especially strong for stern seals with stiffened planing faces, such as those used for both the XR-1B model (Van Dyck, 1972)

and the segmented SES model of Heber (1977). Although more modern SESs tend to use inflated-membrane double- or triple-lobed stern seals, which cannot support the large loads supported by the planing sterns seals and will tend to deform out of the way instead (the results should approach cases of small torsional spring stiffness (K_δ) as shown in Chapter 8), the seal-seal interaction with the air cushion, free-surface waves, and vessel motion will still be present and must be considered. Based on the results of the XR-1B model test (Fig. 1.10), it was seen that the secondary drag hump can be avoided by raising the seals higher above the keels. The vessel draft and trim were also found to be affected by raising the seals, with an increase in the draft and decrease in the trim as the seals were raised. Although this will tend to lead to increased leakage, and hence an increase in required lift-fan power, it may be desirable to operate in this condition for a short amount of time while surpassing the secondary drag hump.

By identifying the stern seal as the primary cause of the secondary hump, it is possible to use this knowledge to minimize the resistance hump magnitude. This possibility corresponds directly to the statement of Heber (1977), which was reproduced at the beginning of Chapter 6. It is possible in principle, through use of the numerical model developed in this thesis, to design the bow/stern seal system with consideration for interaction effects to find a seal system that is more globally optimal, or to design actively- or passively-controlled morphing/contouring seals to control the seal geometry and deformation behavior, and the resultant vessel response. Since the contribution varies as a function of ship speed, it is likely that the optimal seal configuration will change with ship speed.

The major challenges encountered in the prediction of the SES response are related to the calculation of the coupled rigid body vessel motion with the deformable seal model and the hydrodynamic solver due to the low-immersion nature of the seals. Despite this challenge, the numerical method has been found to be successful in predicting the vessel response at the low-speed, subhump regime where the increase in seal resistance due to interaction of the seals, pressure cushion, free-surface waves, and vessel motions are ob-

served to be most important. Due to the flexibility of the architecture of the numerical model, it may be applied in the future to general problems where one or many rigid are flexible planing bodies are to be considered, including stepped planing hulls, flexible planing plates, pressure vessels subject to internal or external loading, etc. Additionally, by comparing the linearized potential-flow method with a CFD method for the planing plate problem, it was found that the potential-flow method is accurate for a large portion of the operational space (high-speed, low angle of attack). Based on this comparative study, it is now possible to apply the linearized potential-flow method with confidence for problems in the regime that it is applicable, which can lead to drastic savings in computational expense. The numerical method presented in this work may thus be used to obtain fast predictions for preliminary design studies, where expensive computations cannot be afforded or justified in the early design/analysis stage.

9.3 Future Work

As previously stated, one of the major contributions of this work has been to identify the root cause of the experimentally-observed subhump drag magnitude. Hence, it would be beneficial to investigate possibilities for drag reduction in the subhump and primary hump regimes by minimizing stern seal drag at certain speeds. This could conceivably be performed by using seals with actively-controlled stiffness, or by developing contouring/morphing seals. Other modifications to the operating conditions may also be used to optimize the resistance characteristics (e.g. changing the L_{CG}). In order to do so, a more systematic study of the effects of parametric variation on the vessel response must be performed. By doing so, a major design constraint may be bypassed, allowing for more fuel efficient oceanic transport at higher speeds in principle due to a minimization of the installed power (and weight).

Several additions to the numerical model might be beneficial in order to improve its

accuracy and applicability. First, a more physically-accurate cushion model that considers changes in cushion pressure and related compressibility effects due to leakage, changes in trim and draft, and 3-D wave effects should be developed. Additionally, a sidehull model must be developed in order to remove the need to assume that the seals provide a certain fixed percentage of the total lift. By incorporating a more accurate cushion pressure model and sidehull model, the effects of parametric variations in design variables such as the L_{CG}, displacement, cushion pressure, etc. can be studied. By doing so, the ability of the numerical method to capture these effects, which were experimentally studied for the segmented SES model of Heber (1977) (summarized in Appendix C), may be examined.

In this work, linearized potential-flow assumptions have been used for the hydrodynamic solver. Although the method was able to offer reasonable predictions for the response for the segmented SES model, it is important to quantify the influence of nonlinearity and wave breaking on the response. Hence, future studies should be performed to compare the linearized potential-flow method with fully-nonlinear CFD results, in a similar manner to the flat plate study shown in Section 3.3 and the work of Maki et al. (2012) for the moving 2-D pressure distribution. By doing so, the effects of nonlinearity and breaking waves may be investigated when the waves become steep.

The model may be extended to consider the unsteady hydrodynamic response to investigate dynamic effects, such as the flutter behavior of very flexible membrane or finger seals to prevent maintenance issues and dynamic buckling. Finite-depth effects may also be included for investigating the performance in shallow-water, littoral regions. By implementing compressibility and unsteady effects simultaneously, it might also be possible to investigate the problem of cobblestone oscillations. An additional, albeit large, extension would be to extend the model to 3-D in order to investigate 3-D wave effects within the cushioned space and its impact on the seals and vessel motion, as well as more realistic deformation behavior of SES seals.

Other possibilities for future work include applying the numerical method to the SES

problem for a wide array of parametric variations so that the characteristic seal response can be accurately included into numerical CFD simulations without the need to model the flexible behavior of the seals. This objective could be met by first simulating the vessel using the relatively simple 2-D method (compared to CFD) to predict the equilibrium seal shapes, draft, and trim. The vessel draft, trim, and seal shapes could then be used to generate the geometry of the CFD seals, as well as to provide an initial condition for the draft and trim of the vessel for the CFD computations. By using the simplified method before simulating the complete SES using CFD, a drastic improvement in the computational time might be attained, since the fully-coupled FSI problem would not need to be solved by the CFD solver and costly re-meshing and fluid-solid iterations might be avoided when manually adjusting the seal height. In order to do so, however, some numerical issues must be dealt with regarding the low-immersion behavior of the seals, which causes instability in the fluid solver for high speeds and low drafts.

The results of this work may be used to examine the scaling effects for SESs with flexible bow and stern seals by performing a more expansive set of simulations for a range of parametric variations, such as changes in cushion pressure (P_C), seal pressure (P_s), vessel displacement (Δ), Longitudinal center of gravity (L_{CG}), etc., as well as changes in seal geometry. By doing so, it may become easier to choose the optimal design parameters for new vessel designs.

Due to the flexible nature of the numerical model, it may be used to investigate a variety of planing problems, including the stepped plate, which is applicable to stepped planing hulls, as well as other planing geometries that may have multiple wetted surfaces that interact. Further, if the method is extended to 3-D, it may be used for modeling planing hulls with or without steps. However, an extension of this magnitude would require considerable work.

Finally, the results may aid in the design of experiments such as those performed by Wiggins et al. (2011); Zalek and Doctors (2010) to identify speeds at which the model

structure may exhibit very large loading or wetting, and to identify the regimes where the bow and/or stern seals are important.

APPENDIX A

On the Assumption of Two-Dimensionality

The numerical model presented in this thesis is based on 2-D theory, in a similar manner to Doctors (2009). In order for the theory to be valid, the flow within the cushion space must be able to be approximated as two-dimensional. In general, the interaction of the bow and stern wave systems becomes more two-dimensional as the length-to-beam ratio is reduced, and as the ship speed is reduced due to the larger contribution of the longitudinal wave system versus the transverse wave system inside the cushioned space. For a given length, as the beam decreases (i.e. the length-to-beam ratio increases), the interaction of the wake pattern of the bow of each sidehull (or corner of the pressure cushion) will begin to interact more upstream, and at some point create a wave focusing effect in the cushion space. However, for cases of sufficiently low speed and high length-to-beam ratio, these wave focusing effects are smaller and the longitudinal waves are dominant.

It is first useful to consider the wave resistance of a moving pressure distribution on the free surface. This method is typically used for estimating the cushion wavemaking resistance. Physically-speaking, a wave system is developed at both the bow and the stern of the cushion, where the pressure first rises from atmospheric to cushion pressure at the bow and drops from cushion pressure to atmospheric pressure at the stern. Each of these changes in pressure creates a wave system, and the interaction of these wave systems causes interference effects which are exhibited as humps in the wave resistance curve. Fig. A.1 shows the resistance coefficient for varying length-to-beam ratio (L_C/B_C) based on the 3-D

potential-flow simulations of Doctors and Sharma (1972). Both the magnitude and speed of the primary hump are seen to vary widely as a function of the length-to-beam ratio. This suggests that the interaction of the transverse wave systems generated by the bow corners of the cushion are important in this speed range. However, at the subhump, the magnitude varies as a function of the length-to-beam ratio, where a lower $L_C/B_C = 2.5$ corresponds to a larger peak due to a relatively wider pressure disturbance for a wider cushion, but the speed of the subhump remains pretty much constant for varying L_C/B_C. The fact that the speed remains constant for the subhump suggests that the interactions at these lower speeds are primarily due to the interaction of the longitudinal wave systems, whereas at the primary hump, transverse wave interference effects become important.

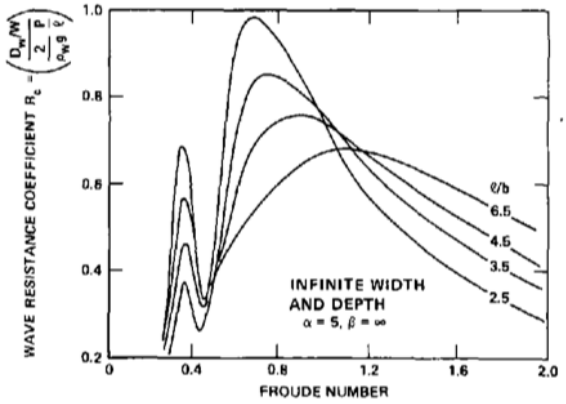

Figure A.1: Doctors' wave resistance coefficient (from Wilson et al., 1979)

The difference between the wave patterns can be viewed by observing the predicted wave profiles from Donnelly (2010), shown in Fig. A.2. These wave profiles are predicted for the T-Craft model, which has a length-to-beam ratio of $L_C/B_C = 4.1$. The results show that, for $Fr_C < 0.3$, the wave patterns within the cushion are fairly two-dimensional. Three-dimensional effects become visible at $Fr_C = 0.4$, although the flow is still fairly two-dimensional. At $Fr_C = 0.5$, the three-dimensional effects become pretty strong.

The wave patterns shown in Fig. A.2 showed that three-dimensional effects within the cushion can be seen for roughly $Fr_C > 0.4$. These results were for a model with $L_C/B_C = 4.1$. The results shown in this thesis are for the segmented SES model of Heber (1977),

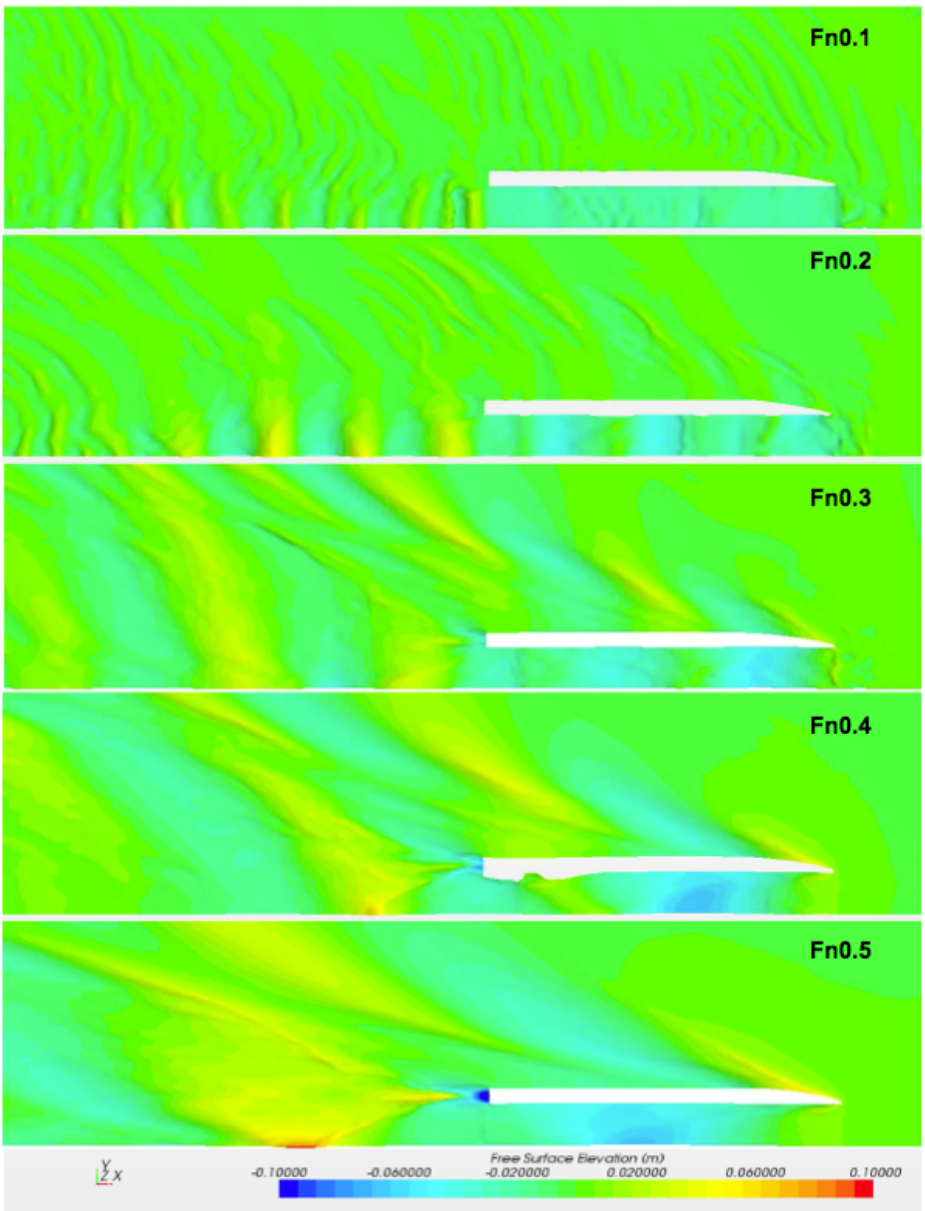

Figure A.2: Predicted wave profiles for T-Craft model ($L_C/B_C = 4.1$) (from Donnelly, 2010)

which had a length-to-beam ratio of $L_C/B_C = 2.5$. Thus, for this model, the results are expected to remain two-dimensional up to a larger Froude number, although the effects are difficult to quantify without further 3-D analysis. Nevertheless, since the seal-cushion-wave-vessel motion model is only applied for $0.35 < Fr_C < 0.45$, the 2-D assumption should be valid. Based on the qualitative observations of the experimental study, however, it is possible to determine whether the effects of three-dimensionality are important for that case, particularly near the subhump where the effects of the seals on the total resistance were measured to be greatest.

In Fig. A.3, an underwater view of the cushion space is shown for the segmented SES model of Heber (1977) at the subhump with SSBM seals, which is the model configuration that is simulated in Chapters 7 and 8 of this thesis. In the photograph, the bow is to the left and the stern is to the right. Although the photograph shows a lot of spray and three-dimensional effects outside the cushioned space, the interior cushioned space is fairly two-dimensional, particularly when the wetted surface of the stern seal is observed. Towards the right of the figure, there is a line of white froth that is observable along the length of the stern seal. This line corresponds to the intersection of the free surface with the cushion surface and shows a wetting of roughly 70% of the seal face length. The intersection is fairly two-dimensional, although some leakage near the sidewalls is visible. In any case, some three-dimensional wave effects are visible, particularly near the stern, and would be expected to become more apparent at higher speeds.

The subject of three-dimensional effects is one that is of great interest and importance, particularly when predicting the performance of vessels with higher length-to-beam ratios, such as the T-Craft. Hence, one of the recommendations for future work is that the 3-D problem is studied. In any case, the 2-D numerical model has been found to offer reasonable predictions in this thesis for the response at lower speeds for an SES with length-to-beam ratio of 2.5, and is found to offer a reasonable explanation for the physical cause of the subhump, which was experimentally measured but has not yet been predicted. In

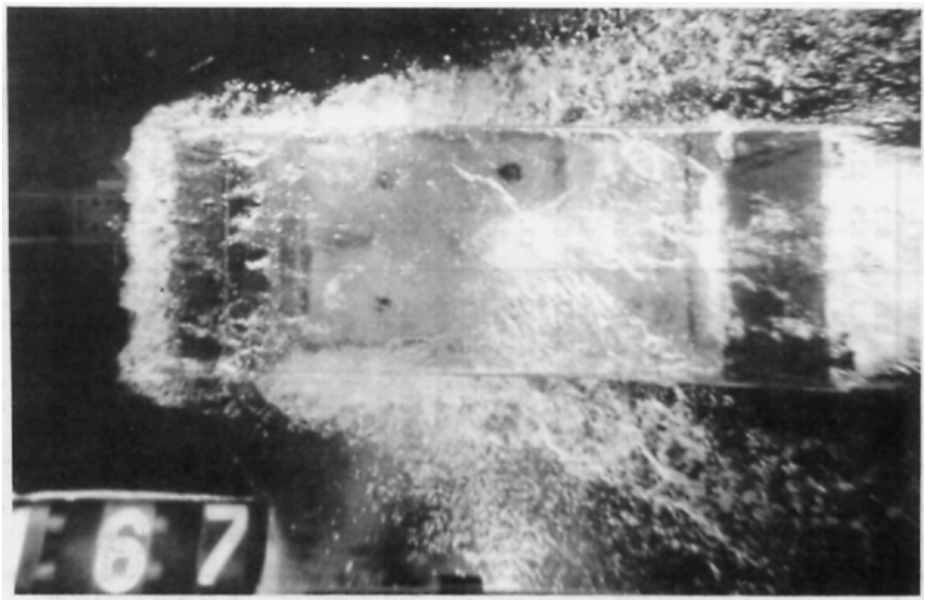

Figure A.3: Segmented SES model ($L_C/B_C = 2.5$) operating with SSBM seals at the subhump, looking from the bottom with the bow at the left. The wetted portion of the stern seal is visible on the right of the figure, where the intersection of the wave and the seal can be observed as a white froth that is nearly two-dimensional.

order to apply more confidently apply the 2-D model, the seal-cushion-wave-vessel motion is only applied for $Fr_C < 0.45$, where the waves inside the cushioned space are expected to be two-dimensional. For $Fr_C > 0.45$, a traditional resistance prediction method is employed which considers the effects of 3-D cushion wavemaking drag. Although the 2-D assumption should be valid for the cases modeled in this study, particularly in the speed range where seal effects are important, future extensions of the numerical method to consider the full 3-D problem are warranted. Thus, the work presented in this thesis offers a step towards the prediction of seal drag for a general 3-D SES that demonstrates the effects of seal interaction for a case where the flow can be approximated as 2-D; however, future extensions are necessary in order to account for 3-D wave effects within (and outside) the cushion space.

APPENDIX B

A Sample Hydrodynamic Solution for Multiple Planing Surfaces

In order to illustrate the flexibility of the linearized potential-flow method proposed in Chapter 3, a simulation was run for a quadruple-stepped planing flat plate. In this case, the plate is divided into five planing surfaces, each separated by a step. Although this example does not have any data with which to compare, it provides a nice illustration of the ability of the fluid model to consider complex problems of multiple planing surfaces.

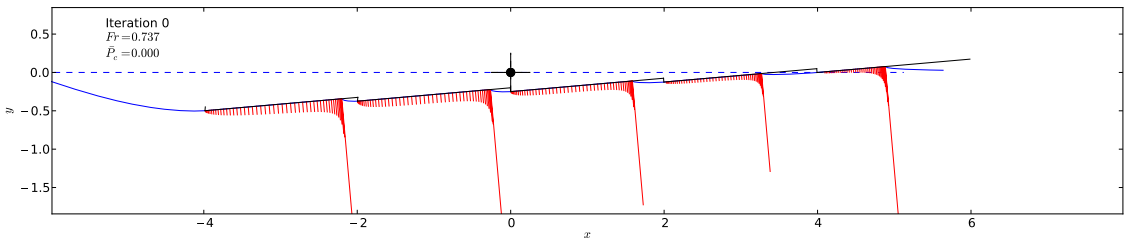

Figure B.1: An example of a quadruple-stepped plate, illustrating the ability of the fluid solver to consider multiple planing surfaces. The plate surface is shown in black, the free surface is shown in blue, the undeformed free surface is shown in a dashed blue line, and the pressure distributions are shown in red.

APPENDIX C

Extended Summary of Results from Segmented SES Model Tests

This appendix provides an overview of some of the major findings from the US Navy segmented model test, as reported by Heber (1977); Van Dyck and Fridsma (1979). The details of the model that was tested are described in Chapter 6. Since a wide array of parametric variations were measured during the model tests, the complete set will not be presented here. It is, however, useful to provide an overview of the results to show the main experimental findings and identify the trends.

C.1 Effects of Seal Type on Performance

In order to identify the differences and similarities between the three types of bow seals tested, the model was run at comparable conditions for the three bow seal modules (Fig. 6.4). Although there were minor differences in the model configuration resulting from physical differences in the seal designs, the conditions were similar. The results for these cases are shown in Fig. C.1. It is particularly informative to compare the results from all subplots simultaneously. From the total resistance plot, two resistance humps are apparent. For this model, the secondary hump is found to occur at $V_s = 5.2\,\text{fps}$ ($Fr_C = 0.4$) and the primary hump occurs at $V_s = 9.1\,\text{fps}$ ($Fr_C = 0.7$). The total drag at the secondary hump is seen to be larger in magnitude than the primary hump for all three of the seal types.

By investigating the bow seal drag and stern seal drag (Figs. C.1(d) and C.1(e)), it can be seen that the stern seal drag contributes largely at both the secondary and primary humps, while the bow seal's contribution exists primarily at the secondary hump. In addition, the stern seal drag is generally observed to be higher than the bow seal drag. The physical mechanism responsible for this observation was qualitatively described by Heber (1977) as an interaction effect of the waves generated by the bow and stern seals. The tests qualitatively identified that the seals exhibited a large immersion (high drag) when operating near a wave trough and a low immersion (low drag) when operating near a wave crest. This concept is illustrated in Fig. C.2. At the secondary hump, both seals are located at wave troughs, while at the primary hump, the bow seal is operating near a wave crest while the stern seal is operating in a wave trough. This effect demonstrates qualitatively what causes the large magnitudes of the drag humps in this case, and is consistent with the predictions shown in Chapters 7 and 8.

In addition to large changes in resistance near the humps, there is a corresponding set of trim and draft humps, which are highly related to the previously-described phenomena. In particular, the trim and draft are both found to increase at the secondary and primary humps.

Although the three types of seals tested were rather different in design, they were all found to exhibit similar trends and similar behavior. This fact increases confidence that a simplified numerical seal model may be able to accurately capture these effects.

C.2 Effect of Downstop Height for SSBM Seal

A series of runs were performed for the SSBM seal in order to test the effects of seal downstop height on the resistance components. The results are shown in Fig. C.3. The results show that the downstop height has a large effect on the magnitude of the total resistance. Interestingly, the downstop height settings that produce the largest resistance at the sec-

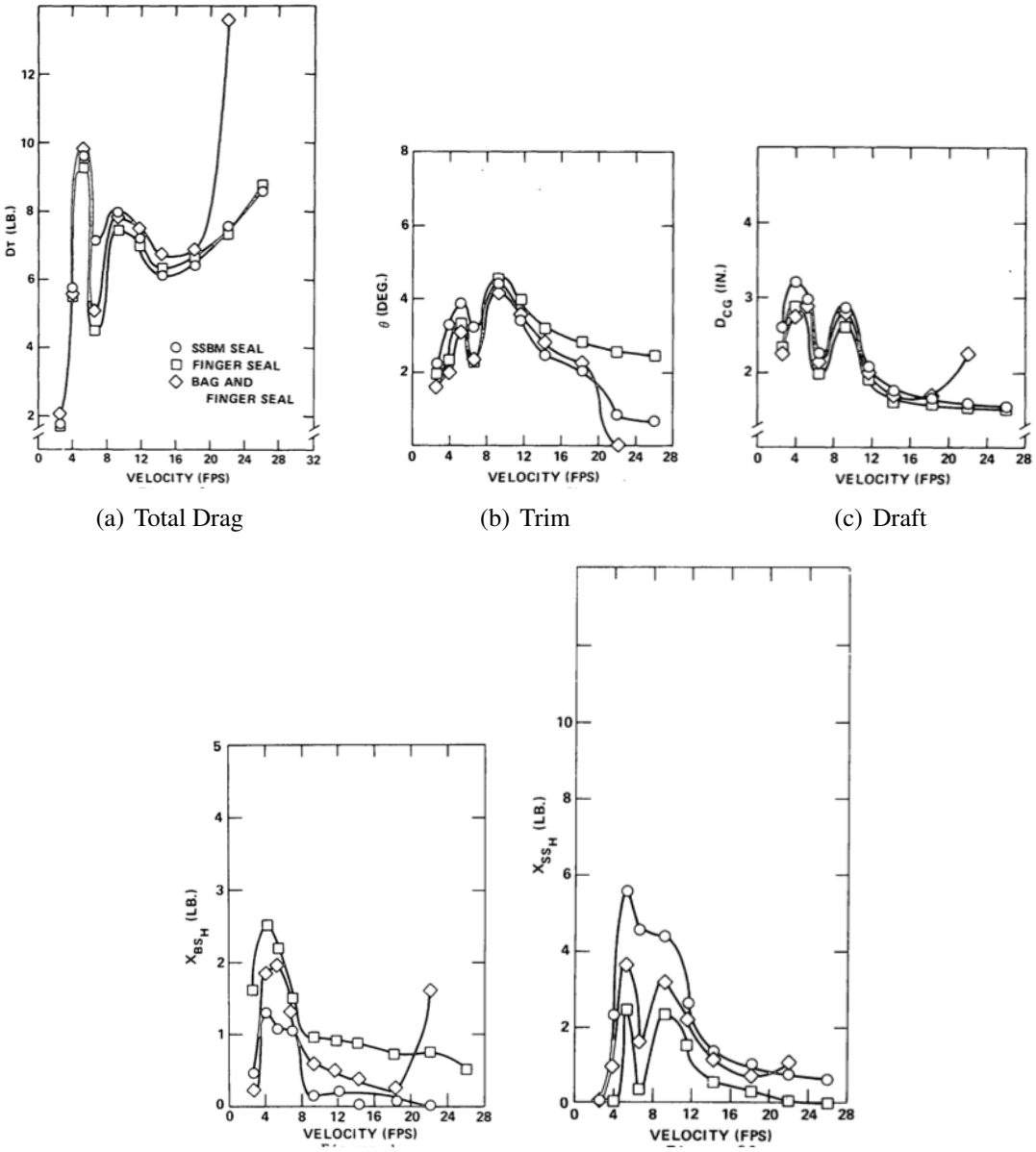

(a) Total Drag (b) Trim (c) Draft

(d) Bow Seal Drag (e) Stern Seal Drag

Figure C.1: Comparison of three bow seal configurations at comparable conditions. $\Delta = 45.36\,\mathrm{kg}\,(100\,\mathrm{lb})$, $h_{SF} = h_{SA} = 0.0\,\mathrm{cm}\,(0.0\,\mathrm{in})$. (from Heber, 1977)

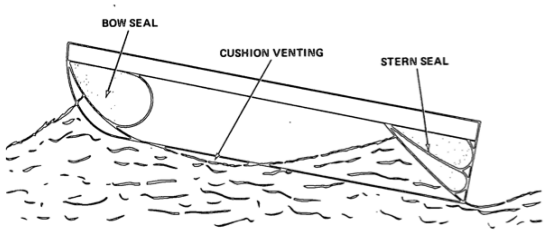

(a) At secondary hump

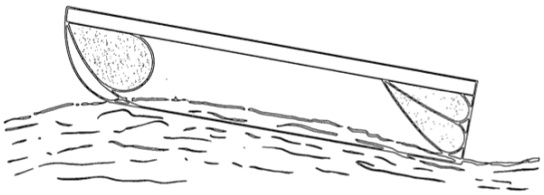

(b) At primary hump

Figure C.2: Relation of cushion waves to bow and stern seals (from Heber, 1977)

ondary hump produce the lowest resistance at the primary hump and higher speeds. The same trend was observed during model tests for the XR-1B test craft (Van Dyck, 1972). At the subhump, the pressure drag of the stern seal dominates and hence a stern seal that is more raised is beneficial due to lower form drag. Conversely, at post-hump speeds, the trend is reversed since raised seals will lead the the vessel operating at a higher draft, which increases the frictional resistance. Consequently, a seal that is lowered is more beneficial at higher speeds. This suggests that the optimal seal configuration should vary with operating speed and promotes the possible use of actively-controlled seals.

C.3 Effect of Downstop Height for Finger Seal

Although the finger seal is not modeled in this thesis, it is useful to show the effect of downstop height for the finger bow seal tests in addition to the SSBM bow seal tests, which were shown in the previous section. As is shown in Fig. C.4, the same trends are shown for the finger seal as for the SSBM seal. It should be noted that in these cases, only the stern seal has a downstop, and the finger seal is always located at the same initial position. These results suggest that the qualities of the secondary and primary humps are primarily

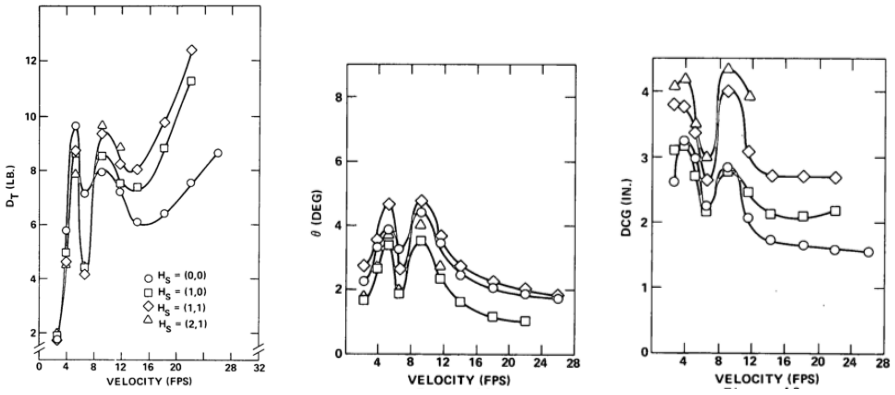

(a) Total Drag (b) Trim (c) Draft

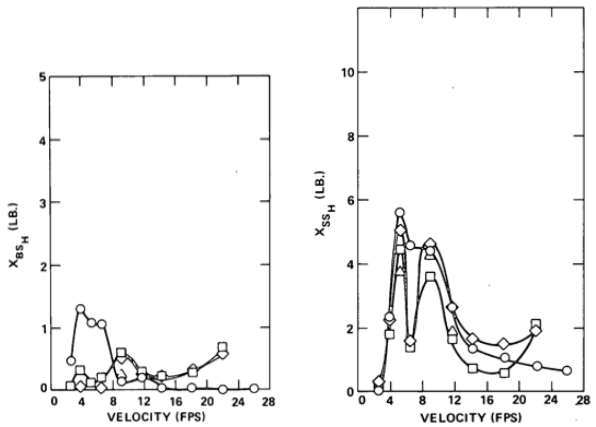

(d) Bow Seal Drag (e) Stern Seal Drag

Figure C.3: Comparison of downstop seal height setting ($H_S = (h_{SF}, h_{SA})$) for SSBM seal. $\Delta = 45.36\,\text{kg}\,(100\,\text{lb})$ (from Heber, 1977)

dependent on the stern seal height, which is related to the overall stiffness of the stern seal in that changes in the stern seal stiffness or internal seal pressure will lead to changes in the seal height.

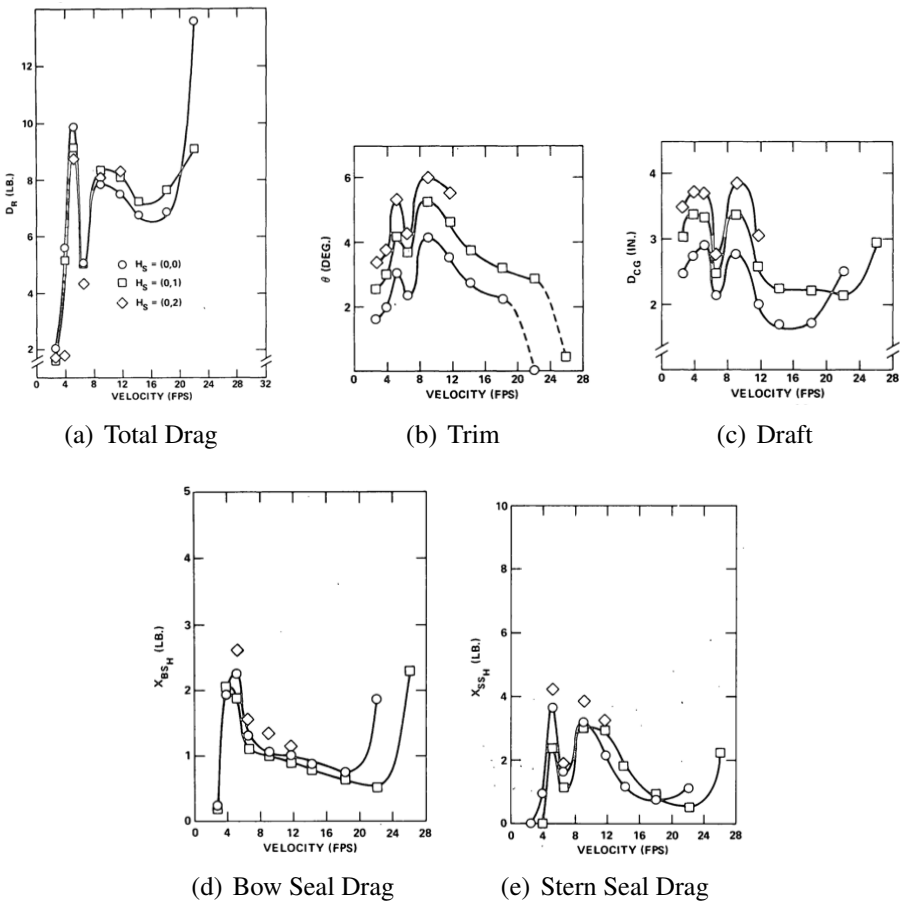

(a) Total Drag (b) Trim (c) Draft

(d) Bow Seal Drag (e) Stern Seal Drag

Figure C.4: Comparison of downstop seal height setting ($H_S = (h_{SF}, h_{SA})$) for Finger seal. $\Delta = 45.36\,\text{kg}\,(100\,\text{lb})$ (from Heber, 1977)

C.4 Effects for Other Parametric Variations

In addition to variations in seal type and seal stop height, which were discussed in the previous sections, the experimental study investigated the effects of fan flow rate, L_{CG}, and displacement on the vessel performance. The fan flow rate was found to yield relatively small effects on the resistance characteristics. Additionally, the proposed numerical model does not consider the dynamics of the fan system. The effects of seal pressure ratio

($P_{s,f}/P_C$) were explored, however negligible effects were observed for all three seals. In the case of the SSBM seal, this is likely due to the large stiffness of the planing face of the bow seal. In the case of the Finger and Bag and Finger seals, the portion of the seal in contact with the water is composed of fabric fingers, and hence is not affected by changes in internal seal pressure. Consequently, these effects are not compared in this study. The range of seal pressure ratios that were tested was very small ($P_{s,f}/P_C = 1.05 - 1.3$). It is therefore difficult to know what the effects of seal pressure ratio will truly be.

The effects of L_{CG} variation for the SSBM bow seal are shown in Fig. C.5. It was found that the L_{CG} location had a large effect on the total resistance, particularly at the primary and secondary drag humps. This effect can be partially attributed to the fact that the seals had to provide varying amounts of lift in order for the model to reach equilibrium in trim and draft as the L_{CG} was moved forward or aft of the "optimal" configuration. The results are not simple in the sense that moving the L_{CG} one way or the other does not yield an increase or decrease at all speeds. The effect is more complicated than that, owing to the phasing of the cushion-generated wave system in combination with the amount of lift that is required from each seal at each particular operating speed.

Finally, the displacement was varied for two cases: $100\,\mathrm{lb}$ and $80\,\mathrm{lb}$. The results are shown in Fig. C.6. The results show that the model displacement had a large effect on the total resistance, body attitude, and seal loads.

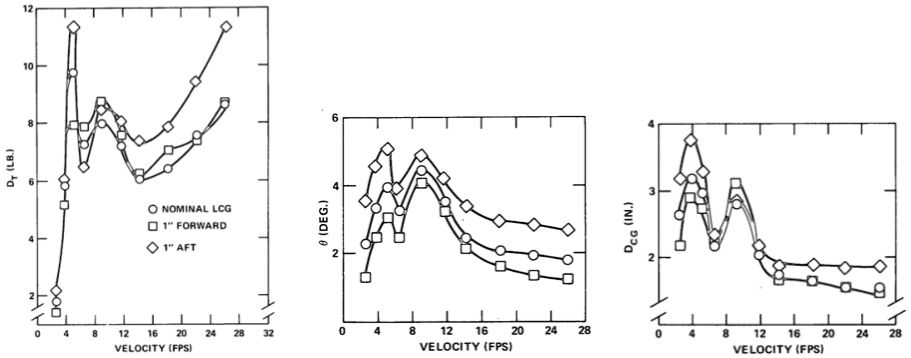

(a) Total Drag (b) Trim (c) Draft

(d) Bow Seal Drag (e) Stern Seal Drag

Figure C.5: Comparison of L_{CG} positions for SSBM bow seal. $\Delta = 45.36\,\text{kg}\,(100\,\text{lb})$ (from Heber, 1977)

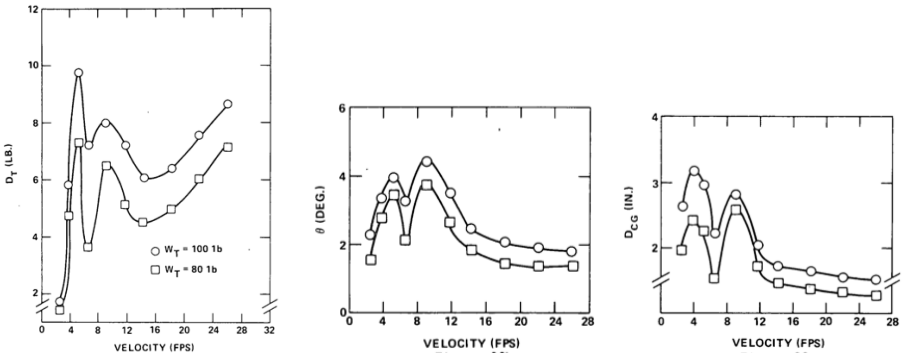

(a) Total Drag (b) Trim (c) Draft

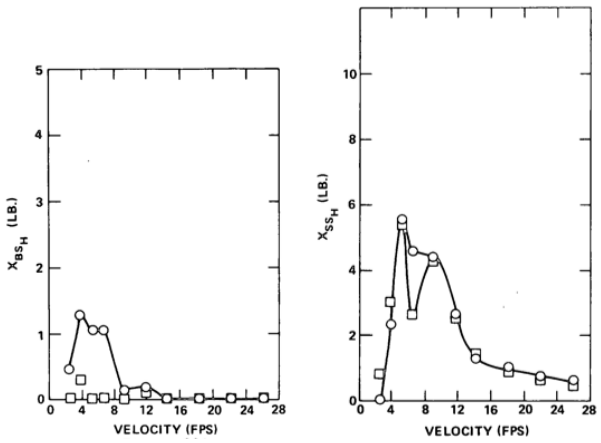

(d) Bow Seal Drag (e) Stern Seal Drag

Figure C.6: Comparison of results for SSBM bow seal for two different model displacements (from Heber, 1977)

APPENDIX D

Overview of 3-D Wave Resistance Prediction

In order to estimate the total resistance of the full, 3-D segmented model tested by Heber (1977), three major components of the resistance must be estimated, as discussed in Chapter 2 and defined in Eq. (2.2). The seal resistance (R_S) is calculated using the 2-D seal resistance model proposed in this thesis and the sidewall frictional resistance ($R_{F,\mathrm{SW}}$) is calculated based on an estimation of the sidewall form and frictional drag using a friction line and experimental tare runs, as described in Chapter 6. The final major resistance component that must be considered is the cushion wavemaking resistance (R_W), which results from the free-surface wave generation due to the presence of the air cushion.

In the current work, the 3-D wavemaking resistance is estimated using the method proposed by Doctors and Sharma (1972), which has been shown to be accurate for many cases in the past. In this method, the pressure cushion is represented by a 2-D smoothed rectangular pressure patch acting on the free surface. The distribution is similar to the 1-D pressure distribution presented in Section 3.6.2 and defined by Eq. (3.50) (which yields the wave resistance for a 2-D SES). For a 3-D SES, the pressure distribution is extended to a 2-D pressure patch, which is defined by the following equation:

$$p(x,z) = \frac{1}{4} P_C \left[\tanh \alpha_s \left(x + \frac{L_C}{2} \right) - \tanh \alpha_s \left(x - \frac{L_C}{2} \right) \right] \times \left[\tanh \beta_s \left(z + \frac{B_C}{2} \right) - \tanh \beta_s \left(z - \frac{B_C}{2} \right) \right] \tag{D.1}$$

where α_s is the longitudinal smoothing factor and β_s is the transverse smoothing factor. For the case of an SES, which has sidehulls, the pressure drop is typically assumed to be sharp at the sidewalls (i.e. $\beta_s = \infty$).

Doctors' wave resistance coefficient is shown in Fig. D.1, where it can be seen that the length-to-beam ratio has a large effect on the wave resistance.

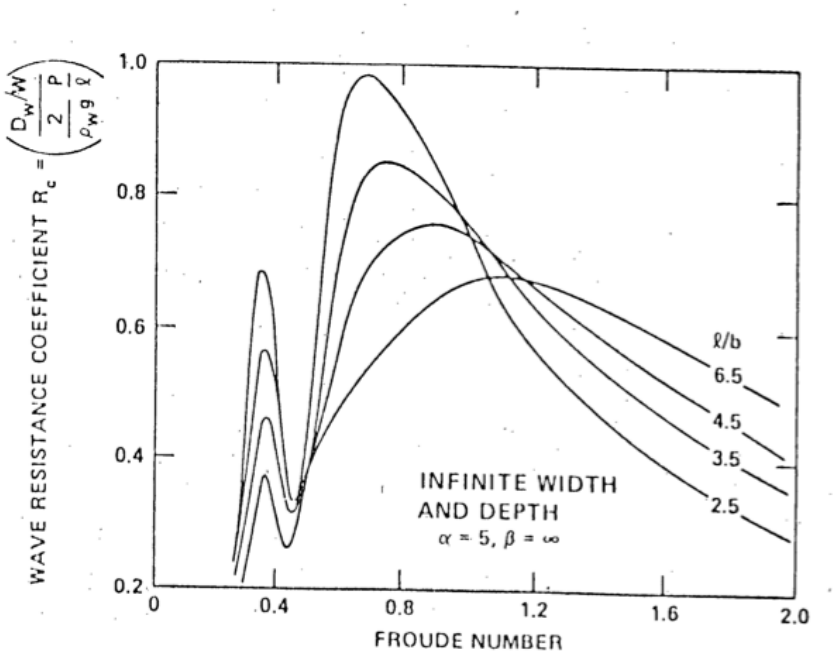

Figure D.1: Doctors' wave resistance coefficient for varying cushion length-to-beam ratio (L_C/B_C) with $\alpha_s = 5$, $\beta_s = \infty$ (from Wilson et al., 1979)

The length-to-beam ratio of the segmented SES model that was tested by Heber (1977) (described in detail in Chapter 6 and Appendix C) had a length-to-beam ratio of 2.5. In order to determine the appropriate longitudinal smoothing factor (α_s), a series of experimental runs was performed where the model was held just above the free surface such that no part of the model touched the water and the Froude number based on the cushion length (Fr_C) was varied. The fans were turned on and seals were included to contain the pressure cushion. The results of these tests are shown in Fig. D.2. The results show a good comparison between experimental results and the numerical results of Doctors and Sharma (1972) using the following parameters: $L_C/B_C = 2.5$, $\alpha_s = 5$, $\beta_s = \infty$. In addition, it was

found that a multiplicative factor of 1.2 was necessary to match the two sets of data. Using these parameters, the cushion wavemaking drag can be calculated for varying Fr_C and P_C. This is the method used in Chapters 7 and 8 for estimating the 3-D cushion wavemaking contribution to the total resistance.

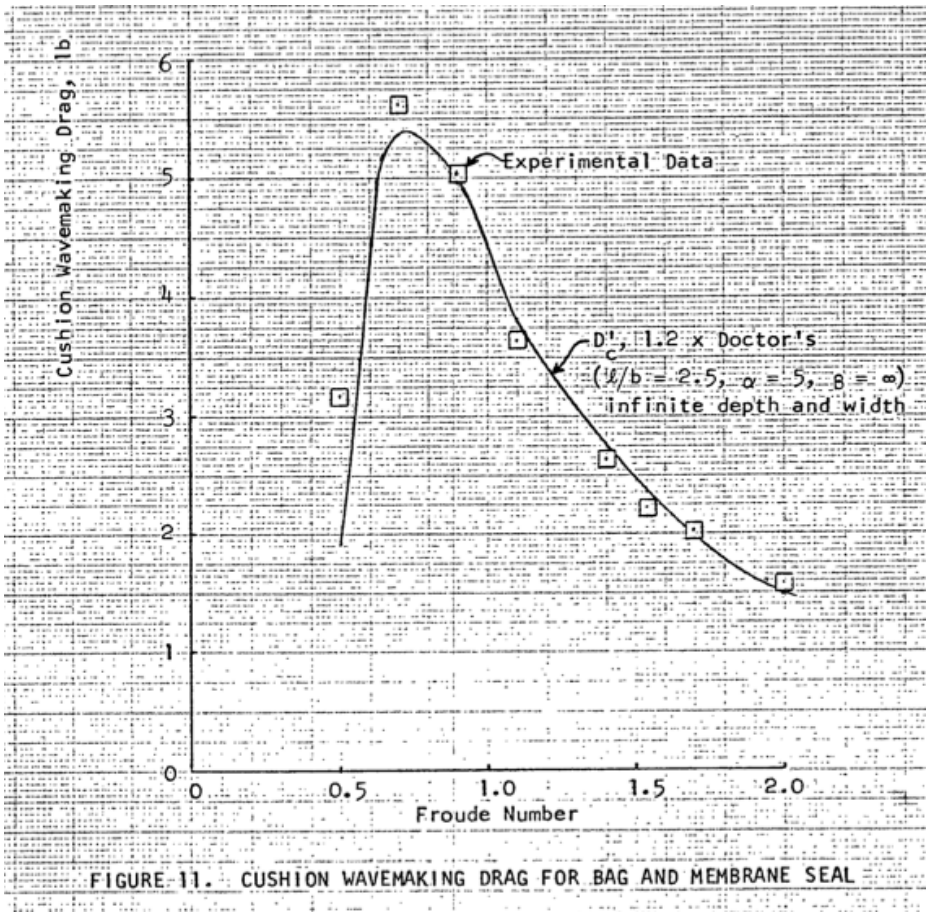

Figure D.2: Experimentally-measured and numerically-predicted cushion wavemaking drag for segmented SES model without contact with the water (i.e. pressure cushion only) (from Van Dyck and Fridsma, 1979)

BIBLIOGRAPHY

IMO Resolution MEPC.212(63) - 2012 guidelines on the method of calculation of the attained energy efficiency design index (EEDI) for new ships, March 2012.

Abrahamowitz, M. and Stegun, I. A. *Handbook of Mathematical Functions*. Applied Mathematics Seris-55, Nat. Bureau of Standards, U.S. Govt. Printing Office, Washington, 1965.

Barratt, M. J. The wave drag of a hovercraft. *Journal of Fluid Mechanics*, 22:39–47, 1965.

Bathe, K. J. *Finite Element Procedures in Engineering Analysis*. Prentice Hall, 1982.

Besch, P. K. Motions of bow fingers in a surface effect ship flexible seal. Technical report, David Taylor Naval Ship Research and Development Center, West Bethesda, MD 20084, 1976.

Bhushan, S., Stern, F., and Doctors, L. J. T-craft calm water resistance and motions, and seakeeping in regular waves. In *Proceedings of the 11th Conference on Fast Sea Transportation (FAST '11)*, September 2011.

Bishop, R. C., Silver, A. L., Tahmasian, D., Lee, S. S., Park, J. T., Snyder, L. A., and Kim, J. T-Craft seabase seakeeping model test data report. Technical Report NSWCCD-50-TR-2009/055, Naval Surface Warfare Center Carderock Division, 2009.

Broyden, C. G. A class of methods for solving nonlinear simultaneous equations. *Mathematics of Computation*, 19:577–593, 1965.

Butler, E. A. The surface effect ship. *Naval Engineers Journal*, 97(2):200–258, February 1985.

Doctors, L. J. Representation of planing surfaces by finite pressure elements. In *Proceedings of the Fifth Australasian Conference on Hydraulics and Fluid Mechanics*, volume 2, pages 480–488, Christchurch, New Zealand, December 1974.

Doctors, L. J. Theory of compliant planing surfaces. Technical report, Aviation and Surface Effects Department, David W. Taylor Naval Ship Reserach and Development Center, Bethesda, Maryland 20084, June 1977.

Doctors, L. J. Hydrodynamics of high-speed small craft. Technical Report 292, University of Michigan, January 1985.

Doctors, L. J. On the use of pressure distributions to model the hydrodynamics of air-cushion vehicles and surface-effect ships. *Naval Engineers Journal*, 105(2):69–89, March 1993.

Doctors, L. J. A study of the resistance characteristics of surface-effect-ship seals. In *Proceedings of the High-Performance Marine-Vehicle Symposium*, November 2009.

Doctors, L. J. and McKesson, C. B. The resistance components of a surface-effect ship. In *Proceedings of the 26th Symposium on Naval Hydrodynamics*, September 2006.

Doctors, L. J. and Sharma, S. D. Wave resistance of an air-cushion vehicle in steady and accelerated motion. *Journal of Ship Research*, 16(4):248–260, December 1972.

Donnelly, D. J. and Neu, W. L. Numerical simulation of flow about a surface-effect ship. In *Proceedings of the 11th Conference on Fast Sea Transportation (FAST '11)*, September 2011.

Donnelly, D. J. Numerical simulation of surface effect ship air cushion and free surface interaction. Master's thesis, Virginia Polytechnic Institute and State University, Blacksburg, VA, September 2010.

Faltinsen, O. M. *Hydrodynamics of high-speed marine vehicles*. Cambridge University Press, 2005.

Fridman, G. and Tuck, E. O. Two-dimensional finite-depth planing hydrofoil under gravity. In *High-Speed Hydrodynamics and Numerical Simulation*, Kemerovo, Russia, June 2006.

Garland, W. and Maki, K. J. A numerical study of a two-dimensional stepped planing surface. *Journal of Ship Production and Design*, 28(2):1–13, May 2012.

Ghavanloo, E. and Daneshmand, F. Analytical analysis of the static interaction of fluid and cylindrical membrane structures. *European Journal of Mechanics - A/Solids*, 29(4):600 – 610, 2010. ISSN 0997-7538.

Heber Jr., C. E. An analysis of seal loads and their effect on the performance of a surface effect ship in calm water. Technical Report 77-0056, David W. Taylor Naval Ship Research and Development Center, December 1977.

Hirt, C. and Nichols, B. Volume of fluid (VOF) method for the dynamics of free boundaries. *Journal of Computational Physics*, 39(1):201–225, 1981.

Hsieh, J.-C., Plaut, R., and Yucel, O. Vibrations of an inextensible cylindrical membrane inflated with liquid. *Journal of Fluids and Structures*, 3(2):151 – 163, 1989. ISSN 0889-9746.

Jabbarizadeh, S. *New Analytical and Numerical Methods in Structural Analysis of Nonlinear Two-Dimensional Curved Membranes*. PhD thesis, University of Michigan, 2012.

Jabbarizadeh, S. and Karr, D. G. Analytical and numerical analyses of partially submerged membranes. *Journal of Engineering Mechanics*, in press, 2013.

Karr, D. G. and Jabbarizadeh, S. Membrane finite element analysis: A report in support of materials presented at the T-Craft tool development review meeting. Technical report, University of Michigan, 2010.

Kramer, M. R., Young, Y. L., and Maki, K. J. Numerical prediction of the flow past a 2-D planing plate at low Froude number. *Ocean Engineering*, under review, 2012.

Kramer, M. R., Young, Y. L., and Motley, M. R. An integrated probability-based propulsor-hull matching methodology. *Journal of Offshore Mechanics and Arctic Engineering*, 135 (1):011801, February 2013.

Lamb, H. *Hydrodynamics*. Dover Publications, New York, 6th edition, 1945.

Maki, K. J., Broglia, R., Doctors, L. J., and Di Mascio, A. Nonlinear wave resistance of a two-dimensional pressure patch moving on a free surface. *Ocean Engineering*, 39: 62–71, 2012.

Maki, K. J., Broglia, R., Doctors, L. J., and Di Mascio, A. Numerical investigation of the components of calm-water resistance of a surface-effect ship. *Ocean Engineering*, in press, 2013.

Maki, K. J. *Transom Stern Hydrodynamics*. Phd, University of Michigan, 2006.

Maki, K. J., Doctors, L. J., Broglia, R., McKesson, C., and DiMascio, A. Calm-water resistance prediction of a surface-effect ship. In *Proceedings of the 10th International Conference on Fast Sea Transportation (FAST '09)*, Athens, Greece, October 2009.

Mantle, P. J. Development of the USN surface effect ship, SES-100B. *Naval Engineers Journal*, 85(2):65–78, October 1973.

Naval-Technology.com. Skjold class missile fast patrol boats, norway.

Newman, J. N. and Poole, F. A. P. The wave resistance of a moving pressure distribution in a canal. *Schiffstechnik*, 9(45):21–26, 1962.

OpenFOAM. v2.0.1 documentation, 2011.

Ryken, J. Test data analysis and correlation report: SES-100B finger motions and finger drag. Technical Report 7593-925003, Bell Aerospace Textron, September 1978.

Sedov, L. *Two-dimensional problems of hydrodynamics and aerodynamics*, chapter 7, pages 238–282. Interscience Publishers, 1965.

Steen, S. Experiences with seakeeping capabilities of SES ships. In *RTO AVT Symposium on "Habitability of Combat and Transport Vehicles: Noise, Vibration, and Motion"*, Prague, Czech Republic, 2004.

Van Dyck, R. L. Hump and sub-hump performance tests of a surface effect ship, Part I - Deep and shallow water tests. Letter Report 1592, Stevens Instutute of Technology, April 1972.

Van Dyck, R. L. and Fridsma, G. The contribution of seals and sidewalls to the force and moment characteristics of an SES. Technical Report SIT-DL-79-1861, Davidson Laboratory, Stevens Institute of Technology, Hoboken, NJ, USA, April 1979.

Wars, N. Marines: From procurement tragedy to triumph. URL http://newwars.wordpress.com/2010/05/11/marines-from-procurement-tragedy-to-triumph/.

Wiggins, A. D., Zalek, S. F., Perlin, M., Ceccio, S. L., Doctors, L. J., and Etter, R. J. Development of a large scale surface effect ship bow seal testing platform. In *Proceedings of the 11th Conference on Fast Sea Transportation (FAST '11)*, September 2011.

Wilson, R. A., Wells, S. M., and Heber, C. E. Powering prediction for surface effect ships based on model results. *Journal of Hydronautics*, 13(4):113–119, October 1979.

Wu, T. Y.-T. W. and Whitney, A. K. Theory of optimum shapes in free-surface flows. part 1. optimum profile of sprayless planing surface. *Journal of Fluid Mechanics*, 55:439–455, 1972.

Young, Y. L., Savander, B. R., and Kramer, M. R. Numerical investigation of the impact of SES-Waterjet interactions and flow non-uniformity on pump performance. In *Proceedings of the 11th Conference on Fast Sea Transportation (FAST '11)*, September 2011.

Yun, L. and Bliault, A. *Theory and Design of Air Cushion Craft*. Butterworth-Heinemann, 2000.

Zalek, S. F. and Doctors, L. J. Experimental study of the resistance of surface-effect ship seals. In *Proceedings of the Twenty-Eight Symposium on Naval Hydrodynamics*, Pasadena, California, 2010.

Zalek, S. F., Karr, D. G., Jabbarizadeh, S., and Maki, K. J. Modeling of air cushion vehicle's flexible seals under steady state conditions. *Ocean Systems Engineering*, 1(1):17–29, 2011.